Investigating persulfidation-related protective mechanisms in aging and age-related diseases



Doctoral thesis

for

the award of the doctoral degree

of the Faculty of Mathematics and Natural Sciences

of the University of Cologne

submitted by

Thibaut Vignane

2024

The work presented in this dissertation have been performed between October 2020 and September 2024 under the supervision of Dr. Milos Filipovic at the Leibniz Institute for Analytical Sciences - ISAS – eV., Otto-Hahn str 6B, 44227 Dortmund. This research was supported by the European Research Council (ERC) Consolidator Grant.





European Research Council

Established by the European Commission

Abstract

Hydrogen sulfide (H_2S)-mediated protein persulfidation is an evolutionarily conserved posttranslational modification that occurs at the cysteine residues, playing an important role in redox signaling and regulation of numerous biological functions. Although the importance of persulfidation in these processes has been recognized, its precise role remained elusive until recent advancements enabled the selective labeling of persulfidated proteins. These developments have highlighted the involvement of H_2S and persulfidation in response to oxidative stress, aging, and neurodegeneration. Notably, persulfidation plays a central role in the protection against cysteine overoxidation, process that has been proposed to be impaired with age. Comprehensive, proteome-wide studies on age-induced changes in cysteine posttranslational modifications have been scarce.

In this study, we employed chemoselective proteomic approaches to monitor age-related changes in cysteine persulfidation (RSSH), sulfenylation (RSOH), and sulfonylation (RSO_3H) in the brains of aging wild-type mice as well as mice lacking H_2S producing enzyme cystathionine gamma lyase (CSE). Our in-depth temporal analysis of RSSH and RSOH reveals a steady increase in cysteine oxidation to RSOH with age, while the protective persulfidation decreases, representing a resource for all researchers interested in this field. Moreover, we demonstrate, for the first time, the accumulation of cysteine sulfonylation, which is more pronounced in mice lacking CSE.

Furthermore, while H_2S has been recognized as a protective agent against various neurodegenerative diseases, the mechanisms underlying its action have remained unclear. Our findings demonstrate that the absence of H_2S leads to protein

aggregation and neurodegeneration. Conversely, we showed that H_2S prevents protein aggregation by regulating the liquid-liquid phase separation (LLPS) of key proteins. Specifically, we identified that cysteine overoxidation of synapsin 1, G3BP2 and GAPDH tends to increase their propensity to undergo phase separation whereas H_2S-controlled persulfidation facilitates the dissolution of these condensates. We propose that persulfidation acts as a protective mechanism against aberrant phase separation driven by cysteine overoxidation. In the context of age-related decline in persulfidation, increased cysteine overoxidation may predispose the brain for neurodegeneration.

Finally, we extended the relevance of H_2S protective mechanism to metaplastic Barrett's esophagus (BE) disease. BE occurs under chronic acid reflux increasing oxidative stress and remodeling of normal squamous mucosa. Using our chemoproteomic approaches on human samples, we identified potential biomarkers for the progression of the disease in both total proteome changes and persulfidome changes. These results allowed us to better understand the remodeling in metaplastic tissues and to propose potential therapeutic approaches using H_2S donors.

Zusammenfassung

Schwefelwasserstoff (H_2S)-vermittelte Protein-Persulfidierung ist eine evolutionär konservierte posttranslationale Modifikation, die an den Cysteinresten auftritt und eine wichtige Rolle beim Redox-Signalweg, sowie in der Regulation zahlreicher biologischer Funktionen spielt. Obwohl die Bedeutung der Persulfidierung in diesen Prozessen anerkannt ist, blieb ihre genaue Rolle lange Zeit unklar, bis jüngste Fortschritte die selektive Markierung persulfidierter Proteine ermöglichten. Diese Entwicklungen haben die Beteiligung von H_2S und der Persulfidierung an der Reaktion auf oxidativen Stress, Alterung und Neurodegeneration hervorgehoben. Bemerkenswerterweise spielt die Persulfidierung eine zentrale Rolle beim Schutz vor Cystein-Überoxidation, einem Prozess, der im Alter beeinträchtigt sein könnte. Umfassende, proteomweite Studien zu altersbedingten Veränderungen der posttranslationalen Cystein-Modifikationen sind jedoch selten.

In dieser Studie setzten wir chemoselektive proteomische Verfahren ein, um altersbedingte Veränderungen in der Cystein-Persulfidierung (RSSH), Sulfenylierung (RSOH) und Sulfonylierung (RSO_3H) im Gehirn alternder Wildtyp-Mäuse, sowie von Mäusen ohne das H_2S-produzierende Enzym Cystathionin-γ-Lyase (CSE), zu untersuchen. Unsere detaillierte zeitliche Analyse von RSSH und RSOH zeigt einen stetigen Anstieg der Cystein-Oxidation zu RSOH mit zunehmendem Alter, während die schützende Persulfidierung abnimmt, was eine wertvolle Ressource für alle Forschenden auf diesem Gebiet darstellt. Darüber hinaus zeigen wir erstmals die Akkumulation von Cystein-Sulfonylierung, die bei Mäusen ohne CSE stärker ausgeprägt ist.

Während H_2S als Schutzmittel gegen verschiedene neurodegenerative Erkrankungen anerkannt ist, blieben die Mechanismen, die seiner Wirkung zugrunde liegen, unklar. Unsere Ergebnisse zeigen, dass das Fehlen von H_2S zu Proteinaggregation und Neurodegeneration führt. Im Gegensatz dazu konnten wir nachweisen, dass H_2S die Proteinaggregation durch die Regulation der Flüssig-Flüssig-Phasentrennung (LLPS) von Schlüsselproteinen verhindert. Insbesondere identifizierten wir, dass die Cystein-Überoxidation von Synapsin 1, G3BP2 und GAPDH ihre Neigung zur Phasentrennung erhöht, während die H_2S-kontrollierte Persulfidierung die Auflösung dieser Kondensate erleichtert. Wir schlagen vor, dass die Persulfidierung als Schutzmechanismus gegen eine durch Cystein-Überoxidation hervorgerufene fehlerhafte Phasentrennung wirkt. Im Kontext des altersbedingten Rückgangs der Persulfidierung könnte eine erhöhte Cystein-Überoxidation das Gehirn für Neurodegeneration anfälliger machen.

Abschließend erweiterten wir die Relevanz des H_2S-Schutzmechanismus auf die metaplastische Barrett-Ösophagus (BE)-Erkrankung. BE tritt unter chronischem saurem Reflux auf, was oxidativen Stress und eine Umgestaltung der normalen Plattenepithel-Mukosa erhöht. Mithilfe unserer chemoproteomischen Verfahren an menschlichen Proben identifizierten wir potenzielle Biomarker für das Fortschreiten der Erkrankung sowohl in Bezug auf Veränderungen im Gesamtproteom als auch im Persulfidom. Diese Ergebnisse ermöglichten es uns, die Umgestaltungsprozesse in metaplastischem Gewebe besser zu verstehen und potenzielle therapeutische Ansätze unter Verwendung von H_2S-Donoren vorzuschlagen.

Table of content

Abstract I

Zusammenfassung III

Table of content V

List of abbreviations VIII

List of main figures XI

List of supplementary tables XIV

1. Introduction 1

1.1. From hydrogen sulfide to persulfidation 1

1.1.1. Chemical properties of hydrogen sulfide 1

1.1.2. H_2S production in plants and animals 2

1.1.3. H_2S biological role 10

1.2. Biological chemistry of protein persulfidation 12

1.2.1. Acidity and nucleophilicity 12

1.2.2. Electrophilicity and stability 14

1.2.3. Reaction with one- and two-electron oxidants 16

1.3. Persulfide detection 19

1.3.4. Labelling protein persulfides 20

1.4. Cellular mechanism of persulfide formation and removal 25

1.4.1. Disulfide reduction by H_2S as a source of protein persulfidation 25

1.4.2. Metal-catalyzed protein persulfidation via radical formation 26

1.4.3. Reaction of RSOH with H_2S 28

1.4.4. Enzymatic production of LMW RSSH 30

1.4.5. Transpersulfidation 32

1.4.6. Depersulfidation 35

1.5. Persulfidation as a regulator of protein function 38

1.5.1. Gain of enzymatic activity 38

1.5.2. Loss of enzymatic activity 40

1.6. Persulfidation in aging and neurodegeneration 41

1.6.1. Imsbalance in persulfidation: new aging hallmark? 44

1.6.2. Persulfidation protects against neurodegeneration.....45
1.6.3. Persulfidation's protection against over-oxidation of proteins 50
1.7. Biomolecular condensates: definition and biological role 53
1.7.1. Driving forces and characteristics of biomolecular condensates.....53
1.7.2. Molecular aging of the condensates.....55
1.7.3. Posttranslational modification regulates the formation, dissolution, and aging of LLPS 57
1.7.4. Biomolecular condensates and neurodegeneration.....59
2. Project aims 61
3. Protein thiol alterations drive aberrant phase separation in aging brain64
3.1. Abstract..... 66
3.2. Introduction 67
3.3. Results 68
3.3.1. Aging is associated with proteome wide increase of PSOH and decrease of PSSH 68
3.3.2. CSE is a main regulator of the PSOH to PSSH switch in the aging brain 78
3.3.3. Sulfonylation stimulates while persulfidation dissolves GAPDH phase separation 95
3.3.4. LLPS of GAPDH affects its activity and reactivity of its cysteines.....102
3.3.5. Sulfonylation-driven aberrant LLPS of GAPDH leads to protein aggregation in aging brain 105
3.4. Discussion 108
3.5. Material and methods 110
3.6. References 124
4. PSOH/PSSH redox switch of G3BP2 controls dynamics of stress granule formation and dissolution 129
4.1. Abstract..... 131
4.2. Introduction 132
4.3. Results 134
4.4. Discussion 144
4.5. Material and methods 146
4.6. References 152

5. Pathway-specific persulfidation shifts and sulfide signaling underlie esophageal (patho)physiology 155

5.1. Context of the study: H_2S role in intestinal tract protection 155

5.2. Abstract 159

5.3. Introduction 160

5.4. Results 162

5.4.1. PSSH level and H_2S-bioavailability are altered in metaplastic epithelium 162

5.4.2. PSSH-shifts are developmental and pathway-specific in SE and BE 168

5.4.3. Interventional restoration/inhibition of H_2S-signaling affects metaplastic turnover 174

5.4.4. PSSH-shifts of metaplasia-activating IL-1β, cyclooxygenase (COX)-2/PGE2 and mammalian target of rapamycin (mTOR) pathways. H_2S as a rescue molecule 188

5.5. Discussion 193

5.6. Material and methods 198

5.7. References 217

6. General discussion 221

6.1. Age-associated imbalance in cysteine PTMs drives aberrant phase separation and aggregation in aging brain 225

6.1.1. G3BP2 redox switch regulates stress granule dynamics 229

6.1.2. Over-oxidation of GAPDH enhances its phase separation and forces its phase transition to aggregation 231

6.2. Persulfidation analysis of Barrett's esophagus reveal the essential role of H_2S and persulfidation in the disease 233

References 236

List of abbreviations

3-MP	3-mercaptopyruvate
AD	Alzheimer's disease
AdoMet	S-adenosyl-methionine
APS	ATP sulfurylase 1
ATF4	Activating transcription factor 4
BACE-1	Protein cleaving enzyme 1
BE	Barrett's oesophagus
BTA	Biotin thiol assay
CARS	Cysteinyl-tRNA synthetase
CAT	Cysteine aminotransferase
CBS	Cystathionine β-synthase
CoA	Coenzyme A
cPGA	Cyclic 3-phosphoglyceric anhydride
CSE	Cystathionine gamma-lyase
CYSC1	Cyanoalanine synthase C1
Cyt C	Cytochrome C
DAO	D-amino acid oxidase
DJ1	Protein deglycase DJ-1
DTT	Dithiothreitol
EGF	Epidermal growth factor
EGFR	Epidermal growth factor receptor
ER	Endoplasmic reticulum
ETHE1	Persulfide dioxygenase
FUS	Fused in sarcoma
G3BP1 / G3BP2	GTPase-activating protein-binding proteins 1 / 2
GPX4	Glutathione peroxidase-4
GR	Glutathione reductase
Grx	Glutaredoxin
GSH	Glutathione
GSK3β	Glycogen synthase kinase 3 beta

GSSH	Glutathione persulfide
H_2O_2	Hydrogen peroxide
H_2S	Hydrogen sulfide
HTT	Huntingtin protein
IDR	Intrinsically disordered region
ISCU	Iron-sulfur cluster assembly scaffold protein
LCYD1	L-cysteine desulfhydrase 1
LLPS	Liquid-liquid phase separation
LMW	Low molecular weight
MAPK	Mitogen-activated protein kinase
MAPT	Microtubule-associated protein tau
MEF	Mouse embryonic fibroblast
MEK-1	Mitogen-activated protein kinase kinase 1
MPST	Mercaptopyruvate sulfurtransferase
MS	Mass spectrometry
MSBT	Methylsulfonyl benzothiazole
NBF-Cl	4-Chloro-7-nitrobenzofurazan
NFS	Cysteine desulfurase
NO	Nitric oxide
PARK7	Parkinson's disease protein 7
PARP1	Poly(ADP-ribose) polymerase 1
PDR	Primate differential redoxome
PLP	Pyridoxal 5’-phosphate
polyQ	Poly-glutamine domain
Prx	Peroxiredoxin
PTM	Posttranslational modification
QTRP	Low-pH quantitative thiol reactivity profiling
RNS	Reactive nitrogen species
ROS	Reactive oxygen species
RSO_2H	Sulfinic acid
RSO_3H	Sulfonic acid

RSOH	Sulfenic acid
RSSH	Persulfide
$RSSO_2H$	Perthiosulfinic acid
$RSSO_3H$	Perthiosulfonic acid
RSSOH	Perthiosulfenic acid
S^0	Sulfane sulfur
$S_2O_3^{2-}$	Thiosulfate
SBP1	Methanethiol oxidase
SO_3^{2-}	Sulfite
SO_4^{2-}	Sulfate
SQOR	Sulfide:quinone oxidoreductase
SG	Stress granules
SUOX	Sulfite oxidase
TCEP	Tris(2-carboxyethyl)phosphine
TDP-43	TAR DNA-binding protein 43
Thil	tRNA sulfurtransferase
TIA1	T cell-restricted intracellular antigen-1
TRP14	Thioredoxin-related proteins of 14 KDa
Trx	Thioredoxin
TrxR	Thioredoxin reductase
TST	Thiosulfate sulfur transferase
TSTD1 protein	Thiosulfate sulfur transferase-like domain-containing 1
TTP	Tristetraprolin
UV	Ultraviolet
α-KB	α-ketobutyrate
α-KG	α-ketoglutarate

List of main figures

Figure 1.1. ***Biosynthesis of H_2S in plants.*** 3

Figure 1.2. ***Biosynthesis of H_2S in animal kingdom*** 4

Figure 1.3. ***Enzymatic activity, organization, and structure of CBS*** 6

Figure 1.4. ***Structure and enzymatic activity of CSE*** 8

Figure 1.5. ***Extended biological roles of the transsulfuration pathway and H_2S production.*** 11

Figure 1.6. ***Electrophilic nature of organic persulfides and polysulfides*** 15

Figure 1.7. ***H-atom donor properties of RSSH and Its importance in ferroptosis prevention.*** 17

Figure 1.8. ***Reaction of persulfides with two-electron oxidants.*** 18

Figure 1.9. ***Methods for protein persulfidation labelling and their applications.*** 22

Figure 1.10. ***Principle of dimedone switch and its various applications for persulfide labelling*** 24

Figure 1.11. ***Metalloproteins catalyse RSSH formation.*** 27

Figure 1.12. ***Role of protein persulfidation in EGFR signaling: RSOH to RSSH switch*** 29

Figure 1.13. ***Low molecular weight persulfide formation and direct cysteine persulfide integration into proteins.*** 31

Figure 1.14. ***Transpersulfidation is involved in the iron-sulfur cluster assembly and RNA thiolation*** 33

Figure 1.15. ***Enzymatic system for protein depersulfidation.*** 37

Figure 1.16. ***Persulfidation regulates protein function.*** 41

Figure 1.17. ***Hallmarks of aging and H_2S anti-aging effect.*** *..... 43*

Figure 1.18. ***Parkin activation upon persulfidation protects against protein aggregation.*** *..... 47*

Figure 1.19. ***Tau-stimulating CSE activity contributes to positive feedback against tau hyperphosphorylation and aggregation*** *..... 49*

Figure 1.20. ***Proposed mechanism of protective and anti-aging effects of protein persulfidation.*** *..... 52*

Figure 1.21. ***Biomolecular condensates of proteins.*** *. 54*

Figure 1.22. ***Molecular aging of biomolecular condensates.*** *..... 56*

Figure 1.23. ***Aberrant phase separation of tau, FUS and TDP-43 leads to aggregation and neurodegeneration.*** *..... 60*

Figure 3.1. ***Chemoproteomic analysis of protein sulfenylation and persulfidation reveals substantial alteration of cysteine modifications in aging.*** *..... 71*

Figure 3.2. ***$CSE^{-/-}$ mice exhibit higher PSOH and PSO_3H levels but lower PSSH, shorter lifespan and spontaneous formation of neurofibrillary tangles*** *. 80*

Figure 3.3. A ***ge-related thiol remodeling of synapsin 1 controls it LLPS and neurotransmitter release.*** *..... 91*

Figure 3.4. ***Age-induced cysteine sulfonylation drives aberrant phase separation and aggregation of GAPDH.*** *..... 98*

Figure 4.1. ***The evolutionary conserved cysteine 73 of G3BP2 is sulfenylated upon sodium arsenite stress and persulfidated during stress recovery*** *..... 135*

Figure 4.2. ***In-vitro G3BP2 cysteine modification modulates its phase separation*** *..137*

Figure 4.3. ***H_2S affect stress granule formation dynamic in a G3BP2 C73 dependent manner.*** *..... 140*

Figure 4.4. ***CSE-dependent H_2S production is necessary to dissolve arsenite-induced stress granules upon recovery.*** *..... 143*

Figure 5.1. ***H_2S protective in gastrointestinal disorders and novel therapeutic approach for NSAID-induced mucosa damages.*** *..... 156*

Figure 5.2. ***Esophageal persulfidation (PSSH) and H_2S-bioavailability in metaplastic epithelium*** *..... 165*

Figure 5.3. ***Selective posttranslational persulfidation of proteins (PSSH).*** *..... 171*

Figure 5.4. ***Pharmacological modulation of H_2S-bioavailability impacts metaplastic turnovers in esophageal mucosa.*** *..... 177*

Figure 5.5. ***Modulation of H_2S bioavailability and the resistance of human esophageal cells to GERD in vitro.*** *..... 181*

Figure 5.6. ***H_2S-dependent molecular response to GERD of squamous and metaplastic human epithelial cells.*** *..... 184*

Figure 5.7. ***PSSH-sensitive IL-1β, COX-2/PGE2 and mTOR pathways as mechanistic targets of H_2S-mediated metaplasia inhibition.*** *..... 192*

Figure 6.1. ***Boxplot of the raw and normalized intensities of persulfidome dataset.*** *223*

Figure 6.2. ***Overview of the Sulfenylation Potential Fate.*** *..... 224*

Figure 6.3. ***Redox switch from PSSH to PSO_xH forces aberrant phase separation predisposing brain to neurodegeneration.*** *..... 227*

Figure 6.4. ***Stress granule proteins are both sulfenylated and persulfidated*** *..... 229*

List of supplementary tables

Chapter 3:

Supplementary table 3.1. ***Sulfenylome in aging mice brain***

Supplementary table 3.2. ***Total proteome analysis in aging mice brain***

Supplementary table 3.3. ***Persulfidome in aging mice brain***

Supplementary table 3.4. ***Sulfenylome and Persulfidome in 10-week old CSE$^{-/-}$ compared to WT mice***

Supplementary table 3.5. ***Cysteine-SO3H peptides in WT aging and CSE$^{-/-}$ 10 weeks old mice brain***

Supplementary table 3.6. ***Thermal proteome profiling of WT and CSE$^{-/-}$ upon 60 min H_2O_2 treatment***

Proteomic data and tables are available through PRIDE repository under following identifiers: PXD045785 (sulfenylome and total proteome); PXD045806 (persulfidation and sulfonylation); PXD045820 (TPP of WT and CSE$^{-/-}$ MEFs upon H_2O_2 stress).

Chapter 5:

Supplementary table S5.1. ***Total proteome changes in Barrett's syndrome***

Supplementary table S5.2. ***Total proteome cluster list***

Supplementary table S5.3. ***Persulfidation changes in Barrett's syndrome***

Supplementary table S5.4. ***Persulfidation cluster list***

Proteomic data and tables are available through PRIDE repository under following identifier: PXD047338

1. Introduction

1.1. From hydrogen sulfide to persulfidation

About three decades ago, Abe and Kimura[1] (1996) discovered the gasotransmitter properties of hydrogen sulfide (H_2S). Since then, the interest in its biological functions has drastically increased. For a very long time, H_2S was only considered a toxic and smelly gas. However, current evidence suggests that H_2S played an essential role in the origin of life; H_2S is proposed to be one of the building blocks of life, together with cyanide, ultraviolet light and traces of metal ions, establishing the basis for the cyanosulfide hypothesis of the origin of life[2,3]. Furthermore, Foden et al. recently demonstrated cysteine formation from sulfide and highlighted cysteine's role as a catalyst and precursor in prebiotic peptide synthesis[4]. These new pieces of evidence underline the importance of sulfur chemistry not only for the origin of life but for its successful maintenance through evolution.

1.1.1. Chemical properties of hydrogen sulfide

H_2S is a gaseous compound characterized by its strong odor of rotten egg[5]. It is a diprotic compound, therefore exhibiting two constants of dissociation. In an aqueous solution, the pK_{a1} = 6.98 at 25 °C and 6.76 at 37 °C [Eq. (1)]. pK_{a2} has been estimated at > 17 at 25 °C[6] [Eq. (2)].

$$H_2S \rightleftharpoons HS^- + H^+ \qquad (1)$$

$$HS^- \rightleftharpoons S^{2-} + H^+ \qquad (2)$$

Under physiological conditions (pH 7 and 37°C), H_2S exists in an equilibrium between [H_2S] and [HS^-] with [HS^-] as the predominant form. The relatively low electronegativity of sulfur, combined with the negative charge and high polarizability of HS^-, results in excellent nucleophilicity and a strong ability to form covalent bonds[5]. In addition, H_2S is also soluble in lipophilic solutions and exerts a high permeability across biological membranes that is decreased in its HS^- form[7]. Throughout this thesis, H_2S (or hydrogen sulfide) refers to both H_2S and HS^- species.

1.1.2. H_2S production in plants and animals

The primitive life flourished in an H_2S-rich environment, where H_2S served as a basis for peptide synthesis and a source of metabolic energy[8]. The primary chemical reactions established during this time were and still are crucial for the evolution and maintenance of living organisms. Consequently, cells have developed enzymes to control H_2S production and consumption.

The production of H_2S differs between the animal and plant systems. In plants, H_2S is mainly produced by two enzymes, cyanoalanine synthase C1 (CYSC1)[9] in the mitochondria and L-cysteine desulfhydrase 1 (LCYD1)[10] in the cytosol[11]. Other proteins contributing to L-cysteine synthesis, such as cysteine synthase, could also participate in H_2S production[12] (Figure 1.1).

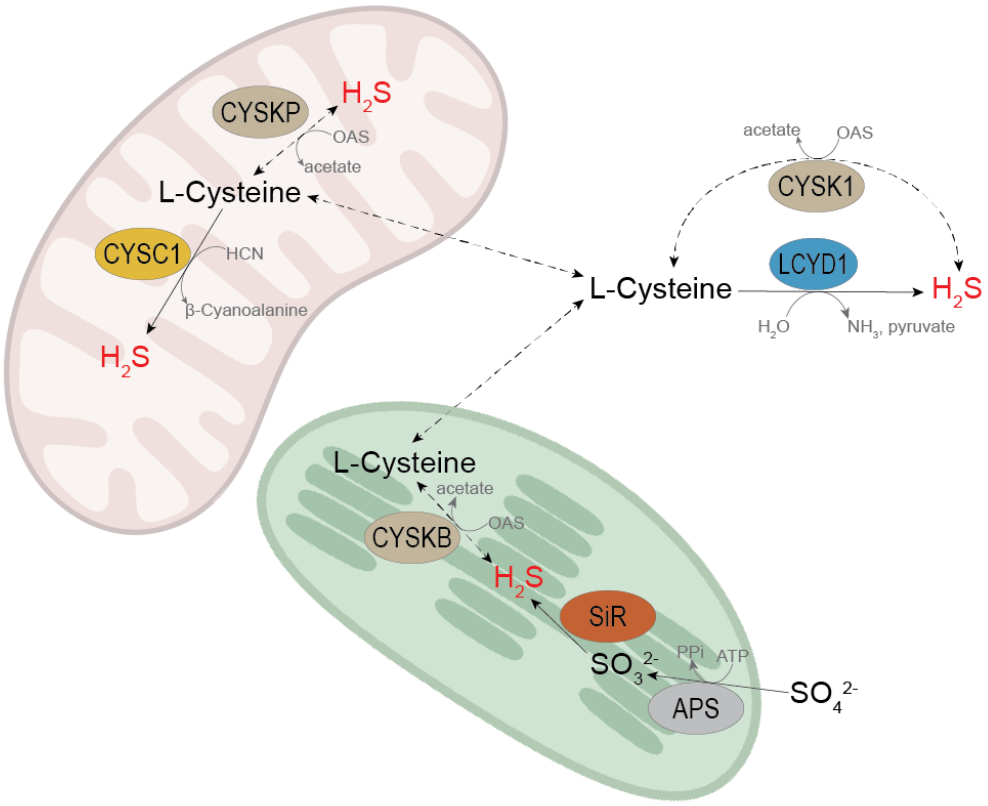


Figure 1.1. Biosynthesis of H_2S in plants. APS, ATP sulfurylase 1 (chloroplastic); CYSC1, bifunctional L-3-cyanoalanine synthase/cysteine synthase C1 (mitochondrial); CYSK1, cysteine synthase; CYSKB, cysteine synthase (chloroplastic/chromoplastic); CYSKP, cysteine synthase (mitochondrial); H_2S, hydrogen sulfide; LCYD1, L-cysteine desulfhydrase 1; SiR, sulfite reductase (chloroplastic).

In the animal system, the transsulfuration pathway is mainly responsible for producing H_2S through the activity of two pyridoxal 5'-phosphate (PLP)-dependent enzymes, cystathionine β-synthase (CBS) and cystathionine γ-lyase (CSE) (Figure 1.2). While these enzymatic activities occur in the cytosol, a third enzyme, mercaptopyruvate sulfurtransferase (MPST) coupled to cysteine aminotransferase (CAT), can also produce H_2S *via* the cysteine catabolism pathway in the mitochondria[13–15]. Furthermore, a fourth enzyme, methanethiol oxidase (SBP1), can use methanethiol to produce H_2S,

formaldehyde, and hydrogen peroxide (H_2O_2)[16]. The efficiency and the role of these enzymes in H_2S production will vary depending on their tissue expression and cellular localization.

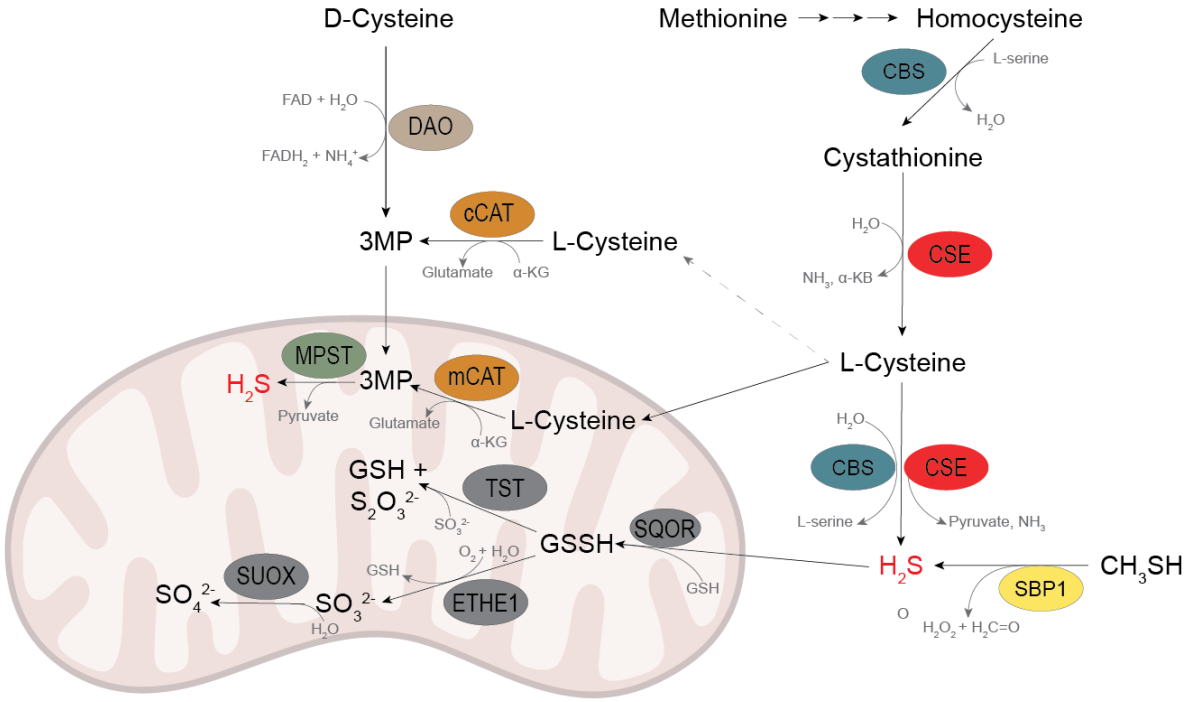


Figure 1.2. Biosynthesis of H_2S in animal kingdom. α-KB, α-ketobutyrate; α-KG, α-ketoglutarate; 3MP, 3-mercaptopyruvate; mCAT/cCAT, mitochondrial and cytosolic cysteine aminotransferase; CBS, cystathionine β-synthase; CSE, cystathionine γ-lyase; DAO, D-amino acid oxidase; ETHE1, persulfide dioxygenase; GSH, glutathione; MPST, mercaptopyruvate sulfur transferase; SBP1 (alternatively SELENBP1), methanethiol oxidase; SUOX, sulfite oxidase; SQOR, sulfide:quinone oxidoreductase; TST, thiosulfate sulfur transferase (alternatively rhodanese).

CBS is a central enzyme linking the methionine metabolism and other sulfur metabolites. In the transsulfuration pathway, CBS catalyzes the β-replacement of serine with homocysteine via a ping-pong mechanism, resulting in cystathionine and H_2O formation[5]. CBS ability to bind substrates such as serine, homocysteine, and cysteine enables the enzyme to perform a spectrum of reactions resulting in H_2S release[5] (Figure 1.3A). It has been proposed that CBS multimodal activity is regulated by the substrate availability[17]. Under biological conditions, intracellular serine concentrations are higher than those of cysteine, and the CBS affinity for serine is also higher than that for cysteine[17], suggesting that the CBS's main activity is expected to be reaction 1 (Figure 1.3A).

In the cytosol, CBS is a homodimer with a subunit of ~63 kDa. The N-terminal domain of CBS binds PLP and a regulatory heme b cofactor. In the ferrous form, heme binds to exogenous ligands such as carbon monoxide or nitric oxide, leading to the inactivation of CBS. CBS C-terminal domain, in its original conformation, inhibits CBS activity (Figure 1.3B). The binding of S-adenosyl-methionine (AdoMet), an allosteric activator, to the C-terminal domain induces a major conformational rearrangement preventing CBS auto-inhibition[5] (Figure 1.3C). In addition to allosteric regulation, CBS activity is modulated through posttranslational modifications such as SUMOylation and glutathionylation. While the latter increases CBS activity[18], SUMOylation has been reported to inactivate the enzyme and cause its nuclear relocalization[19].

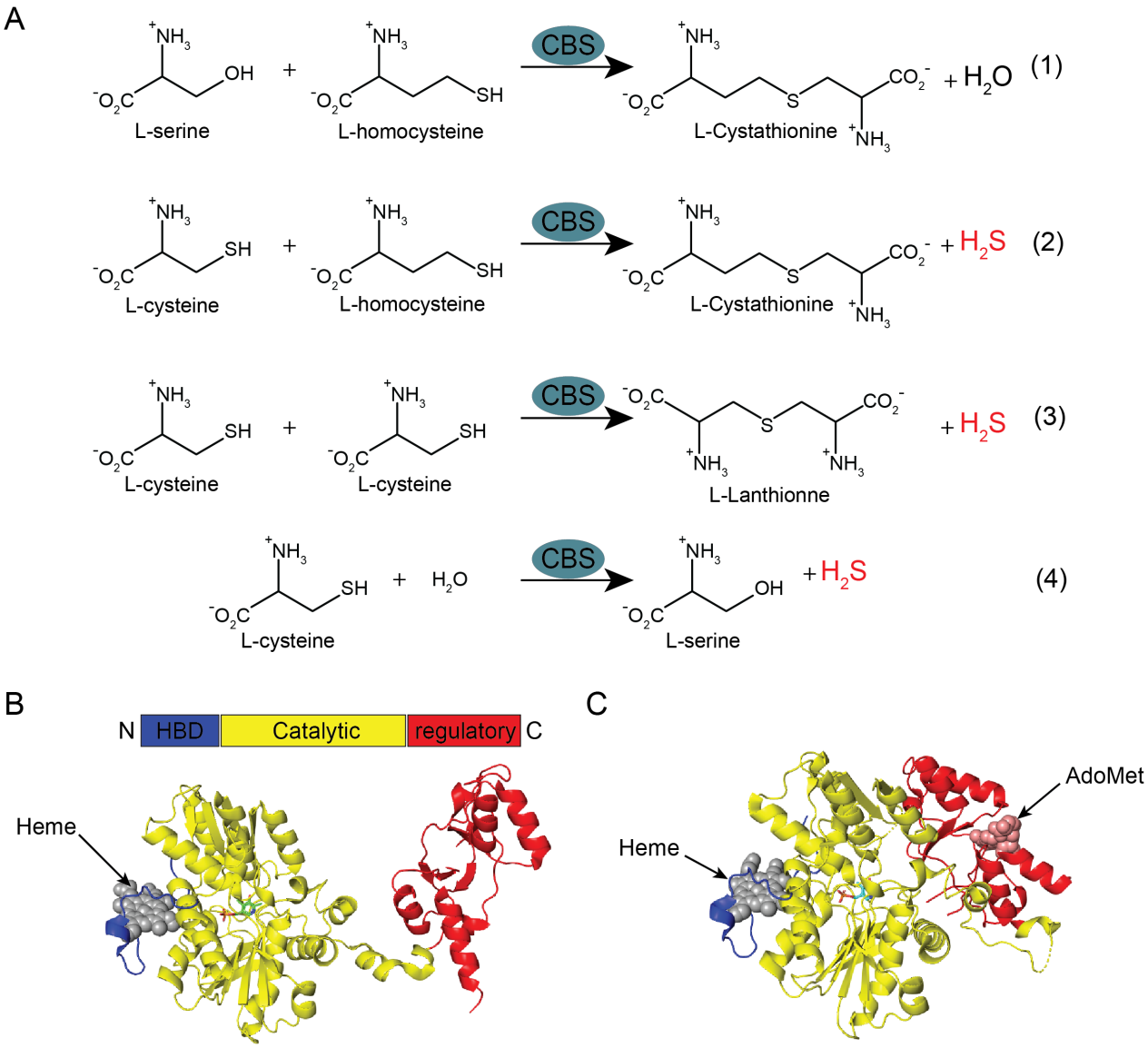


Figure 1.3. Enzymatic activity, organization, and structure of CBS. (**A**) Reactions catalyzed by CBS: (1) Formation of cystathionine in the transsulfuration pathway; (2-4) H_2S production from cysteine and/or homocysteine. (**B**) CBS structure in absence of S-adenosyl-methionine **(**AdoMet; PDB:4L27)[20]. The protein contains two regulatory domains, one at the N-terminal binding site (in blue) that binds heme (represented with gray spheres) and one at the C-terminal (in red) binding site for AdoMet. (C) The binding between AdoMet and CBS C-terminal domain induces substantial conformational rearrangement leading to CBS activation (PDB: 4PCU)[20].

The second enzyme of the transsulfuration pathway, CSE, is a homotetramer of a 45 kDa subunit containing a PLP binding site (Figure 1.4A). The canonical role of CSE is to catalyze the elimination of the γ-carbon of cystathionine, releasing cysteine, α-ketobutyrate, and ammonia[5,21]. Due to its promiscuous substrate specificity, the enzyme also catalyzes several other chemical reaction involving the β- or the γ-carbons of cystathionine, cysteine, or homocysteine[22], resulting in H_2S release (Reactions 2-6, Figure 1.4B). The β-elimination of cysteine forming pyruvate, H_2S, and ammonia (Reaction 4, Figure 1.4B) has been proposed to be the primary H_2S-producing reaction catalyzed by CSE under physiological conditions[5].

The regulation of CSE activity remains mainly unknown. Substrate availability was proposed to modulate CSE activity, and as such H_2S production has been predicted to increase from 20 to 200-fold in homocystinuria[22]. CSE possesses two CXXC motifs that may play a role in the redox-sensitive regulation of the enzyme[5]. CSE-catalyzed H_2S production was also suggested to be regulated by intracellular Ca^{2+} concentration[23,24]; however, the mechanism through which Ca^{2+} controls CSE activity remains unclear. CSE also undergoes posttranslational modification, such as phosphorylation of Ser377, which has been reported to inhibit its H_2S production activity[25]. *In-vitro* SUMOylation of CSE was also reported[26], but its physiological role remains unknown. Furthermore, CSE expression increases upon ER stress via upregulation by the activating transcription factor 4 (ATF4)[27,28], resulting in an increased H_2S production.

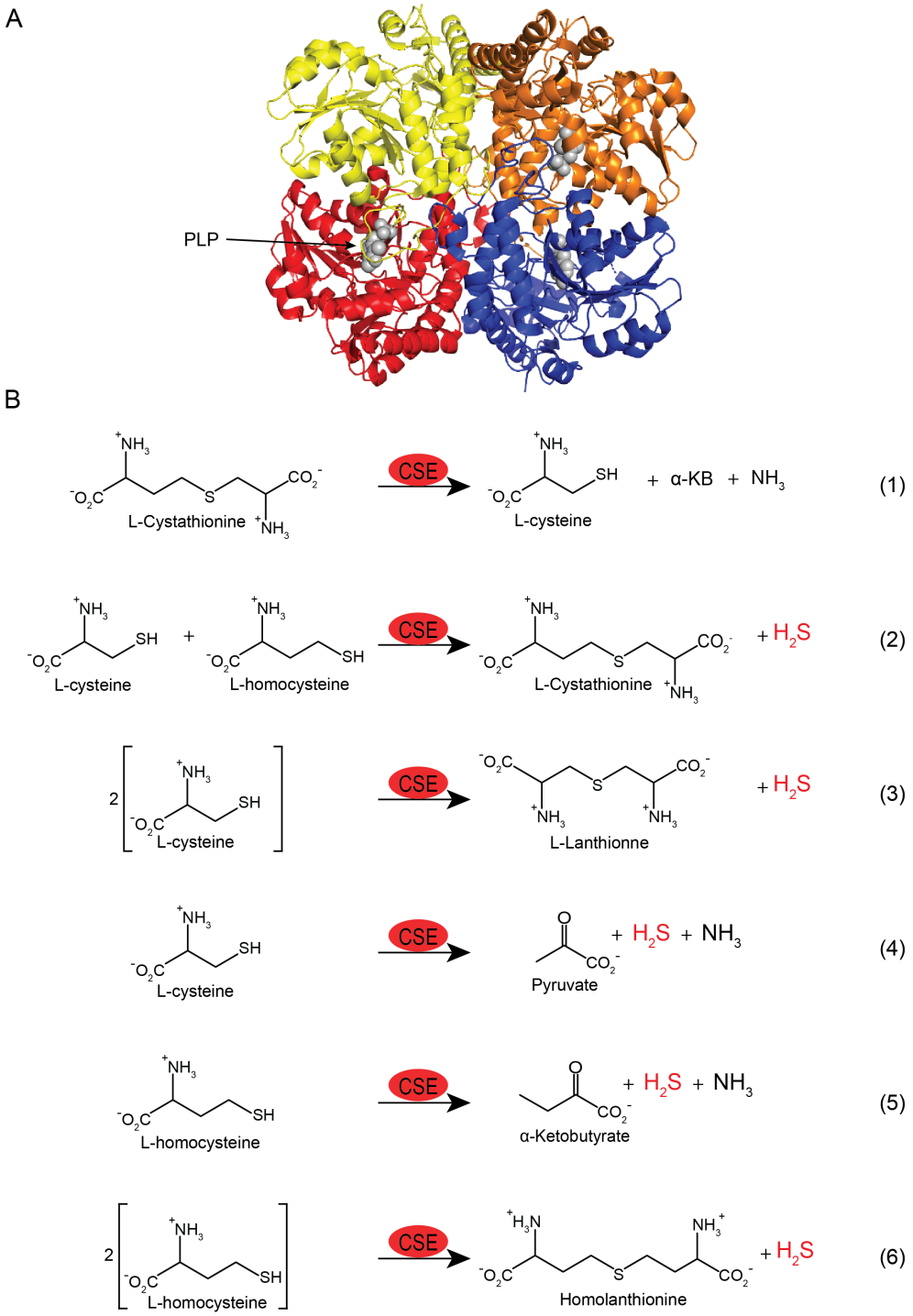


Figure 1.4. Structure and enzymatic activity of CSE. (**A**) Homotetrameric organization of the human CSE (PDB: 2NMP)[29]. Each monomer is distinguished by different colors and the PLP is indicated and represented as grey spheres. (**B**) Enzymatic reactions catalyzed by CSE: (1) cleavage of cystathionine into cysteine, α-ketobutyrate (α-KB), and ammonia in the transsulfuration pathway; (2-6) H_2S production catalyzed by CSE using cysteine and/or homocysteine.

The third enzyme of the transsulfuration pathway, MPST, is mainly located in the mitochondria but was also found in the cytoplasm[30]. The MPST substrate, 3-mercaptopyruvate (3-MP), is produced either through the conversion of L-cysteine into 3-MP by cysteine aminotransferase (CAT)[5] or through the conversion of D-cysteine into 3-MP catalyzed by D-amino acid oxidase (DAO)[31]. MPST catalyzes the conversion of 3-MP into pyruvate, resulting in persulfidated MPST (Figure 1.2). H_2S is then released upon the reduction of MPST-SSH by low molecular weight thiols or the thioredoxin/thioredoxin reductase system thiol[32]. Similar to CSE, MPST regulation remains understudied. MPST activity may be redox-regulated as it decreases upon oxidative stress[33], and some of its cysteines have been proposed to be redox-sensitive. The possible inhibition of CAT by calcium, leading to reduced MSPT substrate availability, was also proposed as a regulatory mechanism for H_2S synthesis *via* CAT/MPST pathway[5].

Although the sulfur flux into H_2S has been estimated to be similar to that into glutathione (GSH) production[14,34], cellular H_2S levels remain low (submicromolar for most tissues)[13]. This suggests that H_2S clearance and/or consumption are very high. Hydrogen sulfide is oxidized in the mitochondria by sulfide:quinone oxidoreductase (SQOR), forming glutathione persulfide (GSSH). GSSH can then be processed either by thiosulfate sulfur transferase (TST) to form GSH and thiosulfate ($S_2O_3^{2-}$) or by persulfide dioxygenase (ETHE1) to produce GSH and sulfite (SO_3^{2-}). SO_3^{2-} is then oxidized into sulfate (SO_4^{2-}), which is eliminated from the cell through excretion (Figure 1.2). One of the main challenges is to understand how these enzymes control H_2S production over time and in response to stress. However, the knockout of certain genes of the

transsulfuration pathway results in clear phenotype in animal models, underlining the importance of the H_2S production (Figure 1.5A).

1.1.3. H_2S biological role

Mice lacking CBS suffer from severe growth retardation, with most progeny dying by five weeks of age[35]. CSB deficiency in mice and humans results in hyperhomocysteinemia, and could present a risk factor for age-dependent diseases such as Alzheimer's[36] and cardiovascular diseases[37] (Figure 1.5A). However, while those studies are purely correlative, conditional knockout of CBS during adulthood shows no sign of faster aging compared to the non-induced mice[38]. These results must be taken with caution as the authors did not achieve the conditional knockout in the brain and showed a response to tamoxifen only in the liver and kidney. More generally, the phenotype of CBS knockout cannot only be attributed to H_2S deficiency, resulting in a lack of specificity in studying H_2S in model organisms.

Although their phenotype seems less severe, CSE knockout mice may be a better model for understanding the role of H_2S in a complex biological system. Indeed, mice lacking CSE show abnormal hind limb clasping and clenching reminiscent of Huntington's disease[39], suggesting the essential role of H_2S in protecting against neurodegeneration. Moreover, $CSE^{-/-}$ mice display phenotype at multiple levels such as acute skeletal muscle atrophy, postnatal growth retardation, increased susceptibility to induced morbidity/mortality[40] but also hypertension and decreased vasodilation[24] (Figure 1.5A). Many of these phenotypes were not observed in $CBS^{-/-}$ mice, suggesting that CSE plays a more central role in H_2S production in various tissues.

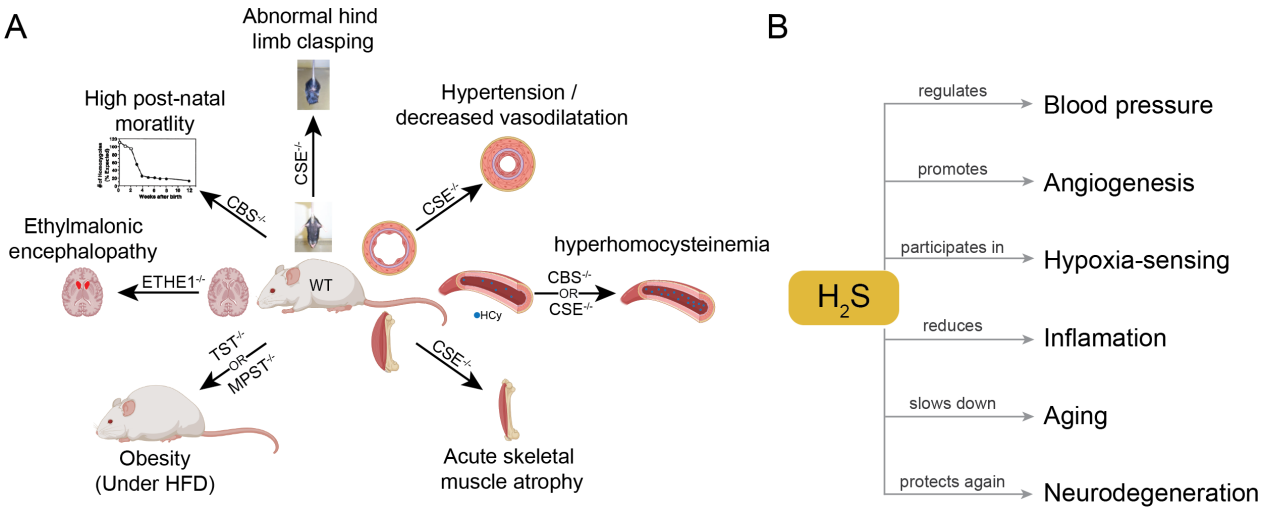


Figure 1.5. Extended biological roles of the transsulfuration pathway and H_2S production. (**A**) Associated phenotype to the knockout of the transsulfuration pathway in mice. CSE knockout mice present multiple phenotypes including hypertension[24], acute skeletal muscle atrophy[40,] and abnormal hind limb clasping[39]. $CBS^{-/-}$ mice exhibit higher postnatal mortality and severe hyperhomocysteinemia[35], making the role of H_2S difficult to untangle in those mice (HCy: Homocysteine). $ETHE1^{-/-}$ are suffering from ethylmalonic encephalopathy, while $TST^{-/-}$ and $MPST^{-/-}$ suffer from obesity when grown on a high-fat diet (HFD). (**B**) H_2S is known for its beneficial effect on blood pressure[24,41,42], angiogenesis[43–45], hypoxia-sensing[46–48], inflammation[49] and for its protecting role against aging[50,51] and neurodegegneration[39,52,53].

Knockout animals of other proteins in the transsulfuration pathway also exhibit phenotypes worth investigating (Figure 1.5A). $TST^{-/-}$ and $MPST^{-/-}$ mice develop obesity[54], while $ETHE1^{-/-}$ mice develop ethylmalonic encephalopathy[55]. These studies suggest that regulating the production and consumption of H_2S is essential for cellular homeostasis. Additionally, although H_2S can diffuse through the membranes and compartments, its local production in different cellular compartments is necessary for regulating specific subcellular processes. For example, H_2S production by MPST in the mitochondria impacts the cell's bioenergetic by modulating the mitochondrial electron flow[56].

Modulation of the cellular bioenergetics is one of the many roles attributed to H_2S in biological processes. H_2S is also known for its essential role in regulating blood pressure[24,41,42], angiogenesis[43–45], hypoxia sensing[46–48], inflammation[49], neurodegeneration[39,52,53], and aging[50,51] (Figure 1.5B). One of the main mechanisms through which H_2S acts in biological systems is by modifying the thiol group of cysteine residues (RSH), resulting in persulfide (RSSH) formation, a posttranslational modification (PTM) called persulfidation. To study the biological roles of persulfides, it is essential to understand the formation and chemical properties of this specific PTM.

1.2. Biological chemistry of protein persulfidation

Protein persulfidation was first introduced by Snyder's group[57], who defined it as a general and widespread modification. This work provided a solid basis for studying persulfidation and understanding the physiological and pharmacological effects of H_2S[13,58]. One of the significant challenges in studying protein persulfides is that their chemical reactivity is similar to that of thiols, disulfides, and sulfenic acids. These similarities make it challenging to differentiate the biological role of persulfides from that of other species.

1.2.1. Acidity and nucleophilicity

Hydropersulfides are the protonated form of persulfides and can ionize into anionic persulfide [Eq. (3)]:

$$RSSH \rightarrow RSS^- + H^+ \qquad (3)$$

The weaker S-H bond in persulfides compared to their corresponding thiol[13] results in a higher acidity of persulfides. The pK_a of cysteine persulfides has been estimated at ~4, about 4 points less than that of cysteine[7]. Supporting the in-silico work, it has been measured that the pK_a of GSSH is 5.45, about 3.5 points lower than GSH[59]. Therefore, persulfides exist mainly as anionic species (RSS^-) at physiological pH. However, in proteins, the interaction with the groups in the vicinity of the persulfides can influence the pK_a of cysteine-derived persulfides. It is therefore important to understand the environment of the modified cysteine when studying specific proteins, as it could be important for its functional properties.

Another relevant characteristic of persulfides is their nucleophilicity. Since RSSH has a weaker basicity than RSH, it should be a weaker nucleophile than RSH. Indeed, nucleophilicity and basicity can usually be correlated, as the stronger basicity leads to a higher nucleophilicity. However, an important exception called the alpha effect must be taken into account here. The presence of an adjacent atom (α) carrying a non-bonding pair of electrons results in an increased nucleophilicity. Therefore, due to the alpha effect, RSSH is more nucleophilic than the corresponding RSH. The nucleophilicity combined with the low pK_a of RSSH keeps the persulfide in an optimal ionized state for reaction with electrophiles [Eq.(4)]:

$$RSS^- + E^+ \rightarrow RSSE \qquad (4)$$

Few examples of these "super nucleophilic" properties have emerged over the last decade. The electrophile 4,4′-dithiodipyridin reacts ~20 times faster with albumin persulfides than its reduced form[60] and 43 times faster with the persulfide of the one-

cysteine peroxiredoxin (Prx) alkyl hydroperoxide reductase E from *Mycobacterium tuberculosis* compared to its RSH form[61].

Higher nucleophilicity of RSSH is also demonstrated by their increased reactivity with alkylating agents, different disulfides, as well as electrophiles (e.g., 8-nitroguanosine 3',5'-cyclic monophosphate[62,63] and methyl mercury[64]).

1.2.2. Electrophilicity and stability

Persulfides are sulfane sulfur-containing compounds where sulfane sulfur (S^0) is defined as a sulfur atom bound to two other sulfurs or a sulfur and an ionizable hydrogen[13]. Therefore, in their protonated form, persulfides are also weak electrophiles. Upon nucleophilic attack, the nucleophile can react either with the inner sulfur (Figure 1.6A, path "a'), releasing H_2S, or the outer sulfur (Figure 1.6A, path 'b'), removing the thiol. Due to its lower pK_a (6.98) compared to the average pK_a of thiols (8-9), H_2S is a better leaving group. Therefore, the reaction with the first sulfur (Figure 1.6A, path 'a') will always be preferred unless the electrophilicity of the cysteine residue is modified by its surroundings.

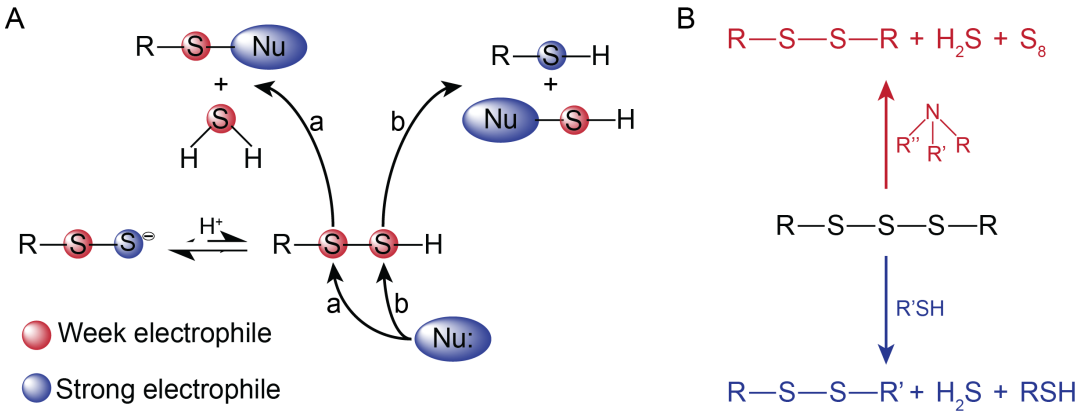


Figure 1.6. Electrophilic nature of organic persulfides and polysulfides. (**A**) In their protonated form, persulfides can undergo nucleophilic attack on both sulfur atoms with a preference for the path 'a', releasing H_2S. (**B**) Instability of organic trisulfides. Trisulfide can be decomposed by amine (in red) or other thiols (in blue).

One exception to this rule is the reaction of persulfides with cyanide[65], utilized during evolution for the enzymatic detoxification of cyanide by rhodanese (TST)[66]. Throughout this process, the formation of thiocyanide occurs, leaving the thiol in a reduced form [Eq. (5)]:

$$RSSH + CN^- \rightarrow RSH + SCN^- \qquad (5)$$

Apart from cyanide, experiments have shown that both low molecular weight (LMW) persulfides[62,67,68] or protein persulfides[69], react to release H_2S. Thiols are present in millimolar concentration in the cell, representing a significant potential for releasing a high amount of H_2S. A recent example emerged with the development of MitoPerSulf, an LMW mitochondrial-targeted RSSH[70]. By designing this probe, the Murphy's group showed that this molecule readily reacts with GSH to release H_2S. In addition to H_2S release, persulfides formed in the active site of specific proteins can also be transferred to another thiol. This reaction is called transpersulfidation [Eq. (6)].

$$RSSH + R'S^- \rightarrow RSH + R'SS^- \qquad (6)$$

Because of their nucleophilic and electrophilic properties, RSSH are very unstable. N-acetyl penicillamine persulfides show a half-life decay of 2.7 ± 0.3 minutes[71], as measured by real-time mass spectrometry. Cysteine-SSH exhibits a slightly longer $t_{½}$ decay of 35 ± 3.5 minutes[72]. In both cases, the decay of persulfides happens mainly through the following equation [Eq. (7)]:

$$RSSH + RSS^- \rightarrow RSSSH + RS^- \quad (7)$$

Attention was raised on trisulfides as they could be potential precursors for RSSH[73]. However, cysteine and glutathione trisulfides are unstable under physiological conditions, usually undergoing amine-induced decomposition[74] (Figure 1.6B). Trisulfides directly modify cysteine residues through electrophilic attack[75], so their biological effects cannot be compared to those of persulfides.

1.2.3. Reaction with one- and two-electron oxidants

RSSH are effective one- and two-electron reductants. They have lower energy of dissociation of the S-H bond than thiols (293 kJ/mol *vs* 385 kJ/mol)[13], and their one-electron reduction potential is more favorable (E°' [$RSS^\bullet/RSS^-$] = 0.68 V *vs* E°' [$RS^\bullet$, H^+/RSH] = 0.96 V)[76]. Additionally, Everett's studies showed that in perthiyl radicals, the unpaired electron is delocalized between the two sulfur atoms, resulting in the resonance stabilization and increased stability of these radicals[77,78]. Therefore, depending on the one-electron oxidant, persulfides can participate in electron or hydrogen atom transfer [Eq. (8) and (9)]:

$$RSS^- + A_2^\bullet \rightarrow RSS^\bullet + A_2^- \quad (8)$$

$$RSSH + A_1^\bullet \rightarrow RSS^\bullet + A_1H \quad (9)$$

LMW RSSH are, in fact, excellent hydrogen atom donors and react quickly with alkyl ($k \sim 5 \times 10^8\ M^{-1}\ s^{-1}$), alkolyl ($k \sim 1 \times 10^9\ M^{-1}\ s^{-1}$), peroxyl ($k \sim 2 \times 10^6\ M^{-1}\ s^{-1}$), and thiyl ($k > 1 \times 10^{10}\ M^{-1}\ s^{-1}$), radicals[79] (Figure 1.7A).

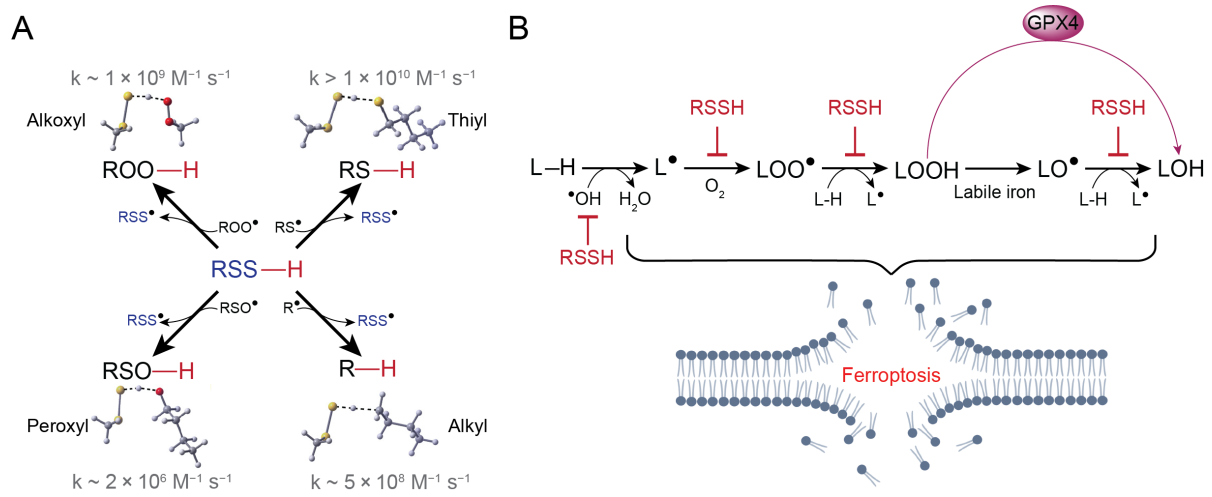


Figure 1.7. H-atom donor properties of RSSH and Its importance in ferroptosis prevention. (**A**) Persulfides are excellent H-atom donors and rapidly react with alkyl, alkolyl, peroxyl, and thiyl. Rate constants are given in grey. *Modified from Chauvin, J.P.R et al., 2017.* (**B**) H-atom donor properties of persulfides play an essential role in the prevention of radical formation and amplification of lipid radicals ($L^{\bullet}$), peroxyl radicals ($ROO^{\bullet}$), and alkoxyl radicals ($LO^{\bullet}$). These radicals are the primary driver of ferroptosis against which persulfides play a protective role.

Alkoxyl and peroxyl lipid radicals lead to cell membrane damage and ferroptotic cell death[80]. Thus, scavenging those radicals is a key to cell membrane maintenance (Figure 1.7B). Ferroptosis cell death induced by either silencing or inhibiting glutathione peroxidase-4 (GPX4) can be prevented by treating cells with LMW RSSH[73,81]. In addition, lipid peroxidation can be intensified by silencing CSE. On the contrary, silencing ETHE1 prevents this effect[73]. Notably, ETHE1 is present in the mitochondria[82], suggesting that an endogenous increase of LWM RSSH in this organelle could prevent ferroptosis. Further studies are needed to understand the potential anti-ferroptosis role of LMW persulfides such as Cys-SSH or GSSH in the mitochondria.

Besides their one-electron reductant properties, RSSH are also interesting for their reaction with two-electron oxidants such as H_2O_2 and peroxynitrite. Data suggest a faster reaction of the RSSH compared to the corresponding thiol. At 20 °C, albumin persulfide reacts $(1.2 \pm 0.4) \times 10^4\ M^{-1}\ s^{-1}$ with peroxynitrite which is one order of magnitude faster than the reduced protein[60]. In addition, GSSH reacts 22 times faster with H_2O_2 than GSH[59]. Reactive oxygen species (ROS) and reactive nitrogen species (RNS) are involved in cell signaling and the development of diseases[83–85]. Initially suggested by Paul and Snyder[86], the "antioxidant" property of RSSH is, therefore, a biologically relevant process to understand for potential pharmacological outcomes.

Persulfides react with H_2O_2 to form perthiosulfenic acid (RSSOH) (Figure 1.8). Further oxidation by ROS would result in perthiosulfinic and perthiosulfonic acids ($RSSO_2H$ and $RSSO_3H$, respectively)[12,50,87,88]. Perthiosulfonic acid has been detected in numerous experiments on different protein persulfides[60,89,90].

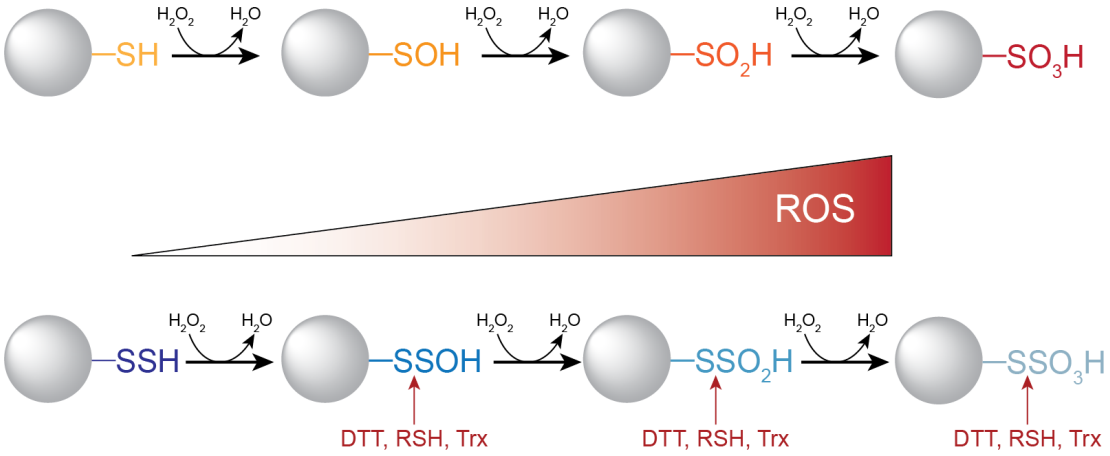


Figure 1.8. Reaction of persulfides with two-electron oxidants. While the reaction of a two-electron oxidant (H_2O_2) with RSH lead to the formation of two irreversible species (RSO_2H and RSO_3H), the reaction with a persulfide forms perthiosulfinic and perthiosulfonic acids, both reducible. (DTT: dithiothreitol; ROS: reactive oxygen species; Trx: thioredoxin.)

In contrast to the oxidation of RSH into sulfinic (RSO_2H) and sulfonic (RSO_3H) acids, which are largely irreversible[91,92], $RSSO_2H$ and $RSSO_3H$ are reducible. Indeed, due to the S-S bond, it is possible to restore the thiol (Figure 1.8). Two recent studies showed that (i) thioredoxin reacts ~ 2 orders of magnitude faster with cysteine perthiosulfonate than with cystine[50], (ii) different thioredoxins (Trx1 and TRP14) could reduce protein-bound $RSSO_3H$[93]. This is not surprising as 3'-phosphoadenosine-5'-phosphosulfate reductase, which produces perthiosulfonate in its active site during its catalytic cycle[94] is a well-known substrate of Trx.

The ability of the cell to reduce perthiolsulfonate to RSH, combined with the higher reactivity of persulfides towards ROS, form the basis for the protective mechanism and anti-aging effect of RSSH[50]. This "rescue loop" will be further discussed in Section 1.6.3.

1.3. Persulfide detection

Detecting persulfides is very challenging, as they exhibit reactivity similar to thiols and disulfides. The initial persulfide quantifications was performed within the total sulfane sulfur pool[65,95]. Using methods based on the same chemical principles, 25 years apart, two studies demonstrated that total persulfide concentration is in the low micromolar range[65,95]. Both studies used the triphenylphosphine-based approaches for sulfane sulfur extraction, and these estimations appear to be the most realistic values, as S^0 mainly comes from RSSH

Over the past 20 years, several methods have been developed to label and quantify protein persulfides. This following section focuses on the methods developed for the measurement of protein persulfides by mass spectrometry (MS).

1.3.4. Labelling protein persulfides

The first reports of large-scale identification and quantification of persulfides came from Snyder's group[57]. The authors identified 39 proteins persulfidated by looking at the peptides containing one extra sulfur atom. However, the mass of sulfur is only 0.2 Daltons different from that of two oxygens, which makes distinction between RSSH and RSO_2H difficult.

Later, the biotin thiol assay (BTA)[96], ProPerDP[97], and q-PerS-SID[98] methods were also reported as tools for proteomic detection of protein persulfidation. These methods use a thiol-blocking reagent that reacts with RSH and RSSH. This thiol-blocking reagent is coupled to biotin, providing an easy way to enrich the tagged cysteines. After streptavidin enrichment at the protein or peptide level, DTT or TCEP are used to cleave the persulfides selectively (Figure 1.9A). However, some concerns have been raised about this approach[99]. Thiol blocking reagents used in these methods also reacts with RSOH, forming an adduct that can be cleaved with DTT and TCEP[100].

Moreover, the reaction between N-ethylmaleimide (used in BTA) and thiols results in thioether formation, also known to be cleaved by DTT[101]. To overcome these concerns, the methods were recently modified by first lysing tissue and cells with a dimedone probe, blocking the sulfenic acids, and then blocking other thiols with the

biotin-containing probe[102]. By enriching at the peptide level, they could identify 1536 cysteine residues differentially persulfidated in endothelial cells[102].

To date, only one method has been reported to “directly” detect persulfides by mass spectrometry: low-pH quantitative thiol reactivity profiling (QTRP)[103]. In this method alkylation is performed by using alkynyl-iodoacetamide at pH 5. At this pH, persulfides are expected to remain reactive, while other thiols are less reactive. Using click chemistry and a UV-cleavable probe, a site-centric enrichment at the peptide level could be achieved[104] (Figure 1.9B). Taking into account that persulfidated peptides (now transformed into disulfides) contain additional sulfur, the method avoids the reduction step and allows direct detection of persulfides. 1547 persulfidated cysteine sites on 994 proteins were identified using QTRP in different cell lines.

The comparison between the persulfidomes obtained from the BTA[96], qPerS-SID[98], and QTPR[103] methods revealed a poor overlap, with only a few common proteins identified (82; Figure 1.9C). Notably, the QTPR and qPerS-SID methods were performed on the same cell line, suggesting a selectivity problem with some of these methods. Recently, it has been reported that the mixed disulfides formed during the reaction between nucleophiles and RSSH are prone to decomposition in the presence of high amounts of nucleophiles, such as cyanide[105]. However, in the case of cell or tissue lysis, such amounts are never reached and should only be of concern when working with single proteins[106]. A recent study suggested a lack of specificity for the ProPerDP method, as MS analysis resulted in a high amount of non-cysteine-containing peptides and poor reproducibility between replicates[99].

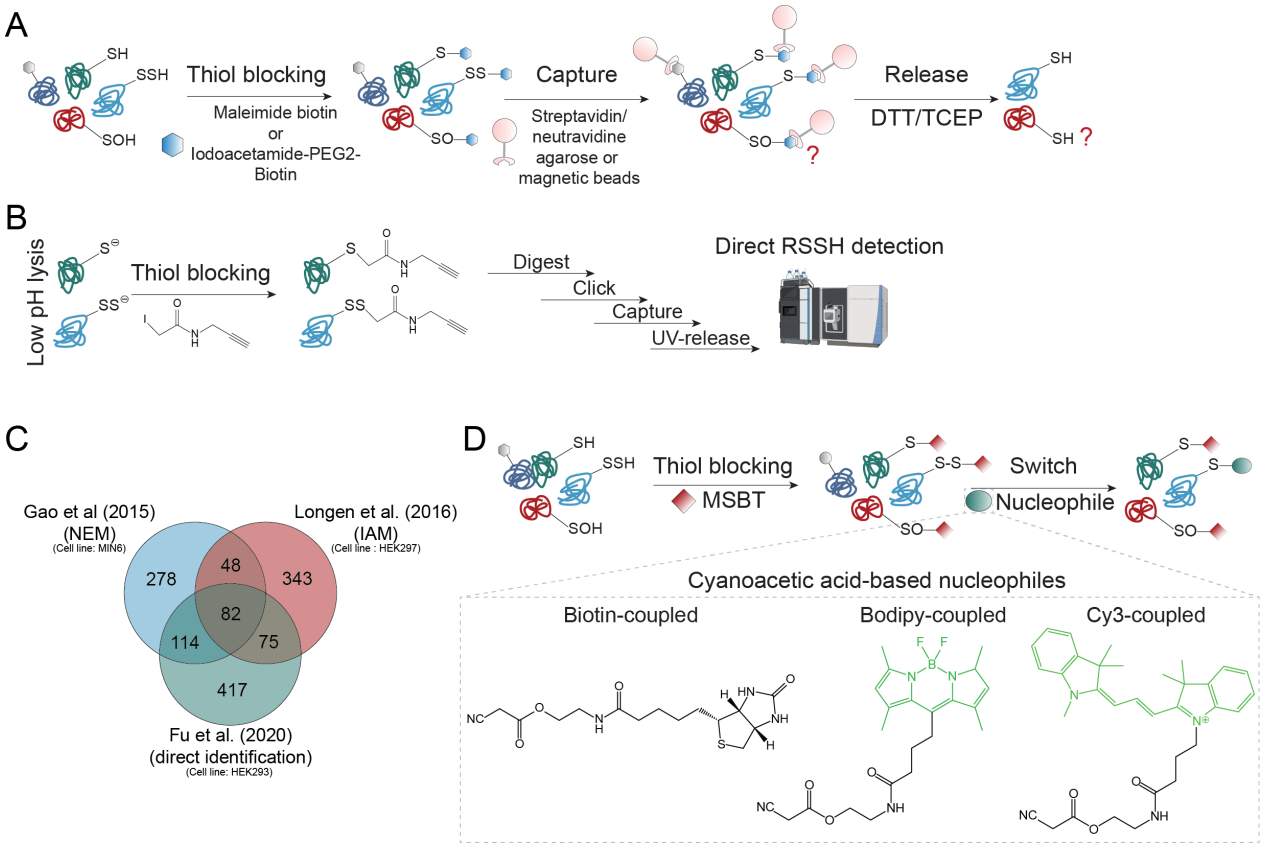


Figure 1.9. Methods for protein persulfidation labelling and their applications. (**A**) Principle of the biotin thiol assay (BTA)[96], ProPerDP[97], and q-PerS-SID[98] methods used to detect persulfidation. One of the significant caveats in this method is that the reducing agent is known also to reduce the blocked RSOH. This could be prevented by blocking RSOH (i.e. dimedone) prior to general thiol blocking[102]. (**B**) The low-pH Quantitative Thiol Reactivity Profiling (QTRP)[103] principle resides in higher reactivity of persulfide at low pH compared to other thiols. Combined with a UV-cleavable probe to enrich cysteine-containing peptide, the method directly detects the carbamidomethylated persulfide by MS. (**C**) Overlap of persulfidated proteins reported in 3 different studies using BTA[96], qPerS-SID[98], or QTPR[103]. Although the QTPR and qPerS-SID measurements were performed on the same cell line, a small protein overlap exists. (D) Chemical principle of the tag-switch method. Due to its various cyanoacetic-based probe variants, the tag-switch assay can be used for in-gel and proteomic detection.

Another approach, the tag-switch method, has been proposed to label protein persulfides selectively[71,90,107] (Figure 1.9D). As thiols and persulfides are nucleophiles, the first step consists of utilizing a thiol-blocking reagent that will react with both species. If an appropriate nucleophile is used, the disulfide bond formed in the reaction with the persulfides will show enhanced reactivity to certain nucleophiles. Thus, a "switch" reagent, usually a nucleophile carrying a fluorescent reporting molecule or a biotin, can selectively label persulfides. It is worth noting that the products of the blocking reagent and thiols are thioethers, which are not expected to react with nucleophiles.

Over the years, this method underwent some modifications. In the original method, methylsulfonyl benzothiazole (MSBT) or MSBT-A (higher solubility in water) was used as a thiol-blocking reagent. Cyanoacetic acid-based nucleophiles were shown to have higher reactivity with persulfides and were used as a specific nucleophilic "switch" reagent[71,90,107]. Aroca and colleagues[108] used this method to measure more than 2000 persulfidated proteins in *Arabidopsis thaliana*. However, this method has two caveats: (1) MSBT is highly insoluble in water, resulting in a laborious blocking protocol step; (2) under MS conditions, cyanoacetate-based probes are very unstable, making the analysis very difficult[13,108].

More recently, a modified tag-switch method named the dimedone-switch has been proposed by Filipovic's group[50]. In this method, MSBT was replaced with a more soluble and well-known thiol-blocking reagent: 4-Chloro-7-nitrobenzofurazan (NBF-Cl)[109,110]. Additionally, the cyanoacetate-based probes were replaced by dimedone-based probes[92,111]. Because dimedone is known to react highly with sulfenic acids[92,111], one main challenge is blocking RSH, RSSH, and RSOH. This is one of the advantages of using NBF-Cl which blocks all three thiol species[110]. Another convenience is that NBF-

Cl reacts with amino groups and exhibits a green fluorescence, which can be used as a loading control. This method has been adapted for different applications, such as in-gel detection, antibody micro-array detection, microscopy and persulfidome analysis using MS[50] (Figure 1.10). About 1500 persulfidated proteins could be quantified in Arabidopsis thaliana[112]. However, this method could present some limitations for MS analysis (for example, the reaction of NBF-Cl with lysine and arginine could cause a higher rate of miss-cleavages during tryptic digestion).

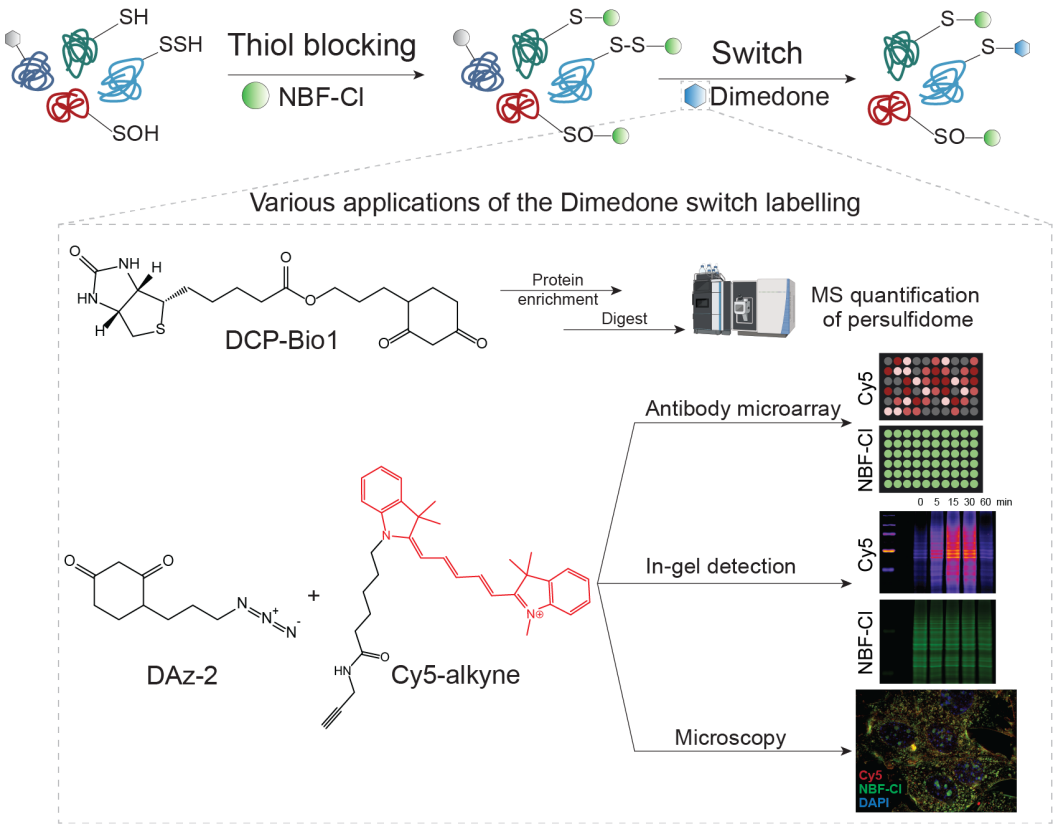


Figure 1.10. Principle of dimedone switch and its various applications for persulfides labelling. The dimedone-switch is a modified version of the tag switch assay, replacing the MSBT blocking reagent with the more soluble 4-chloro-7-nitrobenzofurazan (NBF-Cl) compound. In addition, cyanoacetate acid-based probed were replaced by dimedone probes, enhancing reactivity with persulfides and enabling MS detection.

Globally, all these methods present some limitations, among which the main challenge is selectivity and site-specific detection of the persulfide by MS.

1.4. Cellular mechanism of persulfide formation and removal

Several mechanisms have been identified for RSSH formation in the cell over the past decades. Understanding these mechanisms is crucial for comprehending the role of RSSH in cellular signaling. Therefore, further studies are necessary to fully elucidate their formation and function.

1.4.1. Disulfide reduction by H_2S as a source of protein persulfidation

About 100 years ago, cysteine persulfide was shown to form upon the reaction between H_2S and cystine.[113] More recently, it has been demonstrated that H_2S can react with disulfides to form RSSH.[60,114] The reaction is as follows [Eq. 10)]:

$$RSSR' + HS^- \rightarrow RSS^- + R'SH \qquad (10)$$

The reaction between H_2S and low molecular weight disulfides such as cystines has been calculated to be thermodynamically neutral with an equilibrium constant of ~1 [76]. The kinetics reactions of H_2S with LMW disulfides and albumin disulfides have been demonstrated to be indeed slow ($k_{pH7.4}$ = 2–3 M^{-1} s^{-1} for cysteinylated and glutathionylated albumin Cys34)[60]. Furthermore, steady-state levels of H_2S are quite low in the cells, suggesting that this mechanism may not play a significant role in forming RSSH *in-vivo*[13,71]. However, specific examples, such as Prxs, suggest that this reaction still occurs when the cysteine environment increases its acidity. Indeed, the active site

cysteine of Prx exhibits a pK_a below 6 [115]. In the persulfidome analysis of *Aspergillus fumigatus*, two Prxs (Asfp3 and PrxA) have been identified as persulfidated. In cells lacking H_2S-production enzymes, the levels of Prx's disulfide bonds were increased compared to control [116].

1.4.2. Metal-catalyzed protein persulfidation via radical formation

The reaction between redox active metal centers and H_2S results in an oxidation of H_2S, producing different reactive sulfur species [72,117–120]. A good example is cytochrome C (Cyt C), where the heme group is more exposed, leading to H_2S oxidation and protein persulfidation[121]. Indeed, this oxidation reaction results in the production of $HS^{\bullet}/S^{\bullet-}$ radical that can efficiently react with surrounding proteins to yield RSSH[122,123] [Eq. (11) and (12)].

$$HS^{\bullet} + RS^{-} \rightarrow RSSH^{\bullet-} \qquad (11)$$

$$RSSH^{\bullet-} + O_2 \rightarrow RSSH + O_2^{\bullet-} \qquad (12)$$

The reoxidation of reduced Cyt C during the electron transfer to complex IV of the respiratory chain creates a pseudo-catalytic cycle for $HS^{\bullet}/S^{\bullet-}$ radical generation and, therefore, mitochondrial protein persulfidation (Figure 1.11A). Vitvitsky et al.[122] demonstrated that Cyt C plays an important role in mitochondrial protein persulfidation. Indeed, the silencing of Cyt C resulted in a decrease in protein persulfidation[122]. Furthermore, during the initiation of apoptosis, Cyt C is released and relocated close to procaspase 9. This proximity results in procaspase 9 persulfidation and its inhibition[122].

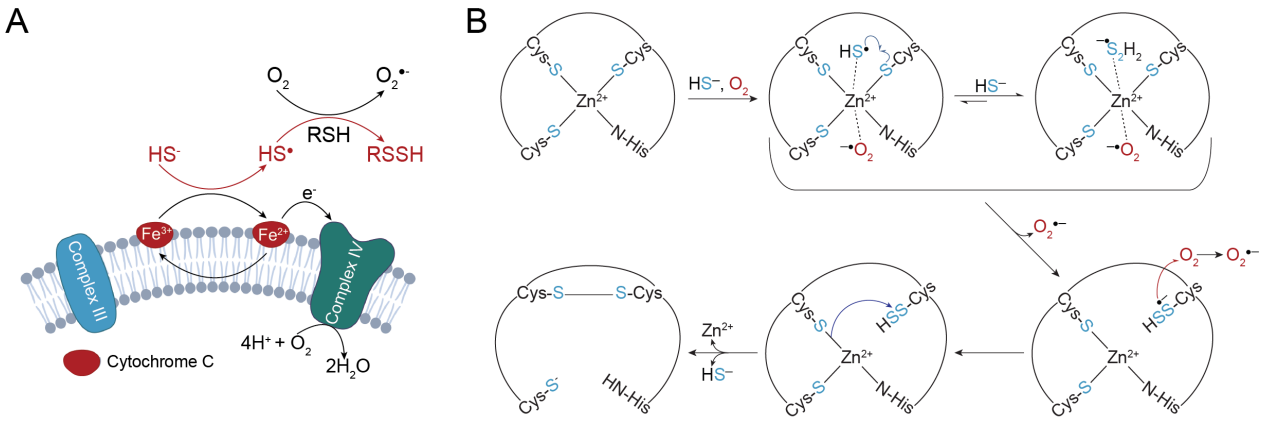


Figure 1.11. Metalloproteins catalyze RSSH formation. (**A**) Cytochrome C oxidizes H_2S into $HS^{\bullet}$ that can further react with protein thiols, resulting in persulfide formation. Reoxidation of the reduced cytochrome C by complex IV of the mitochondrial respiratory chain enables a pseudo-catalytic cycle for persulfide formation. (**B**) The coordinated zinc from zinc finger proteins could contribute to the persulfidation of these proteins in (i) facilitating the formation of superoxide from O_2, (ii) decreasing the pK_a of H_2S, favorable to the formation of $HS^{\bullet}$, and (iii) bringing O_2 and H_2S in proximity resulting in an effective electron shuttling.

Although zinc is not a redox-active metal, intriguing findings have emerged concerning zinc finger protein persulfidation. It has been demonstrated that H_2S can react with zinc finger proteins resulting in their persulfidation[124]. For example, treating tristetraprolin (TTP) with H_2S results in persulfide formation that occurs exclusively under aerobic conditions. Under these conditions, zinc coordinates HS^- and catalyzes the electron transfer to O_2, leading to the formation of $HS^{\bullet}/S^{\bullet-}$ and a superoxide anion (Figure 1.11B)[124]. While further research is needed to explore whether this mechanism applies to other zinc containing proteins, reanalysis of the site-specific persulfidome dataset[103] indicates that a significant number of zinc finger proteins are persulfidated (104/994). This suggests that the phenomenon observed in TPP might be extended to other zinc finger proteins.

1.4.3. Reaction of RSOH with H_2S

The reaction of H_2O_2 with RSH leads to the formation of sulfenylated cysteine, which constitute the basis of H_2O_2-based redox signaling[85,92,125]. Over the last decade, it has been shown that protein persulfides can form upon co-treatment with H_2O_2 and H_2S[63,90]. The reaction of H_2O_2 with protein thiol results the formation of RSOH, which can further react with H_2S to form RSSH [Eq. (11)].

$$RSOH + HS^- \rightarrow RSS^- + H_2O \qquad (11)$$

In certain proteins, such as albumin, the reaction of RSOH with H_2S can be considerably faster (~600 times for albumin) than with GSH at pH 7.4. In cells treated with H_2O_2, intracellular RSSH increases[60,71]. This increase is dependent on the H_2S-producing enzyme activity[60,71].

To understand the importance of endogenous H_2S and its reaction with RSOH, Filipovic's group[50] used cells lacking CSE. Treatment of these cells with H_2O_2 substantially increased RSOH levels, an effect not observed in WT cells. Interestingly, this increase can be mitigated using an H_2S donor (GYY4137), suggesting that converting RSOH to RSSH could be one of the primary mechanisms for resolving sulfenylation.

The interplay between H_2O_2 and H_2S has been also shown to play an important role in the signaling by the receptor tyrosine kinases. Namely, activation of the epidermal growth factor receptor (EGFR) increases H_2O_2 production[92,126,127]. Epidermal growth factor (EGF) treatment of MEF cells causes a rapid spike in global RSOH levels, subsequently declining as global persulfidation rises (Figure 1.12). Experimental modulation of H_2S levels affects the amplitude and the duration of the RSOH and RSSH

waves[50]. This suggests that converting RSH → RSOH → RSSH is an inherent redox switch essential for signal transduction and modulation (Figure 1.12).

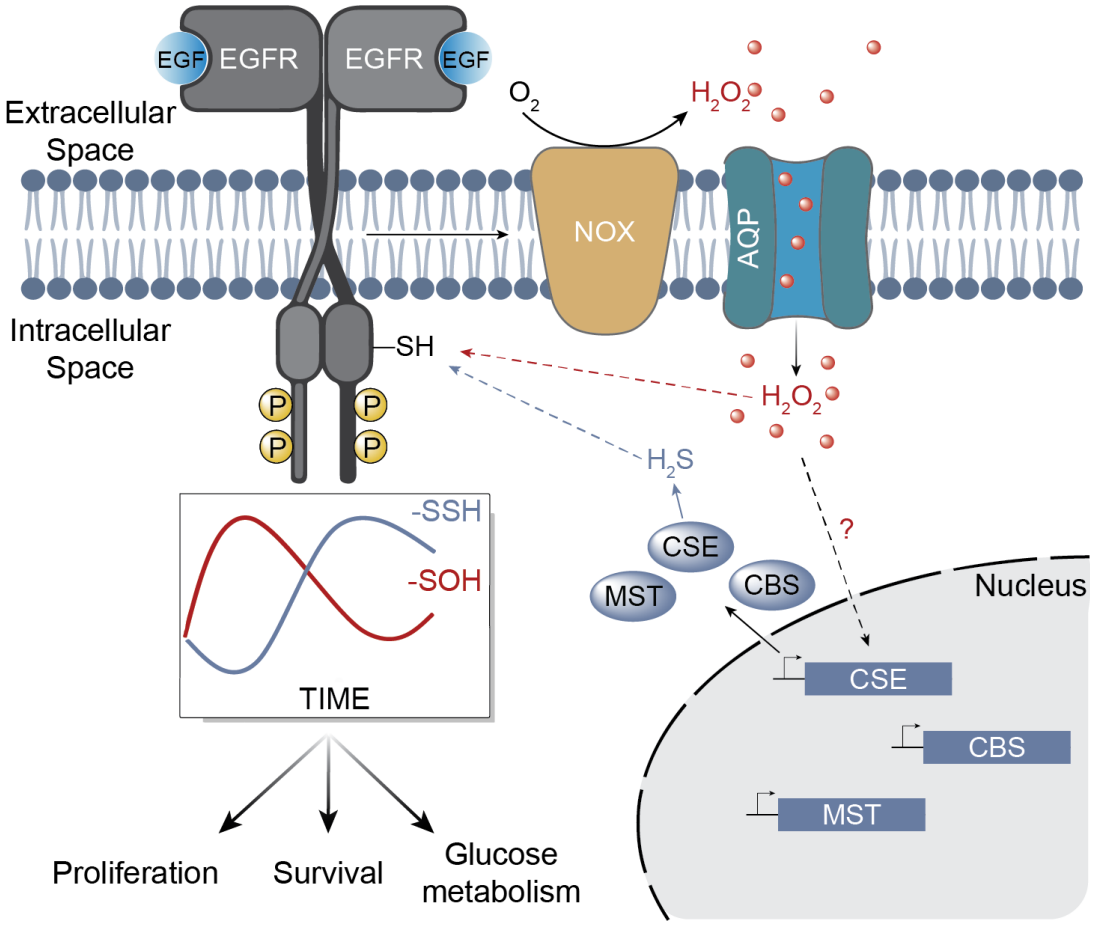


Figure 1.12. Role of protein persulfidation in EGFR signaling: RSOH to RSSH switch. Stimulation of the epidermal growth factor (EGFR) with EGF stimulates the NADPH oxidase to produce H_2O_2. Once transported in the intracellular space through the aquaporins (AQP), H_2O_2 reacts with the C797 of EGFR forming RSOH and enhancing its kinase activity. In addition, H_2O_2 stimulates the expression of the H_2S-producing enzymes, increasing H_2S production in the cell. H_2S reacts with C797-SOH, forming C797-SSH and inhibiting EGFR kinase activity (and downstream signaling). Therefore, the waves of RSOH and RSSH represent a redox switch that is controlling cellular response (such as proliferation, cell survival, or glucose metabolism) to the stimuli.

Thiol redox switching is known to regulate protein structure and function[83]. Upon EGFR activation, its C797 switches from RSH to RSOH, enhancing its kinase activity[126]. Moreover, activation of EGFR was shown to upregulate MPST, CSE, and CBS expression, which are responsible for the increase in H_2S levels and the RSOH to RSSH conversion[50]. Cells treated with H_2S donors exhibit decreased receptor activity and Y1068 phosphorylation[50]. This suggests that EGFR persulfidation could be important for ending its signal transduction in the cells[50]. Further investigation of the effect of persulfidation on the pathway would be necessary, as other downstream targets have also been found persulfidated.

1.4.4. Enzymatic production of LMW RSSH

Besides their canonical reactions, CBS and CSE use cystine to produce cysteine persulfide[63,72]. Additionally, CSE also uses homocystine and cysteine-homocysteine disulfide to produce their corresponding persulfides.

It has been suggested that CSE and CBS could be the primary source of cysteine persulfide in the cells[63]. However, simulations of these reactions showed that its formation is very low[72]. For example, at physiological substrate concentrations, CSE produces Cys-SSH at a rate of ~2.6 x 10^{-2} μmol mg^{-1} h^{-1}, much lower than its total H_2S rate production (~1.97 μmol mg^{-1} h^{-1})[72]. In addition, the synthesis of homocysteine persulfide by CSE is negligible, considering the intracellular substrate availability[72]. However, this reaction could become important under certain pathological conditions that increase cystine and homocystine concentration.

CARS, a cysteinyl-tRNA synthetase, also functions as a cysteine persulfide synthetase, making it an interesting source of LMW RSSH[128]. CARS2 knockout mice exhibit lower levels of mitochondrial LMW RSSH. Notably, Akaike and colleagues[129] proposed that CARS2 uses cysteine to form cysteine persulfide (Cys-SSH), which is subsequently used by CARS to form tRNA-Cys-SSH, suggesting that cysteine persulfide could be directly integrated into nascent proteins (Figure 1.13).

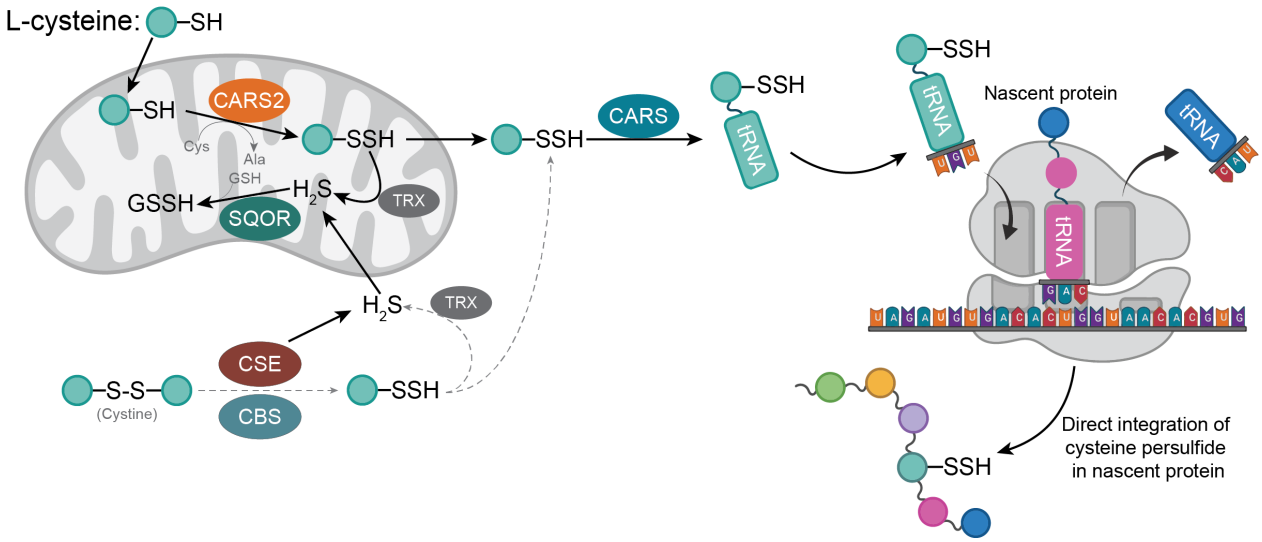


Figure 1.13. Low molecular weight persulfide formation and direct cysteine persulfide integration into proteins. Cystathionine gamma-lyase (CSE) and cystathionine beta-synthase (CBS) can use cystine to produce cysteine persulfide (Cys-SSH) in the cytoplasm. In addition, the mitochondrial cysteinyl-tRNA synthetase (CARS2) can produce Cys-SSH by converting L-cysteine into L-alanine (Ala), transferring the sulfur into another cysteine. From then, two fates are possible for the cysteine persulfide: (i) to be used by the cytoplasmic cysteinyl-tRNA synthetase (CARS), resulting in a direct incorporation of Cys-SSH into nascent proteins; (ii) to be reduced by the Trx/TrxR system producing H_2S that can be converted into another LMW persulfide (GSSH) by the sulfide:quinone oxidoreductase (SQOR).

Finally, SQOR, localized at the mitochondrial inner membrane, remains the primary source of LMW RSSH (Figure 1.13). It belongs to the flavin disulfide reductase superfamily, which is involved in the H_2S detoxification process[13,130,131]. As revealed by the crystal structure, the human SQOR active site's resting state is in the form of a trisulfide[130]. The reaction with H_2S and SQOR results in the persulfidation of its cysteine 201, forming an intense charge transfer complex with flavin adenine dinucleotide and another persulfide at C379. This additional sulfur can be transferred to an external acceptor, either GSH or coenzyme A (CoA), resulting in an efficient formation of GSSH or CoA-SSH[130]. The electrons from the abovementioned process are transferred to coenzyme Q, feeding the respiration chain; therefore, H_2S has been proposed as an inorganic substrate for mammalian respiration[132].

It is worth noting that MPST and TST could also be involved in forming LMW RSSH, particularly GSSH[13,32,131].

1.4.5. Transpersulfidation

The transfer of sulfane sulfur has emerged as an essential mechanism for iron-sulfur cluster assembly and transcription regulation through thionucleoside generation on tRNA[133,134]. These processes require sulfane sulfur to be transferred from one protein to another *via* transpersulfidation.

During the iron-sulfur assembly, the cysteine desulfurase, NFS, converts cysteine to alanine and forms a persulfide in its active site[135,136]. NFS can then transfer this additional sulfur to ISCU, the protein responsible for iron-sulfur cluster assembly (Figure 1.14A). On the way to the iron-sulfur cluster, NFS may as well transfer its persulfide to

other proteins and LMW thiols[137]. For example, in the NFS homolog in bacteria, IscS transfers its sulfur to tRNA sulfurtransferase (ThiI)[138]. The persulfidated ThiI eventually uses the sulfur to synthesize 2-thiouridine modification in tRNA (Figure 1.14B).

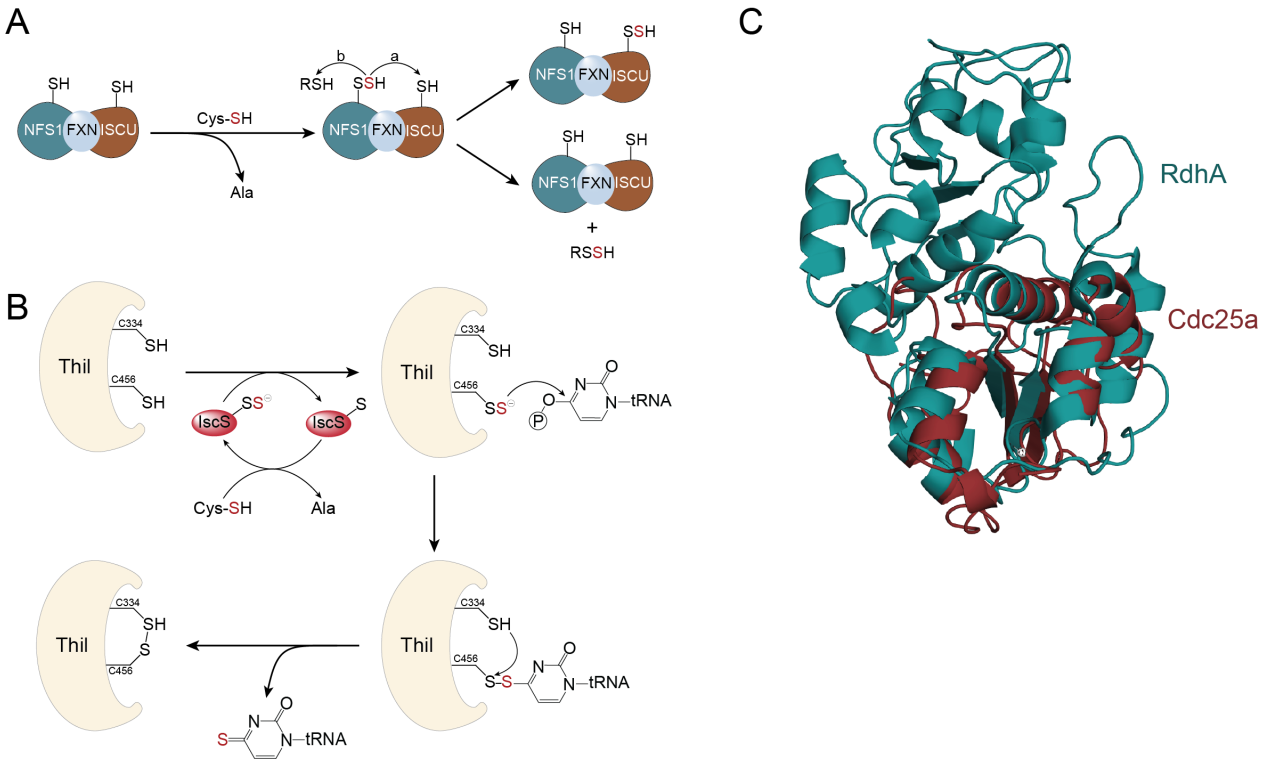


Figure 1.14. Transpersulfidation is involved in the iron-sulfur cluster assembly and RNA thiolation. (**A-B**) IscS (in procaryotes) or NFS1 (in eukaryotes) converts cysteine to alanine, transferring the sulfur onto their reactive cysteine, resulting in an intermediate persulfide. This additional sulfur can be transferred onto another protein, a phenomenon called transpersulfidation. (**A**) NFS1 transfer its additional sulfur to ISCU (iron-sulfur cluster assembly scaffold protein), enabling the iron-sulfur cluster assembly. FXN (Frataxin) links NFS1 and ISCU, enhancing the transpersulfidation reaction. (**B**) IscS uses its additional sulfur to transfer it onto ThiI (tRNA sulfur transferase), which leads to RNA thiolation. (**C**) The conserved α/β topology[139,140] of RdhA (Rhodanese; PBD: 1E0C) and Cdc25a phosphatase (PDB: 1C25).

One common characteristic of the sulfur transferases is their rhodanese domain fold with an α/β topology (Figure 1.14C). The number of these domains can vary and

they can be fused with other domains[139,140]. Notably, rhodanese can transfer sulfane sulfur to different targets, including succinate dehydrogenase, yeast alcohol dehydrogenase, and bovine serum albumin[141,142]. MPST also transfers sulfur from its substrate, 3-mercaptopyruvate, to the iron-sulfur chromophore and adrenal-ferredoxin[143]. Although its active site is distinct from the rhodanese domain, a recent study identified thiosulfate sulfur transferase-like domain-containing 1 protein (TSTD1) as a new sulfur transferase protein[144]. TSTD1 exhibits a highly exposed active site that can quickly transfer its sulfur to Trx, forming thioredoxin persulfide. Further investigations are required to understand the targets and role of TSTD1[144].

The transpersulfidation process is only possible due to the specific environment of the cysteine in the active site. For example, in rhodanese, C247 is located at the intersection of two helices, which lowers the pK_a of the thiol group by ~3.5 units, resulting in a more nucleophilic sulfur. When persulfidated, the terminal sulfur interacts with the positively charged groups of Ard186 and Lys249. These interactions mask this sulfur's negative charge, making it more electrophilic[145,146]. In these conditions, the terminal sulfur becomes highly susceptible to nucleophilic attack, favoring transpersulfidation.

In humans, about 100 proteins contain a rhodanese-like domain. Some of those proteins belong to the sulfur transferase family, but others belong to different families. These include the phosphatases of the Cdc25 family, phosphatases of the mitogen-activated protein kinase family, several ubiquitin hydrolases, as well as heat shock, cold shock, and phase shock proteins[140]. Therefore, one could hypothesize that some of these proteins could also serve as transpersulfidases. The idea that specific transpersulfidases could exist is attractive because persulfidation would not be only a

global modification of proteins depending on protein oxidation status and H_2S production. Indeed, identifying transpersulfidases with specific targets could provide more context and a better understanding of how persulfidation specifically regulates certain protein activities. Pedre et al.[147] recently attempted to show that MPST could serve as a transpersulfidase. The authors used TUM1, the *Saccharomyces cerevisiae* ortholog and showed that overexpression of TUM1 in mammalian cells increases protein persulfidation. However, these results are in disagreement with observations made by Zivanovic et al[50] where knockout of TUM1 in *S. cerevisiae* resulted in no change in persulfidation levels. Complementary studies, such as MPST interactome analysis, would be needed to understand its role as transpersulfidase in the cell.

Finally, transpersulfidation is not expected to happen with LMW RSSH. As previously mentioned, the preferred reaction of thiols with LMW RSSH is a nucleophilic attack at the electrophilic sulfur which results in mixed disulfide and H_2S release. In the case of LMW RSSH, RSSH tautomerisation to its thiosulfoxide form [RS(H) = S] would be needed for transpersulfidation to occur[148]. Simulation studies showed that the energy barrier for isomerization is >100kJ/mol, which makes the process highly improbable.

1.4.6. Depersulfidation

For the cell to use persulfidation as a protective and regulatory posttranslational modification, it must have a mechanism(s) to remove it. In the cell, Trx, a disulfide oxidoreductase, in conjunction with thioredoxin reductase (TrxR)[149,150], performs disulfide reduction of many partners. Since disulfides and persulfides are analogous, Trx/TrxR system could be one of the main depersulfidase. Studies have shown that Trx

is involved in the H_2S release from MPST[32]. Moreover, Krishnan et al.[151] demonstrated that Trx reduces persulfide from the phosphatase PTP1B ~ 200 times faster than DTT, which indicating that it is a highly efficient enzyme. Nagy[93] and Filipovic's[71] group both observed that Trx plays a key role in protein depersulfidation.

The depersulfidation by Trx could be explained by two mechanisms (Figure 1.15A). The first mechanism involves transferring the outer sulfur from the persulfide to the catalytic cysteine of Trx, resulting in Trx-SSH. This persulfide would then be removed through interaction with the resolving cysteine of Trx, releasing HS^- and forming an intramolecular disulfide bond in Trx. The second mechanism involves a nucleophilic attack by one of the Trx cysteines towards the inner sulfur of the persulfide. H_2S would then be immediately eliminated, and a Trx-client mixed disulfide would be formed. The client is then released upon a second nucleophilic attack from the resolving cysteine on the catalytic cysteine, again leading to the intramolecular disulfide bond formation in Trx. In both cases, TrxR is needed to restore the reduced form in Trx; this reaction requires NADPH as a cofactor. The second mechanism is generally used to explain Trx's disulfide activity. However, both mechanisms could account for Trx's depersulfidase activity, leading to H_2S release[144].

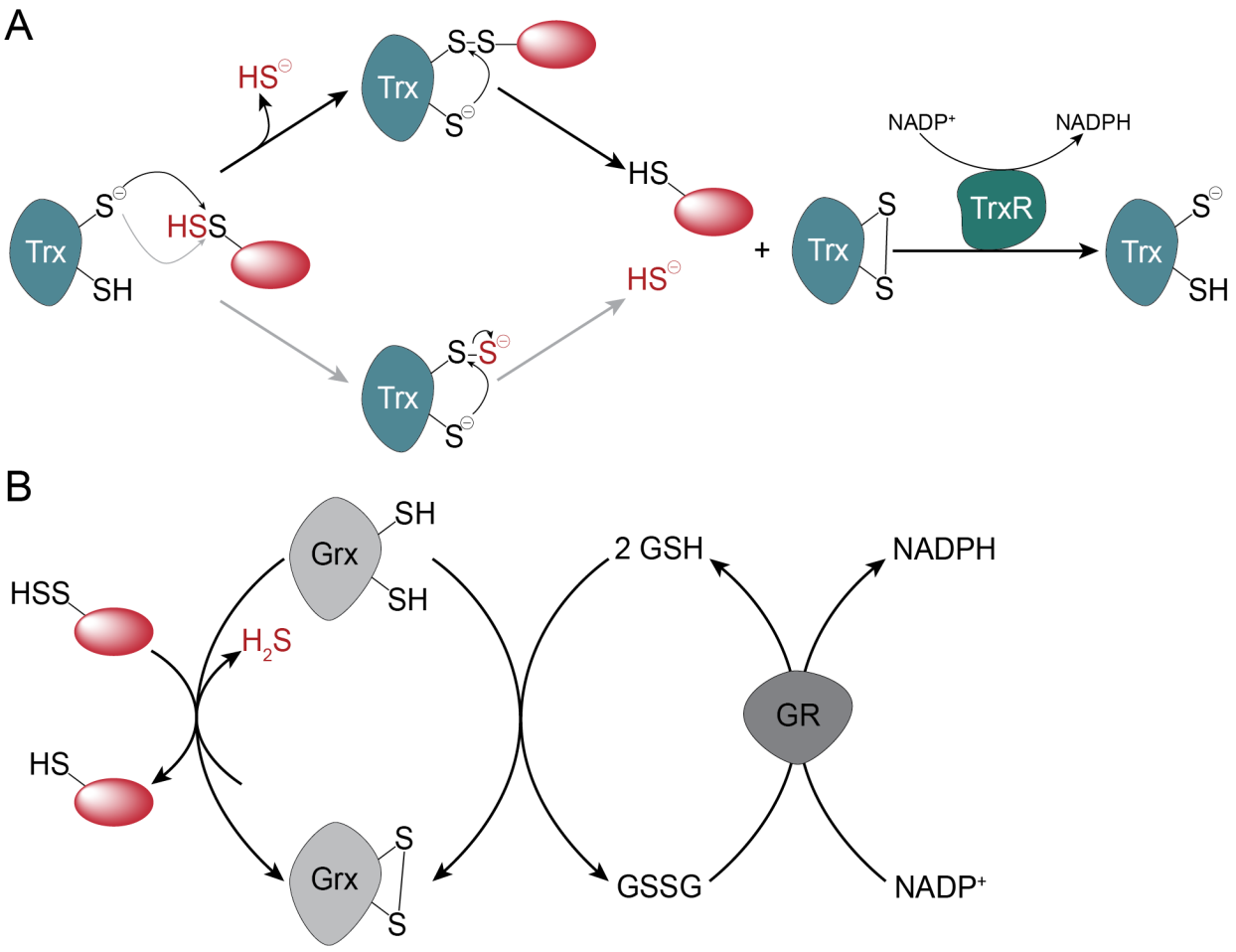


Figure 1.15. Enzymatic system for protein depersulfidation. (**A**) Thioredoxin (Trx) catalyzes depersulfidation using two different mechanisms, resulting in HS^- release and Trx oxidation. Oxidized Trx can be reduced by thioredoxin reductase (TrxR). (**B**) Grx (Glutaredoxin) oxidizes GSH into GSSH to catalyze depersulfidation of proteins. GSSG is then reduced by GR (Glutathione reductase). $NADP^+$ is an essential cofactor in the turnover of both systems.

Besides the cytosolic Trx, thioredoxin-related proteins of 14 kDa (TRP14) was also proposed as a potential depersulfidase. Indeed, its knockdown leads to increased persulfidation[97]. TRP14 could be the main depersulfidase during oxidative stress, as the Trx/TrxR system would be fully occupied by the peroxyredoxin system turnover[97].

Finally, the Grx/GR system has also been studied for its depersulfidase function[152] (Figure 1.15B). This system consists of two proteins, the glutathione

reductase (GR) and the glutaredoxin (Grx). Evolutionarily conserved, GR exhibits structural similarities with TrxR, such as FAD-containing oxidoreductase using NADPH as an electron source. However, one significant difference is the active site, composed of a cysteine for GR[153] and a selenocysteine for TrxR, contributing to their reactivity difference. In vitro, polysulfides or BSA-SSH can be efficiently reduced by GR in the presence of NADPH and GSH and even faster in the presence of Grx[97].

In both GSH and Trx/TrxR systems, NADPH is an essential cofactor for depersulfidation. No studies have yet shown how changes in NADPH/$NADP^+$ ratio control persulfidation levels.

1.5. Persulfidation as a regulator of protein function

Although many targets of persulfidation have been revealed through persulfidome analysis, very few examples of persulfide regulation of enzymatic activity or protein function exist. This chapter will provide some examples of gain or loss of activity.

1.5.1. Gain of enzymatic activity

GADPH is probably one of the most studied proteins in the context of its redox regulation. It is also one of the first proteins reported to be persulfidated[57]. GAPDH is an important glycolytic enzyme that converts glyceraldehyde-3-phosphate into 1,3 biphosphoglycerate using NAD as a cofactor, also known as a regulator of cell death[154]. The active site of GAPDH is highly conserved in the eukaryotic kingdom, including its cysteine residue responsible for its catalytic activity. Snyder's group proposed that persulfidation at C152 increases GAPDH activity by approximately 7-fold. In addition,

$CSE^{-/-}$ mice exhibit ~35% reduced GAPDH activity compared to the control mice[57]. When H_2S production is stimulated (through endoplasmic reticulum stress), the activity of GAPDH increases, although the total amount of protein remains unchanged[96]. This suggests that the persulfidation levels of GAPDH regulate its activity, and the cell could use persulfidation as a fine-tuning for glycolysis and gluconeogenesis activation.

In vitro experiments, where GAPDH was treated with H_2O_2 and H_2S, resulting in C152 persulfidation, also showed increased enzyme activity upon treatment, supporting previous findings[96]. In contradiction to these studies, treatment of purified GAPDH with polysulfides showed opposite results, where GAPDH activity was inhibited by ~42% compared to the untreated enzyme[155]. Further investigations identified C156 and C247 as persulfidated, while C152 persulfide could not be detected, suggesting that the persulfidation of those two residues would be inhibitory. Mutation of C156 into serine led to the persulfidation of C152. However, the inhibition of the enzyme remained, suggesting that persulfidation of both residues C152 and C156 could have an inhibitory effect on GAPDH activity. The authors also indicated that C247 persulfidation did not correlate with any change in GAPDH activity. Other studies also confirmed the persulfidation at the C156 and C247 sites but not at the C152[103]. Further investigations are required to understand the role of each cysteine on GAPDH activity. For example, persulfidation at C247 could affect the protein conformation and, consequently, its activity.

Persulfidation has also been shown to activate mitogen-activated protein kinase kinase 1 (MEK-1; Figure 1.16A)[156]. The signaling cascade MEK-1 – ERK1/2 – PARP1 is essential in recognizing DNA damage and recruiting partners to repair the damage. It is activated during oxidative stress[157], one of the primary causes of DNA damage.[158]

Treatment of HUVEC cells with 10 μM NaHS leads to an increased phosphorylation of ERK1/2 which is a key step for the response to stress activation. It has been suggested that persulfidation of C341 kinase MEK-1 increases its kinase activity[156].

1.5.2. Loss of enzymatic activity

In *A. thaliana*, ATG18a is a core protein for the induction of autophagy under abiotic stress. The protein binds to phosphoinositides[159,160] and complexes with ATG2, leading to the formation of autophagosomes. In a recent study, Aroca et al.[161] demonstrated that ATG18a is persulfidated at C103 and that this modification inhibits autophagy formation triggered by the endoplasmic reticulum (ER) stress (Figure 1.16B). Co-treatment of seedlings with tunicamycin and NaHS drastically reduced the number and size of autophagosomes compared to the tunicamycin-treated condition. On the other hand, NaHS did not affect the conditions where ER stress was not induced. As tunicamycin is known to trigger ROS signaling[162], it suggests that persulfidation of this cysteine occurs through the RSOH/RSSH switch, demonstrating the importance of H_2S and persulfidation regulatory effect under stress conditions. The C103 residue is inside a hydrophobic cavity formed by ^{83}FNQD^{86} and F90 amino acids, also found in human orthologs of this protein. Through electrostatic interactions, the positive charge of this region helps with binding negatively charged phosphatidylinositide molecules. Upon persulfidation, which would result in addition of a bulky and negatively charged sulfur atom in this region, this interaction is modified. This new charge also affects the cavity's size, increasing the interaction with phosphoinositide molecules[161].

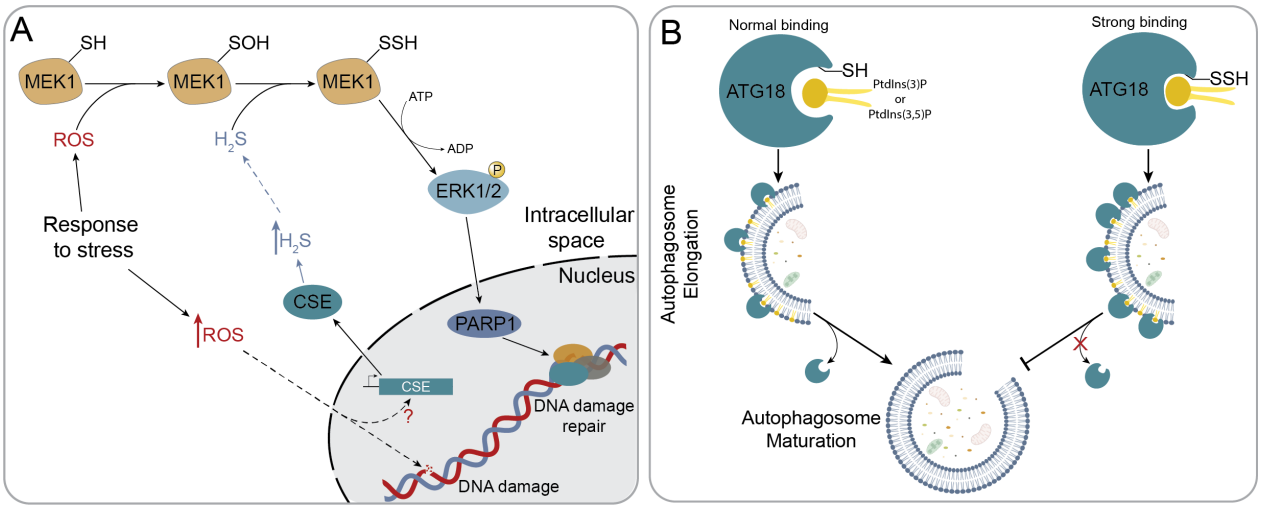


Figure 1.16. Persulfidation regulates protein function. (**A**) Persulfidation is involved in the DNA repair mechanism in response to oxidative stress. Persulfidation of MEK1 upon increase of H_2O_2 activates the protein, enabling the phosphorylation of ERK1/2 and activating the DNA repair surveillance system[157]. MEK1: Mitogen-activated protein kinase kinase 1; ERK1/2: Mitogen-activated protein kinase 1/2; PARP1: poly(ADP-ribose) polymerase 1; ROS: ; (**B**) In *Arabidopsis thaliana*, structural changes of the autophagy-related protein (ATG18) upon persulfidation increase its affinity for phosphatidylinositides. The stronger binding of ATG18 to these lipids disables its departure from the autophagosome, leading to the inhibition of the autophagosome maturation[161]. PtdIns(3)P: Phosphatidylinositol 3-phosphate; PtdIns(3,5)P: Phosphatidylinositol 3,5-phosphate.

1.6. Persulfidation in aging and neurodegeneration

Aging can be defined as a progressive and time-dependent loss of function at the molecular, cellular, and, ultimately, at the organism level.[163] This decline results from an increase in the deletoriome, defined by an accumulation of “damages”. In the last decade, the concept of aging hallmarks has become widely accepted, defining both the causes and consequences of aging[164] (Figure 1.17). Nine hallmarks were defined and grouped into three categories of interacting factors: (i) the primary hallmarks usually defined as the causes of the damages in the cells, (ii) the antagonistic hallmarks

representing the organism or cell response to the damages, (iii) the integrative hallmarks being the culprits of the phenotype[164]. Recently, the same authors updated this list, adding 3 new hallmarks: disabled macroautophagy, chronic inflammation, and dysbiosis [163]. Previously discussed in detail by Perridon et al.[165], H_2S has been shown to positively affect 8 out of 9 of the previously defined aging hallmarks. A few examples of these are the control of genomic instability through the activation of the MEK-1 – ERK1/2 – PARP-1 pathway, promoting the DNA damage surveillance and repair, the prevention of mitochondrial dysfunction through the modulation of complex IV and SOD activity leading to reduced ROS production and injury prevention[166,167]. In addition, H_2S is known to activate (macro)autophagy by inhibiting the PI3K/Akt/mTOR pathway [168]. Similar effects are observed with the life-extension drug rapamycin [168]. H_2S positively affects the microbiome, regulating microbiota biofilm in the context of inflammatory bowel disease [169,170], and acts as an anti-inflammatory compound [171]. Therefore, hydrogen sulfide has been shown to modulate at least 11 out of the 12 updated aging hallmarks, where only its effect on telomere attrition has never been assessed (Figure 1.17).

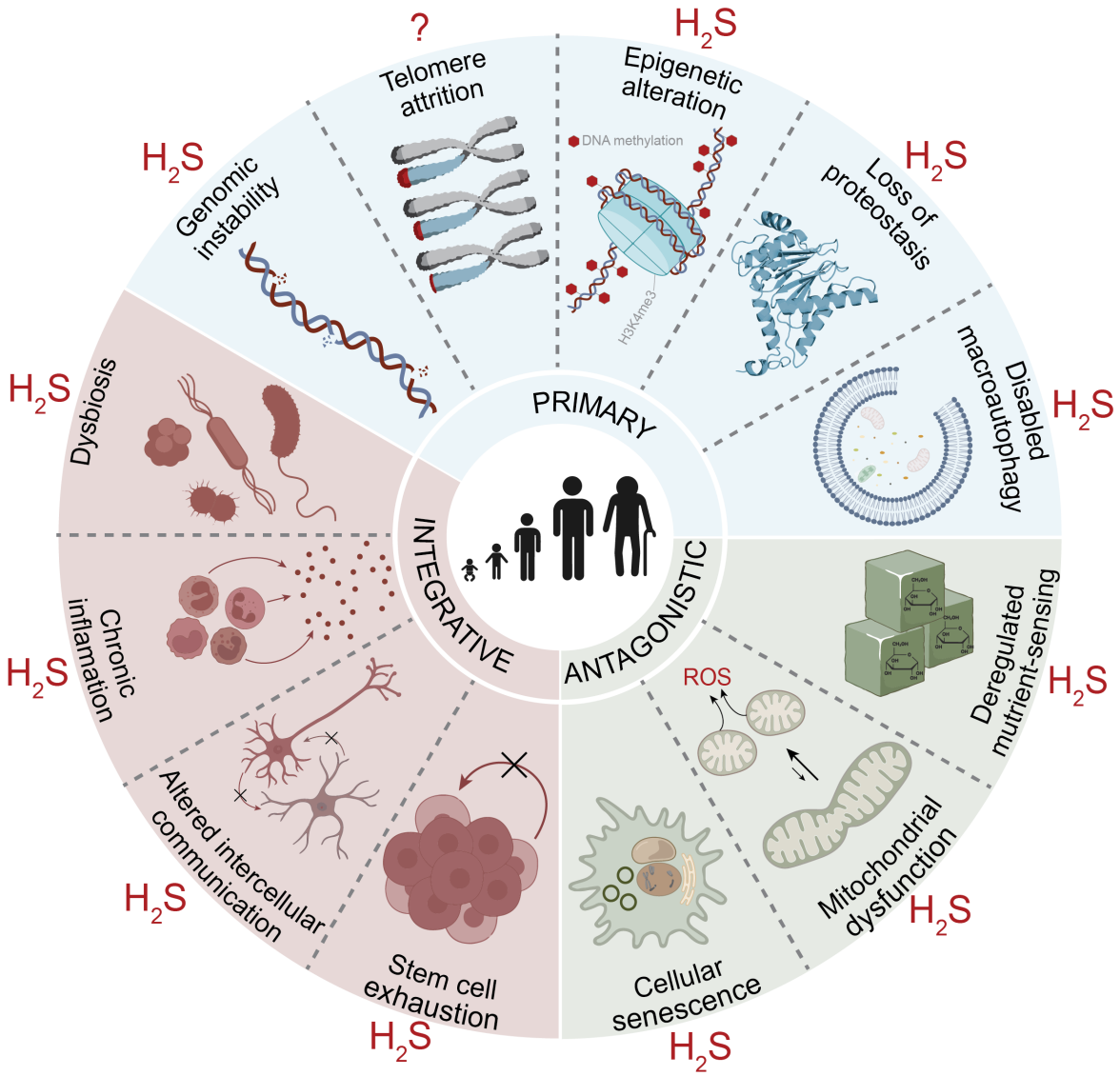


Figure 1.17. Hallmarks of aging and H_2S anti-aging effect. The primary, antagonistic, and integrative categories define the hallmarks of aging. Each of these categories are defined by multiple hallmarks, most of which are affected by H_2S. Positive effect of H_2S was observed on: (i) the primary hallmarks: genomic instability[156,172], epigenetic alteration[173,174], loss of proteostasis[175,176] and disabled macroautophagy[168]; (ii) the antagonistic hallmarks: dysregulation of nutrient sensing[177,178], mitochondrial dysfunction[166,167] and cellular senescence[179,180]; (iii) the integrative hallmarks: stem cell exhaustion[181,182], altered intercellular communication[183], chronic inflammation[171] and dysbiosis[169,170].

1.6.1. Imbalance in persulfidation: new aging hallmark?

In the updated version of the hallmarks of aging, authors defined three criteria to identify aging hallmarks: (1) time-dependent manifestation or alteration, (2) accentuating the hallmark leads to accelerated aging, (3) reversing the hallmark results in deceleration, halt or reverse aging processes[163]. In addition to its effect on most of the defined hallmarks and following this guideline, H_2S signaling through persulfidation shares similar characteristics to those specified for the aging hallmarks.

Time-dependent decrease of persulfidation

Using tag-switch method, Zivanovic et al. reported an age-dependent decrease in protein persulfidation, which is conserved among species[50]. In addition, proteomics studies of *C.elegans* showed a time-dependent decrease in CSE expression with age.[184,185] Large-scale RNAseq studies also measured decreased CTH mRNA in humans[186,187] and mice[188,189]. Furthermore, a decline in persulfidation was measured in rat brains from 6 to 24 months old, caused by decreased CSE, CBS, and MPST expression[50,190].

Decreased persulfidation levels lead to accelerated aging

In *C. elegans*, knockout of transsulfuration pathway genes such as mpst-3 and cth-2 decreases the lifespan of these organisms when compared to WT[27,50]. While further studies are needed in mice to understand the effect of the lack of H_2S on their lifespan, decreases in CSE or CBS are associated with age-related diseases such as Alzheimer's[52], Huntington's[39], and cardiovascular diseases[24,191], all of which lead to health complications and decreased life expectancy[192,193].

Increase of exogenous and endogenous H_2S decelerates aging

Either through genetic manipulation or slow-releasing donor treatment, H_2S has shown remarkable anti-aging effects in different organisms. Indeed, the overexpression of CSE or CBS in *Drosophila melanogaster* extends their lifespan[194]. In *C. elegans,* similar effects were observed when they were exposed to an H_2S-rich atmosphere. Indeed, worms showed an increase of ~70% of their median lifespan when exposed to H_2S[195]*.* Moreover, a systematic increase of *Cth* mRNA levels was found in different lifespan extension interventions[196], including metformin and rapamycin treatments, suggesting its role in decelerating aging and extending lifespan. In addition, mimicking rapamycin's effect through the knockout of *raga-1* in *C. elegans* prolongs its lifespan in a "*cth-2*-dependent" manner.[27] Finally, the striking effect of H_2S inducing a suspended animation-like state in mice underlines its potential for pausing aging[197].

1.6.2. Persulfidation protects against neurodegeneration.

Neurodegeneration is often caused by the loss of proteostasis[198], closely linked to the dysregulation of autophagy[199]. Both of these aging hallmarks were shown to be affected by H_2S and persulfidation. To maintain protein homeostasis, cells developed complex mechanisms for protein turnover, such as protein synthesis, folding, unfolding, and degradation[200]. Control of these mechanisms remains a significant challenge in maintaining proteostasis upon cellular stress. PTMs play a key role in regulating proteome homeostasis quickly and reliably[201]. Precise regulation of PTMs in the cell is necessary to maintain protein balance[201]. Thus, uncontrolled posttranslational modification of proteins is often linked to unbalanced protein homeostasis and

neurodegeneration[202]. Classical examples of this phenomenon are the hyperphosphorylation of Tau protein leading to its aggregation[203] or histone H3 hypo-acetylation, usually observed in polyQ diseases , which often leads to an aggravation of their respective disease phenotype[204].

As previously mentioned, $CSE^{-/-}$ mice have been characterized by multiple phenotypes often associated with aging, linking the enzyme and its ability to produce H_2S to neurodegeneration[39,52,53]. In addition, decline or loss of CSE expression followed by a global decrease of protein persulfidation has been reported in various neurodegenerative diseases such as Parkinson's, Alzheimer's, and Huntington's diseases in humans and their corresponding animal models[39,50,52,53].

Parkinson's disease

In Parkinson's disease, persulfidation is protective at many levels, but most notably by activating parkin E3 ligase[53] and controlling the level of DJ-1 cysteine overoxidation[50].

Parkin is an E3 ligase involved in cell fate decisions in Parkinson's disease. Sensitive to the PTM changes of its cysteine residues, parkin activity is inhibited when *S*-nitrosylated[205] and activated when persulfidated[53]. Parkin activation enables neurons to recover from cell death by efficiently removing damaged proteins[53] (Figure 1.18). In the brains of Parkinson's disease patients, a switch between persulfidated parkin (decreasing) and *S*-nitrosylated parkin (increasing) has been observed, suggesting that loss of persulfidation may be pathological[53].

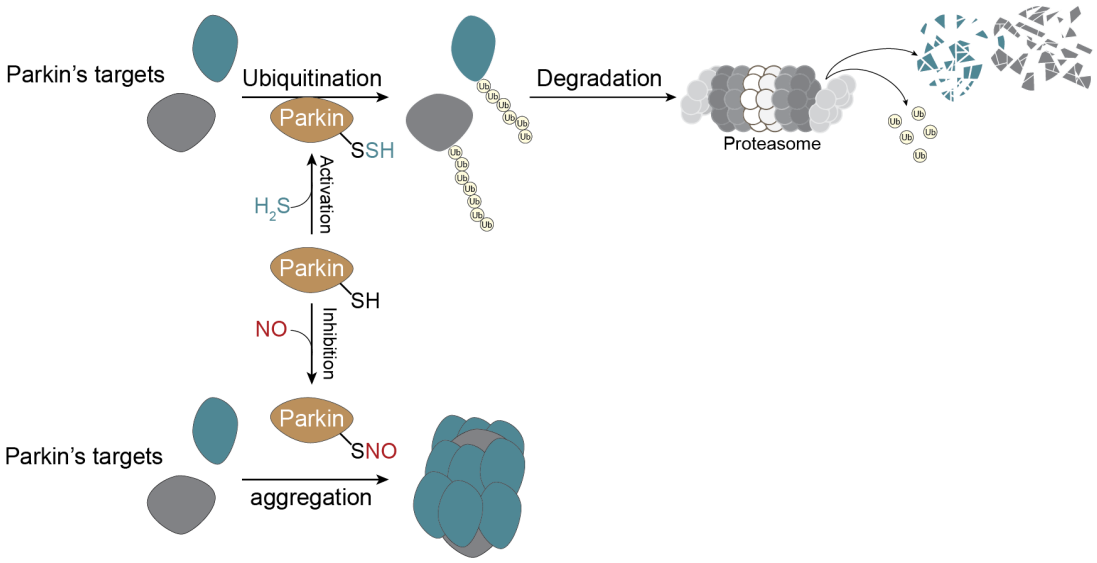


Figure 1.18. Parkin activation upon persulfidation protects against protein aggregation. Persulfidation of the E3 ligase parkin activates the enzyme, resulting in polyubiquitination and proteasomal degradation of its targets. On the contrary, *S*-nitrosylation of parkin inactivates the protein, allowing its targets to aggregate. Parkinson's disease patient exhibits lower persulfidation and higher *S*-nitrosylation, suggesting that the switch between RSSH and RSNO may be pathologic[53]. Age-dependent decrease of persulfidation[50] and increase of *S*-nitrosylation[206] could be one of the factors leading to sporadic cases of Parkinson's disease. NO: nitric oxide; H_2S: hydrogen sulfide.

DJ1, also known as PARK7 (Parkinson disease protein 7), is associated with autosomal recessive early-onset Parkinson's disease[207]. The protein exhibits two types of enzymatic activity, glyoxalase and deglycase, but also serves as a redox sensor for reactive oxygen species[208–210]. Upon overoxidation (RSO_2H and RSO_3H) of its C106 residue, DJ1 relocates to the mitochondria, protecting cells against cell death[208]. DJ1 was found to be endogenously persulfidated in red blood cells[50], prompting an investigation into the effect of various thiol oxidation states (RSH, RSSH, RSOH, RSO_2H, and RSO_3H) on DJ1 activity.

In wild-type mouse embryonic fibroblast (MEF), a protective wave of persulfidation in DJ1 was observed upon H_2O_2 treatment, while $CSE^{-/-}$ cells exhibited a burst of C106 overoxidation[50]. Recently, the effects of RSO_2H and RSSH on DJ1 activity and structure have been compared[211]. Both PTMs inhibited its activity, however, important structural differences exist between RSSH and RSO_2H. In the persulfidated protein, essential structures that stabilize the reduced dimers are lost or weakened. Opposite to overoxidation of C106, its persulfidation exposes the C106 site more, which is then easily targeted by the depersulfidase activity of the Trx/TrxR system, reverting DJ1 to its reduced form[211].

A novel activity of DJ1 was reported recently, where the protein hydrolyses the reactive cyclic 3-phosphoglyceric anhydride (cPGA), protecting proteins against lysine acylation[212]. Lysine acylation by cPGA creates long and hydrophobic chains potentially involved in protein aggregation[212]. Notably, cPGA is a byproduct of glycolysis known to be promoted upon oxidative stress[213]. Further investigations are required to understand if persulfidation could be used as a switch between different activities of DJ1, providing context-dependent protection against oxidative stress.

Alzheimer's disease

In addition to the observed low H_2S production and persulfidation in Alzheimer's disease (AD) patients[214,215], it has been proven that treatment with NaHS improves the memory deficit in rat AD model[216].

Glycogen synthase kinase 3β (GSK3β) is one of the busiest kinases in the cell and is involved in AD. Its targets are numerous (>100)[217], and include tau protein (MAPT). Phosphorylation of tau by GSK3β leads to its dissociation from the

microtubules[218], increasing its propensity to aggregate. This phenomenon, combined with hyperphosphorylation of tau, generally leads to neurofibrillary tangles formation, one of the most prominent features of the disease[219–221]. The persulfidation levels of GSK3β have been shown to decrease in cells, mouse, and human brain samples of AD patients[52]. C218 of GSK3β has been identified as a target for persulfidation, resulting in a loss of GSK3β kinase activity[52]. It was postulated that the age-related decline of CSE[50] would lead to decreased GSK3β persulfidation, increasing its phosphorylation activity and increasing the risk of sporadic tau hyperphosphorylation and aggregation[52] (Figure 1.19). In addition, *in-vitro* assays demonstrated that tau binds to CSE and increases its activity[52], creating a positive feedback loop against tau hyperphosphorylation. Therefore, loss of tau through its aggregation would decrease CSE activity and diminish the protective effect of persulfidation.

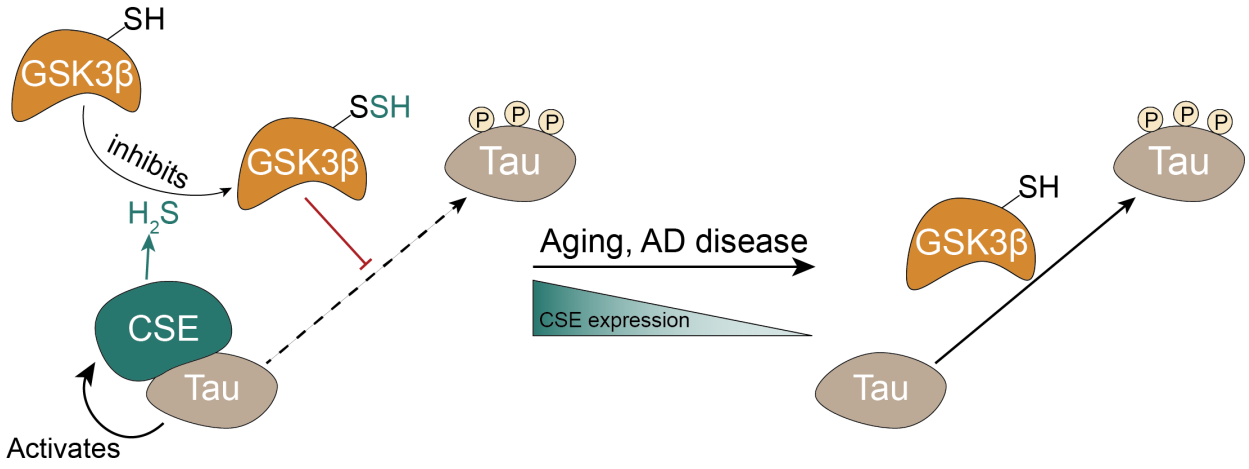


Figure 1.19. Tau-stimulating CSE activity contributes to positive feedback against tau hyperphosphorylation and aggregation. Interaction of tau with CSE stimulates CSE-dependent production of H_2S[52], followed by an increase in GSK3β persulfidation. In its persulfidated form, GSK3β is inhibited[52], preventing tau hyperphosphorylation. During aging or in Alzheimer's disease patients, the decrease of persulfidation results in GSK3β activation and tau

hyperphosphorylation. This unbalance of tau phosphorylation is one of the most prominent features of Alzheimer's disease[219–221]. Tau, MAPT: microtubule associated protein tau; GSK3β, glycogen synthase kinase 3β.

H_2S was also shown to regulate the expression of beta-site amyloid precursor protein cleaving enzyme 1 (BACE-1), which is involved in forming beta amyloids in AD. Treatment with H_2S donors results in a decreased BACE-1 expression via activating the PI3-K/Akt signaling pathway[222]. Decrease in BACE-1 expression subsequently leads to a diminished Aβ1-42 secretion[222].

PolyQ diseases

One of the most direct links between H_2S, persulfidation, and neurodegeneration has been assessed through the phenotypical observation of $CSE^{-/-}$ mice. Mice lacking CSE display hind limb clasping similar to those observed in Huntington's disease (HD) model mice.[39] Also, CSE levels in patients with HD are considerably reduced, negatively correlating with the severity of the clinical symptoms[39]. HD is generally characterized by accumulating huntingtin protein (HTT) with an expended poly-glutamine domain (polyQ)[223]. This mutant of HTT was shown to interact and sequester SP1, the transcription factor regulating CSE gene expression, leading to the downregulation of CSE expression[39,224].

1.6.3. Persulfidation's protection against over-oxidation of proteins

It has been postulated that ROS (mainly H_2O_2) production increases with age and could in part be one of the drivers of aging[225]. In the event of oxidative stress, ROS production in the cell increases, resulting in the oxidation of cysteines (RSOH). This

oxidation also constitutes an essential mechanism for signaling and determines cell fate.[91,92] However, if unresolved, prolonged exposure to ROS would lead to the formation of RSO_2H and RSO_3H[226], irreversible and deleterious modifications (Figure 1.20). Recently, the Filipovic's group proposed that persulfidation, could be an evolutionarily conserved mechanism that protects against overoxidation of cysteines and aging[50]. By reacting with RSOH, H_2S would lead to the formation of RSSH, which are better ROS scavengers. Contrary to the overoxidation of cysteine, the overoxidation of the persulfides is reversible, and can be resolved by the Trx/TrxR system[71,97] or other reducing agents (Figure 1.20). Therefore, persulfidation protects against cysteine overoxidation and general ROS production, preserving cysteine integrity while controlling protein function[190]. The age-related decrease in persulfidation[50] would leave cysteines unprotected from an increased level of ROS. For example, primary fibroblasts collected from a human donor at different ages (31 and 48 years old) exhibit a decrease in persulfidation and an increase in RSO_2H with age[50], supporting the hypothesis of RSSH protecting against overoxidation.

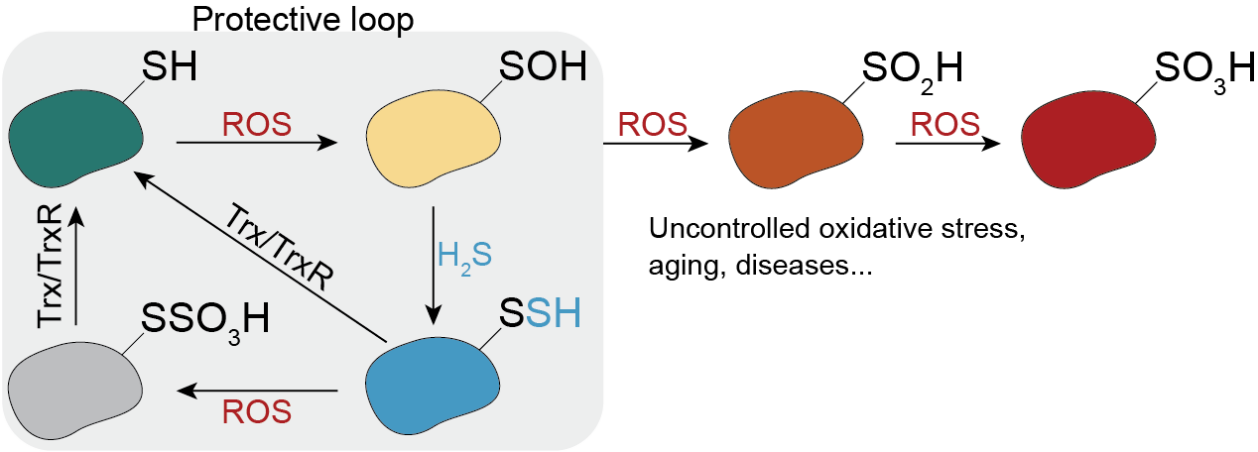


Figure 1.20. Proposed mechanism of protective and anti-aging effects of protein persulfidation. Upon persistent oxidative stress, aging and diseases, an increase in ROS can lead to sulfinic (RSO_2H) and sulfonic (RSO_3H) acid formation on protein thiols[226]. Reaction of H_2S with RSOH to form RSSH has been proposed to protect cysteine from these two irreversible modifications[50]. RSSH are also better ROS scavengers, allowing faster stress removal. In aging, the levels of RSSH decrease, leaving the cysteine susceptible to overoxidation.

A recent proteomic analysis comparing proteins of different species revealed that 16% of proteins contained at least one cysteine exclusively present in primate proteome[227]. In this group of proteins, called the “primate differential redoxome” (PDR), many of these cysteines are surface-exposed and more susceptible to oxidation[227]. Additionally, the PDR contains a substantial number of proteins involved in various neurodegenerative diseases[227]. Taken together these data suggest that crosstalk between persulfidation and overoxidation of cysteines could play an essential role in protein structure integrity and stability. Indeed, analysis of persulfidome data published to date[102,103] reveals that many persulfidated proteins are structural proteins.

Further investigations are needed to determine how, and which cysteines could be responsible for the protein stability. For example, the newly discovered phenomenon of liquid-liquid phase separation is known to affect protein structure and stability. Studies on how cysteine modifications influence protein liquid-liquid phase separation (LLPS) could be essential for understanding the link between redox homeostasis and proteostasis.

1.7. Biomolecular condensates: definition and biological role

LLPS of proteins is the ability of one or more proteins to form membraneless compartments in the cell[228]. Also called biomolecular condensation, this biophysical feature has emerged as an essential regulator of many cellular processes[229] such as response to stress[228], regulation of transcriptional[230–233] and translational[234] processes, and regulation of signal transduction[235,236].

1.7.1. Driving forces and characteristics of biomolecular condensates

Macromolecules such as proteins or RNA can undergo LLPS, forming a dense phase that coexists with a diluted phase[237] (Figure 1.21A). The biophysical forces driving phase separation are mainly multivalent weak interactions, making the exchange easier between the dense and diluted phase[238]. These interactions lead to the emergence of interfacial tension necessary to form condensates[239]. Domains such as “multivalence domains” or intrinsically disordered regions (IDRs) are likely to provide this multivalence property[240,241] (Figure 1.21B). Because of this, many studies on LLPS focus only on proteins carrying those domains. However, a recent high-throughput study identified more than 1500 proteins capable of forming condensates, of which more than 500 have never been reported before[242]. Careful inspection of those targets revealed that many do not carry a multivalence domain or an IDR. Further studies are needed to determine which other domains or interactions play a role in LLPS formation.

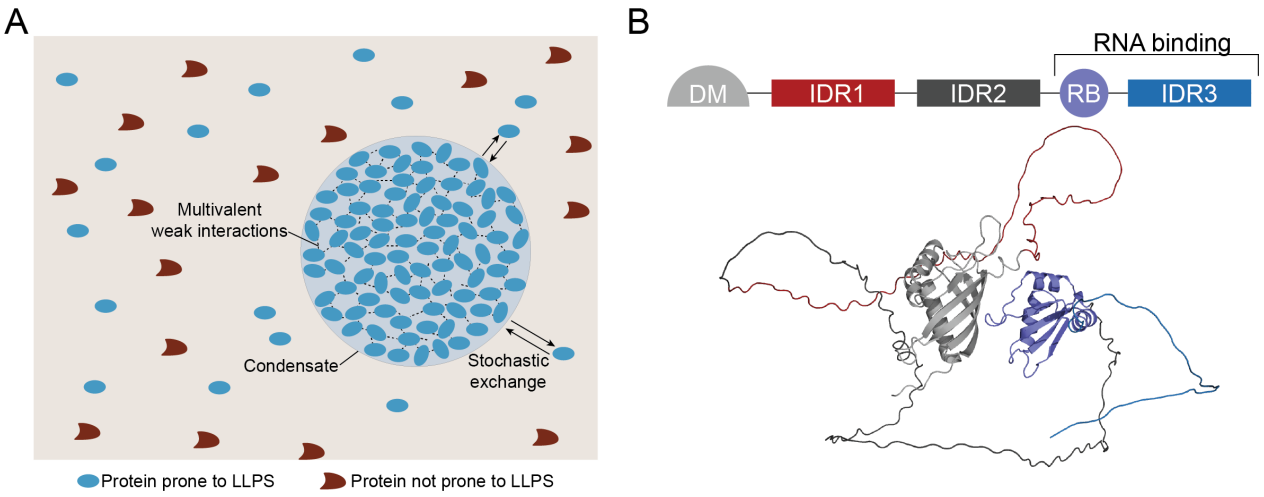


Figure 1.21. Biomolecular condensates of proteins. (**A**) Protein biomolecular condensates result from the ability of one or more proteins to form a dense phase coexisting with a diluted phase. Condensates are formed by the multiple weak interactions between proteins and/or RNA/DNA, resulting in a highly concentrated phase. Due to the weak interactions, stochastic exchanges are still allowed, leading to a dynamic turnover system between the dense and diluted phases. (**B**) An example of a classical protein structure with the ability to phase separate is depicted within the G3BP1 structure (Lower panel: PDB: AF-Q13283-F1-model_v4). The structures' colors correspond to the domains shown in the top panel. The intrinsically disordered region 3 (IDR3) and the RNA binding domain (RB) are both responsible for the interaction with RNA. Under normal conditions, the IDR1 and IDR3 interact, inhibiting the phase separation of the protein. Under stress, the increased amount of free RNA interacts with the IDR3 domain to cause phase separation of G3BP1 and formation of stress granules[243,244].

In the cell, condensates are formed by hundreds of thousands of protein molecules, with heterotypic interactions primarily driving their formation[228]. Protein-protein, RNA-protein and DNA-protein interactions are all possible drivers of phase separation. Therefore, the formation of certain condensates will depend on the concentration or the availability of both the protein and the polynucleotide chain[228]. For example, stress granules (SG) are biomolecular condensates formed upon cellular

stress[244] and comprise of hundreds of different proteins[245]. However, the formation of SG also relies on inhibition of the transcription machinery, which increases free RNA[246].

Among the numerous proteins involved in SG, GTPase-activating protein-binding proteins (G3BP1 and G3BP2) are essential for initial formation of these granules[247]. This example underlines the co-existence of two types of protein in the molecular condensates: the scaffold and the client proteins[248]. Molecular condensates are organized and induced by scaffold proteins while the clients bind to the scaffolds' free interaction site. Therefore, it is tempting to suggest that cells can modulate the composition of different condensates by regulating the relative scaffold protein stoichiometry in the condensates. In agreement with this statement, a recent time-resolved study of SG proteome revealed a shift in the SG composition, with 184 early proteins, 116 late proteins and 85 proteins constantly present[245]. These results suggest a time-dependent change in the valence of the scaffold protein, leading to the remodeling of the composition of stress granules[249]. In addition, the reduced number of different proteins in the granules over time may be correlated with a reduced number and variety of interaction sites within the scaffold protein.

1.7.2. Molecular aging of the condensates

The aging of condensates can be defined by a transition state from liquid to more solid-like droplets[250,251] (Figure 1.22). It is important to distinguish this process from biological aging. The link between the aging of biomolecular condensates and age-related disease will be discussed below.

There are few known mechanisms by which droplets can age, with the first one being gelation[251,252]. Gelation is characterized by increased physical cross-links between the proteins in the condensates. Once those cross-links reach a critical density, called percolation threshold, the polymer network expands through the entire droplet[253]. A specific feature of gelation is its time scale: this process is characterized by a sudden change of state[228] from fluid to solid-like / viscous droplet. Interestingly, protein structures like β-sheet domains seems to be a key structure in the process of gelation and increased condensate solidity in time[254].

The second model, called glassy-system or Maxwell fluids, is distinguished by its different time scale than the one for gelation. Indeed, in the soft glass model, droplets progressively transition to a solid-like state but never reach a thermodynamic equilibrium[228]. A recent example of the protein fused in sarcoma (FUS) aging droplets has been described as a Maxwell fluid[255]. The aging process in droplets remains broadly poorly understood; therefore, it is unclear why different protein condensates age at different time scales.

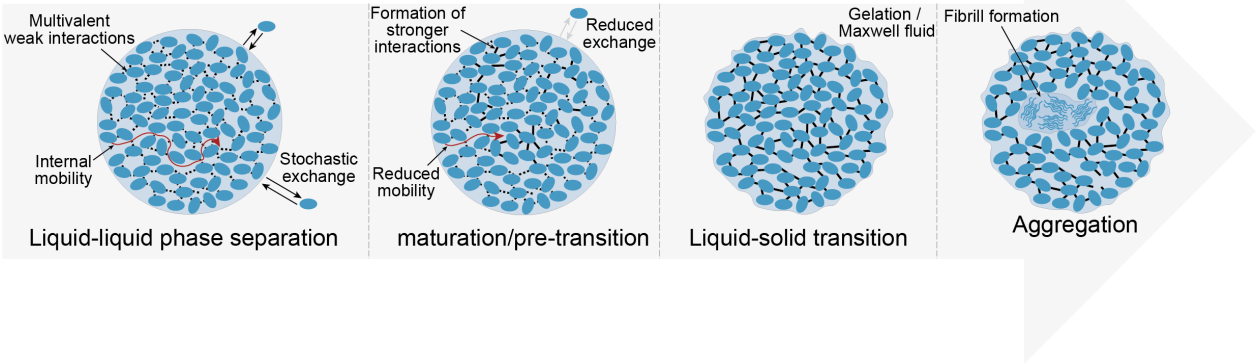


Figure 1.22. Molecular aging of biomolecular condensates. The formation of molecular condensates is driven by weak interactions, allowing exchange between the dilutes and the

dense phase. The condensate structure and biophysical characteristics change as time passes, a phenomenon called molecular aging. Molecular aging can either be defined as a fast and sudden change of the condensates (gelation theory) or a more constant and regular change over time, never reaching a stable state (Maxwell fluid aging theory). In both cases, weak interactions are often replaced by stronger interactions resulting in reduced or fully absent exchange with the diluted phase and a more solid-like condensate state. If uncontrolled, liquid-solid transition could eventually lead to protein fibril formation and aggregation.

1.7.3. Posttranslational modification regulates the formation, dissolution, and aging of LLPS

Cells must regulate various condensates' formation, dissolution, and aging processes to maintain proper homeostasis. One efficient way of doing this is by modulating the posttranslational modifications of the proteins. PTMs are essential in providing a fast response to stress or stimuli. Many PTMs have already been identified as modifiers of LLPS[256]. The most studied are phosphorylation, acetylation, methylation, SUMOylation, neddylation, ubiquitination and methionine oxidation[256]. These modifications act on the capacity of a protein to phase separate by modifying its charge state, conformation, multivalent interaction site properties and/or interactions with other components such as RNA or other proteins[257]. PTMs can either promote or inhibit the protein’s propensity to undergo phase separation.

In the last few years, phosphorylation has been shown to play a significant role in forming stress granules by G3BP1. Indeed, phosphorylation of Serine 149 has been shown to inhibit the protein propensity to phase separate[258]. This site is dephosphorylated during stress, promoting G3BP1 phase separation and stress granule formation[258]. Conversely, ubiquitination of G3BP1 promotes the disassembly of stress

granules and plays a role in cellular stress resolution[259]. However, this disassembly is context-dependent and seems to be dispensable[259,260].

Ubiquitination has also emerged as a crucial regulator of liquid-liquid phase separation[261]. It can either promote[262] or dissolve[263] condensates. Inhibition of proteasome activity with MG-132 or b-AP15 resulted in phase separation of proteasome through the ubiquitin-dependent phase separation of RAD23B[262]. On the other hand, inhibition of the E1 ubiquitin ligase would lead to the absence of condensate under osmotic stress, suggesting that ubiquitin is a key PTM for LLPS and stress response[262]. Conversely, ubiquitination was also found to disrupt the multivalence of UBQLN2, resulting in the melting of its condensates[263].

Many of these modifications are enzyme-dependent, making it challenging to understand how the enzymes, if not part of the condensates already, can profoundly modify the proteins localized in the inner part of the condensates. However, one modification is not driven by enzymes but is a simple chemical reaction: methionine oxidation. Kato et al.[264] demonstrated that the phase separation of ataxin-2 (yeast) with a methionine-rich domain is sensitive to H_2O_2 due to methionine oxidation. However, for many studies investigating methionine oxidation, the effect of H_2O_2 on phase separation of these proteins can be only noticeable at mM range of H_2O_2, often 50-fold higher than the protein concentration[264]. Additionally, these studies rarely consider the cysteine oxidations that usually occur more rapidly. Despite its prevalence, the role of cysteine modification in LLPS formation and dissolution remains unclear and has not been extensively studied.

1.7.4. Biomolecular condensates and neurodegeneration

Aberrant or uncontrolled LLPS of proteins has already been linked to age-related diseases, particularly neurodegeneration[265]. The increasing concentration and interactions between proteins, combined with their intrinsic aging processes, make LLPS an essential process driving protein aggregation[241], often associated with neurodegeneration. Proteins such as α-synuclein, FUS, tau, and TDP-43 (TAR DNA-binding protein 43), all primarily linked to different neurodegenerative diseases, were also found to phase-separate[265]. The phase separation of these proteins occurred under normal physiological conditions except for tau, which only showed *in-vivo* condensates upon over-expression[265]. Therefore, tight regulation of these condensates is necessary to avoid protein aggregation and cellular damage.

During organismal aging, altered mechanisms such as protein expression and degradation[266], RNA availability[265,267], and mutations[267] affect phase separation behavior in the cell. For example, different mutations (found in amyotrophic lateral sclerosis patients) in the low complexity domain of the protein T cell-restricted intracellular antigen-1 (TIA1) have been shown to affect its phase separation behavior. Mutations such as P362L, A381T and E384K were all found to increase the half-recovery time of the *in-vitro* reconstituted droplets while decreasing their mobile fraction[267]. *In vivo*, these mutations impaired the dissolution of stress granules after heat shock stress[267]. This impairment leads to the formation of an aggregation-prone environment where other proteins, such as TDP-43 gradually transition to insoluble aggregates[267] (Figure 1.23).

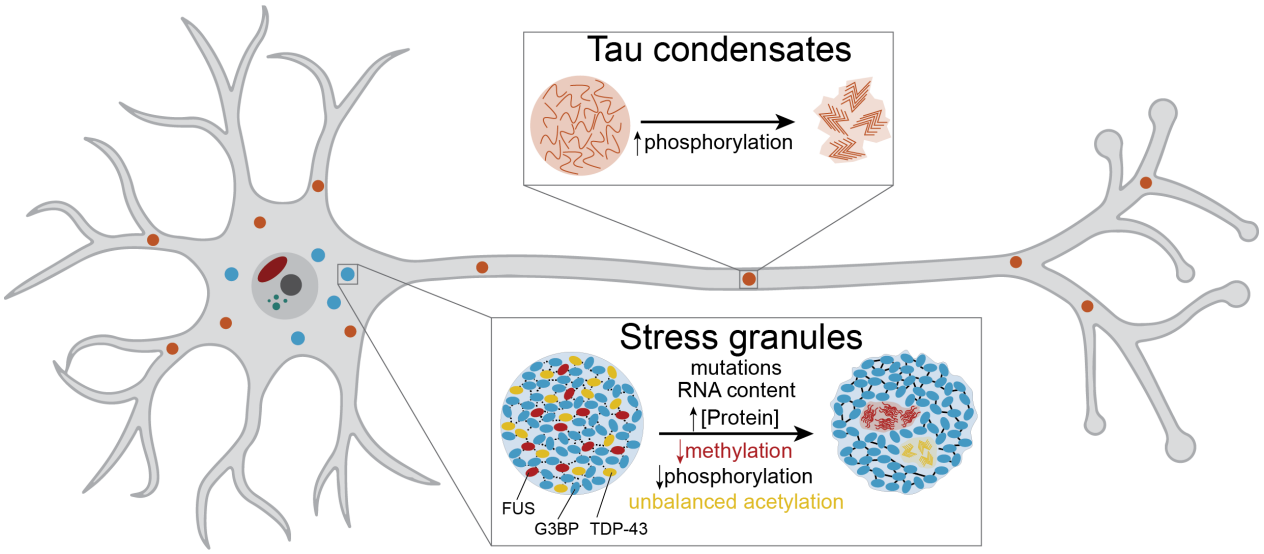


Figure 1.23. Aberrant phase separation of tau, FUS and TDP-43 leads to aggregation and neurodegeneration. Tau has been recently shown to phase separate, and its phase separation is controlled by its phosphorylation[268]. Increased tau phosphorylation leads to aberrant phase separation and phase transition to aggregates[268]. Other proteins, such as FUS[269] and TDP-43[270], are also phase separating. Mutations, unbalanced PTMs, RNA content or concentration can trigger the phase transition of these proteins into gel-like and aggregated forms. Loss of methylation in FUS, inhibits its phase separation[269] while methylated-FUS was observed in frontotemporal dementia associated with (FTD)-FUS aggregation[271]. Furthermore, TDP-43 acetylation has been shown to alter its affinity for RNA binding[265]. Unbalanced TDP-43 acetylation has been proposed to affect its phase separation, leading to phase transition and aggregation[265]. For TDP-43[270] and FUS[272], phosphorylation has been shown to disrupt their condensates. Thus, decreased phosphorylation of these proteins might also lead to uncontrolled phase separation.

LLPS of proteins such as Tau[268], FUS[269] and TDP-43[270] were all shown to be affected by different PTMs[265] (Figure 1.23). Notably, Tau phosphorylation has been shown to promote its phase separation and the phase transition of its condensates, leading to fibrillation of the protein[268].

2. Project aims

The recent proposal that H_2S-controlled protein persulfidation could be an evolutionarily conserved protection mechanism, has raised important questions. Although the cysteine content is relatively low (~2.2%) in total proteome[273], their high reactivity and potential for various posttranslational modifications make them highly attractive to regulate protein function. In recent years, the development of labelling methods allowed a better understanding of H_2S-mediated persulfidation. However, only a few concrete examples of persulfidation biological effects on specific proteins have been studied, and even less in the context of aging. Moreover, the data describing redox homeostasis of specific cysteine PTMs, and their crosstalk have been scarce. This study aimed at understanding better the role of H_2S-controlled persulfidation in aging and age-related disease. The different goals of this thesis were:

1. Identifying and quantifying RSOH and RSSH by mass spectrometry in the aging brain

RSSH and RSOH levels MS measurement in the aging brain of mice were performed using the newly developed dimedone-switch method and an adaptation of the previously published BTD method, respectively. 10 weeks, 10 months and 18 months mice that were either WT or CSE knockout were used to assess the basal changes in RSOH and RSSH in aging and the role of CSE-produced H_2S on brain aging. The bioinformatics analysis developed for these methods revealed a drastic increase in RSOH levels and decrease in persulfidation levels in aging.

2. Understanding the consequence of the RSSH to RSOH to RSO_3H switch in aging and neurodegeneration.

A deeper analysis of the MS data revealed that significant RSSH to RSOH changes occurred on proteins involved in phase separation. The effect of different cysteine PTMs on the phase separation of synapsin 1 and GAPDH was then assessed through different biochemical experiments. Notably, inhibiting H_2S production of primary neurons altered the dissolution of synapsin 1 phase separation, resulting in decreased neuronal transmission. In addition, overoxidation of GAPDH was shown to alter its conformation, leading to a higher propensity for phase separation and phase transition towards aggregation.

3. Studying the role of cysteine PTMs on phase separation, notably G3BP2-mediated stress granules formation, maturation, and dissolution.

To determine the effect of different cysteine PTMs on G3BP2 condensates, a combination of *in-vitro* and *in-cellulo* assays were performed. Mouse embryonic fibroblasts lacking CSE could not recover from arsenite stress. In addition, the mutant C73A of G3BP2 showed a disrupted kinetics of droplet formation suggesting the regulatory role of cysteine. Finally, H_2S treatment dissolves G3BP2 condensates, suggesting that G3BP2-SOH signals to droplet formation while G3BP2-SSH is required for stress granule dissolution.

4. Studying the antioxidant role of persulfidation in Barret's syndrome.

Using mass spectrometry, RSSH levels and total proteome changes were assessed from oesophagus samples from human patients, which showed no trace of inflammation and oesophagus with GERD and non-GERD from the same patient. Data showed a significant remodeling of persulfidation correlated with an essential remodeling of total proteome in patients with GERD. This led to the development of the normalization step of the RSSH changes with the total proteome changes. Using this approach, potential biomarkers such as NQO1 persulfidation were identified. RSSH effect on NQO1 is currently under examination.

3. Protein thiol alterations drive aberrant phase separation in aging brain

Thibaut Vignane[1], Martín Hugo[1], Christian Hoffmann[2], Antonia Katsouda[3,4], Jovan Petric[1], Han Wang[2], Marko Miler[1], Ferran Comas[1], Dunja Petrovic[1], Suyuan Chen[1], Jan Lj. Miljkovic[6], Vladimir M. Jovanovic,[7] Jordan L. Morris,[6] Suvagata Roy Chowdhury,[6] Julien Prudent,[6] Natalija Polovic,[8] Michael P. Murphy[6,9], Andreas Papapetropoulos[3,4], Dragomir Milovanovic[2], Milos R. Filipovic[1*]

[1]Leibniz Institute for Analytical Sciences, ISAS, e.V. Dortmund, Germany

[2]Laboratory of Molecular Neuroscience, German Center for Neurodegenerative Diseases, Berlin, Germany

[3]Clinical, Experimental Surgery and Translational Research Center, Biomedical Research Foundation of the Academy of Athens, Athens, Greece

[4]Laboratory of Pharmacology, Department of Pharmacy, National and Kapodistrian University of Athens, Athens, Greece

[5]Laboratory of Biology-Biochemistry, Faculty of Nursing, School of Health Sciences, National and Kapodistrian University of Athens, Athens, Greece

[6]MRC Mitochondrial Biology Unit, University of Cambridge, Keith Peters Building, CB2 0XY, UK

[7]Bioinformatics Solution Center, Institute for Informatics, Freie Universität Berlin, Berlin, Germany

[8]Department of Biochemistry, Faculty of Chemistry, University of Belgrade, Belgrade, Serbia

[9]Department of Medicine, University of Cambridge, Cambridge, CB2 0QQ, United Kingdom

*Corresponding author. Email: milos.filipovic@isas.de

Submitted to Nature aging on June 14, 2024

Author contributions:

Thibaut Vignane performed all the experiments except the Gallyas staining, FT-IR measurement and live imaging of primary neuron. Thibaut Vignane analyzed

and interpreted the data, prepared the figures. Milos R. Filipovic conceived and supervised the study, designed experiments, and analyzed and interpreted data. Milos R. Filipovic and Thibaut Vignane wrote the manuscript. Drago Milovanovic provided LLPS expertise, designed synapsin experiments, supervised Christian Hoffmann and Han Wang and analyzed and interpreted data. Martin Hugo, Christian Hoffman, Antonia Katsouda, Han Wang, Jovan Petrovic, Ferran Comas, Marko Miller, Dunja Petrovic, Jordan L. Morris, also performed experiments and analyzed the data. Antonia Katsouda, Andreas Papapetropoulos provided aging WT and $CSE^{-/-}$ brain samples, performed lifespan experiments, interpreted, and discussed the data. Natalia Polovic performed FT-IR measurements and analysis. Jordan L. Morris, Jan L. Miljkovic, Suvagata Roy Chowdhury, Julien Prudent and Mike P. Murphy helped with data interpretation. Suyuan Chen synthesized BTD. All authors edited the paper with input from the other authors.

3.1. Abstract

Cellular homeostasis relies on precise regulation through chemical processes, such as protein posttranslational modifications (PTMs) and physical processes, such as biomolecular condensation. Aging disrupts this balance, increasing susceptibility to diseases and death. Using chemoproteomic methods, we investigated cysteine PTMs in mouse brain and observed that age-related increases in thiol (hyper)oxidation promote biomolecular condensate formation, leading to protein aggregation. Conversely, protein persulfidation, controlled by endogenous hydrogen sulfide formation, prevents biomolecular condensation, preserving protein function. Observed alterations in cysteine PTMs influence the phase separation properties of synapsin-1, a key regulator of synaptic release, resulting in disruptions in neurotransmitter release associated with aging and age-related neurodegenerative diseases. Cysteine hyperoxidation of GAPDH, a key glycolytic enzyme, enforces condensation and aggregation, while persulfidation dissolves condensates. Therefore, $CSE^{-/-}$ mice, deficient in the enzyme responsible for endogenous sulfide formation, exhibit a shorter lifespan and spontaneous development of neurofibrillary tangles with age. The ability of protein persulfidation to resolve aberrant LLPS opens up new opportunities for the therapeutic use of sulfide donors in age-related diseases.

3.2. Introduction

Aging could be seen as a progressive decline of fitness caused by the increasing deleteriome, accumulation of “damage” that is both random and deterministic.[1] Versatile redox chemistry of the sulfur amino acid cysteine,[2] makes it one of the main targets for such age-accumulated damage and also an excellent buffer for the first line of defense against it.[3] It has been postulated recently that protein persulfidation (PSSH), an evolutionarily conserved cysteine posttranslational modification (PTM) caused by the gasotransmitter hydrogen sulfide (H_2S), could protect proteins from excessive oxidation and loss of function (Figure 3.1a).[4] Intriguingly, cystathionine gamma lyase (CSE, gene name: *CTH*), a key H_2S producing enzyme involved in regulation of protein persulfidation levels,[4,5] has been identified as a conserved pro-longevity gene in RNA-seq analyses of lifespan-extending interventions in mice.[6,7] This is of particular importance for the aging brain where loss of CSE expression is linked to neurodegenerative diseases.[8–10] However, the dogmatic view that cysteine modifications must affect the enzymatic function of specific targets in order to achieve biological effect has hampered the interest in these PTMs. Recent discoveries that protein function can be controlled simply by its intracellular phase transition to membraneless compartments, the so-called liquid-liquid phase separation (LLPS),[11,12] challenges this view and opens the possibility for a hypothesis that age-induced switch from PSSH towards cysteine oxidation to sulfenic (PSOH) and finally sulfonic acid (PSO_3H) affects the ability of proteins to phase separate and promote their aggregation (Figure 3.1a). This in turn may put more deleterious pressure on the aging cells, causing them to slip into pathophysiology.

3.3. Results

3.3.1. Aging is associated with proteome wide increase of PSOH and decrease of PSSH

General approaches to detect thiol oxidation[13] fail to distinguish between PSOH and PSSH,[14] as both of these modifications are oxidative by nature and intrinsically interconnected, albeit with distinct biological functions.[2,4,15,16] To understand if and how aging affects thiol oxidation we applied selective chemoproteomic approaches for global PSOH and PSSH detection[4,17] in the frontotemporal region of 10-week, 10-month, and 18-month-old mice (Figure 3.1b). Sulfenylated proteins were found in most of the cellular compartments (Figure 3.1c). Given that PSOH is an early step in the thiol oxidation and considered to be a transient modification with multiple fates (Figure 3.1a), it came as a surprise to observe that the abundances of sulfenylated proteins steadily increased throughout the age (Figure 3.1d, Extended data Figure 3.1a-c, Supplementary Table 3.1). Of note, recent study revealed that benzothiazine-based chemoselective probe (BTD) is selective for PSOH, without any side-reactivities,[18] which is why we opted for total protein enrichment and obtained much higher number of sulfenylated proteins than in previous reports,[17,19] where the same method was used for the site-centric peptide enrichment (Figure 3.1e). Proteins found with significantly higher PSOH levels in aging were particularly involved in various metabolic processes, protein folding and turnover, but also in regulation of synaptic transmission, cytoskeleton and mitochondrial organization and cerebral cortex development and aging (Figure 3.1f, Extended data Figure 3.1d).

To discern age-dependent patterns of change, we grouped proteins into clusters using the fuzzy c-means method. About one third of all endogenously

sulfenylated proteins were found to significantly change their PSOH levels at some point as the mouse aged, with about a half of those that significantly changed showing a continuous age-dependent increase (Figure 3.1g). These proteins are involved in critical neuronal pathways (synaptic vesicle cycle, carbon metabolism, proteasome) and the ones controlling neurodegenerative diseases (Amyotrophic lateral sclerosis, Parkinson's, prion and Huntington's disease) are particularly enriched (Figure 3.1g).

To exclude that this effect originates from the variation in protein expression levels, label free quantitative proteomic analysis of the same samples was performed (Supplementary Figure 3.1, Supplementary Table 2). As expected, the aging did affect the brain proteome to a certain extent (Supplementary Figure 3.1a-e), which agrees with previous reports [20], but the differences in protein expression could not be the reason for the observed changes in sulfenylation (Extended data Figure 3.1e-f). Namely, plotting protein changes found in the sulfenylome against the changes of total proteome shows minimal scattering, with only a few PSOH targets following the trend of protein expression (Extended data Figure 3.1e-f). Therefore, the age-induced increase of steady-state levels of PSOH (Figure 3.1d) indicates that brain tissue indeed experiences increasing oxidative stress with aging. This is also reflected in the age-induced changes in protein levels of some key antioxidant enzymes (Extended data Figure 3.2).

In contrast, PSSH decreased with age (Figure 3.1i, Extended data Figure 3.3a-c, Supplementary Table 3). We identified almost 2000 endogenously persulfidated proteins, which is ~1000 proteins more than were reported to be persulfidated to date using different labeling methods (Figure 3.1j).[5,21,22] Although recent studies have shown that dimedone-based probes could have minor side

reaction with very reactive amino groups,[18] in dimedone-switch method for persulfide labeling, they are already blocked with 4-chloro-7-nitrobenzofurazan (NBF-Cl),[4] therefore excluding such possibility. Additionally, precleaning step with neutravidin beads should remove all endogenously biotinylated proteins, leaving only those that are selectively labelled for PSSH (Figure 3.1b).[4]

Similar to sulfenylation, persulfidated proteins were found to be present in most of the cellular compartments (Figure 3.1c) and are involved in various metabolic processes, protein turnover, synaptic signaling, cellular homeostasis etc (Figure 3.1k, Extended data Figure 3.3d). About a half of them showed significant change at least at one point of age (Figure 3.1l), with 4 out of 6 clusters exhibiting age-dependent decline (~80%) and exhibiting enrichment for different metabolic pathways, neurodegeneration, neuronal structure organization and development, etc (Figure 3.1l-m). Total proteome alterations did not significantly affect the observed age-related decline in PSSH (Extended data Figure 3.3e-f).

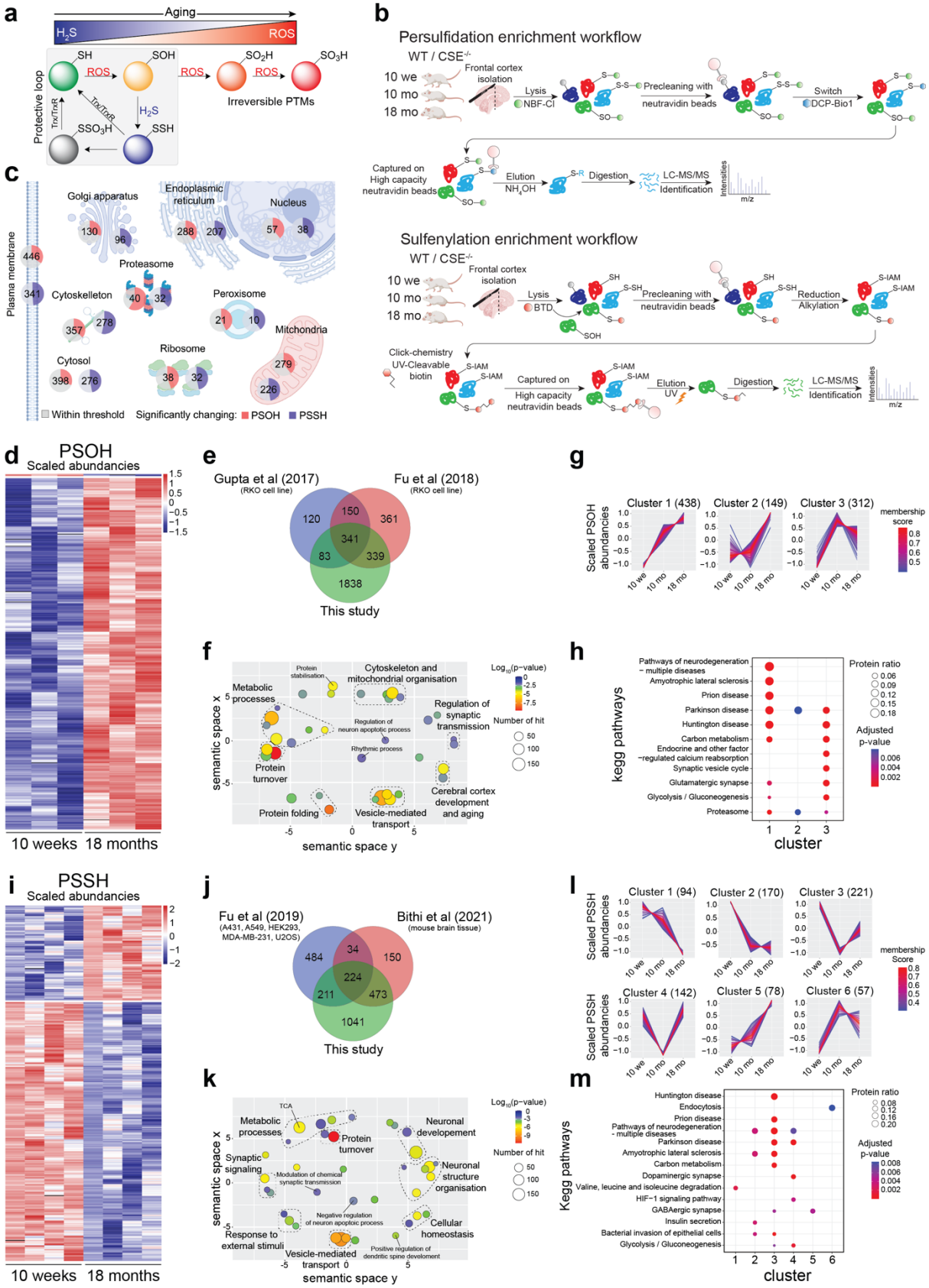
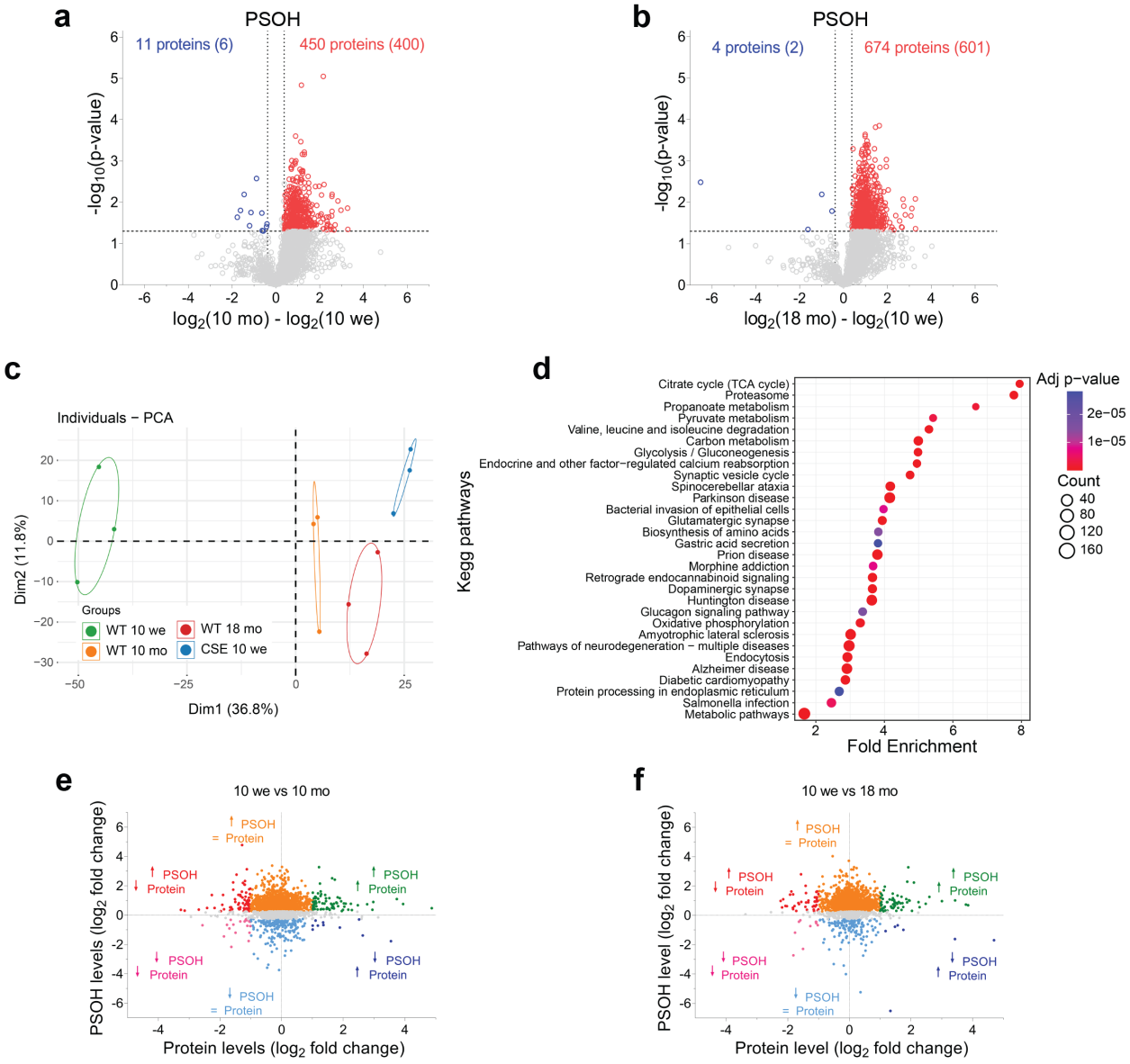
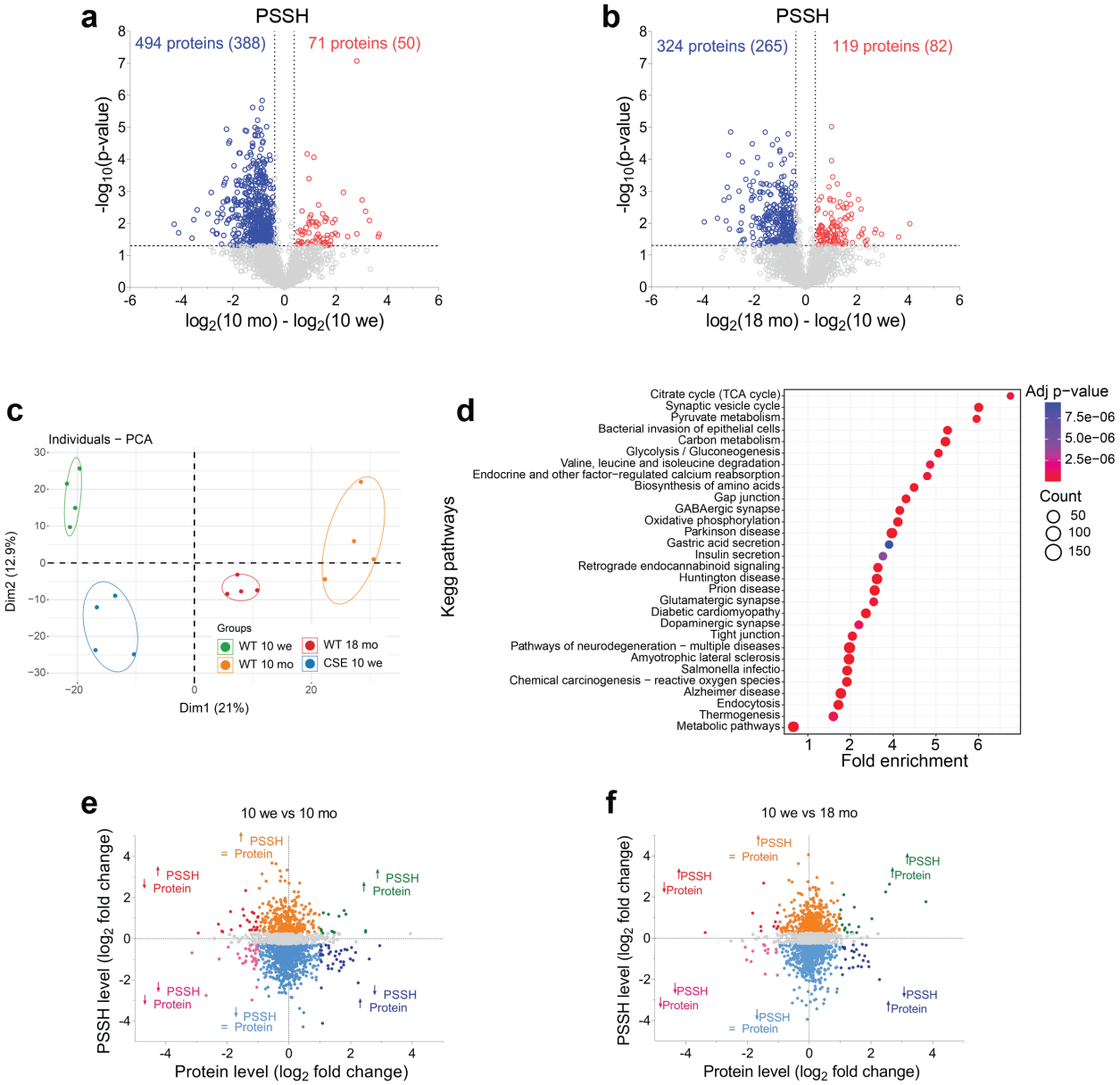


Figure 3.1. Chemoproteomic analysis of protein sulfenylation and persulfidation reveals substantial alteration of cysteine modifications in aging. (**a**) Protective persulfidation loop prevents cysteine hyperoxidation. (**b**) Chemoproteomic workflows of

PSOH and PSSH detection. The PSSH workflow is based on Zivanovic et al, 2019,[4] while the PSOH workflow is adapted from Fu et al, 2018.[17] (**c**) PSOH (in red) and PSSH (in blue) changes in subcellular compartments. Colors indicate changes in 18-month-old mice compared to 10-week-old mice; grey represents the proportion of proteins in which the cysteine modification is not changing. The number of proteins for each subcellular compartment is indicated. (**d**) Heatmap showing the significant changes of PSOH in 18-month-old mice compared to 10-week-old mice (n = 3; Welch's test, $p<0.05$). (**e**) Venn diagram comparing the sulfenylated proteins identified within our study against two other data sets, Fu et al, 2018[17] and Gupta et al, 2017.[19] (**f**) GO term enrichment (biological process) of the 912 proteins showing significant increase of PSOH at least once across the age. Enrichment was done using DAVID and the outcomes visualized through REVIGO. Significant GO terms passed the Benjamini adjusted p-value threshold of 0.01. Circle dimensions correspond to the protein count within specific GO terms and color gradients to the significance. (**g**) Hierarchical cluster analysis of the 912 proteins with PSOH levels significantly changing at least once in all 3 ages based on trend profile. (**h**) KEGG pathway enrichment analysis was applied for each cluster shown in (c). Benjamini adjusted p-value was used to filter for significant enrichment. (**i**) Heatmap showing the significant changes. of PSSH in 18-month-old mice compared to 10-week-old mice (n = 4, Welch's test, $p<0.05$). (**j**) Venn diagram comparing the persulfidated proteins identified within our study against two other data sets, Fu et al, 2019,[21] and Bithi et al, 2021.[5] (**k**) GO term enrichment (biological process) of the 714 proteins showing significant decrease of PSSH in at least once in all 3 ages based on trend profile. (**l**) Hierarchical clustering of the 901 proteins for which persulfidation was found to be changing at least once in all 3 ages, into 6 different groups based on the trend profile. (**m**) Corresponding KEGG pathway analysis for the 6 clusters. Benjamini adjusted p-value was used to filter for significant enrichment.

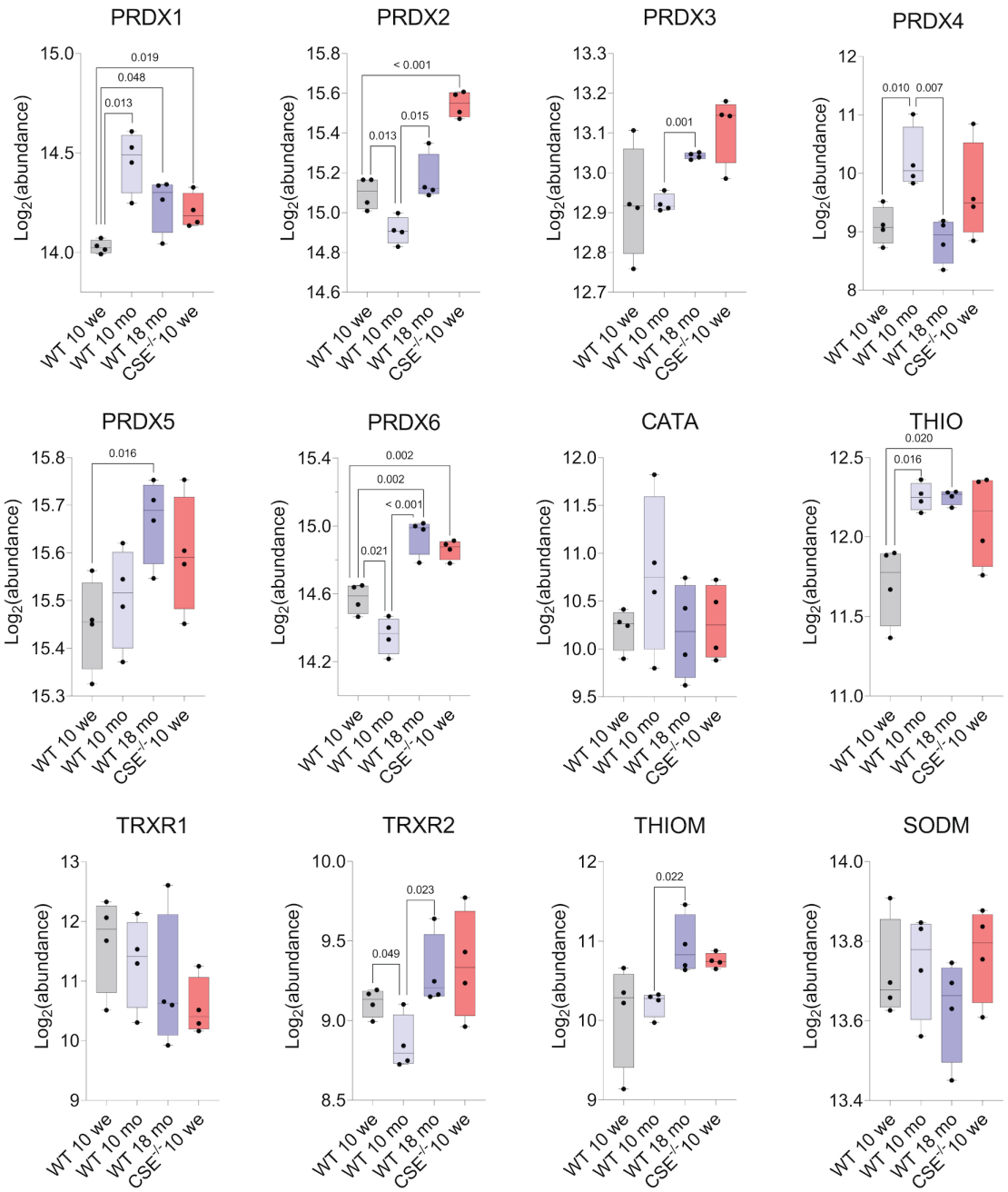


Extended data Figure 3.1. Quantitative sulfenylomics analysis of aging brain. (**a-b**) Volcano plot analysis of PSOH changes in (a) 10-month-old mice or (b) 18-month-old mice relative to 10-week-old mice (n = 3, Welch's t-test). The number of proteins with significantly altered PSOH levels is indicated, with the number in parentheses reflecting proteins identified through a minimum of 2 unique peptides. (**c**) Principal component analysis (PCA) underscoring the reproducibility of sulfenylome measurements across all replicates. (**d**) KEGG pathway enrichment analysis of proteins showing significant PSOH changes with age. The graph shows the top 30 significant (Benjamini adjusted p-value < 0.01) and most enriched pathways, with the color gradient indicating adjusted p-values and circle size the number of proteins. (**e-f**) Scatter plot analysis of sulfenylome and protein expression relationships. log2 fold changes within the sulfenylome (y-axis) were plotted against total proteome changes (x-axis) for the (e) 10-month-old vs. 10-week-old mice and (f) 18-month-old vs. 10-week-old mice.



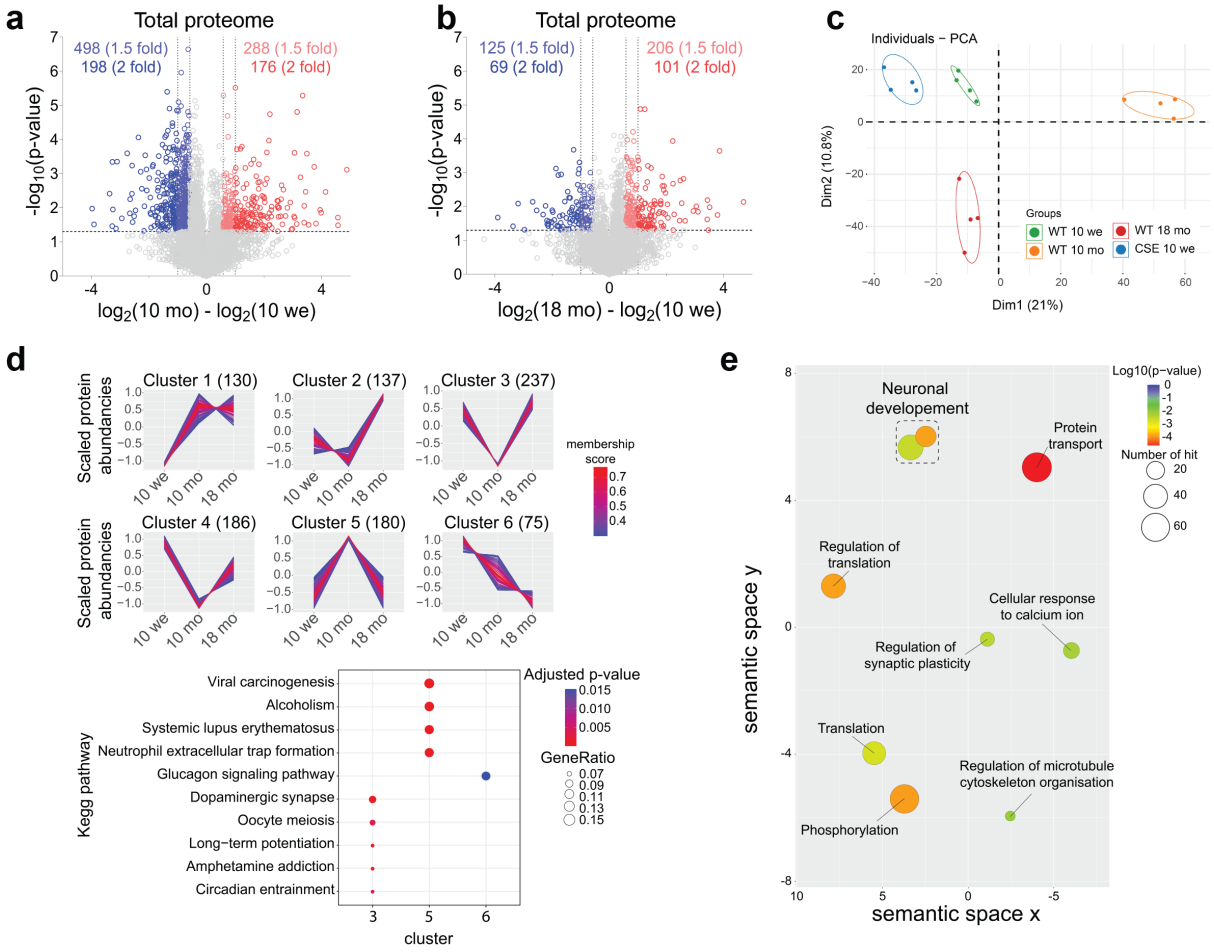
Extended data Figure 3.2. Quantitative persulfidomics analysis of aging brain. (**a-b**) Volcano plot analysis of persulfidome changes in (**a**) 10-month-old mice or (**b**) 18-month-old mice relative to 10-week-old mice (n = 4, Welch's t-test). The number of proteins with significantly altered PSSH levels is indicated, with the number in parentheses reflecting proteins identified through a minimum of 2 unique peptides. (**c**) Principal component analysis (PCA) underscoring the reproducibility of persulfidome measurements across all replicates. (**d**) KEGG pathway enrichment analysis of proteins showing significant PSSH changes with age. The graph shows the top 30 significant (Benjamini adjusted p-value < 0.01) and most enriched pathways, with the color gradient indicating adjusted p-values and circle size the number of proteins. (**e-f**) Scatter plot analysis of PSSH and protein expression relationships.

log2 fold changes within the persulfidome (y-axis) were plotted against total proteome changes (x-axis) for the (e) 10-month-old vs. 10-week-old mice and (f) 18-month-old vs. 10-week-old mice.



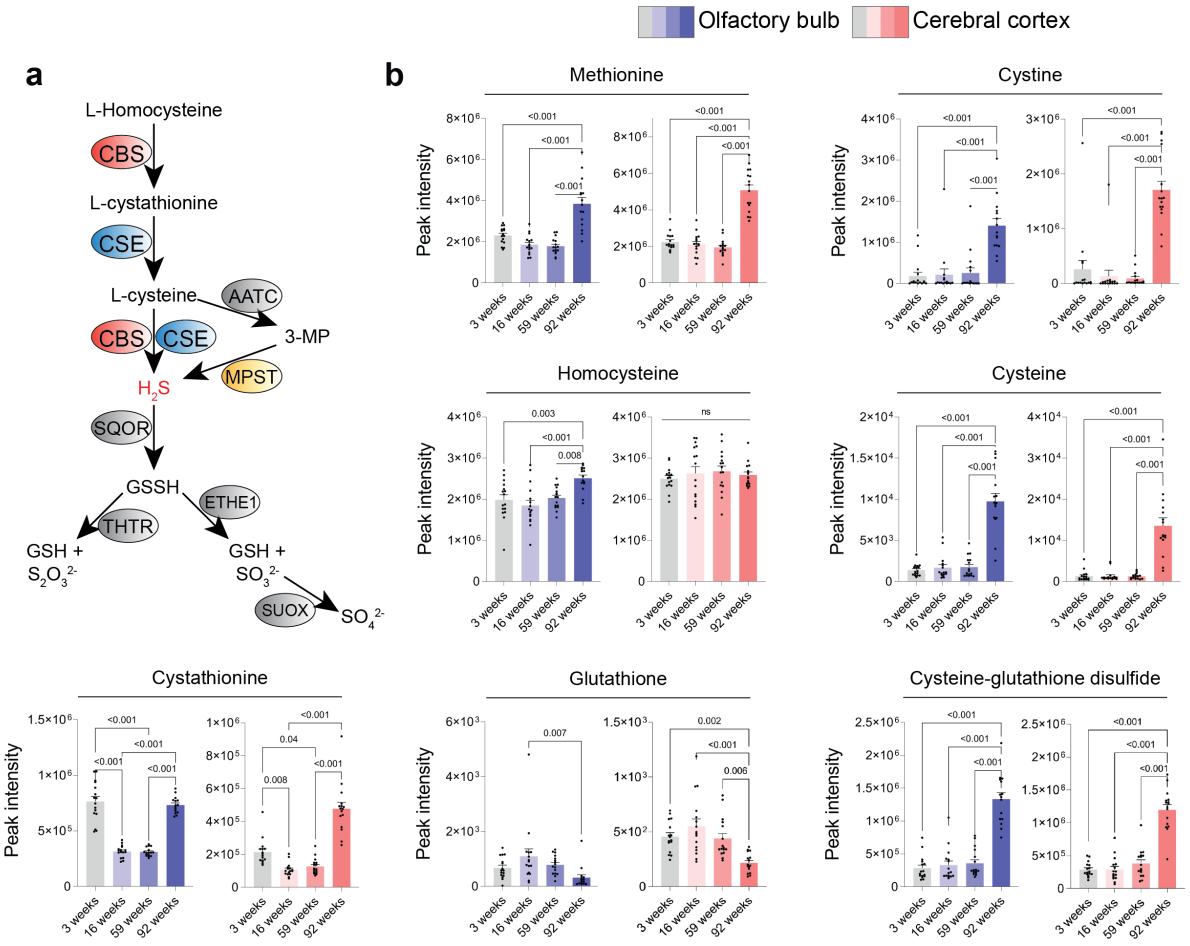
Extended data Figure 3.3. Expression profiles of antioxidant proteins across aging and in CSE$^{-/-}$ mice. Whiskers and box plots of the log2 transformed abundances of antioxidant proteins identified in the proteome analysis. Reported significance levels accompanying the plots are directly correlated with the p-values calculated through the proteome analysis (n =

4). PRDX (1-6): peroxiredoxin (1-6); CATA: Catalase; THIO: thioredoxin, THIOM: mitochondrial thioredoxin; TRXR (1-2): thioredoxin reductase (1-2); SODM: mitochondrial superoxide dismutase.



Supplementary Figure 3.1. Total proteome changes in aging mice. (**a-b**) Volcano plot analysis of total proteome changes in (a) 10-month-old mice vs. 10-week-old mice and (b) 18-month-old mice vs. 10-week-old mice (Welch's t-test, n = 4). (**c**) Principal component analysis underscoring the reproducibility of total proteome measurements across all replicates. (**d**) Hierarchical cluster analysis of proteins displaying significant changes at least at one time point during aging and KEGG pathway enrichment analysis of protein clusters. Only clusters 3, 5, and 6 display significant enrichment in KEGG pathway terms (Benjamini corrected p-value < 0.05). (**e**) GO term (biological process) enrichment analysis of the proteins displaying age-related changes. REVIGO was used to plot the enrichment analysis performed in DAVID. Significant GO terms passed the Benjamini adjusted p-value threshold

of 0.01. Circle dimensions denote the protein count within specific GO terms, while color gradients represent the degree of significance.



Supplementary Figure 3.2. Changes in CSE substrate levels in olfactory bulb and cerebral cortex, based on aging mouse metabolome atlas. (**a**) Transsulfuration pathway. (**b**) Age-induced changes in methionine, cystine, homocysteine, cysteine, glutathione, cystathionine, and cysteine-glutathione disulfide, based on Ding et al, 2021 metabolome atlas of the aging mouse brain.

3.3.2. CSE is a main regulator of the PSOH to PSSH switch in the aging brain

Recent studies have suggested the key role of CSE-produced hydrogen sulfide and subsequent persulfidation in lifespan interventions such as dietary restriction[4,5,23] and CSE has been identified as a pro-longevity gene in studies using lifespan-extending interventions in mice.[6,7] In brain, its decline is associated with Alzheimer's disease and spinocerebellar ataxia[3,8,10] and mice lacking it exhibit a Huntington disease-like phenotype.[9] Indeed, an additional analysis of mouse aging brain metabolome[24] and transcriptome25 datasets confirms that Cth gene expression decreases in cerebral cortex of aged mice resulting in accumulation of its substrates, such as homocysteine and cysteine (Supplementary Figure 3.2 and Supplementary Figure 3.3a). Furthermore, a significant age-related decline of CTH mRNA expression (both isoforms 1 and 2) could also be observed in human frontal cortex of both sexes[26] (Supplementary Figure 3.3b,c). No change could be observed in other two H_2S producing enzyme (mercaptopyruvate sulfur transferase, Mpst, and cystathionine beta synthase, Cbs) in aging mice (Supplementary Figure 3.3a) while significant increase with age is noticeable in humans (Supplementary Figure 3.3d).

To test the importance of CSE-produced H_2S-induced protein persulfidation in protection against thiol oxidation on a global proteome level, we compared PSOH and PSSH levels in wild type vs CSE knockout mice (Supplementary Table 4). Indeed, much higher PSOH levels were observed in 10-week-old $CSE^{-/-}$ mice compared to wild type animals of the same age (Figure 3.2a, Extended data Figure 3.4a,b). Moreover, ~200 proteins showed higher PSOH levels in 10-week-old $CSE^{-/-}$ brains than in 18-month-old wild type brain samples, implying that the absence of CSE results in increased steady-state levels of oxidative damage (Supporting Table 4), despite the higher levels of antioxidant enzymes (Extended data Figure 3.2).

Substantial overlap of targets found to have higher PSOH levels in $CSE^{-/-}$ mice with the targets found to have higher PSOH levels in aging could be observed (Figure 3.2b), with pathways essential for healthy neuronal function being particularly enriched (Figure 3.2c, Extended data Figure 3.4c).

Consistent with this protective hypothesis (Figure 3.1a), PSSH levels were predominantly reduced in $CSE^{-/-}$ mice (Figure 3.2d, Extended data Figure 3.4d,e). ~70% of proteins that showed decrease in PSSH in $CSE^{-/-}$ mice, exhibit the same behavior in aging mice (Figure 3.2e). Furthermore, pathway enrichment analyses show patterns similar to the ones observed in aging (Figure 3.2f, Extended data Figure 3.4d,e).

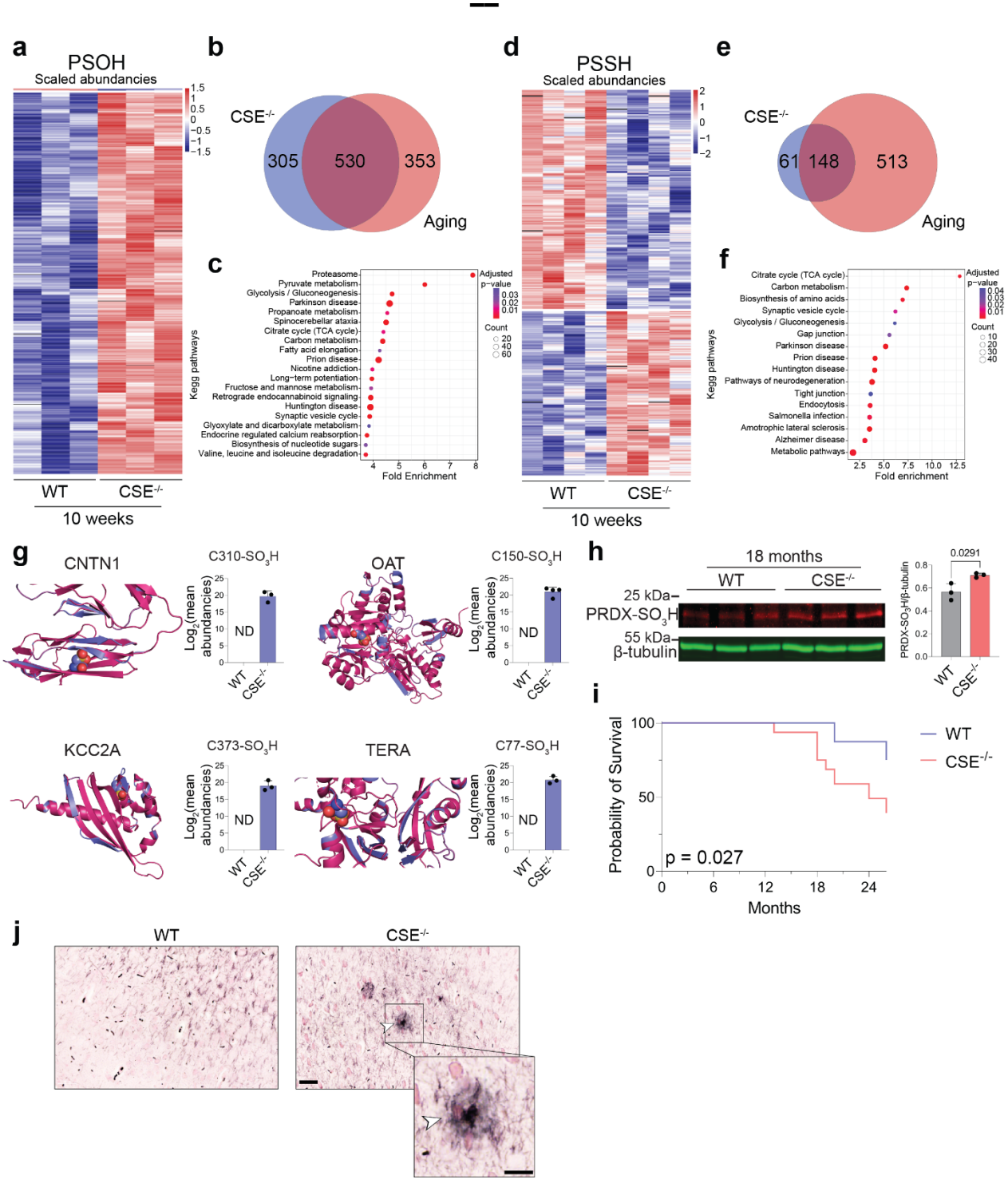
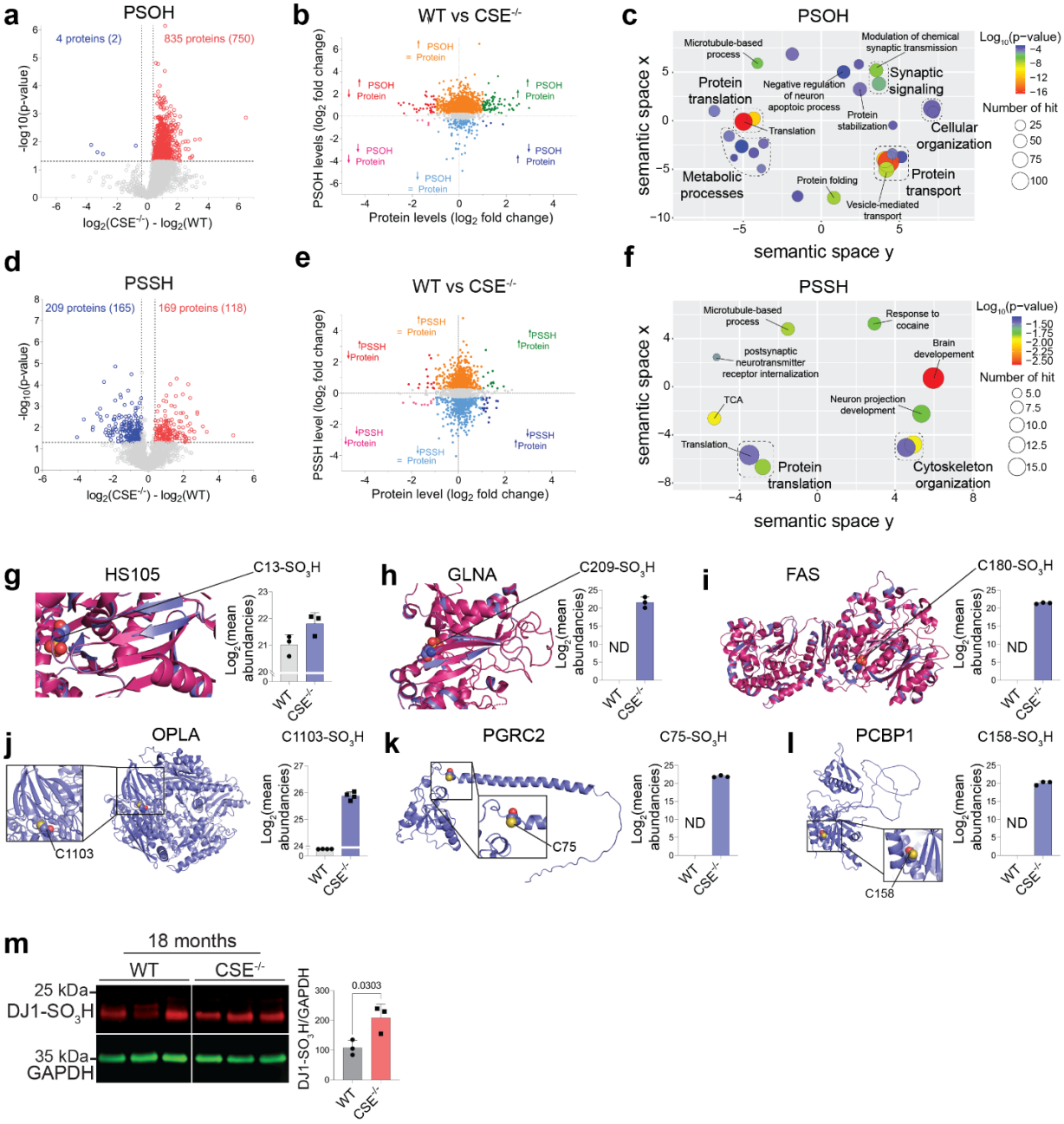


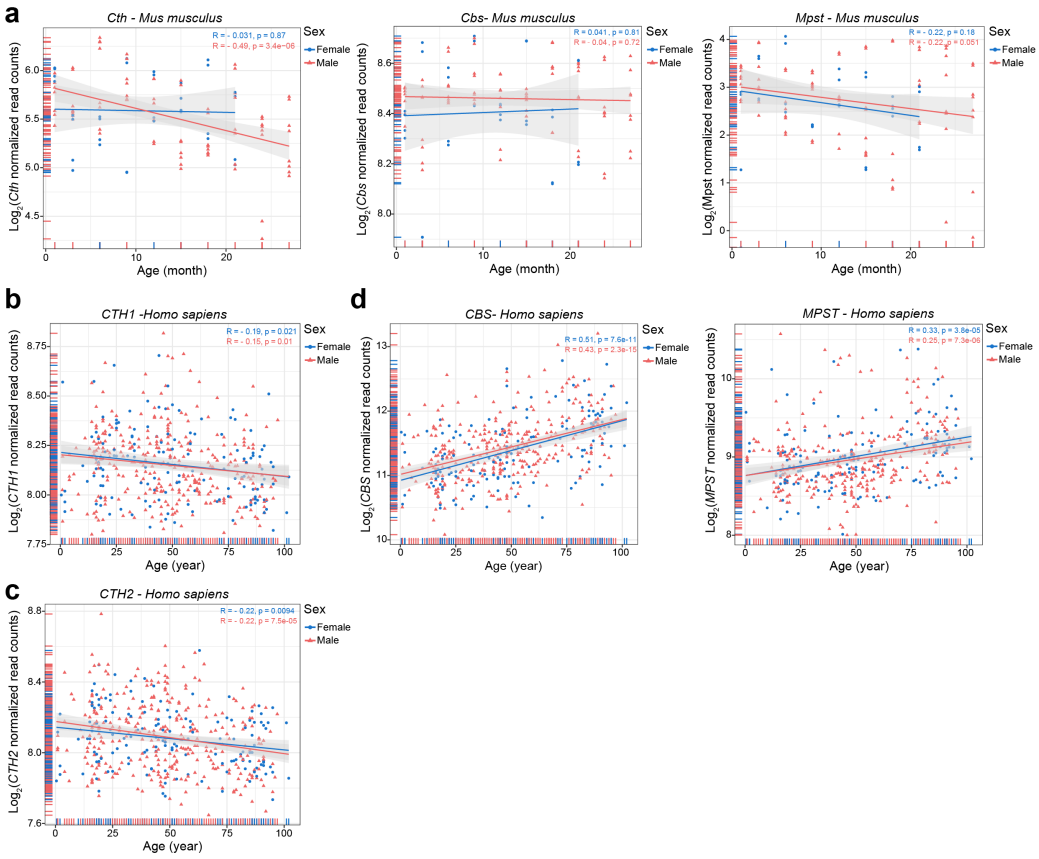
Figure 3.2. CSE$^{-/-}$ mice exhibit higher PSOH and PSO$_3$H levels but lower PSSH, shorter lifespan and spontaneous formation of neurofibrillary tangles. (**a**) Heatmaps of the significant PSOH changes found in the CSE$^{-/-}$ 10-week-old mice compared to the wild type (WT) 10-week-old mice (n = 3; Welch's test, p<0.05). (**b**) Venn diagram comparison of sulfenylated targets found to be significantly affected by age and CSE knockout. (**c**) KEGG pathway enrichment analysis of proteins showing significant PSOH changes in CSE$^{-/-}$. (Benjamini adjusted p-value < 0.05; color gradient indicates adjusted p-values and circle size

the number of proteins). (**d**) Heatmaps of the significant PSSH changes found in the $CSE^{-/-}$ 10-week-old mice compared to the wild type (WT) 10-week-old mice (n = 4; Welch's test, $p<0.05$). (e) Venn diagram comparison of persulfidated targets found to be significantly affected by age and CSE knockout. (**f**) KEGG pathway enrichment analysis of proteins showing significant PSSH changes in $CSE^{-/-}$. (Benjamini adjusted p-value < 0.05; color gradient indicates adjusted p-values and circle size the number of proteins). (**g**) Prediction of the structural changes caused by cysteine sulfonylation found exclusively in $CSE^{-/-}$ mice. Modeling was performed using VIENNA-PTM. The original crystal structure is depicted in pink, and the predicted model in blue. Contactin-1 (CNTN1; 3S97.pdb[27]); Ornithine aminotransferase (OAT; 2OAT.pdb[28]); Calcium/calmodulin-dependent protein kinase type II subunit alpha (KCC2A; 1HKX.pdb[29]); Transitional endoplasmic reticulum ATPase (TERA; 1R7R.pdb[30]). (**h**) PRDX sulfonylation levels in 18-month-old WT and $CSE^{-/-}$ mice. The intensities were normalized to the β-tubulin expression levels. Values represent mean ± SD (Student's t-test n = 3). (**i**) Survival rates of $CSE^{-/-}$ vs. WT mice. n = 16 per group. Kaplan-Meier survival analysis, Mantel-Cox log-rank test. (**j**) Gallyas silver staining of WT and $CSE^{-/-}$ 18-month-old mouse brain sections for the neurofibrillary tangles identified by white arrows. Global stained sections are shown in Supplementary Figure 3.4. n = 4. Scale bar = 40 μm; zoomed image 20 μm.

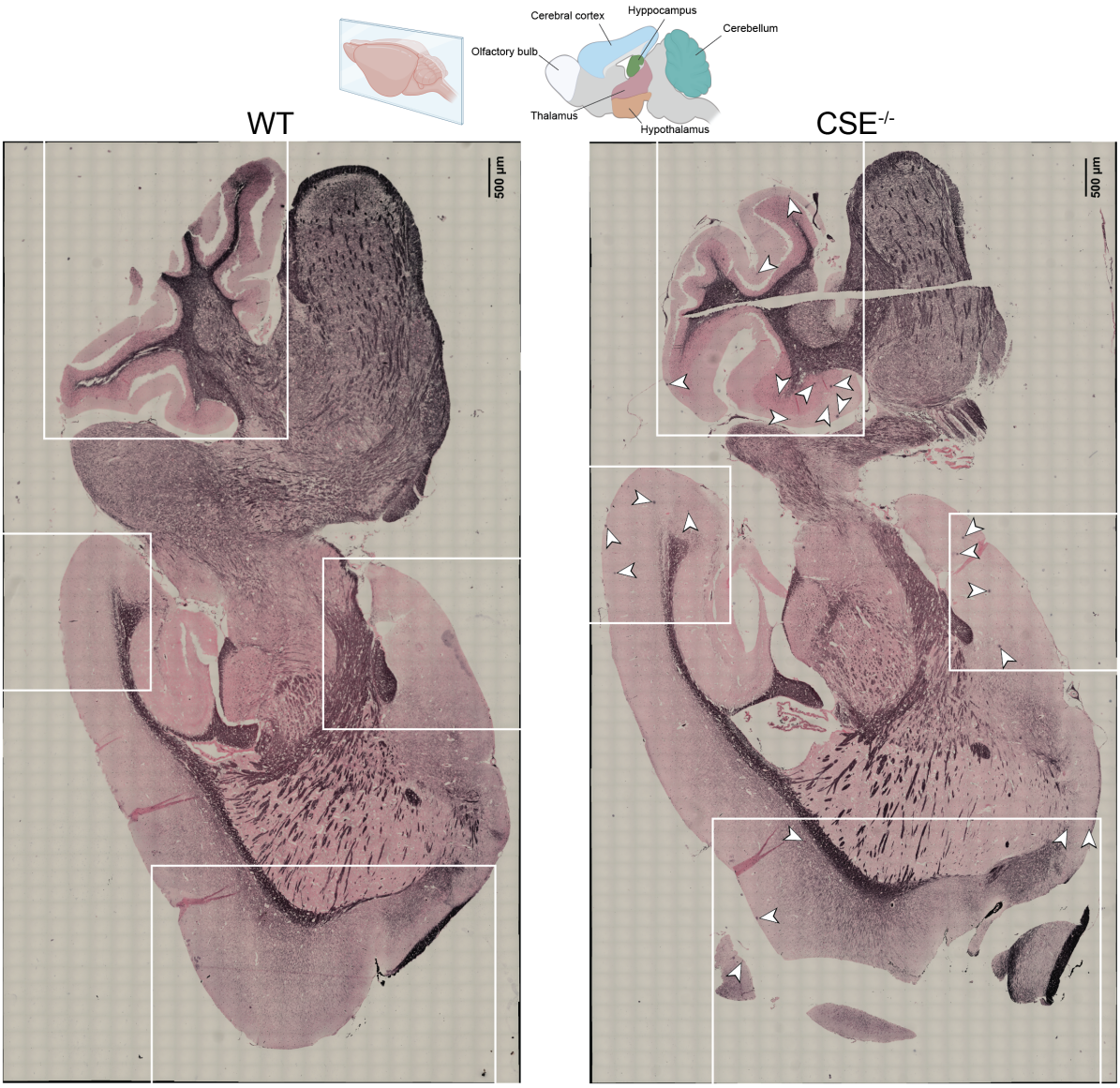


Extended data Figure 3.4. The effect of CSE on persulfidation, sulfenylation and sulfonylation of proteins. (**a**) Volcano plot analysis of PSOH changes in 10-month-old CSE$^{-/-}$ mice vs. 10-month-old wild type mice. (**b**) Scatter plot analysis of PSOH and protein expression relationships. log2 fold changes within the persulfidome (y-axis) were plotted against total proteome changes (x-axis) for the 10-month-old CSE$^{-/-}$ and wild type mice. (**c**) GO (Biological process) term enrichment analysis of proteins showing PSOH increase in CSE$^{-/-}$ mice. Enrichment was performed using DAVID and the results visualized through REVIGO. Benjamini adjusted p-value < 0.05. (**d**) Volcano plot analysis of PSSH changes in 10-month-old CSE$^{-/-}$ mice vs. 10-month-old wild type mice. (**e**) Scatter plot characterizing log2 fold changes within the persulfidome (y-axis) and protein expression (x-axis) for

comparison between 10-month-old $CSE^{-/-}$ and wild type mice. (**f**) GO (Biological process) term enrichment analysis of proteins showing PSSH decrease in $CSE^{-/-}$ mice (Benjamini adjusted p-value < 0.05). (**g-l**) Prediction of the structural changes caused by cysteine sulfonylation that is observed in $CSE^{-/-}$ mice. Modeling was performed using VIENNA-PTM. (**g**) Heat shock protein 105 kDa (HS105) is based on the 6GFA.pdb model[31]. (**h**) Glutamine synthetase (GLNA) is based on the 2OJW.pdb model[32]. (**i**) Fatty acid synthase (FAS) is based on 5MY2.pdb model[33]. (**j**) 5-oxoprolinase (OPLA) is based on the AF-O14841-F1-model_v4.pdb model[34,35]. (**k**) Membrane-associated progesterone receptor component 2 (PGRC2) based on AF-Q80UU9-F1- model_v4.pdb model[34,35]. (**l**) Poly(rC)-binding protein 1 (PCBP1) is based on the AF-Q15365-F1- model_v4.pdb model[34,35]. (**m**) DJ1 (PARK7) sulfonylation levels in 18-months-old WT and $CSE^{-/-}$ mice. The intensities were normalized to the GAPDH expression levels. Values represent mean ± SD (Student's t-test, n = 3).



Supplementary Figure 3.3. Changes in mRNA levels of H_2S producing enzymes in mouse and human brain during aging. (**a**) Plot of cth, cbs and mpst changes in aging brain of male and female mice (based on dataset GSE132040; 56 animals,40 males, 16 females). (**b-c**) Age-induced changes in expression levels of two cth isoforms (b) cth-1 and (c) cth-2 in human frontal cortex. (**d**) Age-induced changes in expression levels of cbs and mpst in human frontal cortex (based on dataset GSE36192, 455 subjects, 310 males, 145 females.



Supplementary Figure 3.4. Old CSE$^{-/-}$ mice exhibit multiple Gallyas silver–stained neuritic-like plaques. Representative microscopy images of Gallyas staining of the sagittal brain section in 18-month-old WT and CSE$^{-/-}$ mice. Fibrillary tangles (white arrows) were present in different regions of the CSE$^{-/-}$ mice such as the hypothalamus, the cerebral cortex, and the cerebellum (indicated by the white boxes). WT mice did not show any detectable lesion (n = 4 animals, scale bar = 500 µM).

2.3.1. Age-induced PSSH to PSO_3H switch is more profound in $CSE^{-/-}$ mice

Following the protective hypothesis (Figure 3.1a), both aging and CSE knockout should also result in increased thiol hyperoxidation, i.e. sulfonylation. Although there are no established methods to selectively label and enrich PSO_3H, we analyzed the proteome data obtained by lysing the tissues with NBF-Cl, which would block all thiols including sulfenic acids (Figure 3.1b) and therefore prevent unwanted cysteine hyperoxidation during sample preparation. Out of 645 detected sulfonylated peptides, 382 were absent in all wild type 10-week-old mice, suggesting that both aging and absence of CSE are characterized with increase of PSO_3H (Supplementary Table 5). We therefore used Vienna PTM 2.0, a resource for exploring PTMs based on molecular dynamics simulations,[36] to predict the effect that PSO_3H could have on the structures of several targets.

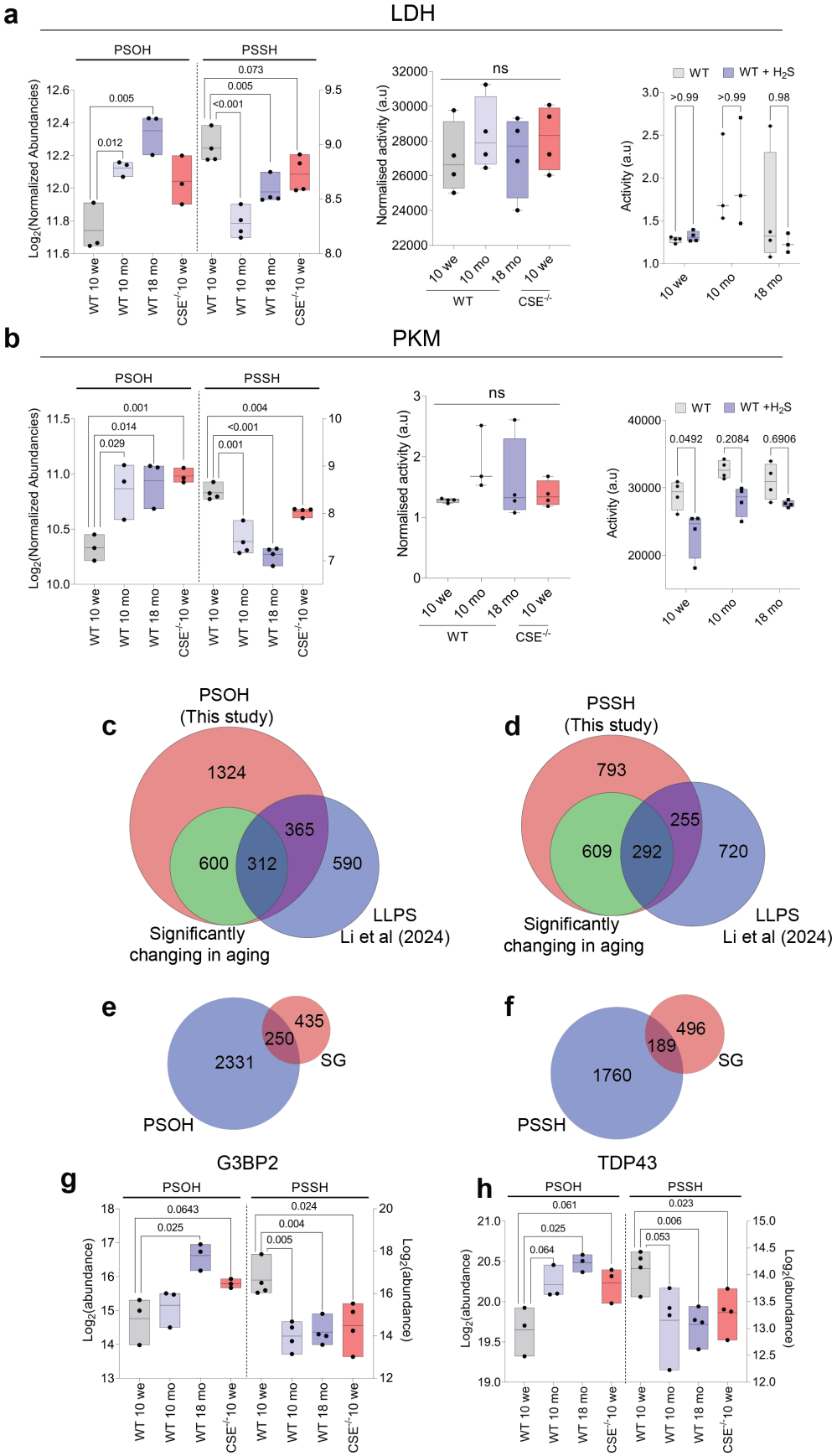
Overlapping the original crystal structures with the ones modeled for PSO_3H at sites found to be exclusively sulfonylated in $CSE^{-/-}$ mice, we could observe presence of conformational changes (Figure 3.2g, Extended data Figure 3.4g-l). The sulfonylated cysteines are predominantly located in the beta-sheet domains or in loops preceding beta-strands. Immunoblotting for the well-defined sulfonylated proteins, PRDX (Figure 3.2h) and DJ-1 (Extended data Figure 3.4m), also confirmed the importance of endogenously produced H_2S in controlling PSO_3H levels.

These observations suggest that aging, coupled with the additional reduction of H_2S formation, contributes to significant thiol remodeling that might have global impact on the survival of these mice. Having observed significant death rate even before $CSE^{-/-}$ mice reached 18 months, we next compared the lifespans of those animals and found that $CSE^{-/-}$ lifespan is shorter than wild type control (Figure 3.2i).

Furthermore, we also compared the brain sections of 18-month-old mice from $CSE^{-/-}$ and wild type. As mice do not spontaneously develop neurodegenerative diseases, complete absence of Gallyas silver staining for neurofibrillary tangles was observed in wild type mice, while $CSE^{-/-}$ mice exhibited numerous lesions throughout the whole brain section not only limited to the frontotemporal region, but including cerebellum and hippocampus (Figure 3.2j, Supplementary Figure 3.4).

2.3.2. Age-induced cysteine PTMs contribute to the LLPS of synapsin 1

To understand the reasons behind these observations, a deeper look at the obtained proteomic data suggested that two types of proteins, enzymes (like the ones observed in different metabolic pathways), and structural and signaling proteins (like the ones that play role in neuronal structure/synapse organization, vesicle mediated transport or regulation of neurotransmission) are particularly subjected to age-induced thiol remodeling. The traditional views on PTM-controlled signaling imply that the modification of protein should result in the gain or loss of function. We selected LDH and PKM, whose PSOH and PSSH levels showed clear age-dependent changes, and tested how those changes correlate with their actual enzymatic functions in the brain lysates. To our surprise, we could not observe significant changes in enzyme function in any of the tested ages nor in $CSE^{-/-}$ even after the addition of external H_2S (Extended data Figure 3.5a,b). However, we did observe that substantial portion of proteins found to undergo biomolecular condensation, i.e. LLPS[37], overlaps with proteins whose thiol redox status changes with aging (Extended data Figure 3.5c-h).



Extended data Figure 3.5. Age-induced thiol remodeling predominantly affects proteins known to undergo LLPS. (**a-b**) Age-induced sulfenylation and persulfidation

changes of metabolic enzymes show no impact on their activity. (a) Lactate dehydrogenase (LDH) and (b) pyruvate kinase (PKM), both key metabolic enzymes, show significant changes in sulfenylation and persulfidation in aging and in $CSE^{-/-}$ mice (left, Welch's t-test) but no significant change could be observed in their activity (middle, 1-way Anova, n.s. non-significant) even after addition of 10 μM H_2S to a freshly prepared brain lysate (right, paired two-way Anova). (**c-d**) Venn diagram representing the overlap of (c) sulfenylated or (d) persulfidated proteins identified in our study (all proteins are red circle, significantly changing with aging are green) with proteins found to undergo biomolecular condensation in Li et al, 2024[37]. (**e-f**) Venn diagram representing the overlap of proteins present in stress granules (SG) and those identified to significantly change their (e) PSOH and (f) PSSH levels with aging. (**g**) Boxplot of the age-induced PSOH and PSSH changes of G3BP2. (**h**) Boxplot of the age-induced PSOH and PSSH changes of TDP43. Log2 abundances of G3BP2 and TDP43 PTMs in aging WT and $CSE^{-/-}$ mouse brain are normalized to total protein levels (n = 4, Welch's t-test; p-value reported from proteomic analysis).

We therefore turned our attention at testing the hypothesis that the age-induced thiol oxidation remodeling of proteins could be affecting their mesoscale organization in neurons. Interestingly, we noticed that synapsin 1, the most abundant phosphoprotein in nerve terminals known to phase separate,[38] showed age-dependent increase in PSOH and decrease in PSSH (Figure 3.3a). These changes were already as profound in 10-week-old $CSE^{-/-}$ mice as they were in 18-month-old wild type animals (Figure 3.3a). Similar age-induced effects could be seen for other synapsin isoforms (Extended data Figure 3.6a,b).

Synapsin 1 has two cysteines (Figure 3.3b) and we observed that C360 could be found in all three forms, PSOH, PSSH and PSO_3H, the latter being found only in aged $CSE^{-/-}$ mice (Figure 3.3c, Extended data Figure 3.6c). C360 is a part of the highly structured, ATP-binding domain of synapsin 1 responsible for its multimerization. Posttranslational modification of a cysteine in that region is not expected to affect phase separation, which has been shown to depend primarily on

the intrinsically disordered regions of synapsin 1.[38] Keeping in mind the fact that PSOH and PSSH are intrinsically unstable,[39,40] we designed the protocol to prepare all these different forms of synapsin 1 (Extended data Figure 3.6d), and compared their ability to phase separate. Indeed, when incubated with crowding agent (3 % PEG 3,000), regardless of cysteine redox form, synapsin 1 readily formed condensates (Figure 3.3d). However, synapsin 1 PSO_3H formed much bigger droplets than fully reduced protein, while droplets formed by synapsin 1 PSSH were significantly smaller (Figure 3.3d,e, Extended data Figure 3.6e). We found that these condensates harbored dynamic behavior and recovered promptly after photobleaching, but they exhibited different kinetics of recovery (Figure 3.3f, Extended data Figure 3.6f,g). The percentage and the rate of recovery increased in synapsin 1 PSO_3H (11.6 s *vs.* 13.0 s; 25 % increase in recovery) while both parameters decreased in synapsin 1 PSSH (29.9 s *vs.* 13.0 s; 30 % decrease in recovery) (Figure 3.3e). From the $t_{1/2}$, we estimated the apparent diffusion coefficient (*D*app) of the protein molecules to be 8.6, 7.7 and 3.3 x 10^{-4} μm^2 s^{-1} for the PSH, PSO_3H and PSSH, respectively.

The size and FRAP recovery kinetics of droplets formed from synapsin 1 treated with just H_2O_2 (to form PSOH/disulfide mix) or H_2S (expected not to react at all) was undistinguishable from those formed by fully reduced synapsin 1 (Figure 3.3d, Extended data Figure 3.6f,g). No effect of H_2O_2 treatment alone also excludes the possibility that methionine oxidation could be playing a role, as it was recently suggested that this modification could play a role in LLPS of ataxin.[41] These data clearly indicated that cysteine redox status of synapsin 1 controls its phase separation propensity with sulfonylation enforcing stronger phase separation. Indeed, phase diagram of synapsin 1 LLPS proves that when sulfonylated protein can phase

separate at lower concentrations of crowding agent and protein (Figure 3.3g, Extended data Figure 3.6h,i).

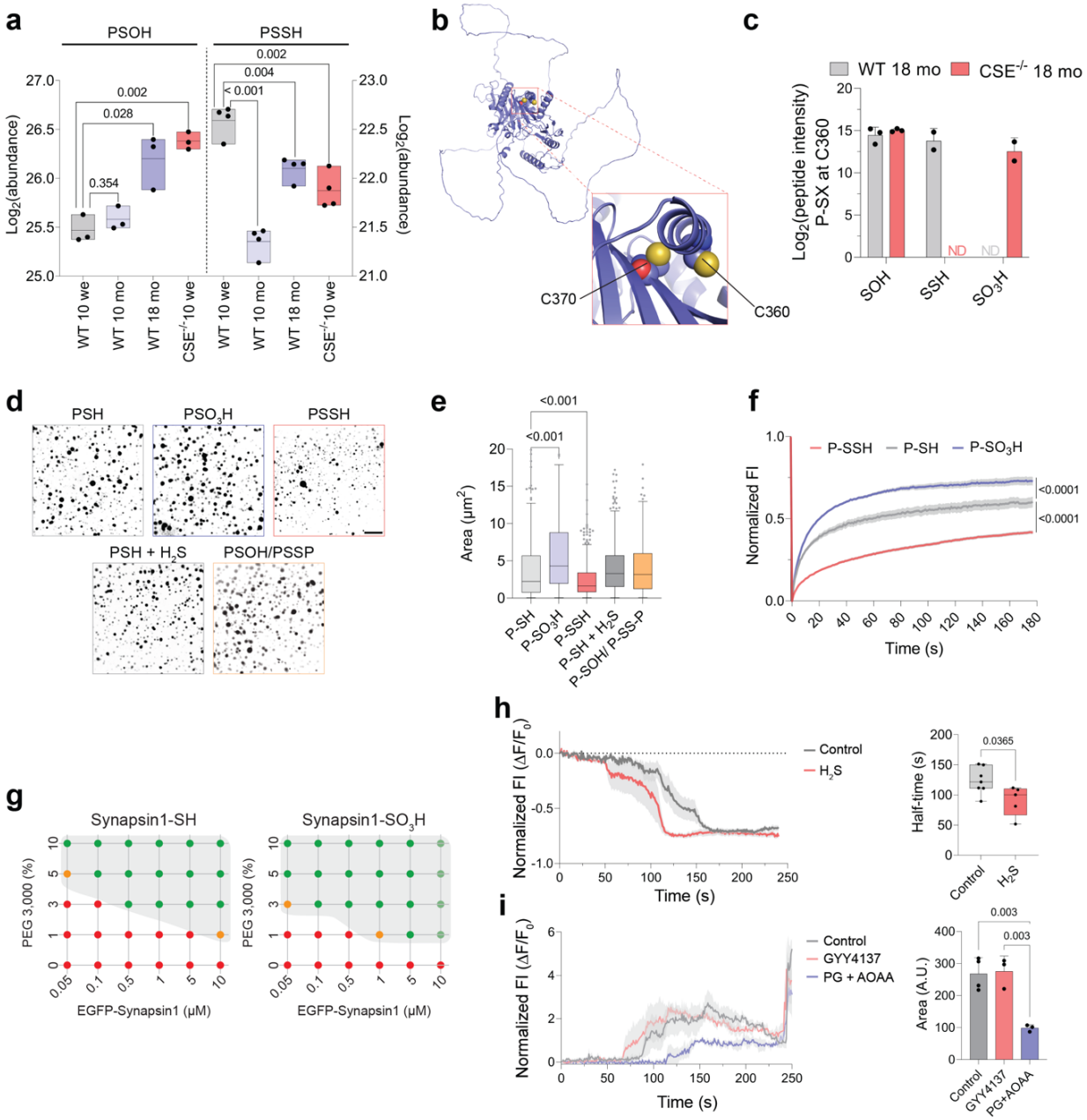
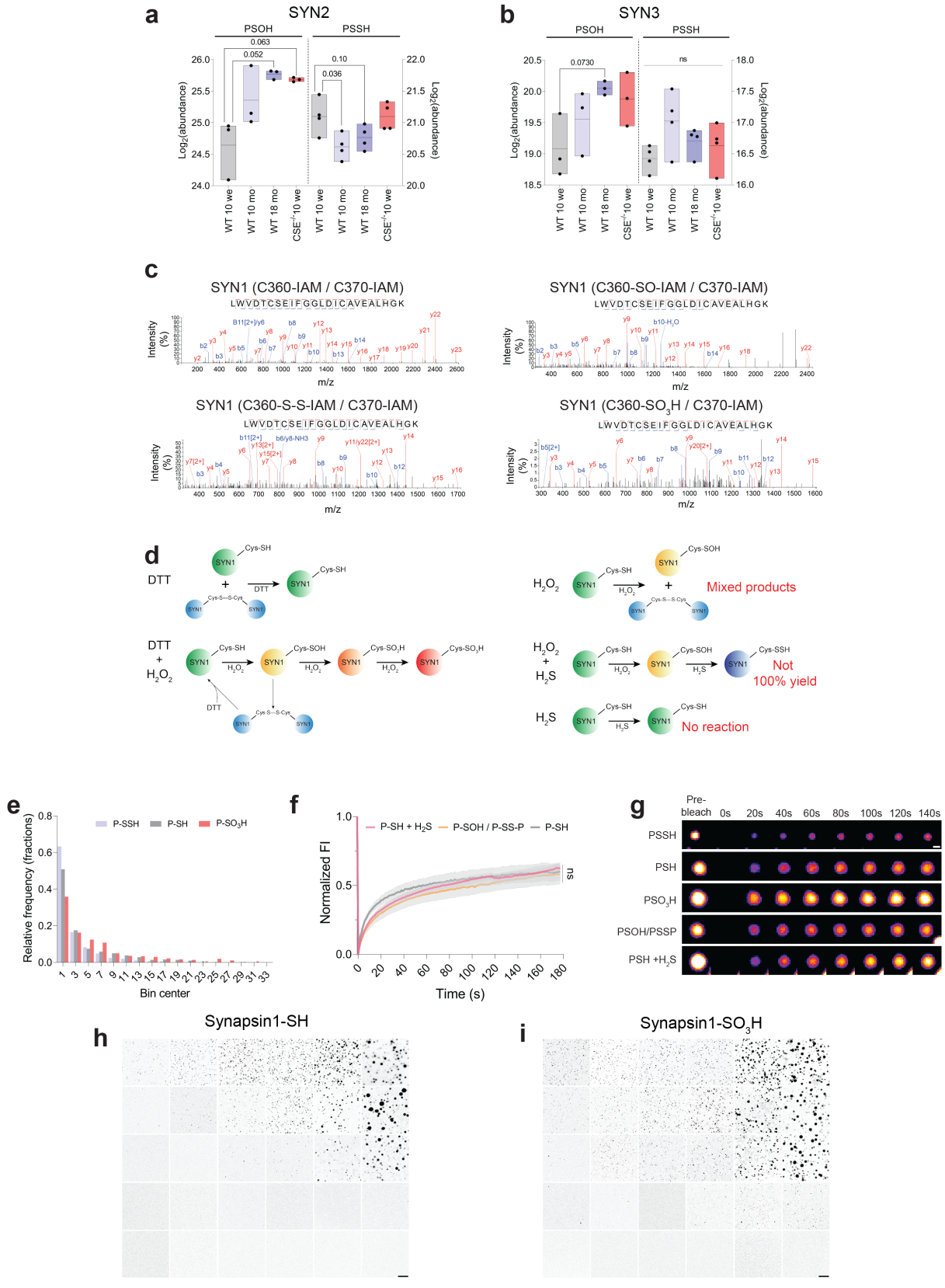


Figure 3.3. Age-related thiol remodeling of synapsin 1 controls it LLPS and neurotransmitter release. (**a**) Boxplot of the age-induced sulfenylation (PSOH) and persulfidation (PSSH) of synapsin 1 (PSOH: n = 3, PSSH: n = 4, Welch's t-test from proteomic analysis). (**b**) Structure of synapsin 1 highlighting two of its cysteines C360 and C370. (**c**) Changes of sulfenylation (SOH), persulfidation (SSH), and sulfonylation (SO_3H) of

the cysteine 360 but not C370, could be observed in WT and $CSE^{-/-}$ 18 months old mice (n = 3, ND: Non-Determined). (**d**) Representative microscopy images for EGFP-synapsin 1 condensates (10 µM in the presence of 3% PEG3000) formed under different cysteine modifications. Scale bar = 20 µm. (**e**) The box and whiskers plots (Tukey style, outlier in gray dots) represent the distribution of the droplet area in μm^2 among the different cysteine modifications (n ≥ 2 independent preparations, N = 360-840 data points per condition, one-way ANOVA). (**f**) Fluorescence recovery after photobleaching quantification of EGFP-synapsin 1. Means are shown as line and standard error as a shade of grey (n ≥ 2 independent preparations, N = 30-50 condensates per condition, two-way ANOVA, Sidak posthoc test). (**g**) Summary of the phase separation behavior of the reduced and sulfonylated EGFP-synapsin 1 with increased concentration of PEG-3000. (**h**) Kinetics of mScarlet-synapsin-1 droplet dissolution in the synapse of primary neurons upon stimulation with 92.5 mM KCl (n = 3 animals, a few preparations per animal, Student's t-test). (**i**) The neurotransmitter release from mouse primary neurons without or pre-treated with 100 µM GYY4137 or 1 mM mixture of propargylglycine (PG) and aminooxyacetic acid (AOAA) for 1 h. Synaptic vesicle release was triggered by perfusion of neurons with 92.5 mM KCl; the fluorescence of synaptophysin-pHluorin was used as a readout. Means are shown as lines and standard error of the mean as a shade of grey. The area under the curve was calculated for each measurement (n ≥ 3 animals, a few preparations per animal, one-way ANOVA, Tukey's HSD Test for multiple comparisons).



Extended data Figure 3.6. Age-induced changes in synapsin's thiol oxidation affect its LLPS properties. (**a-b**) Boxplot of the PSOH and PSSH remodeling of (a) synapsin-2 and (b) synapsin-3 in aging wild-type and CSE$^{-/-}$ mouse brain (n = 4, Welch's t-test; p-value reported from proteomic analysis). (**c**) Annotated TimsTOF CID MS/MS spectra of synapsin-1

peptides highlighting distinct oxidation states of cysteine 360. Spectra originate from quantified peptides extracted from WT and $CSE^{-/-}$ 18-month-old mice, as depicted in Figure 3.3c. The y-ions are denoted in red, while the b-ions are indicated in blue. (**d**) Schematic representation of the protocols for preparation of different cysteine modifications, used for the phase separation and FRAP experiments. PSH (100 µM DTT), PSSH (100 µM H_2O_2 + 500 µM H_2S), PSO_3H (100 µM DTT + 200 µM H_2O_2), and PSOH/PSSP (200 µM H_2O_2). DTT reduced EFGP-synapsin-1 was also treated with 500 µM H_2S as a negative control. e) Relative frequency histogram of EFGP-synapsin-1 droplets in relation to their size. (**f**) Quantification of fluorescence recovery after photobleaching. Prior to initiating phase separation, 10 µM EFGP-synapsin-1 samples underwent treatment with various cysteine-modifying agents as depicted in (d). Subsequent phase separation was induced by 3% PEG3000 (n ≥ 2 replicates, N = 30-50 condensates per condition, two-way ANOVA, Sidak posthoc test, n.s. non-significant). (**g**) Representative microscopy images capturing EGFP-synapsin-1 condensates before and after photobleaching. Scale bar = 1 µm. (**h-i**) Phase diagram of EGFP-synapsin-1 LLPS**.** Representative images of the LLPS phase diagram formed with (h) the reduced or (i) sulfonylated EGFP-synapsin-1. The phase diagram was built using increased concentrations of both the protein and PEG3000. Scale bar = 10 µm.

Smaller condensates and slower diffusion suggest that when persulfidated, the ability of synapsin 1 to phase separate is limited. If this were the case, then H_2S-induced PSSH formation would have profound effects on the dispersion of synaptic vesicles and thus on the neurotransmitter release. Indeed, the exposure of primary neurons to H_2S resulted in much faster KCl-induced dispersion of synapsin 1 from presynaptic terminal in primary hippocampal neurons (Fig. 3h). Consistent with these findings, we also observed that the treatment of primary mouse neurons with the slow releasing H_2S donor GYY4137 resulted in a faster dispersion of synapsin 1 and neurotransmitter release, while the inhibition of CSE not only delayed the release by ~2-fold but also resulted in overall lower release of synaptic vesicles (Figure 3.3l, Supplementary movies 1-3), confirming that the cysteine redox changes affect neurotransmitter release even at the endogenous level. Furthermore, these results provided a mechanistic explanation for the long-suggested role of endogenously produced H_2S in neurotransmitter release,[42–44] particularly in the context of the neurodegenerative diseases associated with lower CSE expression levels and impaired neurotransmitter release.[3,8–10]

3.3.3. Sulfonylation stimulates while persulfidation dissolves GAPDH phase separation

Although not previously reported to undergo phase separation due to the absence of intrinsically disordered regions (Figure 3.4a), glyceraldehyde-3-phosphate dehydrogenase (GAPDH) is the first reported persulfidated protein[45] and it is well-known that its activity is regulated by different cysteine PTMs. Similar to synapsin-1 it is also very abundant protein and GAPDH aggregates have been reported in brains from Alzheimer's disease patients[46,47] akin to the ones observed in $CSE^{-/-}$ mice (Figure 3.2j). When analyzing the cysteine oxidation status of mouse brain samples,

we observed that all three redox sensitive cysteines (C150, C154 and C245, Figure 3.4b) are found to be sulfonylated, but it was C245 that showed strong age-induced increase which was even more pronounced in $CSE^{-/-}$ mice (Figure 3.4c, Extended data Figure 3.7a-e).

Therefore, we tested if purified human recombinant GAPDH could undergo phase separation, and observed that increasing concentrations of PEG3000 resulted in condensates (Extended data Figure 3.7f) that showed liquid-like behavior and were dynamic in FRAP experiments (Extended data Figure 3.7g,h). We then tested if besides crowding agent, RNA could also induce LLPS of GAPDH. Indeed, the interaction with RNA stimulated the condensate formation even more efficiently (Figure 3.4d).

Having observed that PSO_3H of synapsin 1 enhances LLPS while persulfidation reduces it, we wanted to test if this would be true for GAPDH as well. Using the protocol to efficiently generate GAPDH PSO_3H (Extended data Figure 3.7i,j), we tested how cysteine oxidation of GAPDH affects its phase separation. Sulfonylated GAPDH formed condensates that are almost double the size of fully reduced GAPDH (Figure 3.4d). They also showed significantly slower FRAP recovery and lower % recovery (Figure 3.4e). However, our data suggest that thiol oxidation of GAPDH in general results in much bigger condensate formation when compared to the fully reduced enzyme (Extended data Figure 3.7k-n), suggesting that not only sulfonylation but also sulfenylation and/or disulfide formation enhances phase separation.

In contrast to GAPDH PSO_3H, GAPDH PSSH did not form any condensates in the tested range of protein/RNA concentrations (Figure 3.4d). To understand this better, we also tested if H_2S-induced persulfidation could dissolve already formed

GAPDH condensates. We incubated GAPDH with H_2O_2 or with DTT and added RNA for 5 min and recorded condensate formation. Under the conditions favoring PSSH formation (H_2O_2 + H_2S), addition of H_2S completely dissolved preformed condensates within 2 min, while they continued to grow in GAPDH treated with just DTT and H_2S, as no chemical reaction could occur on cysteine residues (Figure 3.4f).

These data suggest that under the conditions that favor lower persulfidation and higher thiol oxidation, GAPDH might undergo stronger LLPS. To quantify that we compared the phase diagrams of RNA induced LLPS of fully reduced and sulfonylated GAPDH. Sulfonylation of GAPDH did not only result in larger droplets but it also significantly enforced phase separation, with as low as 16/1 protein/RNA ratio being sufficient to efficiently result in droplet formation (Fig. 4g, Extended data Fig. 7o,p).

To confirm that GAPDH LLPS also happens in the cells, we stressed cells with 500 μM arsenite, condition commonly used to induce stress granule formation,[48] and observed GAPDH LLPS that co-localized with stress-granule marker G3BP2[48,49] (Fig. 4h). Interestingly, we also observed GAPDH condensates alone, suggesting that GAPDH undergoes LLPS in cells independently of interactions with other well-known ribonucleoproteins (Fig. 4h).

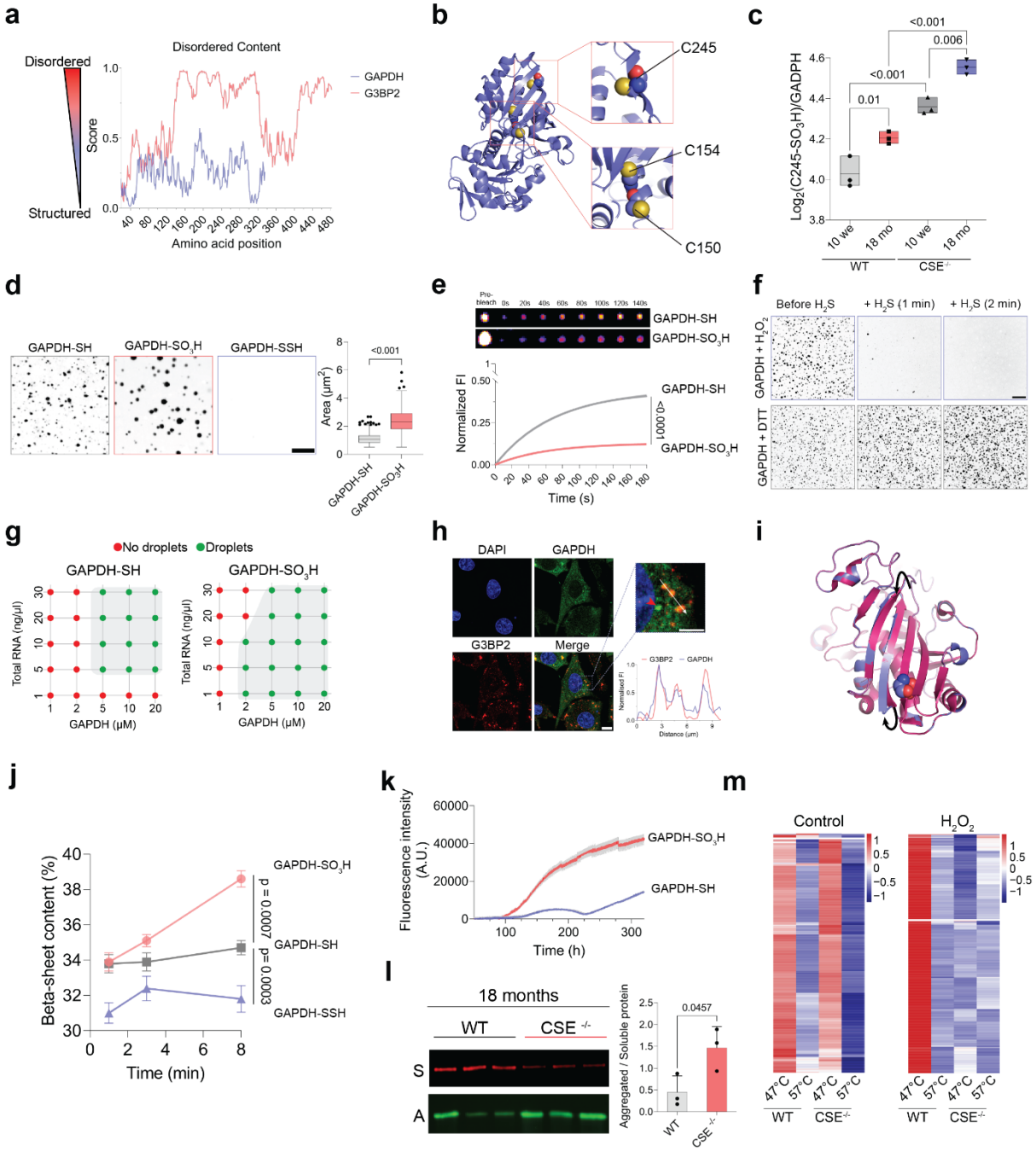
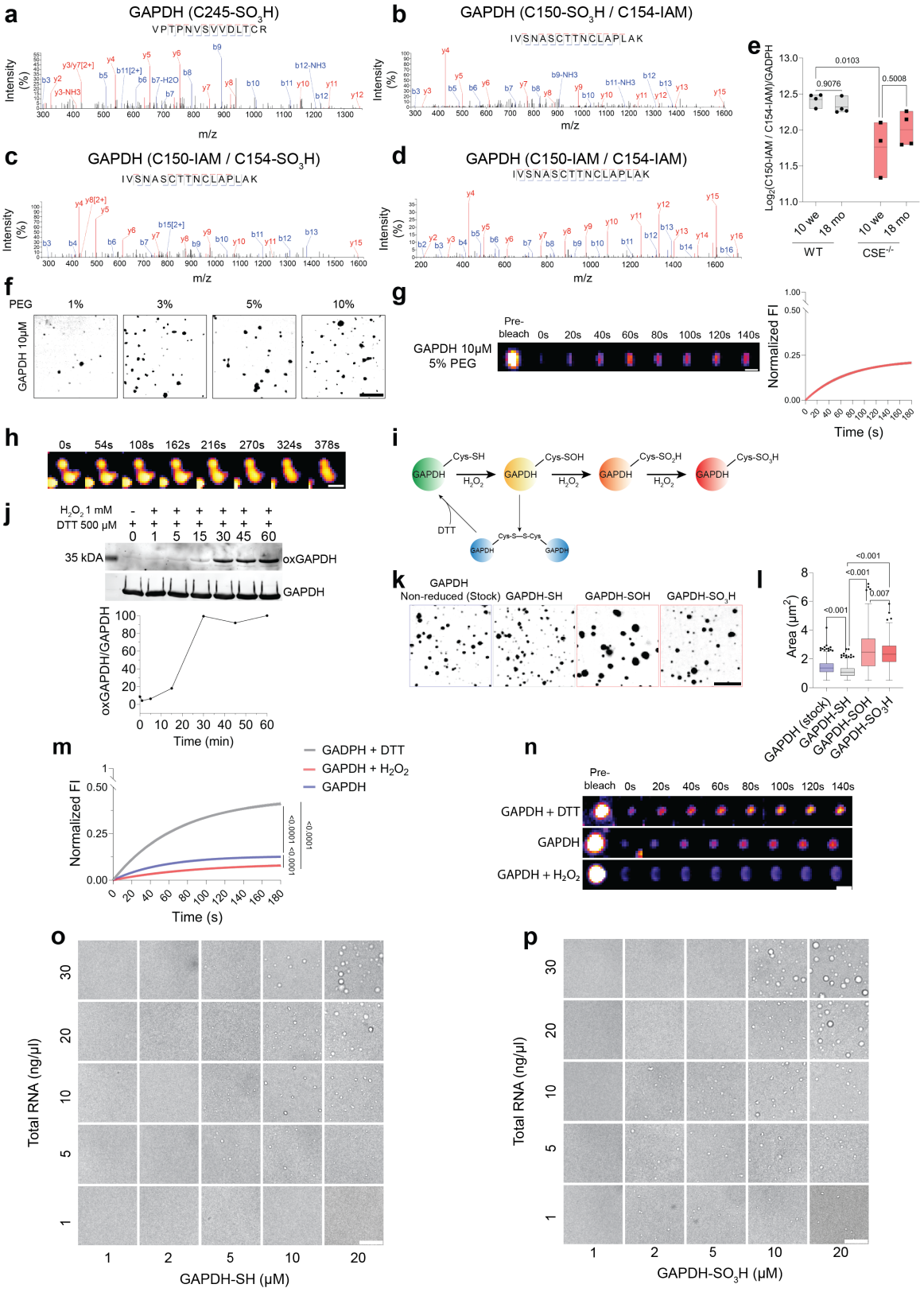


Figure 3.4. Age-induced cysteine sulfonylation drives aberrant phase separation and aggregation of GAPDH. (**a**) Comparison of disordered content distribution in the structures of human GAPDH and G3BP2 obtained by CD-Code. (**b**) Structure of human GAPDH (PDB:1U8F) highlighting the two cysteines in the active site (C150 and C154) and the cysteine 245 on the surface for the protein. (**c**) Log2 abundances of the cysteine 245 PSO_3H peptide normalized to the protein level in aging WT and $CSE^{-/-}$ mouse brain (n = 3, two-way ANOVA and Tukey's HSD test for multiple comparisons). (**d**) Representative images of

GAPDH-Cy3 condensate formation from fully reduced (GAPDH-SH), sulfonylated (GAPDH-SO_3H) and persulfidated (GAPDH-SSH) GAPDH (n = 3). Scale bar = 10 µm. Quantification of the GAPDH condensates area (in μm^2) in the reduced and sulfonylated form (n = 3 independent experiments, N ≥ 370 droplets, 1-way ANOVA, Tukey's HSD Test for multiple comparisons). (**e**) FRAP quantification of the GAPDH-Cy3 and representative microscopy images. Means are shown as lines and standard deviation as a shade of grey (n = 3 independent experiments, N ≥ 19 droplets, Two-way ANOVA, Sidak posthoc test). Scale bar = 2 µm. (**f**) Representative microscopy images of GAPDH condensate dissolution triggered by persulfidation. 20 µM of GAPDH was incubated for 5 min with RNA in the presence of 100 µM H_2O_2 or 100 µM DTT. Droplets were recorded before and 1 and 2 min after the addition of H_2S (200 µM). Scale bar = 40 µm. (**g**) Summary of the phase separation behavior of the reduced and sulfonylated GAPDH with increased concentration of total RNA. Corresponding images are shown in Extended data Figure 3.7o,p. (**h**) Colocalization analysis of GAPDH (green) and G3BP2 (red) condensates in STHdh cell line upon (500 µM) $NaAsO_2$ treatment (1h) (representative confocal images). Fluorescence intensity profiling was performed along the line demarcated by the white arrow. Of note, isolated GAPDH condensates were also observed (red arrowhead). Scale bar = 10 µm and in the zoomed intercept 5 µm. (**i**) Simulation of GADPH structural changes upon C245 sulfonylation. The pink color shows the original crystal structure, and the blue color is the predicted model. Black arrows show the flattening of the beta sheets induced by sulfonylation. (**j**) Fourier transform infrared (FT-IR) analysis of the beta-sheet content (%) in the PSO_3H, PSH, and PSSH GAPDH over time (n = 3, two-way ANOVA). (**k**) PROTEOSTAT® aggregation assay of 20 µM reduced and over-oxidized GAPDH in the presence of 30 ng/µl total RNA. (n = 3) (**l**) GAPDH aggregation in 18-month-old WT and $CSE^{-/-}$ brain samples. Soluble and aggregated fraction were obtained by ultracentrifugation and GAPDH visualized by western blot (A: aggregated fraction, S: soluble fraction). The ratio of aggregated over soluble fraction was quantified and shown as a bar graph with standard deviation (n = 3 animals, Student's t-test). (**m**) Thermal proteome stability assay between WT and $CSE^{-/-}$ MEF cells (n = 2).



Extended data Figure 3.7. Liquid-liquid phase separation of GAPDH. (**a-d**) Detection of GAPDH cysteine modifications in aged wild type (WT) and CSE$^{-/-}$ brain samples. Annotated TimsTOF peptide spectra depicting the sulfonylated (a) C245, (b) C150 and (c) C154 residues in GAPDH. Quantitative evaluation of the latter two peptides was challenging due to

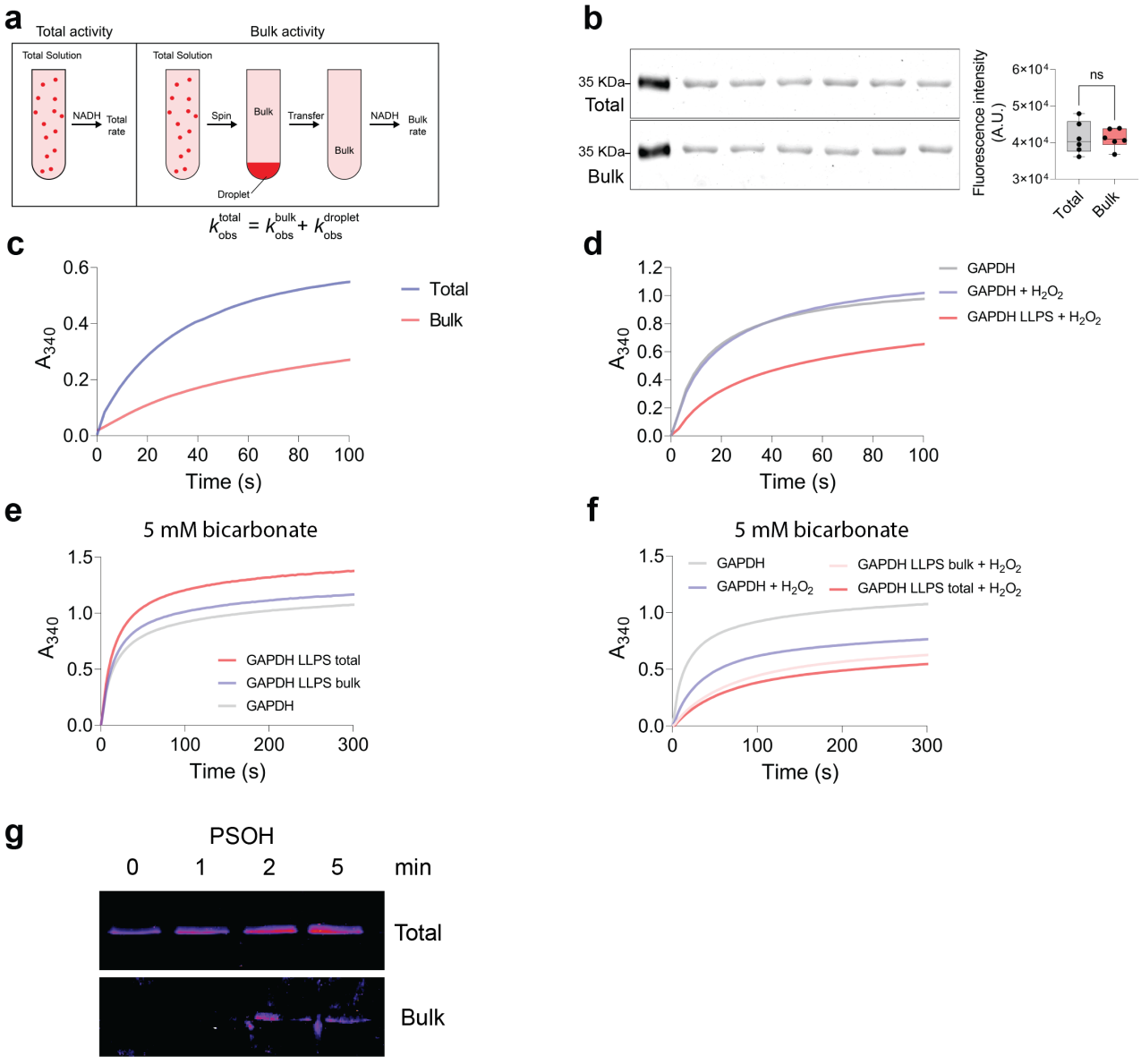
their limited abundance. (**d**) Annotated TimsTOF CID MS/MS peptide spectra illustrating the double carbamidomethylated C150/C154 peptide. (**e**) Quantification of the fully reduced C150/C154 peptide, depicted in (d) (n = 3; two-way ANOVA). (**f**) Representative images of GAPDH (10 µM) LLPS initiated by 10-minute incubation with different PEG3000 concentrations. Scale bar = 10 µm. (**g**) Representative microscopy images capturing GAPDH condensates before and after photobleaching. Scale bar = 2 µm. Mean line depicts recovery profile with standard errors shown in gray shades (n = 2 independent preparations, N = 8 droplets). Scale bar = 2 µm. (**h**) Liquid droplet-like properties of phase-separated GAPDH are exemplified by the depicted fusion event. Scale bar = 2 µm. (**i**) Schematic representation of protocol for preparing sulfonylated GAPDH. (**j**) GAPDH PSO_3H yield assessment through Western blot analysis using anti-GAPDH-SO_3H antibody. Quantitative analysis indicates the relative proportion of sulfonylated GAPDH normalized to the GAPDH loading control. GAPDH (50 µM) underwent treatment with DTT (500 µM) and H_2O_2 (1 mM) over varying time durations. Maximum over-oxidation yield was achieved after 30 minutes of treatment, a duration that was subsequently adopted for all further experiments. (**k**) Representative microscopy images of non-treated (stock), fully reduced, H_2O_2-oxidized and sulfonylated GAPDH droplets after 5 min incubation with 30 ng/µl of total RNA extract. Prior to induction, GAPDH (10 µM) was either untreated (GAPDH [stock]) or treated with DTT (100 µM; reduced) or H_2O_2 (200 µM; oxidized) for 5 minutes at 37 °C. Sulfonylated GAPDH was prepared as described above. Scale bar = 10 µm. (**l**) Quantification of droplet area obtained for different cysteine oxidation states of GAPDH, prepared as described above (n = 3 independent experiments, N ≥ 370 droplets, 1-way ANOVA, tukey's HSD Test for multiple comparisons). (**m**) Quantitative evaluation of the FRAP assay performed on distinct forms of GAPDH: non-treated, reduced and oxidized. Prior to induction, human recombinant GAPDH (10 µM) was either kept as it is (GAPDH) or treated with DTT (100 µM; reduced) or H_2O_2 (200 µM; oxidized) for 5 minutes at 37°. Photobleaching was performed 5 min after the induction of phase separation with 30 ng/µl of RNA. Mean lines depict recovery profile (n = 3 independent experiments, N ≥ 19 droplets, two-way ANOVA, Šidák test for multiple comparisons). (**n**) Representative microscopy images depicting the FRAP assay of GAPDH condensates formed by different thiol modifications, related to (m). Scale bar = 2 µm. (**o-p)** Phase diagram of GAPDH LLPS. Representative images of the LLPS phase diagram formed with (o) the reduced or (p) sulfonylated GAPDH. The phase diagram was built using increased concentrations of both the protein and total RNA extract. Scale bar = 10 µm.

3.3.4. LLPS of GAPDH affects its activity and reactivity of its cysteines

What does phase separation of GAPDH do to its enzymatic activity? Recent studies suggested that when the SUMOylation enzyme cascade was recruited into engineered condensates generated by LLPS, SUMOylation rates increased up to 36-fold.[12] Applying similar experimental design, we tested if and how phase separation affects GAPDH enzymatic activity. After allowing 45 min to the mixture of GAPDH and RNA to phase separate, we centrifuged the droplets to generate “bulk” solution and compared its GAPDH activity to original reaction mixture (“total”) (Extended data Figure 3.8a,b). Significant difference in reaction rates, monitored as NADH formation, was observed, with total solution resulting in faster and more efficient activity (Extended data Figure 3.8c). The difference between total and bulk solution k_{obs} (1.68 x 10^{-2} s^{-1} *vs*. 0.71 x 10^{-2} s^{-1}, respectively) is solely caused by condensates which constitute as little as 1.5-2% of the reaction volume. The observed activation of GAPDH suggests that, once in the phase, enzyme occupies different conformation which makes it more active but could also make it more prone to oxidation.

As hypothesized, the activity of GAPDH that was mixed with RNAs to cause phase separation was significantly inhibited by H_2O_2 (Extended data Figure 3.8c). In the presence of physiological concentration of bicarbonate, which is known to enhance H_2O_2-induced thiol oxidation by forming HCO_4^-,[50] this effect was even more profound (Extended data Figure 3.8e,f). The same inhibition rate in both total and bulk solution suggests that the inhibition was almost completely caused by the oxidation of GAPDH in the phase. Indeed, trapping of PSOH showed that when phase separated, GAPDH becomes more prone to cysteine oxidation even in the absence of H_2O_2 (Extended data Figure 3.8g), confirming that phase separation

changes accessibility and reactivity of GAPDH cysteines, making them more prone for oxidation.



Extended data Figure 3.8. GAPDH LLPS affects enzyme activity and reactivity towards H_2O_2. (**a**) Depiction of the experimental design used to assess the effect of LLPS of GAPDH enzymatic activity. Modified from Peeples et al, 2021. (**b**) Western-blot assessment of GAPDH levels in total and bulk phase obtained following the protocol depicted in a). n = 6, Student's t-test. (**c**) GAPDH (10 μM) activity in total and bulk fractions was measured through NADH production at 340 nm. n = 3. (**d**) The effect of H_2O_2 (100 μM). treatment on the activity of soluble and phase separated (LLPS) GAPDH (10 μM). n = 3. (**e-f**) GAPDH LLPS impact

the protein activity and reactivity with H_2O_2. Kinetics of GAPDH (10 μM) activity in solution (in absence of phase separation), in the bulk fraction, and within the total LLPS fraction (induced by the addition of 30 ng/μL of total RNA). Activity measurements were performed in phase separation buffer (see Material and Methods) (e) in the presence of 2 mM sodium bicarbonate and (f) in the presence of 2 mM sodium bicarbonate and 100 μM H_2O_2. (**g**) BTD trap assay for PSOH formation in the reaction of H_2O_2 with GAPDH in total and bulk solution. n = 2.

3.3.5. Sulfonylation-driven aberrant LLPS of GAPDH leads to protein aggregation in aging brain

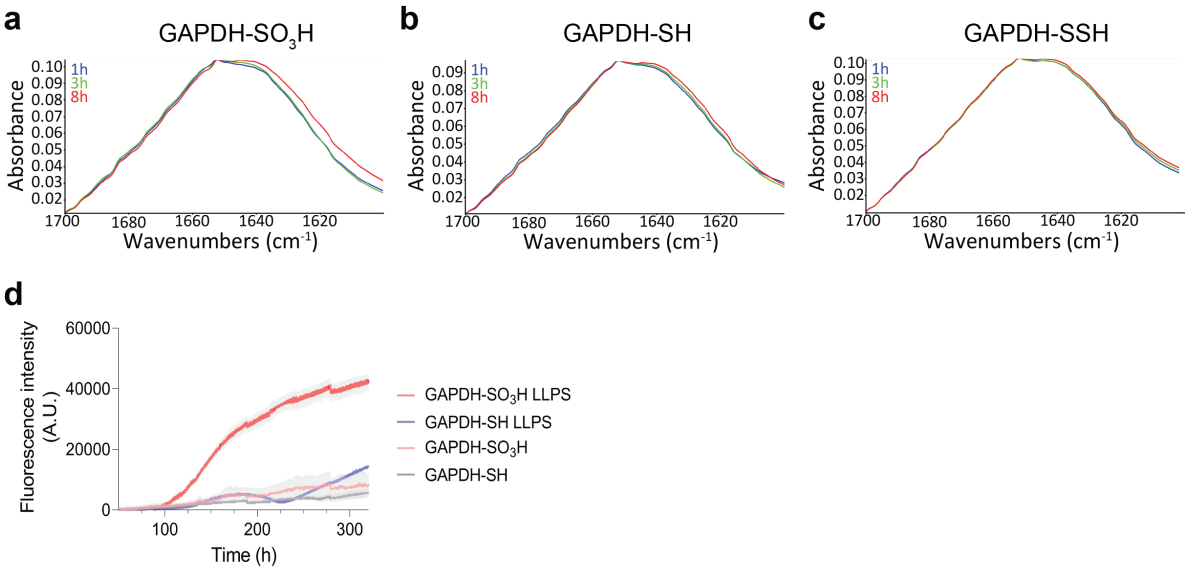
In context of aging and particularly decline of CSE and protein persulfidation to prevent it, this would form a vicious cycle where LLPS of GAPDH will lead to more hyperoxidation even at physiological levels of H_2O_2 and hyperoxidized GAPDH will in turn enforce even stronger LLPS. Proteins that stay longer in biomolecular condensates, risk formation of aberrant aggregates. Furthermore, C245 is located in beta-sheet domain (Figure 3.4i), secondary structure that facilitates aggregation. Vienna PTM modeling of the effect that C245 sulfonylation might have on GAPDH, showed profound changes in the GAPDH structure, particularly in beta-sheet domain which appeared to be more flattened (Figure 3.4i). This observation was further confirmed experimentally by FT-IR analysis of the structure, where significantly higher percentage of beta-sheets could be detected in GAPDH PSO_3H, especially in the spectral region (1616–1625 cm^{-1}) attributed to aggregation prone inter/intramolecular beta-sheets (Figure 3.4j, Extended data Figure 3.9a-c).

Therefore, we first tested if natively folded GAPDH would aggregate but could not observe any aggregation in neither reduced or sulfonylated GAPDH (Extended data Figure 3.9d). However, addition of RNA to induce phase separation caused clear protein aggregation of hyperoxidized GAPDH and much slower and less efficient aggregation in reduced GAPDH (Figure 3.4k), which could be explained by the observed spontaneous thiol oxidation of the proteins which are in LLPS (Extended data Figure 3.8g).

Age-induced decline in protein persulfidation and increase of sulfonylation, particularly in $CSE^{-/-}$ mice should result in increased GAPDH aggregation in brain. To test it, we separated soluble and aggregated fraction of brain lysates from old WT

and $CSE^{-/-}$ mice and observed that indeed there was a ~3-fold increase of GAPDH in aggregated fraction of $CSE^{-/-}$ lysates (Figure 3.4l).

As observed in the molecular dynamics modeling for some of the identified sulfonylated targets, cysteine is usually located within or at the beginning/end of the beta-sheet and it causes significant conformational change in the protein (Figure 3.2g, Extended data Figure 3.4g-l). If these conformational changes have an effect analogous to GAPDH (Figure 3.4i-k), then proteins with hyperoxidized cysteine should be more prone to aggregation. To test this hypothesis, we treated mouse embryonic fibroblasts of wild type and $CSE^{-/-}$ cells with H_2O_2 and performed thermal proteome profiling stability assay, focusing only on the beginning and the end of the melting curve (47 ºC vs 57 ºC). The proteome of the $CSE^{-/-}$ MEF cells, which have lower H_2S production to rescue thiol oxidation from hyperoxidation,[4] was significantly affected by H_2O_2: majority of identified proteins lost their stability and aggregated from the solution even at 47 ºC (Figure 3.4m, Supplementary Table 6). This data confirmed that mimicking age-related switch from persulfidation to sulfonylation could indeed affect not only LLPS ability of affected proteins but also their aggregability.



Extended data Figure 3.9. Conformational change caused by GAPDH sulfonylation results in protein aggregation. (**a-c**) Structural changes of GAPDH induced by different cysteine PTMs, monitored within amide I region of FT-IR spectra. Spectra of samples containing either (a) sulfenylated (-SO_3H), (b) reduced (-SH), or (c) persulfidated GAPDH (-SSH) (30 µM) were analyzed in OMNIC software. Amide I region arises mainly from C = O stretching vibrations thus is very sensitive to changes in secondary structures. Between 1600–1700 cm^{-1} each secondary structure contributes to the absorption in a certain wavenumber range. The most prominent change detected in oxidized GAPDH after 8h was signal increase in the regions attributed to beta-sheets in general, namely 1616–1625 cm^{-1} assigned to aggregation-prone inter/intramolecular beta-sheet, and 1626–1640 cm^{-1} assigned to intramolecular beta-sheet. (**d**) LLPS of sulfonylated GAPDH promotes its aggregation. The aggregation tendencies of sulfonylated GAPDH were assessed using the PROTEOSTAT® assay. Solutions containing either reduced or sulfonylated GAPDH (10 µM) were combined with 500 µM DTT to keep cysteine under the reduced form. This combination was carried out in two conditions: (i) in the presence of total RNA extract, to simulate liquid-liquid phase separation (LLPS), and (ii) in the absence of total extract RNA, free of LLPS.

3.4. Discussion

The emergence of life is inherently intertwined with the presence of hydrogen sulfide (H_2S), which, alongside cyanide, played a fundamental role in the genesis of biomolecules [51]. Cysteine was then used to catalyze first peptide synthesis.[52] LLPS and biocondensate formation have indisputably guided evolution towards the life forms we recognize today.[53–55] These fundamental chemical and biophysical processes remain integral to cellular function and homeostasis. This work identifies the transformative potential of cysteine PTMs on protein LLPS, highlighting the protective and regulatory impact of protein PSSH, while also providing a (bio)chemical link between aging and phase separation. Notably, protein persulfidation leads to the dispersion of phase-separated condensates. In contrast, cysteine sulfonylation appears to drive proteins towards enhanced phase separation, ultimately resulting in protein aggregation. This is largely caused by the profound conformational changes predicted to occur by PSO_3H of cysteine residues located either within or nearby beta-sheets. In the context of the aging brain, where decrease of PSSH and increase of PSOH and PSO_3H is observed, this could lead to (i) compromised synaptic release by disrupting synapsin 1-synaptic vesicle condensates, (ii) increased and unresolved phase separation of GAPDH (and probably other proteins) and (iii) accumulation and aggregation of proteins.

Neuronal transmission relies on the regulated secretion of neurotransmitters,[56] which are packed in synaptic vesicles whose sequestering and dynamics are controlled by synapsin 1.[57] Considering that the loss of proper synaptic transmission is a hallmark of age-induced neurodegenerative diseases, which are generally associated with lower CSE expression levels,[3,8–10] it is tempting to speculate that age-induced thiol remodeling described in this study drives this process.

Additionally, aging brain seem to be overwhelmed by ROS, as evidenced by our sulfenylome and sulfonylome data. The role of ROS in aging has stirred both acclaim and controversy.[1,58,59] While pivotal in early developmental stages, where it could predispose the organism for a longer life,[60,61] it is detrimental in aging organism.[62] Our research demonstrates that steady state levels of PSOH, the first thiol oxidation step in the reaction with ROS, increase continuously with aging leading eventually to PSO_3H and that this process is, in large, prevented by the endogenous production of H_2S.

The compartmentalization of ROS action in the cytoplasm within signaling complexes that “phase out” in solution establishes a new paradigm for ROS signaling. Namely, ROS could modify and damage the proteins even if its levels do not go up; they simply have to react with proteins in biomolecular condensates. Oxidized proteins will then have tendency to stay longer within condensate and even aggregate forming a vicious cycle feedback loop. Thus, age-induced decrease in resolving persulfidation inevitably results in longer lasting LLPS and a conformational change that causes aggregation, as seen with GAPDH. These aggregates, reported in the brains of Alzheimer’s disease patients,[46,47] could nucleate other neuronal proteins, such as Tau. Indeed, we observed neurofibrillary tangles in the brain of $CSE^{-/-}$ mice, as well as their significantly shorter lifespan. Thus, $CSE^{-/-}$ mice could be a useful model to study age-induced neurofibrillary tangle formation in mice. Even the short treatment of $CSE^{-/-}$ cells with ROS results in the global leftward shift of their proteome melting curves, suggesting aggregability. These data also provide experimental evidence to the claims that CSE might be as a pro-longevity gene.[6,7]

In conclusion, age-induced thiol-remodeling through aberrant LLPS results in a global collapse of cellular homeostasis, predisposing proteins for pathological

aggregation. The emergence of H_2S-releasing pharmaceuticals offers a potential avenue for ameliorating the age-triggered thiol oxidation-mediated effects on LLPS, holding promise for the treatment of neurodegenerative disorders.

3.5. Material and methods

Mice. Wild-type and CSE KO animals[63] were bred/housed in ventilated cages, under specific pathogen-free, temperature controlled (22 °C) and 12 h light/dark cycle conditions in full compliance with the guidelines of the Federation of Laboratory Animal Science Association recommendations in the Laboratory Animal Unit of Biomedical Research Foundation of the Academy of Athens (BRFAA) and allowed unrestricted access to chow diet and water. All studies were performed on male mice at the indicated age.

Cell culture. $CSE^{-/-}$ mouse embryonic fibroblasts (MEF) are kind gift from Professor Bindu Paul (Johns Hopkins University) and were generated from $CSE^{+/+}$ and $CSE^{-/-}$ mice and immortalized using SV40T antigen.[64] MEF cells were cultured in DMEM, supplemented with 2 mM L-glutamine, 1 % penicillin-streptomycin, and 10 % fetal bovine serum at 37 °C and 5 % CO_2. The striatal progenitor cell line $STHdh^{Q7/Q7}$, expressing wild-type huntingtin, and $STHdh^{Q111/Q111}$, expressing mutant huntingtin harboring 111 glutamine repeats (referred to as Q7 and Q111 cells, respectively) were maintained in DMEM (low glucose, no pyruvate) supplemented with 2 mM L-glutamine, 1 % penicillin-streptomycin, and 10 % fetal bovine serum at 33 °C and 5 % CO_2.

Persulfidation enrichment for proteomic analysis. The brain frontal cortexes were lysed in cold HEN Buffer (50 mM HEPES, 1 mM EDTA, 0.1 mM neocuproine, 1 % IGEPAL, 2 % SDS, pH 7.4) supplemented with 5 mM 4-Chloro-7-

nitrobenzofurazan (NBF-Cl). Frozen tissue was disrupted in lysis buffer using the TissueLyser II (Qiagen) and 5 mm stainless steel beads. Persulfidation enrichment was performed using previously described method.[4] Enriched proteins were eluted by incubating beads with 2.25 M ammonia solution for 16 h and collected the following morning for lyophilization. Lyophilized samples were dissolved in digestion buffer (50 mM ammonium bicarbonate [ABC], 1 mM calcium chloride) and digested overnight using trypsin at trypsin:protein ratio 1:20. The desalting was performed on Supel™-Select HLB SPE Tube. Eluates were evaporated under vacuum until dryness. Peptides were dissolved in 0.1 % TFA, and digestion and desalting quality control was performed using an Dionex UltiMate 3000 (RSLC) system with a PepSwift Monolithic® Trap 200 µm * 5 mm (Thermo Fisher Scientific).

Sulfenylation enrichment for proteomic analysis. Brain frontal cortexes were lysed in cold HEN Buffer supplemented with 0.5 mM Benzo[c][1,2]thiazine-based BTD (BTD) synthesized in house following established protocol.[19] Lysates were incubated for 2 h at 37 °C followed by two methanol/chloroform precipitations. The sulfenylation enrichment was carried out using a modified method from Fu et al, 2019.[17] Shortly, samples were resuspended in HEPES + 2 % SDS and treated with 10 mM DTT for 1 h at 37 °C, followed by 40 mM iodoacetamide (IAM) for 30 min at RT. Excess DTT and IAM were removed by methanol chloroform precipitation, and proteins were resuspended in 50 mM HEPES pH 7.0, 2 % SDS. 1.5 mg of proteins were incubated for 2 h at 37 °C with 0.2 mM Az-UV-Cleavable-biotin, 1 mM Ascorbic acid, and 0.1 mM Copper-TBTA to perform the click-chemistry reaction. Precipitated proteins were dissolved in neutravidin Binding buffer (50 mM NaOAc, pH 4.5) and 0.2 % SDS. Protein concentration was performed, and 0.9 mg of proteins were incubated with Pierce™ High Capacity NeutrAvidin Agarose beads. After 3 h of mixing at RT, beads were loaded onto columns and washed with neutravidin washing buffer (50

mM NaOAc and 2 M NaCl, pH 4.5). Sulfenylated proteins were then released by incubating beads for 3 h under UV light (365 nm) in 25 mM ammonium bicarbonate buffer. Supernatants were collected and lyophilized. Samples were then digested and desalted as detailed above. Peptides were dissolved in 0.1 % TFA, and digestion quality control was performed as described.

LC/MS analysis. Peptides were analyzed by high-resolution LC-MS/MS using an Dionex UltiMate 3000 RSLC Systems (RSLC) system (Thermo Fisher Scientific) coupled with an Orbitrap Eclipse™ Tribrid™ Mass Spectrometer via an EASY-spray (Thermo Fisher Scientific). Peptide separation was carried out with an Acclaim™ PepMap™ 100 C18 column (Thermo Fisher Scientific) using a 65 min linear gradient from 3 to 35 % of B (84 % Acetonitrile, 0.1 % Formic Acid) at a flow rate of 250 nL/min. The Orbitrap Eclipse™ was operated in a DDA mode, and MS1 survey scans were acquired from m/z 300 to 1,500 at a resolution of 120,000 using the Orbitrap mode. MS2 scans were carried out for 3 seconds with high-energy collision-induced dissociation (HCD) at 32 % using the Normal speed IonTrap mode.

Data were evaluated with PEAKS ONLINE software using 15 ppm for precursor mass tolerance, 0.5 Da for the fragment mass tolerance, specific tryptic digest, and a maximum of 3 missed cleavages. For persulfidation detection, NBF (+163.00961594 Da) on C, K, R, DCP (+168.0786442 Da) on C, N-term acetylation (+42.010565 Da), and methionine oxidation (+15.994915 Da) were added as variable modifications. For sulfenylation detection, BTD–UV-cleavable probe (cleaved, +418.1311 Da), carbamidomethylation (+57.021464 Da) on C, N-term acetylation (+42.010565 Da), and methionine oxidation (+15.994915 Da) were added as variable modifications, peptide spectrum match (PSM) and proteins were filtered at FDR 1 %. Data were normalized using EigenMS on R studio.[65]

Total proteome analysis. Brain frontal cortexes were disrupted in lysis buffer (50 mM TRIS, 150 mM NaCl, 2% SDS, 1% IGEPAL, pH 7.8) using the Tissuelyser II and twenty 1.4 mm ceramic beads (Qiagen, #13113). Lysates were incubated with Benzonase following manufacturer recommendation for 30 min and precipitated. Samples were then resuspended in 50 mM HEPES, 2 % SDS, and incubated with 10 mM DTT at RT followed by incubation with 50 mM IAM for 1h at 37°C. Precipitation was used to stop the reaction and concentrate proteins. For tryptic digestion, samples were resuspended in 6 M guanidine hydrochloride. 250 µg of protein were digested overnight at 37 °C using trypsin with a 1:20 trypsin to sample ratio (Promega, #V5117). The next day, peptides were desalted evaporated under vacuum until dryness as described above.

Peptides were dissolved in 0.1 % TFA, and digestion quality control was performed as described above. Peptides were analyzed by high-resolution LC-MS/MS using an Dionex UltiMate 3000 (RSLC) Systems (Thermo Fisher Scientific) coupled to a timsTOF Pro (Bruker) equipped with a CaptiveSpray source. Peptide separation was carried out with an Acclaim™ PepMap™ 100 C18 column (Thermo Fisher Scientific) using a 65 min linear gradient from 3 to 35 % of B (84 % Acetonitrile, 0.1 % Formic Acid) at a flow rate of 250 nL/min. The timsTOF Pro (Bruker) was operated in PASEF mode using Compass Hystar 5.0.36.0. The TIMS setting was as follows: Mass Range 100 to 1700 m/z, 1/K0 Start 1.6 Vs/cm2 End 1.6 Vs/cm2, Ramp time 100 ms, Lock Duty Cycle to 100 %, Capillary Voltage 1500V, Dry Gas 3 l/min, Dry Temp 180°C. PASEF settings: 10 MS/MS scans, charge range 0-5, active exclusion for 0.4 min, Scheduling Target intensity 20000, Intensity threshold 2500, CID collision energy 49 eV. Data were evaluated with PEAKS ONLINE software using 20 ppm for precursor mass tolerance, 0.5 Da for the fragment mass tolerance, specific tryptic digest, and a maximum of 3 missed cleavages.

Carbamidomethylation (+57.021464 Da) on C, N-term acetylation (+42.010565 Da), and methionine oxidation (+15.994915 Da) were added as variable modifications, PSM and proteins were filtered at FDR 1 %. Data were normalized based on the total ion count (TIC).

Direct detection of Sulfonylated peptides using LC/MS. 50 µg of the NBF-labelled samples dissolved in PBS 2 % SDS (see section “PSSH enrichment for proteomic analysis”) were trypsinized overnight as described above. Samples were subjected to desalting and Pierce® Detergent Removal columns (ThermoFisher, # 87777). Peptides evaporated under vacuum until dryness as described above.

Peptides were dissolved in 0.1 % TFA, and digestion quality was assessed as previously described. Peptides were analyzed by high-resolution LC-MS/MS using Dionex UltiMate 3000 RSLC Systems (RSLC) system (Thermo Fisher Scientific) coupled with an Orbitrap Eclipse™ Tribrid™ Mass Spectrometer via an EASY-spray (Thermo Fisher Scientific). Peptide separation was carried out with an Acclaim™ PepMap™ 100 C18 column using a 160 min linear gradient from 3 to 35 % of B (84 % Acetonitrile, 0.1 % Formic Acid) at a flow rate of 250 nL/min. Parameters were set as described above (see “PSOH enrichment for proteomic analysis” section).

Data were evaluated with PEAKS ONLINE software using 15 ppm for precursor mass tolerance, 0.5 Da for fragment mass tolerance, specific tryptic digest, and a maximum of 3 missed cleavages. NBF (+163.00961594 Da) on C, K, and R, trioxidation (+47.984744 DA) on C, N-term acetylation (+42.010565 Da), and methionine oxidation (+15.994915 Da) were added as variable modifications, PSM and proteins were filtered at FDR 1 %. Data were normalized based on TIC.

Immunoblotting. Cells or tissues were lysed in HEN buffer supplemented with 20 mM IAM and incubated at 37°C for 2 h to allow complete cysteine blocking.

The excess of blocking- reagent was removed by precipitation, as mentioned above. The samples were then resuspended in HEPES + 2 % SDS and readjusted using DC™ protein assay. One equivalent of Laemmli (4X) buffer supplemented with 10 % β-mercaptoethanol was added to three sample equivalents for SDS-PAGE and boiled at 95 °C for 5 min protected from light. Equal amounts of proteins were resolved by SDS-page using standard protocol. Samples were then immunoblotted with the indicated antibodies and dilutions; (anti-Prdx-SO_3 [Abcam, #ab16830], 1:4000; anti-oxDJ-1 [Sigma-Aldrich, #MABN1773], 1:2000; anti-GAPDH-SO_3 [Abfrontier, #LF-PA0006], 1:2000; anti-GAPDH-AF488 [Sigma-Aldrich, #MAB374-AF488],1:20000; anti-β-Tubulin [Sigma-Aldrich, #T0198], 1:5000; anti-Rabbit-AF680 [Abcam, #ab175773], 1:20000; anti-Mouse-AF680 [Abcam, #ab175775], 1:20000).

LDH and PKM activity assays. For all activity assays, the frozen tissues were disrupted in mild lysis buffer (25 mM HEPES, 250 mM sucrose, 20 mM $MgCl_2$, 1 mM EDTA, pH 7.4) using the TissueLyser II and 5 mm Stainless steel beads. Samples were then centrifuged at 14,000 x g for 15 min at 4°C, and supernatant was collected for further application. Protein concentration was performed, samples were readjusted to equal amounts and split for different activity assays. LDH (Sigma, #MAK066) and PKM (Sigma, #MAK072) activity assays were carried out following the manufacturer's protocol.

Direct detection of cysteine PTMs of synapsin 1 and GAPDH by LC-MS/MS. Brain tissues were lysed using the same protocol as for immunoblotting. A modified in-gel digestion protocol from was used to identify GAPDH and synapsin 1 cysteine peptides.[66] An equal amount of protein was loaded and separated by SDS page. Gels were then stained for 2 min with a Coomassie Brilliant Blue solution (1.2 mM Coomassie Brilliant Blue, 10 % acetic acid, 40 % methanol in distilled water) and

destained overnight in a decoloration solution (25 % Methanol, 8 % acetic acid in distilled water). Once destained, the band corresponding to the size of the protein of interest (-/+ 5kDa) was excised. Coomassie Brilliant Blue was removed by alternating washes with 50 mM ABC and 25 mM ABC, 50 % ACN each for 10 min at 37 °C, 450 rpm. Once free from the stain, gel pieces were dried using a speed vacuum concentrator. Gel pieces were then incubated for 10 min at 4 °C with 50 mM ABC, 1 mM $CaCl_2$, and trypsin at 12.5 ng/µl. The excess solution was removed, and samples were trypsinized for 16 h at 37 °C, 750 rpm. The following day, peptides were extracted by incubating the gel pieces two times in 0.1 % TFA for 15 min at 37°C, 450 rpm. This step was followed by two-times incubation with 0.1 % TFA + 60 % ACN for 15 min at 37°C, 450 rpm. Extracts were combined, and peptides were evaporated to dryness.

Peptides were dissolved in 0.1 % TFA, and Digestion was controlled using previously described method. Peptides were analyzed using a Dionex UltiMate 3000 RSLC Systems (RSLC) system (Thermo Fisher Scientific) coupled to a timsTOF Pro (Bruker) equipped with a CaptiveSpray source. Peptide separation was carried out with an Acclaim™ PepMap™ 100 C18 column (Thermo Fisher Scientific) using a 120 min linear gradient from 3 to 35 % of B (84 % Acetonitrile, 0.1 % Formic Acid) at a flow rate of 250 nL/min. The timsTOF Pro (Bruker) was operated as previously described. Data were evaluated with PEAKS ONLINE software using 20 ppm for precursor mass tolerance, 0.5 Da for fragment mass tolerance, specific tryptic digest, and a maximum of 3 missed cleavages. The entire mouse database was used for the search. SO-IAM (+73.020464 Da), SS-IAM (+89.086464 Da), 'Cysteine oxidation to cysteic acid' (-SO_3H, +47.984745 Da, Unimod ID: 345), carbamidomethylation (+57.021464 Da) on C, N-term acetylation (+42.010565 Da), and methionine

oxidation (+15.994915 Da) were added as variable modifications, PSM and proteins were filtered at FDR 1 %. Data were normalized based on TIC.

EGFP-synapsin 1 in-vitro phase separation. The recombinant full-length EGFP-Synapsin 1 was expressed in a mammalian expression system and purified as previously described.[57,67] Before the experiment, EGFP-synapsin 1 was cleaned up from TCEP using a dialysis column, and the buffer was replaced with the phase separation buffer (25 mM Tris, 150 mM NaCl, pH 7.4). Sulfonylated EGFP-synapsin 1 form was obtained by treating SYN1 with 100 µM DTT and 200 µM H_2O_2 at 37 °C for 30 min. Persulfidated EGFP-synapsin 1 was formed by treating the protein with 100 µM H_2O_2 and 500 µM H_2S for 5 min at 37 °C before adding PEG. Respective controls were carried out using the same DTT, H_2O_2, and H_2S concentrations. For the FRAP experiment, 3% w/v polyethylene glycol (PEG 3,000) was used to trigger phase separation of 10 µM EGFP-synapsin 1. Photobleaching was performed after 5 min incubation with PEG, and recovery was recorded for 10 min. 2-3 independent preparations, done on separate days and with separate protein batches, were used per thiol modifications.

Primary neurons experiments. Primary hippocampal neurons were prepared from newborn pups (p0/p1) and the exocytosis assays were performed as described recently.[6] Neurons were pre-incubated with GYY4137 (100 µM) or propargylglycine (1 mM) and aminooxyacetic acid (1 mM). During imaging, neurons were first perfused with Tyrode solution supplemented with 2.5 mM KCl (low KCl); subsequently, to stimulate exocytosis, neurons were perfused with Tyrode solution supplemented with 92.5 mM KCl (high KCl) for 5 min; finally, neurons were briefly perfused with Tyrode solution containing 50 mM NH4Cl to alkalize the sample and visualize the total fluorescence from synaptophysin-pHlurin.

Immunofluorescence of G3BP2 and GAPDH under $NaAsO_2$ treatment. STHdh cells were split in a µ-Dish 35 mm, high Glass Bottom (IBIDI, #81158). Before fixation, cells were washed two times with warm PBS and fixed with 2 % PFA for 10 min, followed by 10 min with 4 % PFA.

For immunofluorescence, the permeabilization step was performed in PBS 0.1 % Triton X100 for 20 min. Cells were then incubated for 1 h in blocking buffer (1 % BSA, 22.52 mg/ml glycine, 0.1 % Tween in PBS) followed by a 2 h incubation at 37 °C with anti-G3BP2, (1:600; Proteintech®, 16276-1-AP). Cells were washed and incubated with secondary antibody (mouse anti-rabbit IgG-CFL 647, [Santa Cruz Biotechnology, INC.; sc-516251]) for 2 h at 37 °C. After washing the cells, GAPDH was stained using anti-GAPDH-AF488 (Sigma-Aldrich, MAB374-AF488, 1:500) as described for G3BP2. DAPI (4',6-Diamidin-2-phenylindol, Dihydrochloride; Thermo Fisher Scientific) staining was performed prior to recording, following the manufacturer protocol. Imaging was performed using Leica SP8 LIGHTNING Confocal Microscope with a 63x oil objective and a resolution of 2048 x 2048. Image analysis was performed using Fiji.

GAPDH PSH/PSO_3H preparation. All GAPDH phase separation experiments were performed using phase separation buffer (25 mM Tris-HCl, 150 mM NaCl, pH 7.4) and microscopy settings as detailed above unless mentioned otherwise. 50 µM of GAPDH was incubated with 500 µM DTT to form GAPDH-SH or 500 µM DTT and 1 mM H_2O_2 for increased time to form GAPDH-SO_3H. Protein was then cleaned 2-times on Micro Bio-Spin™ P-6 gel Columns (BioRad, #732-6221) where buffer was exchanged with phase separation buffer. To assess sulfonylated protein yield, the protein was run on SDS-PAGE, and immunoblotting was performed using anti-GAPDH-SO_3H and GAPDH-AF488. After 30 min treatment, the maximum yield was

reached. For further experiments, 30 min incubation was used to form sulfonylated GAPDH.

GAPDH in-vitro phase separation with PEG. GADPH was labeled with Cyanine 3 NHS ester probe (Lumiprobe, #21020). Following the manufacturer's protocol. Briefly, the protein was incubated with Cy3 NHS ester probe at a ratio of 1:3 (protein : Cyanine3) in 100 mM Sodium Bicarbonate, 50 mM NaCl, pH 8.0. After 1 h incubation at room temperature, the excess of probe was removed using the Micro Bio-Spin™ 6 Columns and the buffer was exchanged with phase separation buffer. To minimize the effect of the Cy3 label on phase separation, the labeled proteins were mixed with non-labeled GAPDH at a 1:9 ratio (labeled : non-labeled).

GAPDH phase separation was first tested by incubating 10 µM protein with an increased concentration of PEG 3,000 (1-10 %) for 5 min. For FRAP experiments, 5 % of PEG3000 and 10 µM of GAPDH were used. Photobleaching was performed after 5 min incubation with PEG3000, and recovery was recorded every second for 10 min.

GAPDH In-vitro phase separation using total RNA extract. Total RNA extract was prepared using $STHdh^{Q7/Q7}$ and the RNeasy Midi Kit (Qiagen, # 75144) following the manufacturer's protocol. RNA concentration was estimated using a nanodrop. Sulfonylated GAPDH was obtained by incubating 10 µM protein with 100 µM DTT and 200 µM H_2O_2 at 37 °C for 30 min. Persulfidated GAPDH was obtained by treating the protein with 100 µM H_2O_2 and 500 µM H_2S for 5 min at 37°C before adding the total RNA extract. Respective controls were carried out using the same DTT (reduced GAPDH) or H_2O_2 (oxidized GAPDH) concentrations. For the FRAP

experiment, 30 ng/µl of total RNA extract was used to trigger phase separation of 10 µM GAPDH. Photobleaching was performed after 5 min of incubation with RNA, and recovery was recorded every second for 10 min. 3 independent preparations, done on separate days and with separate protein batches, were used per thiol modifications.

To assess the dissolution of GAPDH droplets by H_2S, 20 µM GAPDH was incubated for 5 min with RNA in the presence of 100 µM H_2O_2 or 100 µM DTT was added or not. Droplets were recorded at baseline, 1 min, and 2 min after adding H_2S.

To build the phase diagram of reduced and sulfonylated GAPDH, both GAPDH forms were freshly prepared as previously described. GAPDH LLPS was then triggered by adding the indicated total RNA concentration. The solution was then transferred into 15 µ-slide Angiogenesis. All pictures were taken after 5 min incubation using a Leica SP8 LIGHTNING Confocal Microscope with a 63x oil objective in bright field mode.

GAPDH activity in LLPS. For the entire activity assay, total and bulk solutions were prepared in the following way: 10 µM GAPDH was incubated with 30 ng/µl of total RNA in the phase separation buffer. For the total fraction, incubation was performed at RT for 45 min. To prepare the bulk fraction, the protein was incubated for 30 min with RNA and centrifuged for 15 min at 15,000 x g. After centrifugation, equal volumes of total and bulk RNA were taken and incubated with 1 mM NAD^+ for 15 min at RT. 15 mM $NaAsO_2$ and 250 µM glyceraldehyde-3-phosphate were added to start the reaction. NADH formation was recorded using a spectrophotometer at 340 nm. For GAPDH in-solution activity, the experiment was performed by omitting RNA into the mix. The inhibition of GAPDH activity by H_2O_2 was performed by co-incubating total GAPDH LLPS, 100 µM H_2O_2, and 1 mM NAD^+ for 15 min before

recording. The same experiments were carried out in the presence of 2 mM sodium bicarbonate (NaHCO3).

BTD-trap assay. Total and bulk fractions of GAPDH were prepared as previously described. Parts of the fractions were then taken and incubated with 1 mM BTD for 2 min. Before adding H_2O_2, part of the samples was then withdrawn for the control condition (0 min) and incubated with IAM (20 mM) and SDS (2 %), preventing BTD from reacting further. After that, H_2O_2 was added at a final concentration of 10 µM. Part of the sample was taken at 1, 2, and 5 min and directly incubated with catalase, IAM (20 mM), and SDS (2 %) to stop the reaction. Samples were cleaned using Micro Bio-Spin™ 6 Columns before the labeling step. BTD was then labeled with Cy5 using standard click chemistry reaction protocols. Shortly, samples were incubated for 1.5 h at RT in the dark with 150 µM Cyanine5-Azide (Lumiprobe, #D3030), 300 µM Copper (II)-TBTA complex (Lumiprobe, 21050), and 1 mM L-ascorbic acid (Sigma-Aldrich, #A92902). 3 sample parts were mixed with one part of Laemmli (4X) supplemented with 10 % β-Mercaptoethanol and incubated at 95°C for 5 min. An equal amount of samples were then separated by SDS-PAGE. After the run, the gel was incubated in fixation solution (25 % Methanol, 8 % acetic acid in distilled water), and fluorescence was recorded using Amersham Typhoon.

Aggregation assay in LLPS. 20 µM of reduced or sulfonylated GAPDH was incubated with or without RNA (30 ng/µl) for 45 min at RT. The proteins were then mixed with 2 µl of PROTEOSTAT® (Enzo, #ENZ-51023) and 1 x Assay buffer as recommended by the manufacturer's instructions. Samples were placed in a black 96-well plate with clear bottom (Invitrogen™, #M33089), and the plate was sealed. The proteostat fluorescence was measured every 3 min (with 1 min shaking at 300 rpm before measurement) using a CLARIOstar Plus plate reader (BMG LABTECH).

The bottom optic setting was used to excite at 550-/+15 nm and read Proteostat emission at 600 nm.

Fourier Transform Infrared Spectroscopy (FTIR) and secondary structures calculation. The Nicolet 6700 FTIR spectrometer (Thermo Scientific, Carlsbad, CA, USA) was used to record Infrared (IR) spectra of GAPDH samples in attenuated total reflectance (ATR) mode at 1 cm−1 resolution [68]. Spectra of samples containing either reduced, sulfonylated or persulfidated GAPDH (30 μM) were analyzed in OMNIC software. Amide I region arises mainly from C = O stretching vibrations thus is very sensitive to changes in secondary structures. Between 1600–1700 cm−1 each secondary structure contributes to the absorption in a certain wavenumber range. The most prominent change detected in oxidized GAPDH after 8 h was signal increase in the regions attributed to beta-sheets in general, namely 1616–1625 cm−1 assigned to aggregation-prone inter/intramolecular beta-sheet, 1626–1640 cm−1 assigned to intramolecular beta-sheet.

GAPDH aggregation in aging mice brain. Brain tissues were lysed in aggregation lysis buffer (50 mM Tris/HCl pH 8.0, 0.5 M NaCl, 4 mM EDTA, 1 % IGEPAL) supplemented with 1 % Proteinase inhibitors. Frozen tissue was disrupted in lysis buffer using the TissueLyser II and stainless-steel beads. Samples were centrifuged 2-times at 2500 x g for 10 min at 4 °C to remove cell debris. An Equal amount of samples were subjected to ultracentrifugation at 500,000 x g for 15 min at 4°C. Supernatants were kept aside, presenting the soluble fraction. Pellets were washed with 0.5 % SDS in lysis buffer and again ultracentrifuged using the same setting. Pellets were washed again with 1 % SDS in lysis buffer and ultracentrifuged one last time. Pellets were resuspended in 50 mM HEPES pH 7.4, 2 % SDS forming the aggregate fraction. Both supernatant and aggregate fractions were mixed with 1

part of Laemmli (4X) supplemented with 10 % β-Mercaptoethanol and boiled at 95 °C for 15 min. An equal volume of samples was separated on SDS-PAGE and analyzed by immunoblotting using GAPDH-AF488 antibody.

Thermal proteome profiling MEF WT and CSE$^{-/-}$ under H_2O_2 treatment. WT and CSE-/- MEFs were trypsinized and washed 3 times in cold serum-free DMEM. After the last centrifugation, cells were resuspended in 1.2 ml of DMEM supplemented with 10 % FCS and treated for 60 min with 500 µM H_2O_2 on ice. After 60 min, an equal number of cells were aliquoted into different tubes and gently centrifuged. Cell pellets were resuspended in 20 µl serum-free media and heated at 25, 47, or 57 °C for 3 min. Cells were brought back to room temperature for 3 min and lysed with freeze- thaw cycles. Extracted proteins were subjected to ultracentrifugation at 100,000 x g for 20 min at 4 °C. The volume corresponding to 50 µg in the 25 °C-exposed cells was used for all samples. Proteins were subsequently denatured using 3M Gu-HCl for reduction and alkylation steps with 500 µM DTT and 5 mM IAM for 30 min at 37 °C, respectively and then subjected to tryptic-digestion. Peptides were desalted as previously described. Eluates were evaporated to dry and resuspended in 100 mM triethylammonium bicarbonate for TMT labeling. Samples were labeled using the TMTpro™ 16plex Label Reagent Set. Samples were combined, desalted, and dried as previously described and subjected to LC/MS analysis by Orbitrap Eclipse™ Tribrid™ Mass Spectrometer via an EASY-spray (Thermo Fisher Scientific). Data were evaluated using FragPipe software [69] using 10 ppm for precursor mass tolerance, 0.02 Da for fragment mass tolerance, specific tryptic digest, and a maximum of 3 missed cleavages. Carbamidomethylation (+57.021464 Da), N-term acetylation (+42.010565 Da), and methionine oxidation (+15.994915 Da) were added as variable modifications. TMTpro (+304.207146 Da)

was added as fixed modification on K and peptide N-term. PSM, and proteins were filtered at FDR 1 %. TMT quantification was performed at the MS2 level.

Brain Section and Gallya's staining. Brains were extracted and fixed in 4 % paraformaldehyde solution for 24 h at 4 °C, dehydrated in ethanol (30–100 %), and enlightened in xylene. After embedding in Histowax® (Histolab Product AB, Göteborg, Sweden), tissue blocs were sectioned to 5 µm thickness on a rotary microtome (RM 2125RT Leica Microsystems, Wetzlar, Germany). Gallya's silver staining was performed following the manufacturer's protocol (Morphisto, Offenbach am Main, Germany).

3.6. References

1. Gladyshev, V. N. Aging: progressive decline in fitness due to the rising deleteriome adjusted by genetic, environmental, and stochastic processes. Aging Cell vol. 15 594–602 (Blackwell Publishing Ltd, 2016).
2. Paulsen, C. E. & Carroll, K. S. Cysteine-mediated redox signaling: Chemistry, biology, and tools for discovery. Chemical Reviews vol. 113 4633–4679 (2013).
3. Petrovic, D., Kouroussis, E., Vignane, T. & Filipovic, M. R. The Role of Protein Persulfidation in Brain Aging and Neurodegeneration. Front. Aging Neurosci. **13**, 1–12 (2021).
4. Zivanovic, J. et al. Selective Persulfide Detection Reveals Evolutionarily Conserved Antiaging Effects of S-Sulfhydration. Cell Metab. **30**, 1152-1170.e13 (2019).
5. Bithi, N. et al. Dietary restriction transforms the mammalian protein persulfidome in a tissue-specific and cystathionine γ-lyase-dependent manner. Nat. Commun. **12**, (2021).
6. Tyshkovskiy, A. et al. Identification and Application of Gene Expression Signatures Associated with Lifespan Extension. Cell Metab. **30**, 573-593.e8 (2019).
7. Tyshkovskiy, A. et al. Distinct longevity mechanisms across and within species and their association with aging. Cell **186**, 2929-2949.e20 (2023).
8. Giovinazzo, D. et al. Hydrogen sulfide is neuroprotective in Alzheimer's disease by sulfhydrating GSK3β and inhibiting Tau hyperphosphorylation. Proc. Natl. Acad. Sci. U. S. A. **118**, e2017225118 (2021).
9. Paul, B. D. et al. Cystathionine γ-lyase deficiency mediates neurodegeneration in Huntington's disease. Nature **508**, 96–100 (2014).
10. Snijder, P. M. M. et al. Overexpression of cystathionine γ-Lyase suppresses detrimental effects of spinocerebellar ataxia type 3. Mol. Med. **21**, 758–768 (2015).
11. O'Flynn, B. G. & Mittag, T. The role of liquid–liquid phase separation in regulating enzyme activity. Current Opinion in Cell Biology vol. 69 70–79 (2021).
12. Peeples, W. & Rosen, M. K. Mechanistic dissection of increased enzymatic rate in a phase-separated compartment. Nat. Chem. Biol. **17**, 693–702 (2021).
13. Xiao, H. et al. A Quantitative Tissue-Specific Landscape of Protein Redox Regulation during

Aging. Cell **180**, 968-983.e24 (2020).

14. Reisz, J. A. et al. Thiol-blocking electrophiles interfere with labeling and detection of protein sulfenic acids. FEBS J. **280**, 6150–6161 (2013).
15. Dóka et al. Control of protein function through oxidation and reduction of persulfidated states. Sci. Adv. **6**, (2020).
16. Yang, J., Gupta, V., Carroll, K. S. S. & Liebler, D. C. C. Site-specific mapping and quantification of protein S-sulphenylation in cells. Nat. Commun. **5**, 4776 (2014).
17. Fu, L., Liu, K., Ferreira, R. B., Carroll, K. S. & Yang, J. Proteome-Wide Analysis of Cysteine S-Sulfenylation Using a Benzothiazine-Based Probe. Curr. Protoc. Protein Sci. **95**, e76 (2019).
18. He, J.-X. et al. A modification-centric assessment tool for the performance of chemoproteomic probes. Nat. Chem. Biol. **18**, 904–912 (2022).
19. Gupta, V., Yang, J., Liebler, D. C. & Carroll, K. S. Diverse Redoxome Reactivity Profiles of Carbon Nucleophiles. J. Am. Chem. Soc. **139**, 5588–5595 (2017).
20. Kelmer Sacramento, E. et al. Reduced proteasome activity in the aging brain results in ribosome stoichiometry loss and aggregation. Mol. Syst. Biol. **16**, 1–22 (2020).
21. Fu, L. et al. Direct Proteomic Mapping of Cysteine Persulfidation. Antioxidants Redox Signal. **33**, 1061–1076 (2020).
22. Bibli, S. I. et al. Mapping the Endothelial Cell S -Sulfhydrome Highlights the Crucial Role of Integrin Sulfhydration in Vascular Function. Circulation **143**, 935–948 (2021).
23. Hine, C. et al. Endogenous hydrogen sulfide production is essential for dietary restriction benefits. Cell **160**, 132–144 (2015).
24. Ding, J. et al. A metabolome atlas of the aging mouse brain. Nat. Commun. **12**, 6021 (2021).
25. Schaum, N. et al. Ageing hallmarks exhibit organ-specific temporal signatures. Nature **583**, 596–602 (2020).
26. Hernandez, D. G. et al. Integration of GWAS SNPs and tissue specific expression profiling reveal discrete eQTLs for human traits in blood and brain. Neurobiol. Dis. **47**, 20–28 (2012).
27. Lamprianou, S., Chatzopoulou, E., Thomas, J. L., Bouyaing, S. & Harroch, S. A complex between contactin-1 and the protein tyrosine phosphatase PTPRZ controls the development of oligodendrocyte precursor cells. Proc. Natl. Acad. Sci. U. S. A. **108**, 17498–17503 (2011).
28. Storici, P., Capitani, G., Müller, R., Schirmer, T. & Jansonius, J. N. Crystal structure of human ornithine aminotransferase complexed with the highly specific and potent inhibitor 5-fluoromethylornithine. J. Mol. Biol. **285**, 297–309 (1999).
29. Hoelz, A., Nairn, A. C. & Kuriyan, J. Crystal structure of a tetradecameric assembly of the association domain of Ca2+/calmodulin-dependent kinase II. Mol. Cell **11**, 1241–1251 (2003).
30. Huyton, T. et al. The crystal structure of murine p97/VCP at 3.6 Å. J. Struct. Biol. **144**, 337–348 (2003).
31. Gozzi, G. J. et al. Selecting the first chemical molecule inhibitor of HSP110 for colorectal cancer therapy. Cell Death Differ. **27**, 117–129 (2020).
32. Krajewski, W. W. et al. Crystal Structures of Mammalian Glutamine Synthetases Illustrate Substrate-Induced Conformational Changes and Provide Opportunities for Drug and Herbicide Design. J. Mol. Biol. **375**, 217–228 (2008).
33. RCSB PDB - 5MY2: KS-MAT DI-DOMAIN OF MOUSE FAS. https://www.rcsb.org/structure/5MY2.
34. Jumper, J. et al. Highly accurate protein structure prediction with AlphaFold. Nature **596**, 583–589 (2021).
35. Varadi, M. et al. AlphaFold Protein Structure Database in 2024: providing structure coverage for over 214 million protein sequences. Nucleic Acids Res. **52**, D368–D375 (2024).
36. Margreitter, C., Petrov, D. & Zagrovic, B. Vienna-PTM web server: a toolkit for MD simulations of protein post-translational modifications. Nucleic Acids Res. **41**, 422–426 (2013).

37. Li, P. et al. High-throughput and proteome-wide discovery of endogenous biomolecular condensates. Nat. Chem. **16**, 1101–1112 (2024).

38. Milovanovic, D., Wu, Y., Bian, X. & De Camilli, P. A liquid phase of synapsin and lipid vesicles. Science (80-.). **361**, 604–607 (2018).

39. Gupta, V., Paritala, H. & Carroll, K. S. Reactivity, Selectivity, and Stability in Sulfenic Acid Detection: A Comparative Study of Nucleophilic and Electrophilic Probes. Bioconjug. Chem. **27**, 1411–1418 (2016).

40. Filipovic, M. R. R., Zivanovic, J., Alvarez, B. & Banerjee, R. Chemical Biology of H2S Signaling through Persulfidation. Chemical Reviews vol. 118 1253–1337 (2018).

41. Kato, M. et al. Redox State Controls Phase Separation of the Yeast Ataxin-2 Protein via Reversible Oxidation of Its Methionine-Rich Low-Complexity Domain. Cell **177**, 711-721.e8 (2019).

42. Abe, K. & Kimura, H. The possible role of hydrogen sulfide as an endogenous neuromodulator. J. Neurosci. **16**, 1066–1071 (1996).

43. Kamat, P. K., Kalani, A. & Tyagi, N. Role of hydrogen sulfide in brain synaptic remodeling. Methods Enzymol. **555**, 207–229 (2015).

44. Ali, R., Pal, H. A., Hameed, R., Nazir, A. & Verma, S. Controlled release of hydrogen sulfide significantly reduces ROS stress and increases dopamine levels in transgenic: C. elegans. Chem. Commun. **55**, 10142–10145 (2019).

45. Mustafa, A. K. et al. HS signals through protein S-Sulfhydration. Sci. Signal. **2**, ra72–ra72 (2009).

46. Wang, Q. et al. Proteomic analysis of neurofibrillary tangles in Alzheimer disease identifies GAPDH as a detergent-insoluble paired helical filament tau binding protein. FASEB J. **19**, 1–12 (2005).

47. Lazarev, V. F. et al. Extracellular gapdh promotes alzheimer disease progression by enhancing amyloid-β aggregation and cytotoxicity. Aging Dis. **12**, 1223–1237 (2021).

48. Yang, P. et al. G3BP1 Is a Tunable Switch that Triggers Phase Separation to Assemble Stress Granules. Cell **181**, 325-345.e28 (2020).

49. Guillén-Boixet, J. et al. RNA-Induced Conformational Switching and Clustering of G3BP Drive Stress Granule Assembly by Condensation. Cell **181**, 346-361.e17 (2020).

50. Dagnell, M. et al. Bicarbonate is essential for protein-tyrosine phosphatase 1B (PTP1B) oxidation and cellular signaling through EGF-triggered phosphorylation cascades. Journal of Biological Chemistry vol. 294 12330–12338 (2019).

51. Patel, B. H., Percivalle, C., Ritson, D. J., Duffy, C. D. & Sutherland, J. D. Common origins of RNA, protein and lipid precursors in a cyanosulfidic protometabolism. Nat. Chem. **7**, 301–307 (2015).

52. Foden, C. S. et al. Prebiotic synthesis of cysteine peptides that catalyze peptide ligation in neutral water. Science (80-.). **370**, 865–869 (2020).

53. Fox, S. W. W. The evolutionary significance of phase-separated microsystems. Orig. Life **7**, 49–68 (1976).

54. Spruijt, E. Open questions on liquid–liquid phase separation. Communications Chemistry vol. 6 1–5 (2023).

55. Principles, P. NASA Public Access. **57**, 2509–2519 (2020).

56. Jahn, R., Cafiso, D. C. & Tamm, L. K. Mechanisms of SNARE proteins in membrane fusion. Nat. Rev. Mol. Cell Biol. (2023) doi:10.1038/s41580-023-00668-x.

57. Hoffmann, C. et al. Synapsin condensation controls synaptic vesicle sequestering and dynamics. Nat. Commun. **14**, 6730 (2023).

58. Balaban, R. S., Nemoto, S. & Finkel, T. Mitochondria, oxidants, and aging. Cell vol. 120 483–495 (2005).

59. Van Raamsdonk, J. M. & Hekimi, S. Reactive oxygen species and aging in caenorhabditis

elegans: Causal or casual relationship? Antioxidants and Redox Signaling vol. 13 1911–1953 (2010).

60. Knoefler, D. et al. Quantitative In Vivo Redox Sensors Uncover Oxidative Stress as an Early Event in Life. Mol. Cell **47**, 767–776 (2012).
61. Bazopoulou, D. et al. Developmental ROS individualizes organismal stress resistance and lifespan. Nature **576**, 301–305 (2019).
62. Redman, L. M. et al. Metabolic Slowing and Reduced Oxidative Damage with Sustained Caloric Restriction Support the Rate of Living and Oxidative Damage Theories of Aging. Cell Metab. **27**, 805-815.e4 (2018).
63. Yang, G. et al. H2S as a physiologic vasorelaxant: Hypertension in mice with deletion of cystathionine γ-lyase. Science (80-.). **322**, 587–590 (2008).
64. Sbodio, J. I., Snyder, S. H. & Paul, B. D. Transcriptional control of amino acid homeostasis is disrupted in Huntington's disease. Proc. Natl. Acad. Sci. U. S. A. **113**, 8843–8848 (2016).
65. Karpievitch, Y. V. et al. Normalization of peak intensities in bottom-up MS-based proteomics using singular value decomposition. Bioinformatics **25**, 2573–2580 (2009).
66. Shevchenko, A., Tomas, H., Havliš, J., Olsen, J. V. & Mann, M. In-gel digestion for mass spectrometric characterization of proteins and proteomes. Nat. Protoc. **1**, 2856–2860 (2007).
67. Hoffmann, C. et al. Synapsin Condensates Recruit alpha-Synuclein. J. Mol. Biol. **433**, 166961 (2021).
68. Marković, S., Andrejević, N. S., Milošević, J. & Polović, N. n. Structural Transitions of Papain-like Cysteine Proteases: Implications for Sensor Development. Biomimetics **8**, (2023).
69. Kong, A. T., Leprevost, F. V., Avtonomov, D. M., Mellacheruvu, D. & Nesvizhskii, A. I. MSFragger: Ultrafast and comprehensive peptide identification in mass spectrometry-based proteomics. Nat. Methods **14**, 513–520 (2017).

Acknowledgments: We thank Ingo Feldman and Susanne Krois (ISAS e.V.) for their technical assistance with MS and the Advanced Medical Bioimaging Core Facility at Charité for the support.

Funding: This study was funded by European Research Council (ERC) under the European Union's Horizon 2020 research and innovation programme (Grant Agreement No. 864921). The authors also acknowledge support from the start-up funds from DZNE, the grants from the German Research Foundation (SFB 1286/B10 and MI 2104), and the Human Frontiers Science Organization (RGEC32/2023) (to DM), the Hellenic Foundation for Research and Innovation (HFRI-FM17-886) (to AP), the Medical Research Council UK (MC_UU_00028/4 to MPM and MC_UU_00028/5 for JP) and by a Wellcome Trust Investigator award (220257/Z/20/Z) (to MPM), and Ministry of Science, Technological Development and Innovation of Republic of Serbia, Contract number: 451-03-47/2023-01/200168 (to NP). CH is supported by a fellowship of the Innovative Minds Program of the German Dementia Association; HW is supported by the Oversea Study Program of Guangzhou Elite Project (SJ2020/2/JY202025).

Competing interests: Authors declare that they have no competing interests.

Data and materials availability: All raw data that are not included in this study will be available on Mendeley repository. All proteomic data are available through PRIDE under code numbers: **PXD045785** (Sulfenylome and total proteome); **PXD045806** (Persulfidation and Sulfonylation); **PXD045820** (TPP of WT and $CSE^{-/-}$ MEFs upon H_2O_2 stress).

4. PSOH/PSSH redox switch of G3BP2 controls dynamics of stress granule formation and dissolution

Thibaut Vignane[1], Martín Hugo[1†], Christian Hoffmann[2], Suyuan Chen[1], Jan Lj. Miljkovic[3], Jordan L Morris[3], Suvagata Roy Chowdhury[3], Julien Prudent[3], Michael P. Murphy[3,4], Dragomir Milovanovic[2], Milos R. Filipovic[1*]

[1]Leibniz Institute for Analytical Sciences, ISAS, e.V., Dortmund, Germany

[2]Laboratory of Molecular Neuroscience, German Center for Neurodegenerative Diseases, Berlin, Germany

[3]MRC Mitochondrial Biology Unit, University of Cambridge, Keith Peters Building, CB2 0XY, UK

[4]Department of Medicine, University of Cambridge, Cambridge, CB2 0QQ, United Kingdom

[†]Current address: Department of Medicine, Health and Medical University, 14471 Potsdam, Germany

*Corresponding author. Email: milos.filipovic@isas.de

In preparation

Author contributions

Milos R Filipovic and Thibaut Vignane conceptualized the study. Thibaut Vignane performed all the experiments, analyzed the data, prepared the figures. Milos R Filipovic and Thibaut Vignane wrote the manuscript. Drago Milovanovic provided LLPS expertise analyzed and interpreted data. Christian Hoffmann helped with the in-vitro phase separation of G3BP2 and data interpretation. Jan Lj. Miljkovic, Jordan L Morris, Suvagata Roy Chowdhury, Julien Prudent, Michael P. Murphy helped with G3BP2 real-time microscopy measurements and data interpretation. Suyuan Chen synthesized BTD. All authors edited the paper with input from the other authors.

4.1. Abstract

Stress granules (SGs) are dynamic cellular structures that form in response to various stressors, including oxidative stress, and play a critical role in regulating processes such as translation inhibition and signaling pathway modulation. The RNA-binding proteins G3BP1 and G3BP2 are central to SG assembly, but the specific post-translational modifications (PTMs) that regulate their function remain incompletely understood. In this study, we investigate the role of cysteine 73 (C73) in G3BP2, a highly conserved residue, in sensing oxidative stress and modulating SG dynamics. We demonstrate that C73 undergoes sulfenylation (PSOH) and persulfidation (PSSH), two redox-sensitive PTMs, which differentially regulate the assembly and disassembly of SGs. Using in vitro phase separation assays, we show that sulfenylation of G3BP2 promotes the formation of liquid-like condensates, facilitating SG assembly. In contrast, persulfidation enhances SG disassembly during the recovery phase, suggesting a mechanism by which cells resolve SGs after stress subsides. Moreover, cells expressing a G3BP2 C73S mutant, which cannot undergo these modifications, display persistent SGs, indicating impaired SG disassembly. Our findings provide new insights into the molecular mechanisms controlling SG dynamics and suggest that targeting these PTMs could offer novel therapeutic strategies for diseases associated with dysregulated SGs, such as neurodegenerative disorders.

4.2. Introduction

Over the past decade, biomolecular condensates have emerged as an essential biophysical process in regulating biological function[1]. These membraneless protein structures are due to multivalent interactions that could be protein-protein or protein-nucleic acid interactions[2]. Notably, condensates that form upon interaction with DNA or RNA are often associated with transcription, RNA processing and protein translation regulation. In the nucleus, Cajal bodies and paraspeckles participate in snRNPS processing[3,4] and long non-coding RNA regulation[5], respectively. In the cytoplasm, P-bodies are responsible for miRNA/siRNA degradation and translation regulation[6,7]. These biomolecular condensates are usually present under normal physiological conditions.

Conversely, stress granules (SG) are mainly involved in the response to cellular stress. Stress granule formation can be induced by multiple stressors such as heat shock, proteasome inhibition, or oxidative stress[8,9] and are mainly involved in the regulation of translation[10,11] and modulation of different signaling pathways[12]. Notably, stress granule formation is primarily driven by two RNA binding proteins, G3BP1 and G3BP2[13], characterized by one structured domain responsible for dimerization and multiple intrinsically disordered domains (IDRs) responsible for their phase separation ability[14]. These two scaffold proteins are responsible for forming and dissolving stress granules, and their composition changes over time[15]. Therefore, time-dependent regulation of their phase separation is essential to maintain cellular homeostasis during stress. Failure to regulate stress granule dynamics has already been linked to multiple

degenerative diseases such as amyotrophic lateral sclerosis (ALS)[16] or neurodegenerative diseases[17].

For many biological processes, one way to quickly regulate the function of proteins in the cell is through posttranslational modification (PTM) of proteins. Similarly, PTM modulates the phase separation of protein by modifying their structure or their interaction with other proteins or nucleic acids[18,19]. While the PTMs impact on G3BP2 phase separation remains understudied, the phase separation of G3BP1 and, subsequently, the stress granule formation is shown to be affected by acetylation, methylation, and phosphorylation[20]. However, these modifications are mainly located along the different IDR, resulting in an on/off system for RNA binding and the formation of condensates. We speculated that PTM in the NTF2L domain may be used for fine tuning of G3BP condensates.

Interestingly, both G3BP1 and 2 contain only one cysteine in this domain. Therefore, we wondered whether cysteine modifications such as sylfenylation (PSOH) or persulfidation (PSSH) could impact stress granule formation by modulating the G3BPs phase separation. Tissue-specific expression analysis of both G3BPs revealed that G3BP2 is predominantly expressed in the brain[21], one of the organs the most susceptible to oxidative stress[22]. Therefore, we used G3BP2 to study the effect of PSOH and PSSH on its phase separation properties and its ability to form and dissolve stress granules upon stress granule formation.

4.3. Results

We first observed that G3BP2 contains only one cysteine (C73) located within the nuclear transport factor 2-like (NTF2L; Figure 4.1A). This domain is one of the rare, structured domains present in the protein and is usually responsible for the dimerization of the protein.[14] Interestingly, the cysteine is placed at the junction between the alpha helix and the beta-sheet domain, and its modification may modify the protein structure. In addition, protein alignment between G3BP2 orthologs suggests that this cysteine appeared early in evolution and has been conserved in higher eukaryotes (Figure 4.1B). Finally, arsenite is one of the most common drugs used for SGs induction and was proposed to induce SG through ROS production. Therefore, we wonder whether this unique cysteine could be critical in regulating G3BP2 phase separation and stress granule formation.

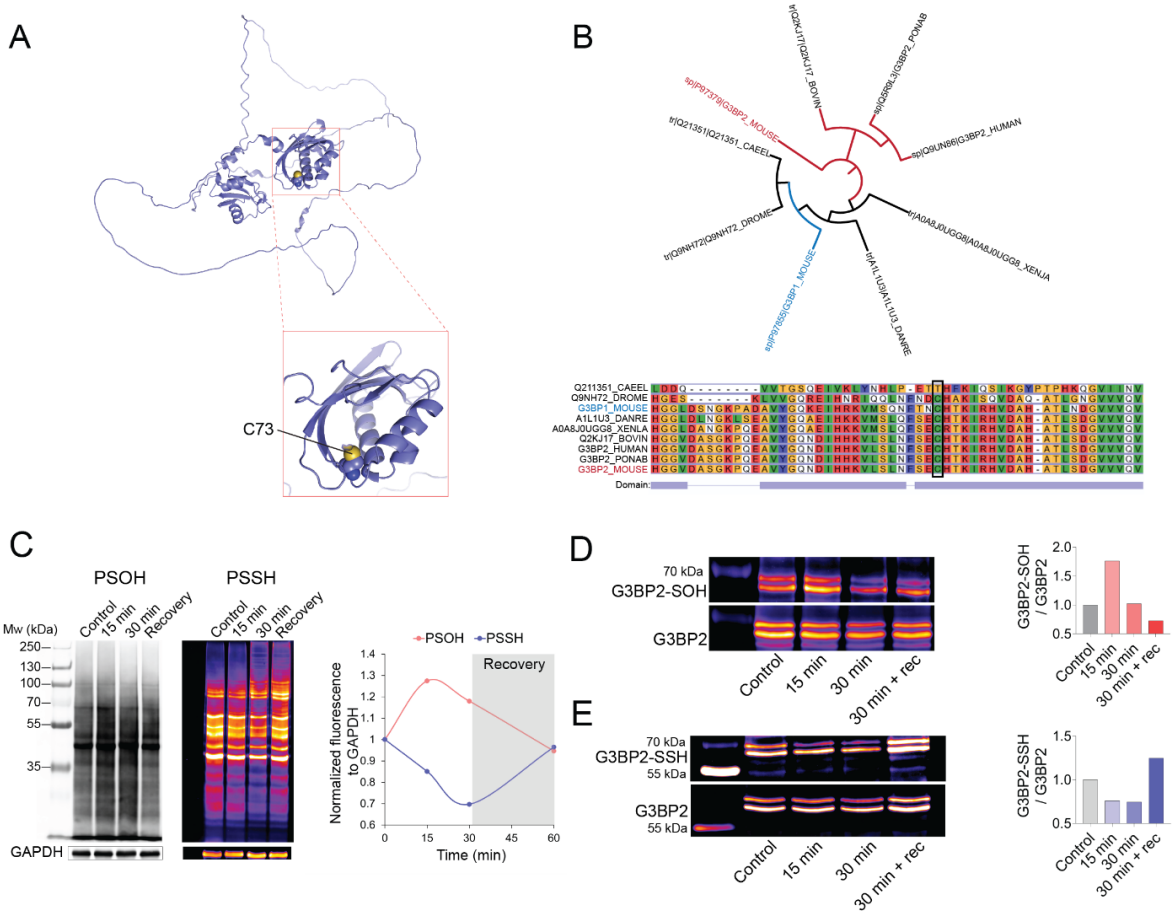


Figure 4.1. The evolutionary conserved cysteine 73 of G3BP2 is sulfenylated upon sodium arsenite stress and persulfidated during stress recovery. (**A**) G3BP2 Alphafold predicted structure (AF-P97379-F1-model_v4.pdb). Cysteine 73 is unique and present in the NTF2-like domain of the protein. (**B**) Circular phylogenetic cladogram (upper panel) built using G3BP2 sequences alignment (lower panel) from a range of species: Mus musculus (MOUSE), Bos taurus (BOVIN), Pongo abelii (PONAB), Homo sapiens (Human), Xenopus laevis (XENA), Danio rerio (DANRE), Drosophila melanogaster (DROME), and Caenorhabditis elegans (CAEEL). For contextual comparison, G3BP1 from Mus musculus is also included. The conserved cysteine residue, notably positioned at C73 in the mouse G3BP2 sequence, is highlighted with a black rectangle. Conservation of this cysteine across species underlines its potentially important role in the protein functions, such as its phase separation potential. (**C**) Global PSOH and PSSH changes in MEF cells treated with 500 µM $NaAsO_2$ for 15 and 30 min. After 30 min $NaAsO_2$ was removed, and cells were allowed to recover for 30 min (recovery). BTD-labelling was used for PSOH, and the dimedone-switch method with DCP-Bio1 was used for PSSH. (**D-E**) Arsenite stress (500 µM)-induced changes in G3BP2 sulfenylation (D) and persulfidation (E).

To test this hypothesis, we first monitored time resolved changes in the global sulfenylation and persulfidation upon arsenite treatment in mouse embryonic fibroblast (MEF) (Figure 4.1C). An increase in sulfenylation correlated well with the time cells were exposed to arsenite. In the recovery phase (when the stressor was removed), these changes were reduced back to starting levels (Figure 4.1C). Conversely, persulfidation levels decreased upon arsenite stress, reaching its minimum when sulfenylation was at its maximum. However, persulfidation then significantly increased during recovery phase (Figure 4.1C). Reflecting those global changes, the sulfenylation and persulfidation of G3BP2 followed the same trends upon treatment and recovery (Figure 4.1D,E). Therefore, we hypothesized that sulfenylation could trigger G3BP2 phase separation while persulfidation may be essential for dissolving G3BP2 condensates during recovery time.

To address the potential effects of cysteine oxidation on G3BP2 phase separation, we first tested PSOH and PSO_3H forms of the protein. Upon addition of RNA, droplet formation was observed in both cases, with G3BP2 PSO_3H forming significantly smaller condensates (Figure 4.2A) that showed slower FRAP recovery and lower % recovery ($t_{1/2}$ = 55.0 s *vs.* 44.5 s, 42 % decrease; Figure 4.2B). Notably, the calculated roundness of the PSO_3H droplets showed a significant decrease when compared to the reduced form of the protein. Interestingly, granules formed by G3BP2 PSOH showed faster kinetics and % of FRAP recovery (37.6 s *vs*. 44.5 s, 25 % increase; Figure 4.2B), suggesting that sulfenylation could increase the diffusion rate of G3BP2.

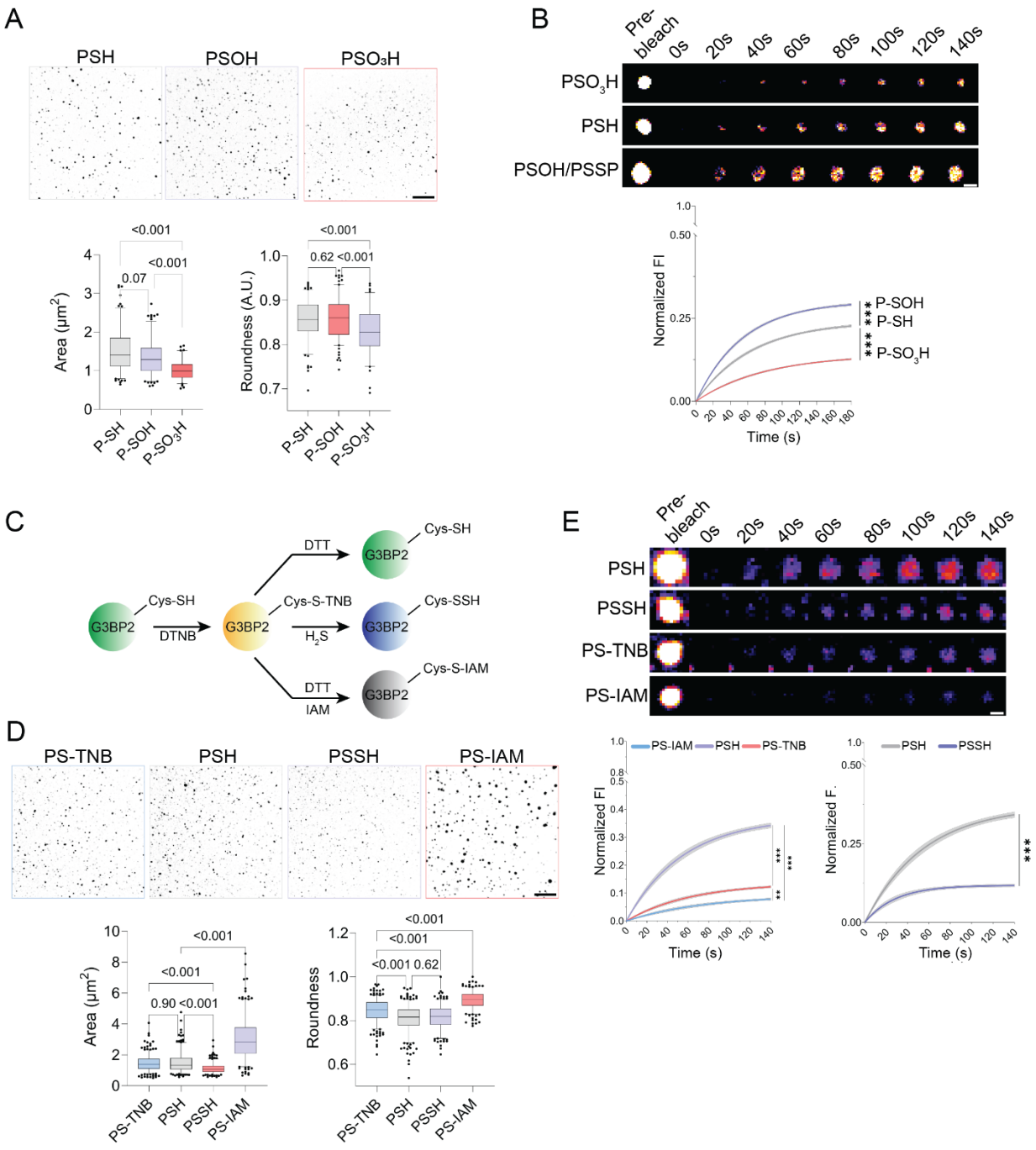


Figure 4.2. In-vitro G3BP2 cysteine modification modulates its phase separation. (**A**) Phase separation of G3BP2 with different cysteine PTMs. Prior to phase separation induction, G3BP2 (10 μM) underwent treatment with DTT (100 μM; PSH), H_2O_2 (200 μM; PSOH), or a combination of DTT and H_2O_2 (100 μM and 200 μM respectively, P-SO_3H), for 30 min at 37 °C. LLPS was induced using 50 ng/μl of total RNA extract, and images were taken 5 min after induction. Quantification of droplet area is shown below (n ≥ 2 independent preparation, one-way

ANOVA, Tukey's HSD Test for multiple comparisons), Scale bar = 20 μm. (**B**) FRAP images and quantification of the G3BP2-Cy3 condensates formed using sulfenylated (PSOH) and sulfonylated (PSO_3H) G3BP2. Means are shown as lines and standard error as shades of grey (n ≥ 2 independent preparation, Two-way ANOVA, Sidak posthoc test, ***: p-value <0.001). (**C**) Schematic illustration of G3BP2 treatment used to prepare various cysteine modifications: PS-TNB, PSSH, PSH, and PS-IAM. DTNB: 5,5′-dithiobis(2-nitrobenzoic acid). IAM: iodoacetamide. (**D**) Representative microscopy images for G3BP2-Cy3 condensates (10 μM) formed under different cysteine modifications prepared as shown in (C). LLPS was induced using 50 ng/μl of total RNA extract. Quantification of droplet area is shown below (n = 3 independent preparation, one-way ANOVA, Tukey's HSD Test for multiple comparisons). Scale bar = 20 μm. (**E**) FRAP images and (D) quantification of the G3BP2-Cy3 condensates formed using PSTNB, PSSH, PSH, and PS-IAM G3BP2. Means are shown as lines and standard error as a shade of grey (n = 3 independent preparation, Two-way ANOVA, Sidak posthoc test, ***: p-value<0.001, **: p-value<0.01).).

We then evaluated the effect of PSSH on G3BP2 by applying a more preparative approach for PSSH generation since this protein contains only one cysteine (Figure 4.2C). A mixed disulfide with thionitrobenzoic acid (TNB) was first generated with Ellman's reagent and protein then either reduced with DTT to form fully reduced form or treated with H_2S to form persulfide (Figure 4.2C). Both TNB-modified and persulfidated protein made condensates which showed reduced FRAP recovery. However, G3BP2 PSSH showed smaller condensates but faster kinetics of FRAP recovery (19.6 s) (Figure 4.2D,E). Interestingly, incubation of G3BP2 with thiol-blocking reagent iodoacetamide resulted in much bigger condensates, but modification almost completely blunted their FRAP recovery (Figure 4.2D,E).). These data confirmed the important role of C73 in modulating G3BP2 phase separation, but they also highlighted complex *in vitro* biophysical behaviours of G3BP2 that harbour different cysteine modifications.

Therefore, to understand the biological role of G3BP2 C73, we focused on G3BP2 SG formation in cells. We first expressed GFP-tagged wild-type or C73S mutant G3BP2 in MEFs and monitored their response to arsenite-induced stress. Cells expressing C73S mutant G3BP2 clearly showed SGs even in the absence of the stressor (Figure 4.3A, External database movie S4.1). However, their number per cell doubled upon arsenite treatment (Figure 4.3B). The condensate size in the mutant was also altered, with droplets being significantly larger when compared to the WT G3BP2 (Figure 4.3B). In addition, the number of SG reached a plateau only after 8 min of stress. Cells expressing wild-type G3BP2 showed no SGs prior to arsenite exposure and showed a time-dependent increase in granule average number and size once cells were exposed to arsenite (Figure 4.3A,B). We then concluded that G3BP2 C73 is essential for modulating the protein's phase separation upon stress.

To apprehend the possible role of H_2S in stress granule formation, we also expressed the GFP-G3BP2 protein MEF lacking CSE and monitored their dynamic. Although $CSE^{-/-}$ MEFs did not show extensive stress granules formation prior to stress, G3BP2 condensates were formed faster when cells were exposed to arsenite (Figure 4.3A,B). After 15 min, $CSE^{-/-}$ MEF cells harboured ~3 times more stress granules than the WT MEFs (Figure 4.3B), suggesting an impairment in the fusion process of nascent condensates. However, the size of these condensates did not differ from WT MEF (Figure 4.3B).

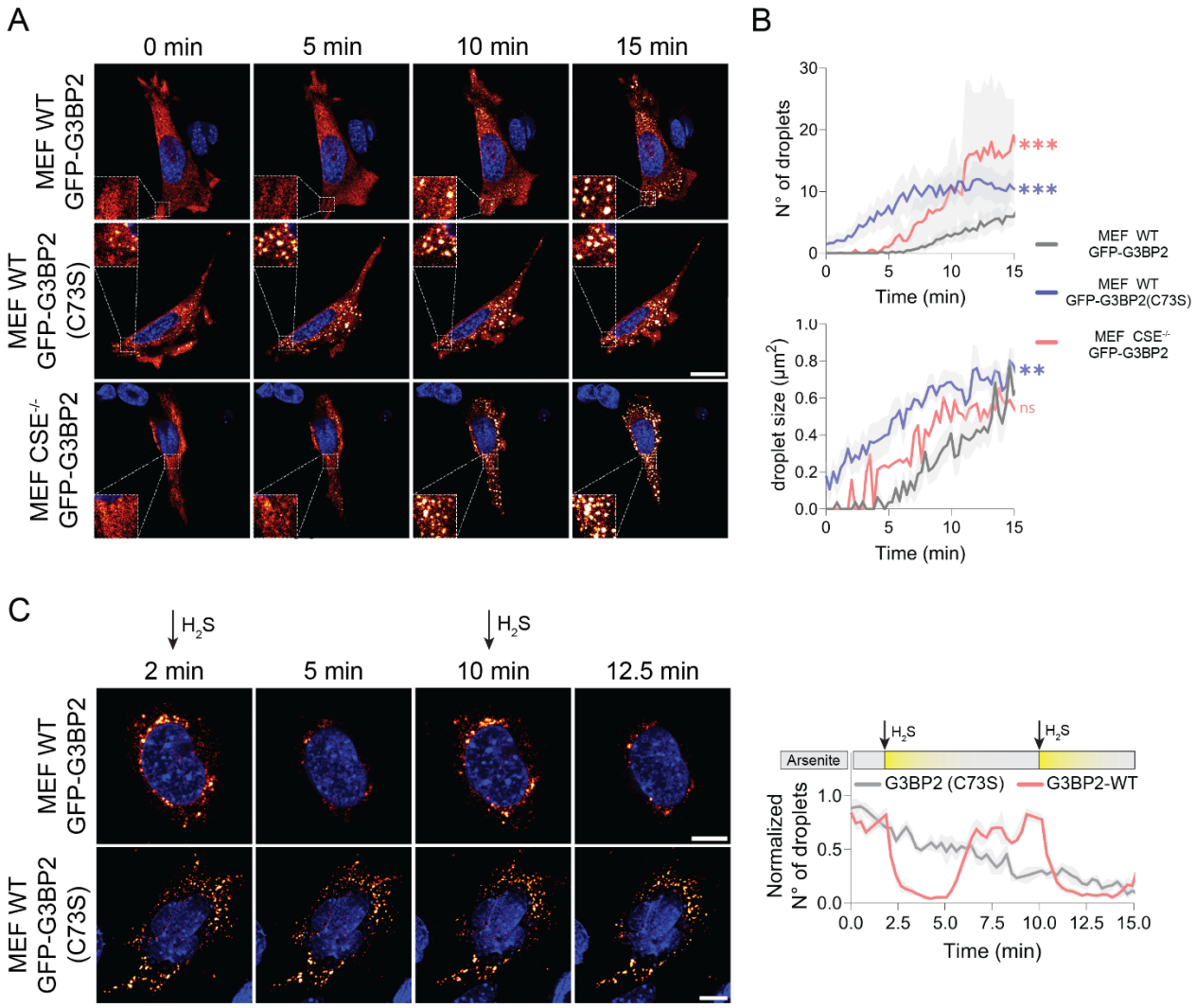


Figure 4.3. H_2S affect stress granule formation dynamic in a G3BP2 C73 dependent manner. (**A**) Arsenite stress (500 µM) induced G3BP2 condensate formation in WT mouse embryonic fibroblasts (MEF) expressing either the wild type (WT) or the C73S mutant of GFP-G3BP2 or $CSE^{-/-}$ MEF expressing the WT GFP-G3BP2 (representative confocal images of the real-time recording of at least 3 biological replicates). Scale bar = 20 µm. (**B**) Quantification of the number (top graph) and size (bottom graph) of the condensates over time formed upon arsenite treatment in WT MEF cells expressing either the wild type (WT) or the C73S mutant of GFP-G3BP2 or $CSE^{-/-}$ MEF expressing the WT GFP-G3BP2. Means are shown as lines and standard error as a shade of grey (at least 3 biological replicates). (**C**) Confocal live cell monitoring of G3BP2-GFP condensate dissolution upon addition of H_2S in WT MEF expressing GFP-G3BP2 WT or GFP-G3BP2 (C73S). Na_2S (100 µM) was added 15 min after SG formation was initiated with arsenite (500 µM). The number of stress granules was measured over time (4 biological replicates). Scale bar = 10 µm.

Since G3BP2 PSSH increases upon recovery after arsenite treatment and the lack of H_2S induces a faster and more robust response to arsenite, we hypothesized that H_2S-induced persulfidation of G3BP2 may induce the dispersion of stress granules. Indeed, when H_2S was added to the cells stressed with arsenite, immediate dissolution of SGs could be recorded in real-time (Figure 4.3C, External database movie S4.2). Due to the constant presence of a stressor, fast H_2S consumption kinetics by the cells[23] and its disappearance in a gas phase[24], SG would reform in time. However, total dissolution could be repeated by adding another bolus of H_2S (Figure 4.3C, External database movie S4.2). When H_2S was applied to the condensates formed by GFP-G3BP2 C73S mutant, no dissolution of stress granules was observed, supporting the role of C73 persulfidation in SG dissolution (Figure 4.3C). The reversible nature of this process suggested that endogenously produced H_2S might play an important role in regulating SG formation/duration.

We compared SG formation in wild type vs. $CSE^{-/-}$ cells to test that. $CSE^{-/-}$ cells show lower PSSH levels and higher PSOH and PSO_xH levels.[25] When treated with arsenite, $CSE^{-/-}$ cells formed a higher number of SGs per cell, albeit their size was significantly smaller (Figure 4.4A), which agrees with PSOH increasing the rate of condensate formation. More interestingly, while wild-type cells almost fully recovered by dissolving their SGs after this stressor was removed, SGs in $CSE^{-/-}$ cells continued to increase their size (Figure 4.4A). Time-resolved SG formation also showed that $CSE^{-/-}$ cells form G3BP2 SGs faster (Figure 4.4A), in agreement with the observation that PSOH stimulates their formation (Figure 4.4A).

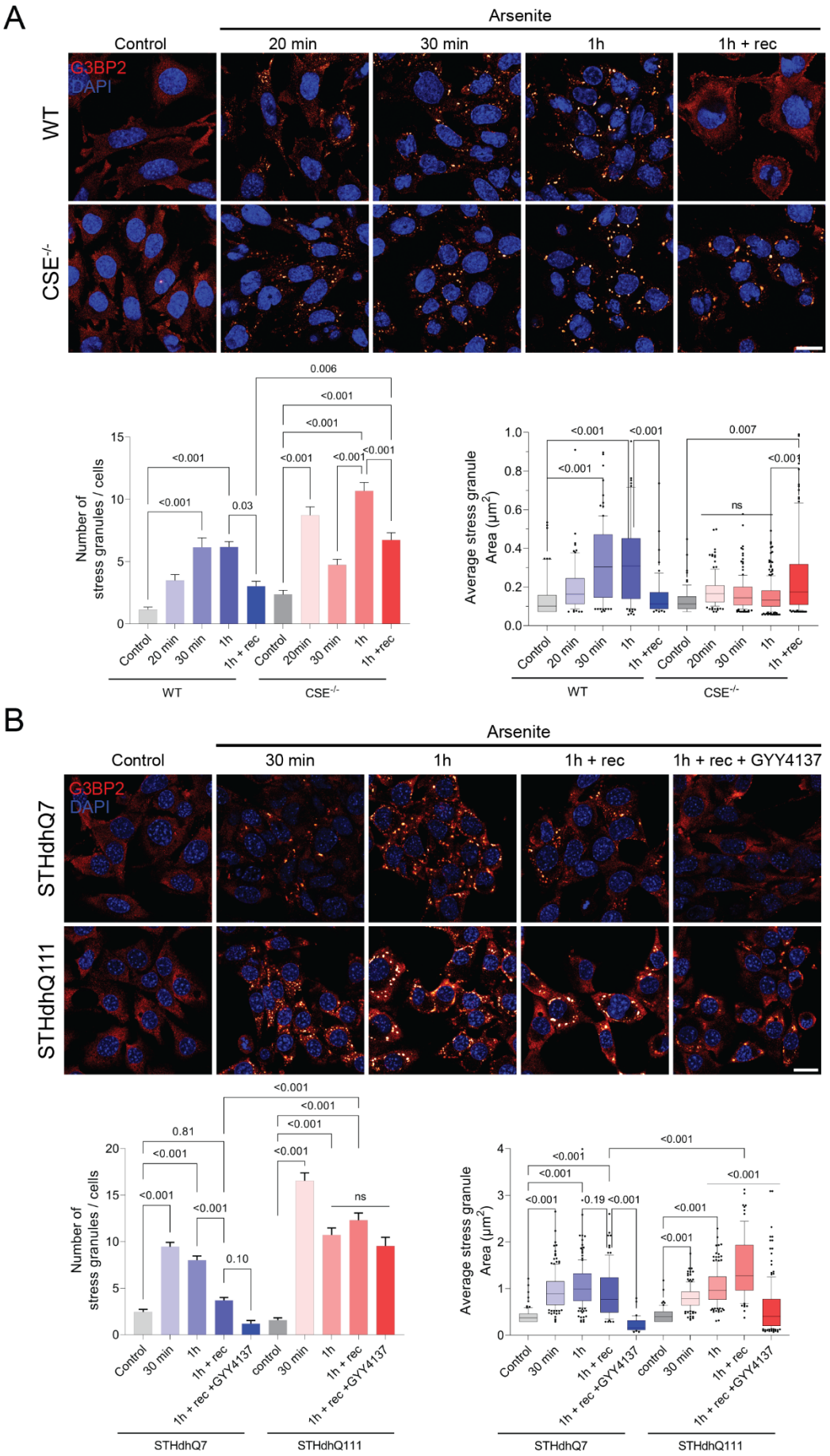

A
Arsenite
Control
20 min
30 min
1h
1h + rec
G3BP2
DAPI
WT
CSE-/-
Number of stress granules / cells
Average stress granule Area (µm2)
Control
20 min
30 min
1h
1h +rec
WT
CSE-/-
B
Arsenite
Control
30 min
1h
1h + rec
1h + rec + GYY4137
STHdhQ7
STHdhQ111
1h + rec +GYY4137
STHdhQ7
STHdhQ111

Figure 4.4. CSE-dependent H_2S production is necessary to dissolve arsenite-induced stress granules upon recovery. (**A-B**) Time-resolved G3BP2 condensates formation in WT and $CSE^{-/-}$ MEF (A) and STHdhQ7 and STHdhQ111 cells (B). Representative confocal images of G3BP2 (dynamic red) immunocytochemical staining upon 500 μM $NaAsO_2$ stress over time. The recovery time (rec) for both cell lines was 1h after washing the sodium arsenite with normal media. During recovery, STHdhQ7 and STHdhQ111 cells were also treated with 200 μM of GYY4137. Scale bar = 20 μm. Respective quantification of the number of stress granules per cell and size of G3BP2 condensates over time are displayed below the microscopy images (n ≥ 2; >100 cells quantified, One-way ANOVA, Tukey's HSD Test for multiple comparisons, ns: non-significant).

We also tested this on another cell type, striatal neurons (STHdh). STHdh cells originating from Huntington's disease ($STHdh^{Q111/Q111}$) mice are known to have diminished CSE and PSSH levels when compared to the STHdh cells from wild-type animals ($STHdh^{Q7/Q7}$)[25]. Arsenite stress resulted in time-dependent increase of SG number and size in $STHdh^{Q7/Q7}$ cells, with recovery reducing this number (Figure 4.4B). Addition of H_2S donor GYY4137 during the recovery almost completely dissolved the remaining SG (Figure 4.4B). $STHdh^{Q111/Q111}$ cells, on the other hand, similarly to $CSE^{-/-}$ MEF cells, showed stronger and faster response to sodium arsenite. Even after 1 h of full recovery from the stressor, cells continued to form bigger SGs. However, this was mainly prevented by the addition of GYY4137 in the recovery phase (Figure 4.4B). These results confirmed the importance of endogenous H_2S production in maintaining the normal SG kinetics but also highlighted the potential of exogenous H_2S donors as therapeutics that could be used to help to dissolve those condensates in pathological conditions.

4.4. Discussion

Upon stress, SG formation is crucial for regulating various cellular processes such as translation inhibition[26] and modulation of TORC signaling pathways [12,27]. The context-dependent nature of SG composition, influenced by the specific stressor, highlights the intricate regulation required for cellular adaptation[9]. The RNA-binding proteins G3BP1 and 2 are essential for forming stress granules in mammalian cells[13]. Therefore, modulation of G3BP1 and/or 2 through posttranslational modification is important mechanism for the cells to provide reversible stress-dependent response. Induction of stress granules through H_2O_2 treatment was shown to be independent of the phosphorylation of eIF2α S51[8], considered as one of the main drivers of stress granule assembly[28]. Notably, both G3BP1 and 2 both contain one sole cysteine located at the NTF2 domain, one of the only structured domains of the proteins. In our previous study of brain aging sulfenylome and persulfidome, we observed an age-dependent increase of G3BP2 sulfenylation and a decrease in persulfidation, an effect even more pronounced in brain samples of CSE knockout mice. It is worth mentioning that the brain is one of the most susceptible organs to oxidative stress[22], and G3BP2 is the isoform most expressed in the brain[21].

Initial observation that C73A mutant of G3BP2 leads to spontaneous SG formation in cells, already suggested that C73 plays a role in modulating SG dynamics and is evolutionarily chosen. This is further corroborated by our observation that sulfenylated G3BP2 exhibits faster and more efficient FRAP recovery, which means that this modification might be the trigger for SG formation upon oxidative stress. In our study we demonstrate that arsenite-induced SG formation does happen due to the global thiol

oxidation. In line with our previous work suggesting that waves of sulfenylation are always followed by the waves of protein persulfidation[25], we now report that arsenite stress too occurs in those two ways, where exposure to stressor leads to the peak of sulfenylation, while the removal of stressor during the recovery phase leads to the peak of persulfidation. Persulfidation of G3BP2 leads to the dissolution of SG. Redox switching from PSOH to PSSH thus plays the role in regulating the dynamics of SG formation and dissolution.

This is best documented in our observations that $CSE^{-/-}$ MEFs or $STHdh^{Q111/Q111}$ could not resolve stress granules even after the stressor is removed. This is in agreement that sulfenylated form of G3BP2 still undergoes LLPS but forming smaller and more compact droplets, that are unable to recover after FRAP. During aging when ROS formation increases and H_2S formation decreases, the dissolution of SG will be impaired making a transition to gel and aggregated state much easier. Indeed, our previous work suggests that GAPDH could enter those SG undergoing sulfonylation and aggregation.

The use of H_2S donor GYY4137 managed to completely dissolve the SG in MEF cells and to significantly reduce the number of aberrant SG in $STHdh^{Q111/Q111}$ cells suggesting that the drug development of H_2S donor might be a promising venue to explore, particularly in preventing neurodegenerative diseases.

To conclude, our study unraveled the importance of sulfenylation and persulfidation in the formation and dissolution of stress granules. Here, we demonstrated that G3BP2 senses oxidative stress through its C73 sulfenylation, which induces stress

granule assembly. More importantly, the same cysteine also serves as a signal for SG disassembly through its persulfidation. However, it remains unclear whether the function of these H_2O_2-induced stress granules is different from that of other stressors. Indeed, it has been proposed that different stress-induced different SG composition[9]. Posttranslational modification of protein modulates the phase separation of the scaffold protein, such as G3BPs and their interaction with other client proteins. Therefore, further investigation on the H_2O_2-induced stress granule composition would be necessary to understand how cysteine modification modulates stress granule composition and if this is responsible for cellular response specific to oxidative stress.

4.5. Material and methods

Cell culture. $CSE^{-/-}$ mouse embryonic fibroblasts (MEF) are a kind gift from Professor Bindu Paul (Johns Hopkins University). MEFs were generated from $CSE^{+/+}$ and $CSE^{-/-}$ mice and immortalized using SV40T antigen. MEF cells were cultured in DMEM, supplemented with 2 mM L-glutamine, 1 % penicillin-streptomycin, and 10 % fetal bovine serum at 37 °C and 5 % CO_2. The striatal progenitor cell line $STHdh^{Q7/Q7}$, expressing wild-type huntingtin, and $STHdh^{Q111/Q111}$, expressing mutant huntingtin harboring 111 glutamine repeats (referred to as Q7 and Q111 cells, respectively) were cultured in DMEM (low glucose, no pyruvate) supplemented with 2 mM L-glutamine, 1 % penicillin-streptomycin, and 10 % fetal bovine serum at 33 °C and 5 % CO2.

G3BP2 in-vitro phase separation. All phase separation assays were performed in 25 mM Tris-HCl, 150 mM NaCl, pH 7.4 (phase separation buffer) and at room temperature. The samples were mixed in protein low-binding tubes (Eppendorf) and

transferred into a 15 µ-slide Angiogenesis (IBIDI, #81507). Fluorescence Recovery After Photo-bleaching (FRAP) experimentations were performed using Nikon spinning disk confocal CSU-X and an Apo objective 60 × 1.49- NA (oil).

Total RNA from STHdh$^{Q7/Q7}$ cells was extracted using the RNeasy Midi Kit (Qiagen, # 75144) and following the manufacturer's protocol. Total RNA was resuspended in RNase-free water, and concentration was assessed using a Nanodrop.

G3BP2 was purchased from Biomol (#349926). First, isolated G3BP2 was labeled with a Cyanine3 NHS ester probe (Lumiprobe, #21020). Following the manufacturer's protocol, the protein buffer was briefly exchanged with a labeling buffer (100 mM Sodium Bicarbonate, 50 mM NaCl, pH 8.0) using the Micro Bio-Spin™ 6 Columns (Biorad, #7326221). The protein was then incubated for 1 h at RT with Cyanine 3 NHS ester probe at a ratio of 1:3 (protein : Cyanine3). After incubation, the excess of the probe was removed using the Micro Bio-Spin™ 6 Columns and the buffer was exchanged with the phase separation buffer (described above). To minimize the effect of the Cy3 label on phase separation, the labeled proteins were mixed with non-labeled G3BP2 at a 1:9 ratio (labeled : non-labeled). For sulfonylated G3BP2, 10 µM of the protein was incubated in the presence of 100 µM DTT and 200 µM H_2O_2 for 30 min at 37°C. The reduced and oxidized G3BP2 were generated using the same concentration of respectively DTT or H_2O_2.

To ensure maximum yield of persulfidated G3BP2, 5,5-dithio-bis-(2-nitrobenzoic acid) (DTNB, Ellman's reagent) was used. G3BP2 was incubated with a 2-fold excess of DTNB for 1 h at RT with constant mixing. The protein was then cleaned from DTNB excess using the Micro Bio-spin columns. Finally, as previously described, part of the

G3BP2-TNB has been labelled with a Cyanine3 NHS ester probe. Cyanine3 non-labeled and labeled proteins were mixed as previously described. To generate the reduced, persulfidated or iodoacetamide-blocked, the protein (G3BP2-TNB) was incubated respectively with 20 µM DTT, 20 µM Na_2S, or 20 µM DTT, and 100 µM IAM for 5 min at 37 °C. For all experiments, G3BP2 phase separation was triggered with 50 ng/µl of total RNA extract and incubated for 7 min before FRAP experiments. Recovery was recorded for 10 min.

Western blot detection of global and G3BP2 persulfidation and sulfenylation levels under $NaAsO_2$ treatment. WT MEFs were treated or not with 500 µM of $NaAsO_2$ for the indicated time. Cells were lysed in HEN buffer supplemented either with 5 mM 4-Chloro-7-nitrobenzofurazan (NBF-Cl; for persulfidation) or 0.5 mM Benzo[c][1,2]thiazine-based BTD (BTD; for sulfenylation). Sample preparation and enrichment steps for both modifications were performed as described for proteomic analysis. After incubation and washing steps, the Pierce™ High Capacity NeutrAvidin Agarose beads were resuspended in 50 mM Hepes, 1X Laemmli and boiled at 95 °C for 10 min to release enriched proteins. Part of the sample before enrichment was collected as a loading control. Both loading control and enriched fraction were then run on a 10% acrylamide gel and transferred to a nitrocellulose membrane. The Dylight™ 633 conjugated streptavidin was used to detect the global persulfidation and sulfenylation levels. Anti-G3BP2 antibody (1:4000, Proteintech®, 16276-1-AP) and secondary anti-rabbit IgG H&L Alexa Fluor® 680 (1:20,000) were used to detect G3BP2.

G3BP2 WT and C73S mutant plasmid construction. The pDEST-CMV-N-EGFP-wtG3BP2 plasmid was built using the gateway cloning method (Thermofisher)[29].

The human G3BP2 sequence from the pENTR4_G3BP2 plasmid was transferred into the pDEST-CMV-N-EGFP plasmid using the Gateway™ LR Clonase™ following the manufacturer's instructions. Both plasmids were obtained through Addgene. pENTR4_G3BP2 was a gift from Thomas Tuschl (Addgene plasmid #127105; http://n2t.net/addgene:127105; RRID: Addgene_127105). pDEST-CMV-N-EGFP was a gift from Robin Ketteler[30] (Addgene plasmid # 122842 ; http://n2t.net/addgene:122842 ; RRID:Addgene_122842).

For the C73S mutation, the point mutation was created following the protocol from Liu et al. (2008)[31]. Briefly, the TGT codon coding for the cysteine was replaced by AGT codon for serine using the following primers FW: GTGAAAGTCATACTAAAATTCGTCATGTGGATG; RV: AGTATGACTTTCACTGAAGTTCAGAGATAATACTTTGTG. The PCR was performed using Phusion™ Plus DNA Polymerase (Thermofisher, F630S), and the following PCR parameters were used: initial denaturation: 98°C, 5 min; {Denaturation: 98°C, 1 min; annealing: 56°C, 1 min; elongation: 72°C, 8 min;} for 12 cycles. PCR was terminated by a final denaturation at 98°C for 1 min, an annealing step at 63°C for 1 min, and a final elongation at 72°C for 30 min. PCR efficiency was checked by agarose gel, and the remaining PCR products were treated with FastDigest DpnI (Thermofisher, FD1703) following the manufacturer's instruction. 2 µl of the digestion was for transformation in E. cloni® 5-alpha competent cells (Lucigen, 60602) following standard protocol. Plasmid was extracted from a few clones using the GenElute™ Plasmid Miniprep-Kit (Sigma-Aldrich, PLN70). Plasmids were first tested for the mutation using PCR primers that allow the elongation of a smaller fragment when the mutation is present (FW: GACTTCAAGGAGGACGG; RV: GTCTCAGCGACGCTG; RV middle primer:

ACATGACGAATTTTAGTATGACT). Positive clones were then sent for sequencing for further validation. Both pDEST-CMV-N-EGFP-wtG3BP2 and pDEST-CMV-N-EGFP-C73SG3BP2 plasmids were amplified and extracted using PureLink™ HiPure Plasmid Maxiprep Kit (Invitrogen™, K210007) before use.

Plasmid transfection and G3BP2 live cell microscopy. WT MEF cells were transfected with pDEST-CMV-N-EGFP-C73SG3BP2 or pDEST- CMV-N-EGFP-wtG3BP2 using a reverse transfection protocol. Briefly, the transfection solution was prepared by mixing 1 part of plasmid DNA (in µg) and 3 parts of TransIT®- 2020 Transfection Reagent (Mirius, #MIR5400) in Opti-MEM™ I Reduced Serum Medium (Gibco™, #31985062) and incubated for 30 min. Meanwhile, cells were trypsinized for 3 min, followed by quenching with DMEM supplemented with 10 % fetal bovine serum. After incubation, the transfection solution was added into a glass bottom µ-slide with 8 wells at 50 ng of DNA per well (IBIDI, #80807). 15,000 cells were seeded in each well on top of the transfection reagent and incubated for 24 hours. The day after, the media was changed 2 h before starting the experiment to allow cell recovery from transfection stress.

Live cell microscopy was carried out using a Leica SP8 LIGHTNING Confocal Microscope with a 63x water objective with environmental control (37 °C, 5 % CO2) and adaptive focus control. Before recording, cells were treated with 5 µg/mL Hoechst 33342 for 5 min. Media containing Hoechst 33342 was washed 2 times and replaced with FluoroBrite™ DMEM supplemented with 2 mM L-glutamine, 1 % penicillin-streptomycin and 10 % fetal bovine serum.

Stress granule formation measurement. WT MEF cells transformed either with WT G3BP2 or with G3BP2 C73S mutant or $CSE^{-/-}$ MEF cells transformed with WT G3BP2 were treated with 500 µM sodium meta-arsenite ($NaAsO_2$), and one image was taken every 16 sec for 20 min. The number and size of stress granules were measured using Fiji.

In-cellulo H_2S dissolution of G3BP2 condensates. WT MEF cells expressing the WT G3BP2 or the G3BP2 C73S were treated for 15 min with 500 µM $NaAsO_2$ to allow the formation of G3BP2 condensates. Cells were recorded every 16 s, and H_2S was injected at a 100 µM final concentration. After the condensate reformed, a second injection of H_2S at the same concentration was performed. The number of stress granule over time was measured using Fiji.

Immunofluorescence of G3BP2 and GAPDH under $NaAsO_2$ treatment. MEF WT and $CSE^{-/-}$ or STHdh cells were split in a µ-Dish 35 mm, high Glass Bottom (IBIDI, #81158). Before fixation, cells were washed two times with warm PBS and fixed with 2 % PFA for 10 min, followed by 10 min with 4 % PFA. Excess of PFA was removed with 3 times washes with cold PBS. For immunofluorescence staining, cells were permeabilized using 0.1 % Triton X100 in PBS for 20 min. Cells were then incubated for 1 h in blocking buffer (1 % BSA, 22.52 mg/ml glycine, 0.1 % Tween in PBS) followed by a 2 h incubation at 37 °C with the primary antibody against G3BP2 (1:600; Proteintech®, 16276-1-AP). Cells were washed and incubated with a secondary antibody (mouse anti-rabbit IgG-CFL 647, [Santa Cruz Biotechnology, INC.; sc-516251]) for 2 h at 37 °C. DAPI (4',6-Diamidin-2-phenylindol, Dihydrochloride; Thermo Fisher Scientific) staining was performed prior to recording, following the manufacturer's protocol. Cells were imaged

using a Leica SP8 LIGHTNING Confocal Microscope with a 63x oil objective and a resolution of 2048 x 2048. Image analysis was performed using Fiji.

4.6. References

1. Banani, S. F., Lee, H. O., Hyman, A. A. & Rosen, M. K. Biomolecular condensates: Organizers of cellular biochemistry. *Nature Reviews Molecular Cell Biology* vol. 18 285–298 (2017).
2. Alberti, S. & Hyman, A. A. Biomolecular condensates at the nexus of cellular stress, protein aggregation disease and ageing. *Nature Reviews Molecular Cell Biology* vol. 22 196–213 (2021).
3. Staněk, D. *et al.* Spliceosomal small nuclear ribonucleoprotein particles repeatedly cycle through Cajal bodies. *Mol. Biol. Cell* **19**, 2534–2543 (2008).
4. Staněk, D., Rader, S. D., Klingauf, M. & Neugebauer, K. M. Targeting of U4/U6 small nuclear RNP assembly factor SART3/p110 to Cajal bodies. *J. Cell Biol.* **160**, 505–516 (2003).
5. Fox, A. H., Nakagawa, S., Hirose, T. & Bond, C. S. Paraspeckles: Where Long Noncoding RNA Meets Phase Separation. *Trends in Biochemical Sciences* vol. 43 124–135 (2018).
6. Parker, R. & Sheth, U. P Bodies and the Control of mRNA Translation and Degradation. *Molecular Cell* vol. 25 635–646 (2007).
7. Luo, Y., Na, Z. & Slavoff, S. A. P-Bodies: Composition, Properties, and Functions. *Biochemistry* vol. 57 2424–2431 (2018).
8. Emara, M. M. *et al.* Hydrogen peroxide induces stress granule formation independent of eIF2α phosphorylation. *Biochem. Biophys. Res. Commun.* **423**, 763–769 (2012).
9. Aulas, A. *et al.* Stress-specific differences in assembly and composition of stress granules and related foci. *J. Cell Sci.* **130**, 927–937 (2017).
10. Buchan, J. R., Muhlrad, D. & Parker, R. P bodies promote stress granule assembly in Saccharomyces cerevisiae. *J. Cell Biol.* **183**, 441–455 (2008).
11. Ivanov, P., Kedersha, N. & Anderson, P. Stress granules and processing bodies in translational control. *Cold Spring Harb. Perspect. Biol.* **11**, (2019).
12. Takahara, T. & Maeda, T. Transient Sequestration of TORC1 into Stress Granules during Heat Stress. *Mol. Cell* **47**, 242–252 (2012).
13. Matsuki, H. *et al.* Both G3BP1 and G3BP2 contribute to stress granule formation. *Genes to Cells* **18**, 135–146 (2013).
14. Yang, P. *et al.* G3BP1 Is a Tunable Switch that Triggers Phase Separation to Assemble Stress Granules. *Cell* **181**, 325-345.e28 (2020).
15. Hu, S. *et al.* Time-resolved proteomic profiling reveals compositional and functional transitions across the stress granule life cycle. *Nat. Commun. 2023 141* **14**, 1–17 (2023).
16. Li, Y. R., King, O. D., Shorter, J. & Gitler, A. D. Stress granules as crucibles of ALS pathogenesis. *Journal of Cell Biology* vol. 201 361–372 (2013).
17. Ramaswami, M., Taylor, J. P. & Parker, R. XAltered ribostasis: RNA-protein granules in degenerative disorders. *Cell* vol. 154 727–736 (2013).
18. Liang, P., Zhang, J. & Wang, B. Emerging Roles of Ubiquitination in Biomolecular Condensates. *Cells* vol. 12 2329 (2023).
19. Luo, Y. Y., Wu, J. J. & Li, Y. M. Regulation of liquid-liquid phase separation with focus on post-

translational modifications. *Chem. Commun.* **57**, 13275–13287 (2021).

20. Sidibé, H., Dubinski, A. & Vande Velde, C. The multi-functional RNA-binding protein G3BP1 and its potential implication in neurodegenerative disease. *Journal of Neurochemistry* vol. 157 944–962 (2021).
21. Kennedy, D. *et al.* Characterization of G3BPs: Tissue specific expression, chromosomal localisation and rasGAP120 binding studies. *J. Cell. Biochem.* **84**, 173–187 (2002).
22. Cobley, J. N., Fiorello, M. L. & Bailey, D. M. 13 reasons why the brain is susceptible to oxidative stress. *Redox Biology* vol. 15 490–503 (2018).
23. Vitvitsky, V., Kabil, O. & Banerjee, R. High turnover rates for hydrogen sulfide allow for rapid regulation of its tissue concentrations. *Antioxidants and Redox Signaling* vol. 17 22–31 (2012).
24. Wedmann, R. *et al.* Working with 'H2S': Facts and apparent artifacts. *Nitric Oxide - Biol. Chem.* **41**, 85–96 (2014).
25. Zivanovic, J. *et al.* Selective Persulfide Detection Reveals Evolutionarily Conserved Antiaging Effects of S-Sulfhydration. *Cell Metab.* **30**, 1152-1170.e13 (2019).
26. Anderson, P. & Kedersha, N. *Visibly stressed: The role of eIF2, TIA-1, and stress granules in protein translation*. *Cell Stress and Chaperones* vol. 7 213–221 (Elsevier, 2002).
27. Thedieck, K. *et al.* XInhibition of mTORC1 by astrin and stress granules prevents apoptosis in cancer cells. *Cell* **154**, 859–874 (2013).
28. McInerney, G. M., Kedersha, N. L., Kaufman, R. J., Anderson, P. & Liljeström, P. Importance of eIF2α phosphorylation and stress granule assembly in alphavirus translation regulation. *Mol. Biol. Cell* **16**, 3753–3763 (2005).
29. Katzen, F. Gateway® recombinational cloning: A biological operating system. *Expert Opinion on Drug Discovery* vol. 2 571–589 (2007).
30. Agrotis, A., Pengo, N., Burden, J. J. & Ketteler, R. Redundancy of human ATG4 protease isoforms in autophagy and LC3/GABARAP processing revealed in cells. *Autophagy* **15**, 976–997 (2019).
31. Liu, H. & Naismith, J. H. An efficient one-step site-directed deletion, insertion, single and multiple-site plasmid mutagenesis protocol. *BMC Biotechnol.* **8**, 91 (2008).

Funding: This study was funded by European Research Council (ERC) under the European Union's Horizon 2020 research and innovation programme (Grant Agreement No. 864921). The authors also acknowledge support from the start-up funds from DZNE, the grants from the German Research Foundation (SFB 1286/B10 and MI 2104), and the Human Frontiers Science Organization (RGEC32/2023) (to DM), the Medical Research Council UK (MC_UU_00028/4 to MPM and MC_UU_00028/5 for JP) and by a Wellcome Trust Investigator award (220257/Z/20/Z) (to MPM). CH is supported by a fellowship of the Innovative Minds Program of the German Dementia Association; HW is

supported by the Oversea Study Program of Guangzhou Elite Project (SJ2020/2/JY202025).

Competing interests: Authors declare that they have no competing interests.

5. Pathway-specific persulfidation shifts and sulfide signaling underlie esophageal (patho)physiology

5.1. Context of the study: H_2S role in intestinal tract protection

In the digestive tract, H_2S is endogenously produced by enzymes involved in the transsulfuration pathway and cysteine catabolism, but it could come from exogenous sources as well, where it is produced by enteric bacteria[1,2]. H_2S is suggested to play a role in the anti-inflammatory response through the inhibition of the nuclear factor-kappa B pathway[3] and downregulation of the expression of several proinflammatory cytokines[4–6]. In rats, upregulation of H_2S production at the site of ulceration seems to enhance the healing of the ulcer[7], while inhibition of its production results in gastrointestinal (GI) mucosal inflammation[2,8] (Figure 5.1A). Consistent with these observations, rats presenting with colitis exhibit faster tissue injury healing when treated with H_2S-donors[2,6], suggesting their therapeutic potential for GI disorders. Non-steroidal anti-inflammatory drugs (NSAIDs) are known to induce mucosal injury in the GI tract[9]. However, rats co-treated with NSAIDs and H_2S donors showed considerably reduced NSAID-induced GI tract injury[10]. Several H_2S-releasing NSAIDs, such as ATB-346, a derivative of naproxen, have also shown reduced NSAID toxicity and accelerated ulcer healing[11]. Several preclinical trials are currently being conducted for different H_2S-releasing NSAIDs, such as ATB-346 and ATB-352 (Figure 5.1B), and slow-releasing H_2S donors, such as GYY3147 (Figure 5.1C).

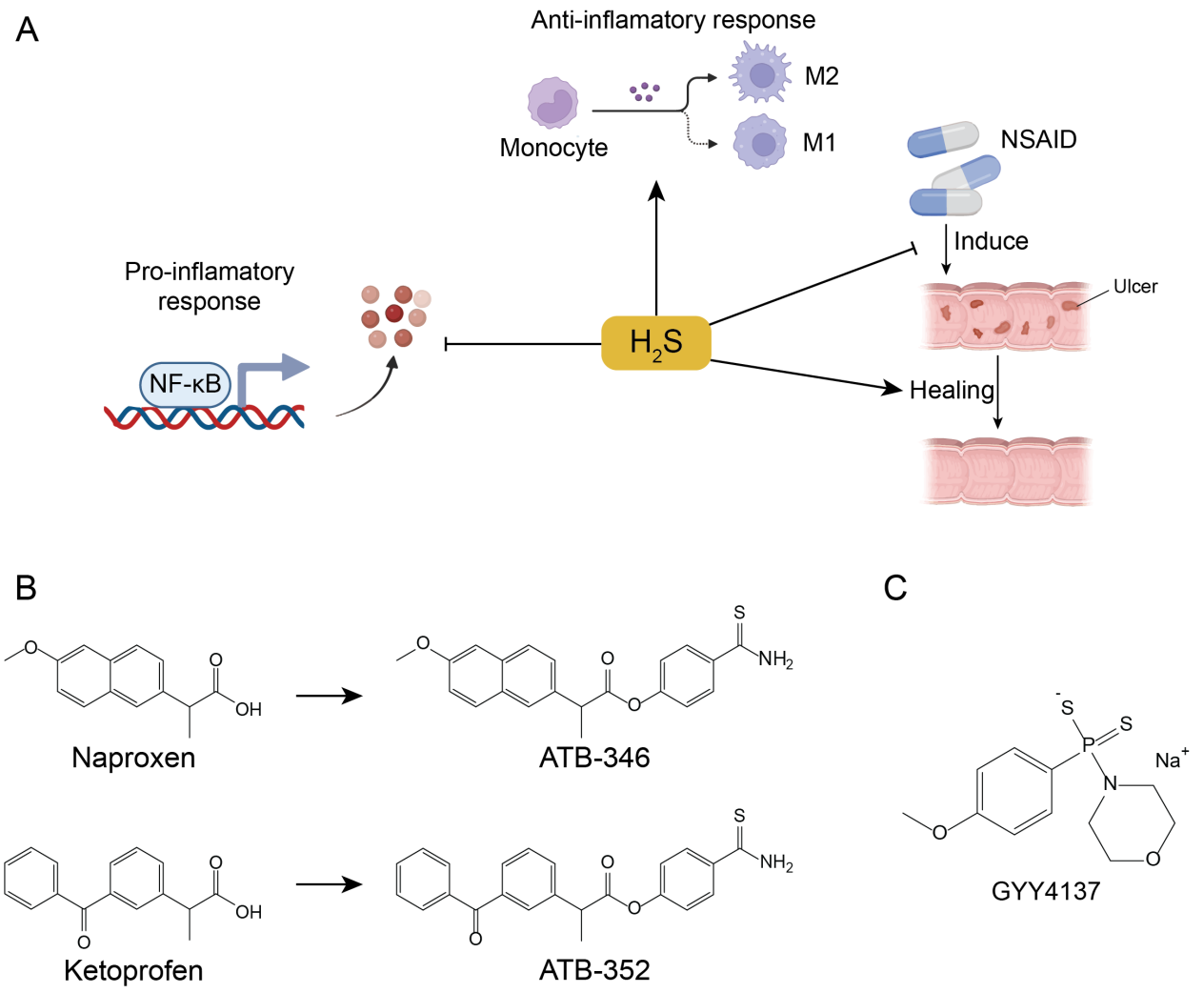


Figure 5.1. H_2S protective effect in gastrointestinal disorders and novel therapeutic approach for NSAID-induced mucosa damages. (**A**) Role of H_2S in the resolution of intestinal inflammation. H_2S inhibits the pro-inflammatory response and drives the differentiation of monocytes to macrophages M2, which are responsible for the anti-inflammatory response. Through these processes, H_2S enhances the healing of the damaged gastrointestinal tract and attenuates the nonsteroidal anti-inflammatory drugs (NSAID)-induced GI tract injury. (**B**) Chemical structures of H_2S-releasing NSAID. ATB-346 and ATB-352 are derived from Naproxen and ketoprofen, respectively. Clinical trials are currently being undertaken to treat osteoarthritis (ATB-346) and acute pain (ATB-352)[1]. (**C**) Chemical structure of GYY4137, a slow releasing H_2S donors with therapeutic potential for the GI tract.

Pathway-specific persulfidation shifts and sulfide signaling underlie esophageal (patho)physiology

Edyta Korbut[1], Mateusz Wierdak[1,2], **Thibaut Vignane**[3], Katarzyna Magierowska[1], Dominik Bakalarz[1,4], Vincent T Janmaat[5], Jerzy Hankus[1], Dagmara Wójcik-Grzybek[1], Matthew Whiteman[6], Michał Kukla[7,8], Ron Smits[5], Rhonda F Souza[9], Milos R Filipovic[3], Marcin Magierowski[1,*]

[1]Department of Physiology, Jagiellonian University Medical College, Cracow, Poland

[2]2nd Department of Surgery, Jagiellonian University Medical College, Cracow, Poland

[3]Leibniz-Institut für Analytische Wissenschaften-ISAS e.V. Dortmund, Germany

[4]Department of Forensic Toxicology, Institute of Forensic Research, Cracow, Poland

[5]Department of Gastroenterology and Hepatology, Erasmus MC Cancer Institute-University Medical Center, Rotterdam, The Netherlands

[6]The Institute of Biomedical and Clinical Science, University of Exeter Medical School, St. Luke's Campus, University of Exeter, Exeter, United Kingdom

[7]Department of Internal Medicine and Geriatrics, Jagiellonian University Medical College, Cracow, Poland

[8]Department of Endoscopy, University Hospital, Cracow, Poland

[9]Division of Gastroenterology, Center for Esophageal Diseases, Baylor University Medical Center, and Center for Esophageal Research, Baylor Scott & White Research Institute,Dallas, TX, USA

*Corresponding author: m.magierowski@uj.edu.pl

Submitted to EMBO journal.

Authors contributions

Conceptualization and study design: M.M., Investigation: E.K., M.W., **T.V**., K.M., D.B., D.W.G., M.M., Methodology (*in vitro*, *in vivo* models and molecular/biochemical methods): E.K., M.W., V.J., D.B., J.H., R.S., M.M., Methodology (clinical procedures): M.W., M.K., **Methodology (proteomics): T.V**., M.R.F., Methodology (chemical synthesis): M.Whiteman, Supervision and coordination: M.M., Funding acquisition: M.M., Resources: V.J., R.F.S., M.R.F., M.M., **Data collection:** E.K., M.W., K.M., D.W.G., D.B., J.H., **T.V**., M.M., Data analysis: E.K., T.V., M.R.F., M.M., **Visualization:** E.K., **T.V**., M.R.F., M.M., Writing original draft: E.K., M.M., Writing—review & editing: R.F.S., M.R.F., M.M., All authors have read and agreed to this version of the manuscript.

For this study, I conducted the proteomic analysis of human esophagus biopsies to examine both protein persulfidation and global protein expression changes. Given the significant alterations observed in the total proteome, I developed a method to normalize the persulfidation changes relative to protein expression changes. Additionally, I created Figures 5.3, S5.5, S5.6, S5.8, and 5.7A, as well as all supplementary tables. I also contributed to the writing of the proteomic analysis results presented in Section 5.4.2.

5.2. Abstract

Posttranslational persulfidation of proteins (PSSH) is anti-oxidative, anti-aging and relies on hydrogen sulfide (H_2S)-bioavailability but remains ignored in esophageal (patho)physiology. Metaplastic and premalignant Barrett's esophagus (BE) develops under gastroesophageal reflux (GERD)-induced oxidation. Thus, we clinically compared PSSH-landscapes between physiological squamous epithelium (SE), GERD-exposed SE and BE. The fall of PSSH/H_2S-levels emerged here as GERD-inducible and metaplasia-specific. We identified 172 pathway-specific PSSH-shifts, even in SE of GERD-patients, that expanded to 1347 in BE. Metaplasia-driving targets, including prostaglandin (PG)E2, interleukin (IL)-1β or mTOR emerged as PSSH-sensitive. Our chemoproteomic approach suggested also new biomarkers of BE, elusive before. Our translational animal and *in vitro* models document that interventionally decreased epithelial H_2S-level accelerates BE, while H_2S-prodrugs silenced IL-1β/PGE2/mTOR-interplay and prevented BE. We conclude that equilibrated PSSH/H_2S-bioactivity determine physiological esophageal balance. Chronic GERD evokes the overload and PSSH-shifts of metaplasia-specific pathways in SE, initiating BE. Developmental PSSH-landscape remodeling and structural rearrangement in BE counteract "H_2S-leakage", explaining adaptative GERD-resistance of metaplastic cells. H_2S-signaling, pharmacologically restored in SE prevents metaplasia-associated turnovers and BE. Thus, H_2S-therapeutics might counteract BE pathogenesis in GERD patients.

KEYWORDS

persulfidation; sulfide signaling; epithelial balance; Barrett's esophagus; metaplasia.

5.3. Introduction

Persulfidation (S-sulfhydration) of proteins (PSSH) is a posttranslational modification that involves the addition of another sulfur molecule onto the thiol group (-SH) of cysteine residues[12,13]. Thus, PSSH prevents irreversible cellular oxidation. PSSH-decline emerged to accompany aging, as revealed recently by the novel chemoproteomic method[12]. PSSH relies on endogenous hydrogen sulfide (H_2S)-signaling and exerts regulatory capacity in pathway-specific manner[14]. Significance of this phenomenon was also indicated in the cardiovascular system[12,15]. However, the contribution of PSSH in gastrointestinal (GI) and esophageal (patho)physiology remains clinically and experimentally unknown.

Barrett's esophagus (BE) is characterized as the defensive but pathological replacement of the physiological squamous epithelium (SE) by intestinal metaplasia after chronic gastroesophageal reflux disease (GERD). GERD is one of the most common pathologies, affecting >20% of population[16], while BE predisposes to esophageal adenocarcinoma[17]. GERD is defined as the pathogenic influx of the lower GI content up to esophageal mucosa, leading to chronic esophagitis, epithelial oxidation and affecting intracellular proteins signaling[17,18]. Souza *et al*. also suggested the contribution of cytokine-mediated injury and chemotaxis of immune cells rather than the direct toxic effects of hydrogen ions[19]. Quante *et al.* demonstrated that increased interleukin-1β (IL-1β) expression induced BE-lesions in transgenic-mice[20]. These alterations might trigger BE pathogenesis. Nevertheless, the molecular origin of BE is unclear and might be more complex than recently assumed[17].

We challenged here the current understanding of BE pathogenesis indicating the significance of persulfidomic PSSH-shifts, that have remained fundamentally ignored and methodologically elusive before in esophageal epithelium. PSSH is a mechanistic target of H_2S signaling and PSSH-levels depend on H_2S-bioavailability[12]. H_2S is an endogenous, anti-oxidative gaseous messenger that regulates plethora of physiological and pathological processes[1]. H_2S biosynthesis in mammalian tissues mainly relies on the enzymatic activity of cystathionine-γ-lyase (CTH), cystathionine-β-synthase (CBS) or mitochondrial 3-mercaptopyruvate sulfur transferase (MPST)[1]. Endogenous H_2S is known to modulate gastric mucosal and colonic repair[21]. Nevertheless, the impact of H_2S-dependent PSSH-shifts and H_2S-signaling on BE pathogenesis are unknown. Clinical and experimental studies of H_2S-prodrugs provided a foundation for the safe and effective modern pharmacology[22,23]. Sodium thiosulfate, mimicking beneficial effects of H_2S (but does not release H_2S directly) is even the FDA-approved drug to reduce the risk of ototoxicity associated with cisplatin, including pediatric patients[24,25]. However, H_2S-therapeutics were never targeted against esophageal metaplasia. Interestingly, clinically randomized controlled trials showed that current approaches based on proton pump inhibitors (burdened by serious side-effects) or invasive, aggravating surgical therapies do not completely prevent or eliminate GERD and BE[26]. These premises indicate the clinical need of alternative anti-BE approaches.

Therefore, we newly report here the significance of equilibrated mucosal persulfidation and H_2S-bioavailability in the physiological balance of esophageal epithelium. However, we also found that altered H_2S-signaling and pathway-specific persulfidomic shifts are developmentally BE-specific and controversially initiate in esophageal squamous epithelium (SE) exposed to GERD. These phenomena were

previously unrecognized in BE pathogenesis that could lead to scientific depreciation of metaplasia-specific turnovers in SE. We uniquely focused on all three subsequent states: physiological SE, GERD-exposed SE and Barrett's metaplasia. We clinically identified the disease phase-related and pathway-specific PSSH-landscapes, implementing for the first time in GI research the recent chemoproteomic method. Consequently, in translational models, by the genetic and pharmacological interventions, we mechanistically indicated that the fall of esophageal H_2S-level and its therapeutic restoration in SE functionally impact PSSH-sensitive metaplastic-turnover and BE development.

5.4. Results

5.4.1. PSSH level and H_2S-bioavailability are altered in metaplastic epithelium

We clinically tested the expression pattern of the three main H_2S-producing enzymes, CTH, CBS and MPST, in endoscopic samples of metaplastic segments and compared them to expression levels in squamous epithelium (SE) of patients with GERD (Figure 5.2A). We observed elevated protein of CTH in clinical BE compared to surrounding GERD-exposed SE (Figure 5.2A). Previous analysis of clinical datasets (GSE1308317, GSE3461918, GSE142019) from Gene Expression Omnibus (GEO) that compared SE and BE, showed no significant changes at mRNA levels neither for CTH nor CBS and MPST (Figure S5.1). However, our chemoproteomic in-gel detection revealed here, for the first time the decreased overall PSSH levels (indicating functionally reduced H_2S-bioavailability) in clinical samples of BE compared to GERD-

exposed SE (Figure 5.2B). We implemented similar attempt in animal model, and we observed that compared to intact animals, esophageal CBS and CTH protein and mRNA expressions were upregulated after chronic GERD in rats with developed Barrett's-like lesions (BE), approx. 10 weeks after micro-surgically induced esophago-gastroduodenal anastomosis (EGDA) (Figure 5.2C, Figure S5.2). Similarly to clinical data, the elevated CBS and CTH was accompanied by a decreased H_2S-levels in pathological esophageal mucosa (Figure 5.2D). We further confirmed GERD-induced reduction of epithelial H_2S using in vitro models. We uniquely implemented the combination of human esophageal epithelial cell line (EPC2) originated from patient w/o GERD, the human squamous cell line established from endoscopic biopsy of the distal esophageal mucosa of patient with GERD but without BE (NES-G2T) and human BE cells (BAR-T). There were no apparent effects of experimental GERD on protein levels of H_2S-enzymes (Figure **5.2**E). However, compared with EPC2, H_2S-content was decreased in NES-G2T and BAR-T (Figure 5.2F). Additional exposure to acidified bile mixture (BM) for one week (experimental GERD) initiated the H_2S fall in squamous EPC2 and enhanced H_2S decline in NES-G2T but not in metaplastic BAR-T (Figure 5.2F). The selective knockout of CBS or CTH by CRISPR/Cas9 (Figure S5.3) decreased H_2S-bioavailability in EPC2, similarly to exp. GERD (Figure 5.2F). Evaluation of total H_2S content, methodologically excluding sulfane sulfur (PSSH pool), did not show significant differences (Figure S5.4). Thus, decreased epithelial PSSH and H_2S-bioavailability emerged as metaplasia-specific but GERD-inducible even in SE. However, metaplastic segments exhibit stable and GERD-resistant PSSH-H_2S levels. These clinical and experimental findings indicated that the esophageal fall of H_2S-dependent anti-oxidative PSSH underlies GERD-triggered BE development.

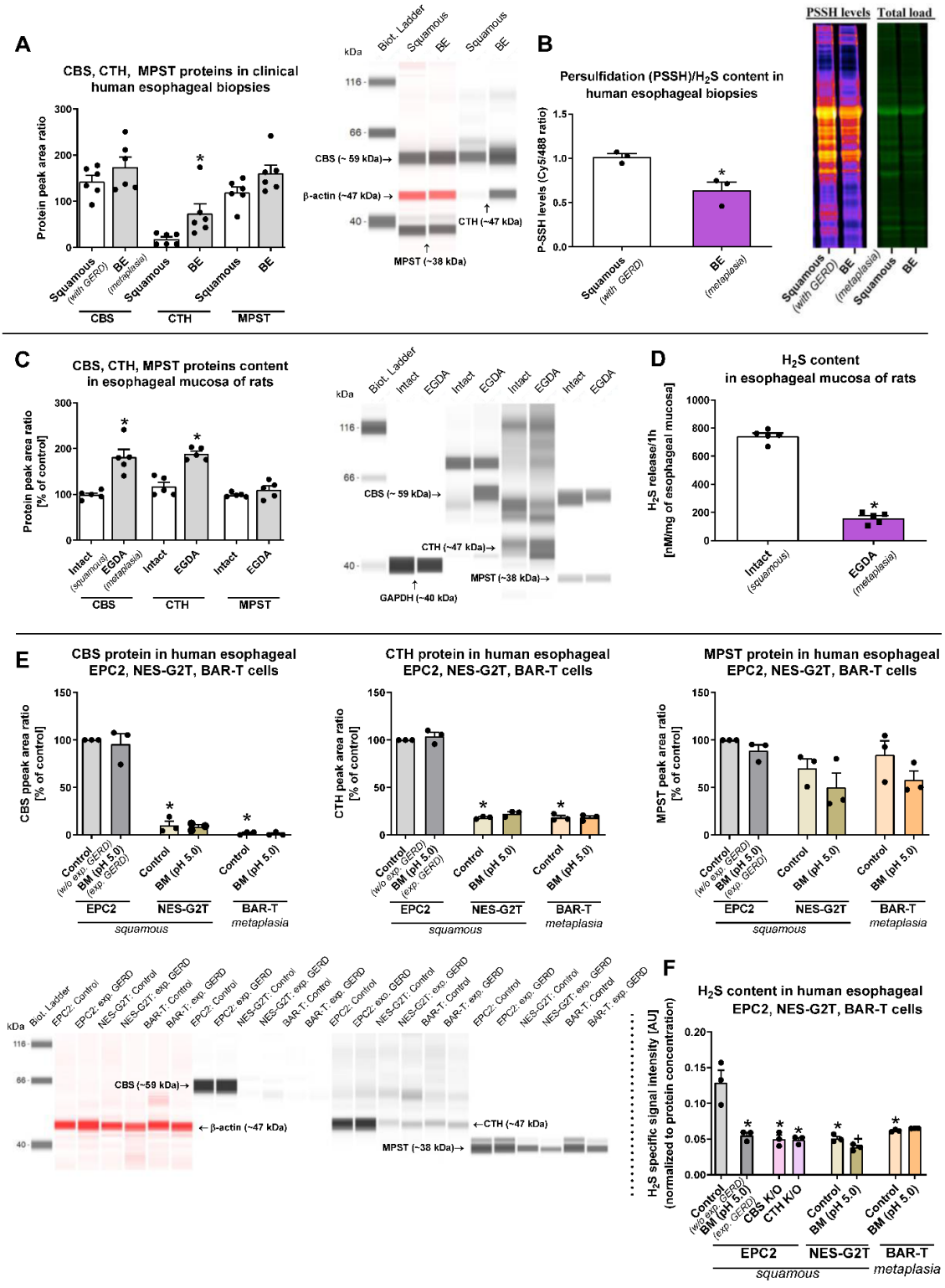

A
CBS, CTH, MPST proteins in clinical human esophageal biopsies
Protein peak area ratio
Squamous (with GERD)
BE (metaplasia)
CBS
CTH
MPST
Biot. Ladder
CBS (~ 59 kDa)→
β-actin (~47 kDa) →
CTH (~47 kDa)
MPST (~38 kDa)
B
Persulfidation (PSSH)/H2S content in human esophageal biopsies
P-SSH levels (Cy5/488 ratio)
PSSH levels
Total load
C
CBS, CTH, MPST proteins content in esophageal mucosa of rats
Protein peak area ratio [% of control]
Intact (squamous)
EGDA (metaplasia)
GAPDH (~40 kDa)
D
H2S content in esophageal mucosa of rats
H2S release/1h [nM/mg of esophageal mucosa]
E
CBS protein in human esophageal EPC2, NES-G2T, BAR-T cells
CTH protein in human esophageal EPC2, NES-G2T, BAR-T cells
MPST protein in human esophageal EPC2, NES-G2T, BAR-T cells
CBS ppeak area ratio [% of control]
CTH peak area ratio [% of control]
MPST peak area ratio [% of control]
Control (w/o exp. GERD)
BM (pH 5.0) (exp. GERD)
EPC2
NES-G2T
BAR-T
squamous
metaplasia
F
H2S content in human esophageal EPC2, NES-G2T, BAR-T cells
H2S specific signal intensity [AU] (normalized to protein concentration)
CBS K/O
CTH K/O

Figure 5.2. Esophageal persulfidation (PSSH) and H_2S-bioavailability in metaplastic epithelium. (**A**) Quantification of CBS, CTH and MPST protein expression and representative capillary immunoblotting lane view image showing CBS, CTH and MPST protein levels in human biopsy of BE segment and squamous mucosa; β-actin served as a loading/reference control. (**B**) Esophageal PSSH levels (reflecting H_2S-bioavailability) showed as the ratio of Cy5/488 signals in human clinical biopsies of Barrett's metaplasia (BE) and paired GERD-exposed squamous mucosa. (**C**) Quantification of CBS, CTH and MPST protein expression and representative capillary immunoblotting lane view image showing CBS, CTH and MPST protein levels in intact (squamous) and EGDA-rats (metaplasia-like); GAPDH served as a loading/reference control. (**D**) H_2S bioavailability in intact and EGDA-rats. (A-D) Values presented as a mean ± SEM, *p<0.05 vs. Intact (n=3-6 samples per group). (**E**) Quantification of CBS, CTH and MPST protein expression and representative capillary immunoblotting lane view image showing CBS, CTH and MPST protein levels in EPC2, NES-G2T and BAR-T cells +/- acidified BM (30 min/day) for one week; β-actin served as a loading/reference control. (**F**) H_2S-bioavailability in EPC2, EPC2-CBS K/O, EPC2-CTH K/O, NES-G2T and BAR-T cells +/- acidified BM (30 min/day) for one week. (E-F) Values presented as a mean ± SEM, n=3 independent experiments, *p<0.05 vs. Control (EPC2), +p<0.05 vs. Control (NES-G2T).

Gene symbol	Gene ID	Database no. GSE1420 (n=16) Target tissue: Barrett's esophagus		Database no. GSE13083 (n=14) Target tissue: Barrett's esophagus		Database no. GSE34619 (n=18) Target tissue: Barrett's esophagus		
		Barrett's esophagus (n=8) vs. normal esophageal epithelium (n=8)		Barrett's esophagus (n=7) vs. normal esophageal epithelium (n=7)		Barrett's esophagus (n=10) vs. normal esophageal epithelium (n=8)		
		p-value	logFc	p-value	logFc	Gene ID	p-value	logFc
CBS	212816_s_at	4.83e-01	0.2600428	1.81e-01	-0.0349186	8070632	3.60e-01	0.126873
CTH	206085_s_at	6.82e-01	-0.1680222	2.79e-01	-0.0257871	7902290	7.76e-02	0.3546138
MPST	203524_s_at	2.51e-01	-0.238187	4.86e-01	0.3091686	8072777	2.67e-01	0.1160983

Figure S5.1. Alterations in CBS, CTH and MPST genes expression in human biopsies derived from patients with Barrett's esophagus (BE) as compared with normal squamous epithelium, based on analysis of the three different databases (GSE13083, GSE34619 and GSE1420). Differential expression analysis of CBS, CTH and MPST did not meet the following criteria p<0.05 and |logFC|≥1 and was not considered significant.

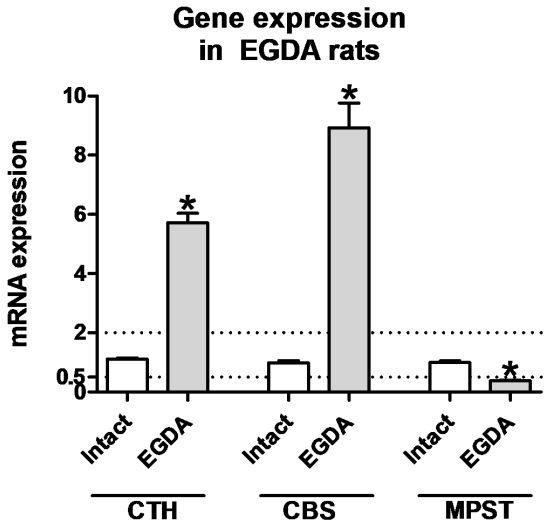


Figure S5.2. Real-time PCR measurement of CBS, CTH and MPST mRNA fold change in esophageal mucosa of healthy rats (Intact) and those with esophago-gastroduodenal anastomosis (EGDA). Values presented as a mean ± SEM, n=3 independent experiments. *p<0.05 vs. Intact.

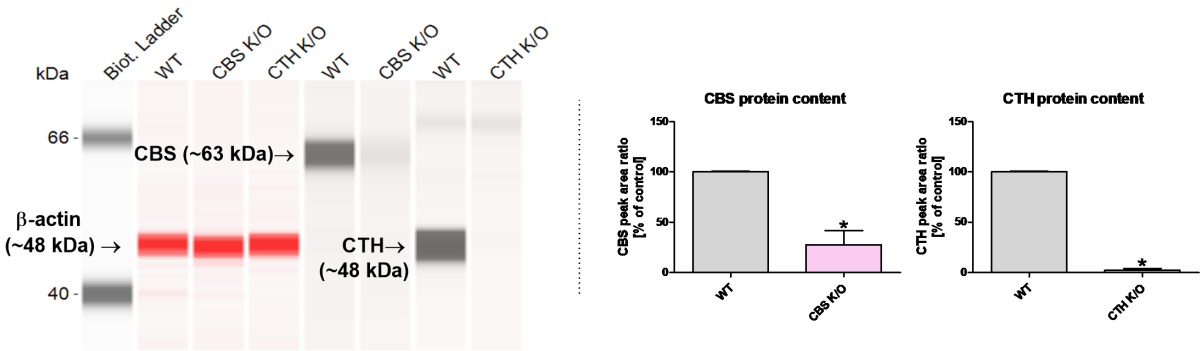


Figure S5.3. Changes in CBS and CTH protein levels in EPC2 WT cells and EPC2 cells with CBS and CTH knockout (K/O); β-actin served as a loading control; *Left* Representative capillary lane view image of EPC2 WT, CBS K/O and CTH K/O cell lysates; *Right* Quantification of protein expression by capillary western blot analysis. Values presented as a mean ± SEM, n=3 independent measurement. *p<0.05 vs. WT.

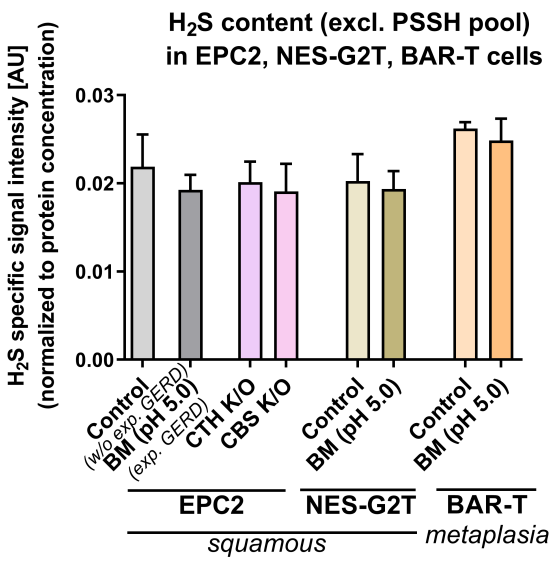


Figure S5.4. H_2S bioavailability (excluding PSSH pool) in EPC2, EPC2-CBS K/O, EPC2-CTH K/O, NES-G2T and BAR-T cells +/- acidified BM (30 min/day) for one week. Values presented as a mean ± SEM, n=3 independent experiments.

5.4.2. PSSH-shifts are developmental and pathway-specific in SE and BE

Considering that GERD-triggered BE was accompanied by decreased H_2S-bioavailability and decline of global persulfidation in esophageal mucosa, we addressed the protein-specific changes in PSSH landscape. Using recent dimedone-switch method for persulfidome analysis[1], we performed the wide-scale proteomic evaluation at subsequent stages of clinical BE development, comparing squamous epithelium (SE) of patients w/o GERD (physiological) to SE of patients with GERD, and the latter to paired metaplastic (BE) segments (Figure 5.3). However, to properly quantify the change, we first performed label-free proteome analysis of those samples. We identified 3423 proteins being present in all 3 conditions, with 41 proteins significantly changing in GERD-exposed SE vs SE w/o GERD (2-fold change, $p<0.05$) and 905 proteins changing in metaplastic vs GERD-exposed SE (paired analysis, 2-fold change, $p<0.05$) (Figure 5.3A, Figure S5.5A,B; Supplementary Table S5.1). Pathway enrichment analysis revealed metabolic pathways such as 2-oxocarboxylic acid metabolism, TCA cycle, fructose and mannose metabolism, arginine biosynthesis and others being particularly enriched, suggesting that transition from GERD-exposed SE to metaplastic cells is accompanied by significant metabolic shift (Figure 5.3B). These data are the first example of total proteome change in human biopsies between BE, the GERD-exposed SE and SE w/o GERD, providing a resource material for future studies. Clustering of all the proteins that significantly changed compared to the SE w/o GERD, by the fuzzy c-means method, identified the disease state-associated patterns (Figure 5.3C,D; Supplementary Table S5.2). For example, NADPH quinone oxidoreductase 1 (NQO1) progressively increased in GERD-exposed SE when compared to the healthy patients

(without GERD) and to even enhance in BE segments (Table S2 (Cluster 2), Figure S5.6).

Next, we analyzed persulfidome changes. 2182 proteins were found to be endogenously persulfidated of which more than half (1347 proteins) were significantly different in BE than in the GERD-exposed SE, and 172 proteins showed different PSSH levels in GERD-exposed SE when compared to SE w/o GERD (Figure 5.3E, Figure S5.5C-D, Supplementary Table S5.3). Having observed significant proteome remodeling, we normalized the protein PSSH levels to their protein expression measured in the label free proteomics. Double plot of PSSH vs proteome change exhibited significant scattering, suggesting that significant portion of PSSH changes followed the change in protein expression (Figure S5.5E). After normalization, 943 remained significantly different in metaplastic vs GERD-exposed SE (Figure 5.3F). It is worth noting that although only 372/943 proteins showed decrease in PSSH, the fold of decreases was much stronger than in the case of proteins exhibiting PSSH increase. Kegg pathway enrichment analysis of proteins decreasing PSSH levels, identified biosynthesis of nucleotide sugars and amino acids, as well as bacterial invasion of epithelial cells, E. coli infection and biosynthesis of cofactors as particularly enriched pathways (Figure 5.3G).

The unidirectional change in clusters 3 and 5 suggest that early PSSH changes observed in GERD-exposed SE when compared to the SE w/o GERD, continue to further emphasize in metaplasia (Figure 5.3H,I, Supplementary Table S5.4). Cluster 2 and 6 show the significant rebound of PSSH in metaplastic segments towards SE w/o GERD (Figure 5.3H,I). Therefore, these targets could contribute mechanistically in early phases of BE pathogenesis (Supplementary Table S5.4).

Taken together, these clinical observations reveal that persulfidomic equilibrium is pathway-specific and crucial for physiological balance in esophageal SE. Chronic GERD impairs this stability, exhausting antioxidative H_2S-signaling in SE and activates metaplasia-specific PSSH-shifts. Subsequently, this pattern becomes dramatically enhanced in Barrett's metaplasia, suggesting the functional contribution of persulfidation in the initiation of metaplastic turnover, adaptative cellular rearrangement and clinical development of BE.

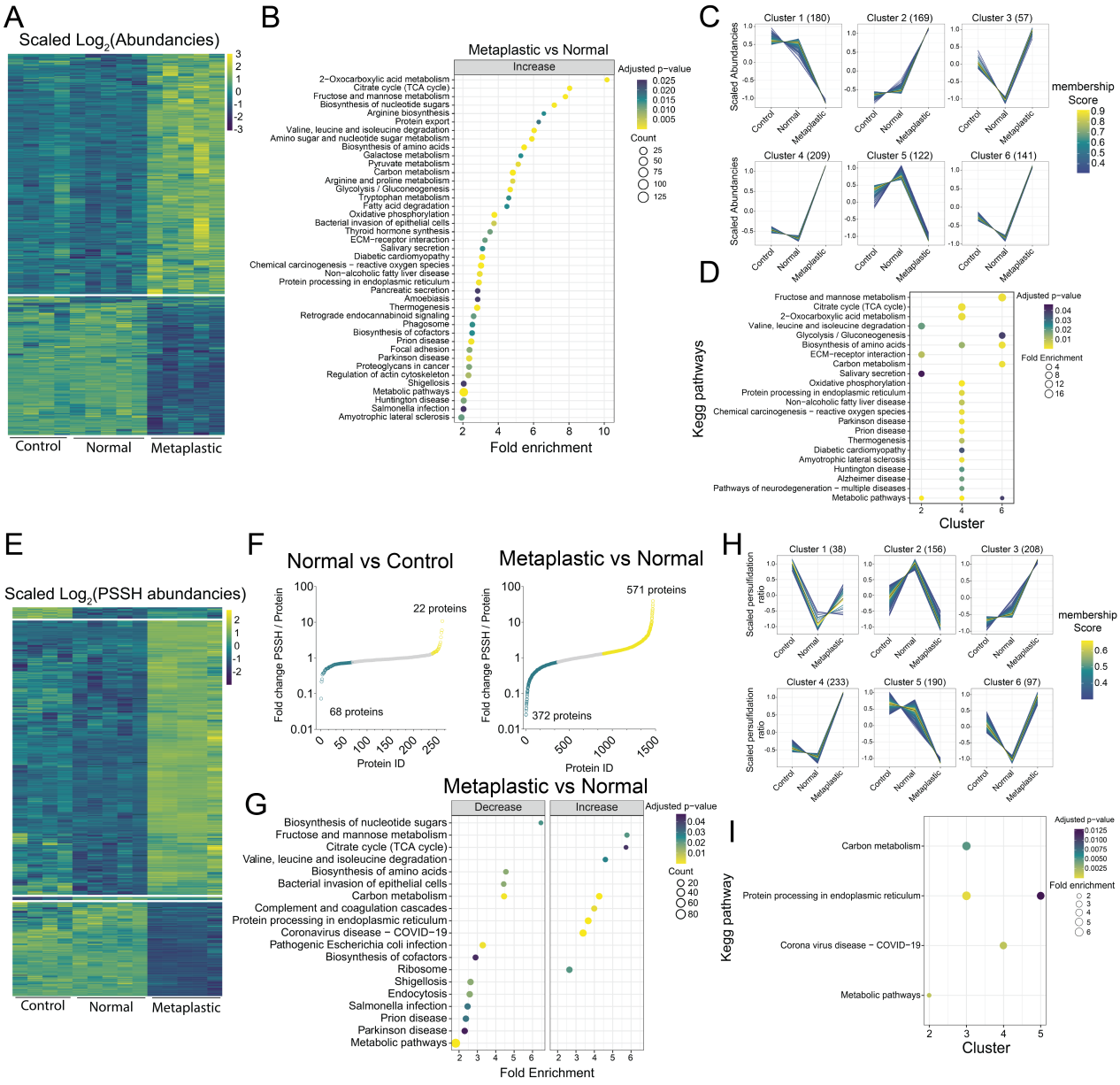


Figure 5.3. Selective posttranslational persulfidation of proteins (PSSH). (**A**) Heatmap showing the significant changes in protein levels of human biopsies from squamous epithelium (SE) of patients without GERD (n=4), SE of patients with GERD (n=5) and metaplastic segments (n=5). Detailed list of proteins in supplementary Table S5.1. (**B**) Kegg pathway enrichment analysis of proteins found to significantly increase in metaplastic vs GERD-exposed SE samples. Benjamini adjusted p-value was used to filter for significant enrichment. (**C**) Hierarchical clustering of the 925 proteins that significantly changes in at least one comparison. Detailed list of proteins in supplementary Table S5.2. (**D**) Corresponding Kegg pathway analysis for the 3 out of 6 clusters. Benjamini adjusted p-value was used to filter for significant

enrichment. (**E**) Heatmap showing the significant changes of PSSH in metaplastic (n=5) vs GERD-exposed SE (n=5) vs SE w/o GERD (n=4). Detailed list of proteins in supplementary Table S5.3. (F) PSSH fold change levels normalized to the corresponding protein expression levels. (**G**) Kegg pathway enrichment analysis of proteins found to significantly change their PSSH levels (increase or decrease) in metaplastic vs GERD-exposed squamous samples. Benjamini adjusted p-value was used to filter for significant enrichment. (**H**) Hierarchical clustering of the 975 proteins that significantly change their PSSH levels in at least one comparison. Detailed list of proteins in supplementary Table S5.4. (**I**) Corresponding Kegg pathway analysis for the 4 out of 6 clusters. Benjamini adjusted p-value was used to filter for significant enrichment.

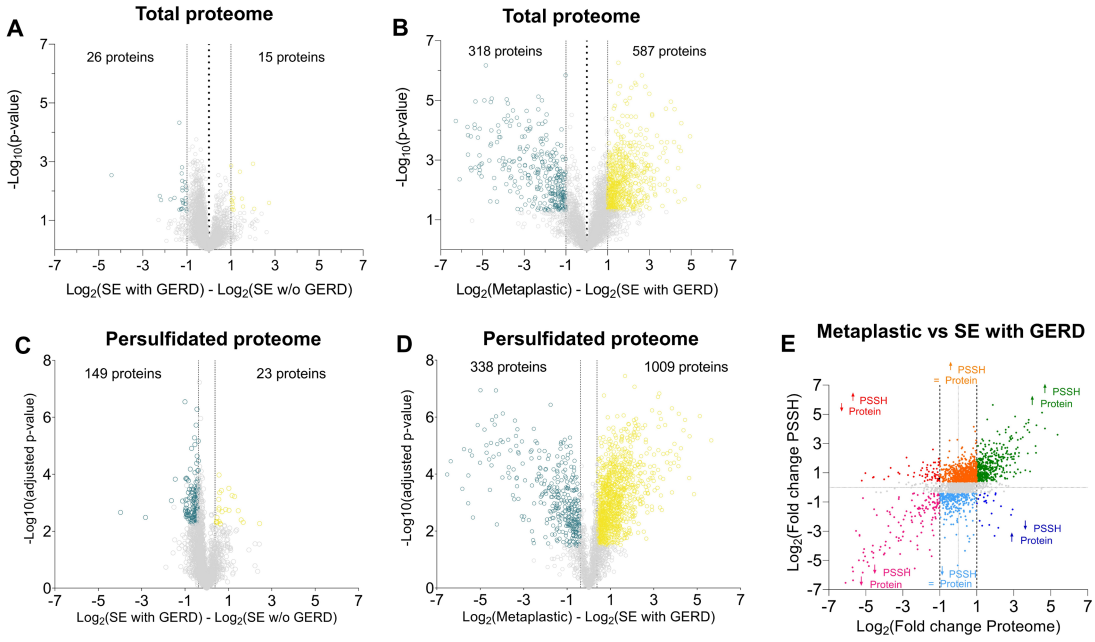


Figure S5.5. Correlation between persulfidome and total proteome changes. Volcano plots representing: (**A**) total proteome profile in squamous epithelium exposed to GERD (SE with GERD) vs squamous epithelium without GERD (SE w/o GERD) and (**B**) metaplastic segments vs paired squamous epithelium exposed to GERD (SE with GERD); (**C**) persulfidation profile in squamous epithelium exposed to GERD (SE with GERD) vs squamous epithelium without GERD (SE w/o GERD) and (**D**) metaplastic segments vs paired squamous epithelium exposed to GERD (SE with GERD); (**E**) Scatter plot characterizing log2 fold changes within the

persulfidome (y-axis) and protein expression (x-axis) for comparison between metaplastic segments and paired, squamous epithelium exposed to GERD (SE with GERD).

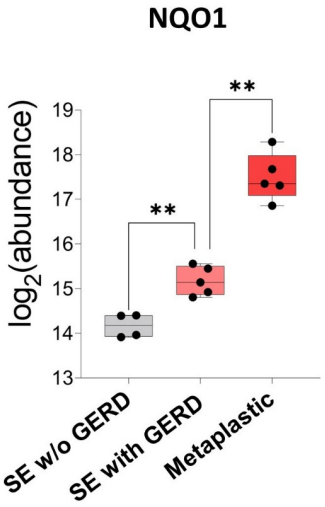


Figure S5.6. Clinical changes in the abundance of NQO1 protein in the squamous epithelium (SE w/o GERD), squamous epithelium exposed to GERD (SE with GERD) and paired metaplastic segments. **p<0.05.

5.4.3. Interventional restoration/inhibition of H_2S-signaling affects metaplastic turnover

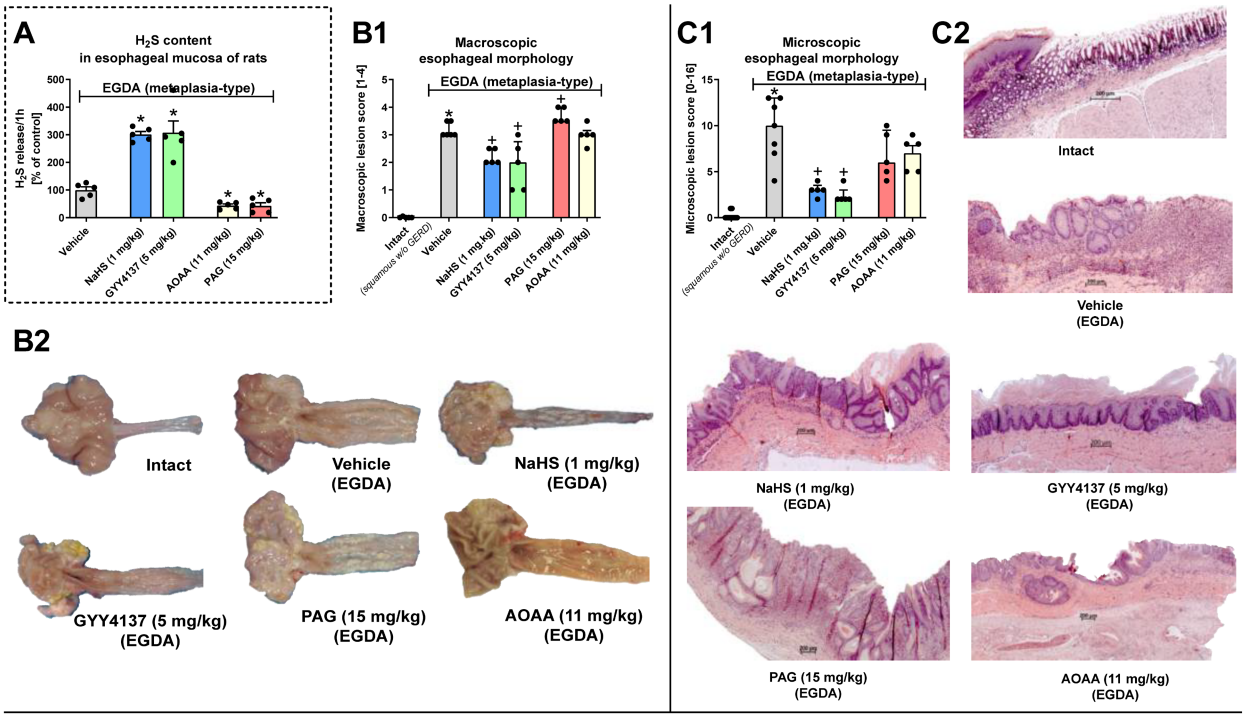
Animal model of BE-lesions

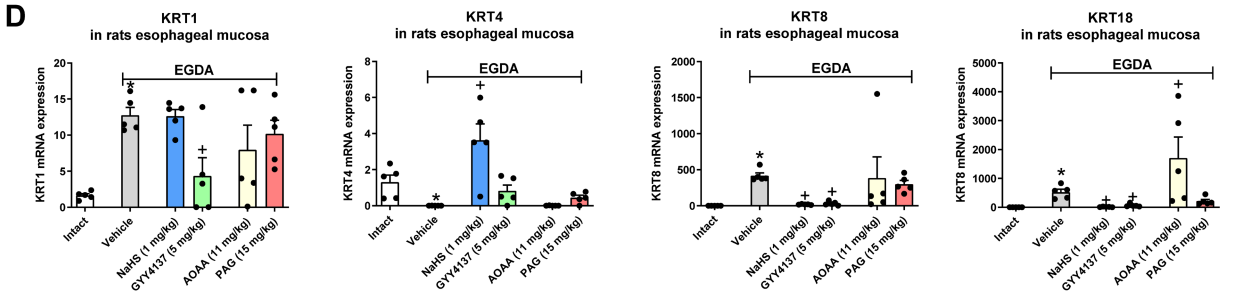
Since PSSH-landscape became altered by GERD in squamous and metaplastic epithelium and was accompanied by the fall in H_2S-bioavailability, we verified whether 10-weeks of daily i.g. treatment with sodium hydrosulfide (NaHS), as a direct source of H_2S, or (4-Methoxyphenyl)-4-morpholinyl-phosphinodithioic acid, sodium salt (GYY4137) a slow-releasing H_2S donor, or selective inhibition of H_2S-enzymes by D,L-propargylglycine (PAG; for CTH) or amino-oxyacetic acid (AOAA; for CBS), would affect BE development in microsurgical animal model of chronic GERD. This demanding translational approach revealed that NaHS (1 mg/kg) and GYY4137 (5 mg/kg) elevated while PAG (15 mg/kg) and AOAA (11 mg/kg) decreased esophageal H_2S-bioavailability in EGDA-rats, compared to vehicle (Figure 5.4A). Subsequently, NaHS or GYY4137 decreased BE lesions score on macro- and/or microscopic levels (Figure 5.4B,C), while inhibition of CTH by PAG (15 mg/kg) increased macroscopic lesions score (Figure 5.4B). Effective doses were carefully selected in the dose-finding experiments (Figure S5.7).

NaHS and GYY4317 reversed the GERD-induced increase in mRNA expression of KRT1, KRT8 and KRT18 and the decrease in KRT4, silencing metaplasia-specific pattern (Figure 5.4D). These KRTs are validated markers of BE[27], including our current clinical proteomic data where “squamous" KRT4 is downregulated and “columnar/metaplastic” KRT18 is upregulated in BE biopsies (Figure S5.8). We also observed GERD-induced chronic esophageal RNA oxidation in rats that was reduced by H_2S-releasing GYY4137 (Figure 5.4E). AOAA and PAG either had no effect or enhanced all these metaplasia-specific events (Figure 5.4D-E).

On systemic level, we noted increased serum level of anti-inflammatory IL-4 and decreased content of pro-inflammatory cytokines IL-5, IL-12p70 and TNF-α (Figure 5.4F) after NaHS and GYY4137. This aligns with the anti-inflammatory activity of NaHS- or GYY4137-derived H_2S, observed in the GI tract[28]. AOAA elevated IL-5, IL-12p70, TNF-α, and decreased IL-13 concentrations. In turn, PAG upregulated IL-6 and TNF-α and downregulated anti-inflammatory IL-4 and IL-13 (Figure 5.4F).

These results showed that interventional restoration of esophageal H_2S-signaling inhibited BE-lesions development functionally and molecularly. H_2S attenuated GERD-triggered and metaplasia-associated esophageal expressions patterns, RNA oxidation and systemic inflammation. Pharmacological depletion of endogenous H_2S evoked opposite effects and promoted metaplasia-specific spectacle. This *in vivo* data corresponds with our clinical observation and mechanistically confirms that H_2S-bioavailability is crucial for the maintenance of PSSH-landscape and functionally for esophageal mucosal balance. Decay of endogenous H_2S, evoked by chronic GERD, contributes to BE pathogenesis.


A
H2S content
in esophageal mucosa of rats
EGDA (metaplasia-type)
H2S release/1h
[% of control]
Vehicle
NaHS (1 mg/kg)
GYY4137 (5 mg/kg)
AOAA (11 mg/kg)
PAG (15 mg/kg)
B1
Macroscopic
esophageal morphology
EGDA (metaplasia-type)
Macroscopic lesion score [1-4]
Intact
(squamous w/o GERD)
Vehicle
NaHS (1 mg/kg)
GYY4137 (5 mg/kg)
PAG (15 mg/kg)
AOAA (11 mg/kg)
B2
Intact
Vehicle
(EGDA)
NaHS (1 mg/kg)
(EGDA)
GYY4137 (5 mg/kg)
(EGDA)
PAG (15 mg/kg)
(EGDA)
AOAA (11 mg/kg)
(EGDA)
C1
Microscopic
esophageal morphology
EGDA (metaplasia-type)
Microscopic lesion score [0-16]
C2
Intact
Vehicle
(EGDA)
NaHS (1 mg/kg)
(EGDA)
GYY4137 (5 mg/kg)
(EGDA)
PAG (15 mg/kg)
(EGDA)
AOAA (11 mg/kg)
(EGDA)


D
KRT1
in rats esophageal mucosa
KRT1 mRNA expression
KRT4
in rats esophageal mucosa
KRT4 mRNA expression
KRT8
in rats esophageal mucosa
KRT8 mRNA expression
KRT18
in rats esophageal mucosa
KRT8 mRNA expression
EGDA
Intact
Vehicle
NaHS (1 mg/kg)
GYY4137 (5 mg/kg)
AOAA (11 mg/kg)
PAG (15 mg/kg)

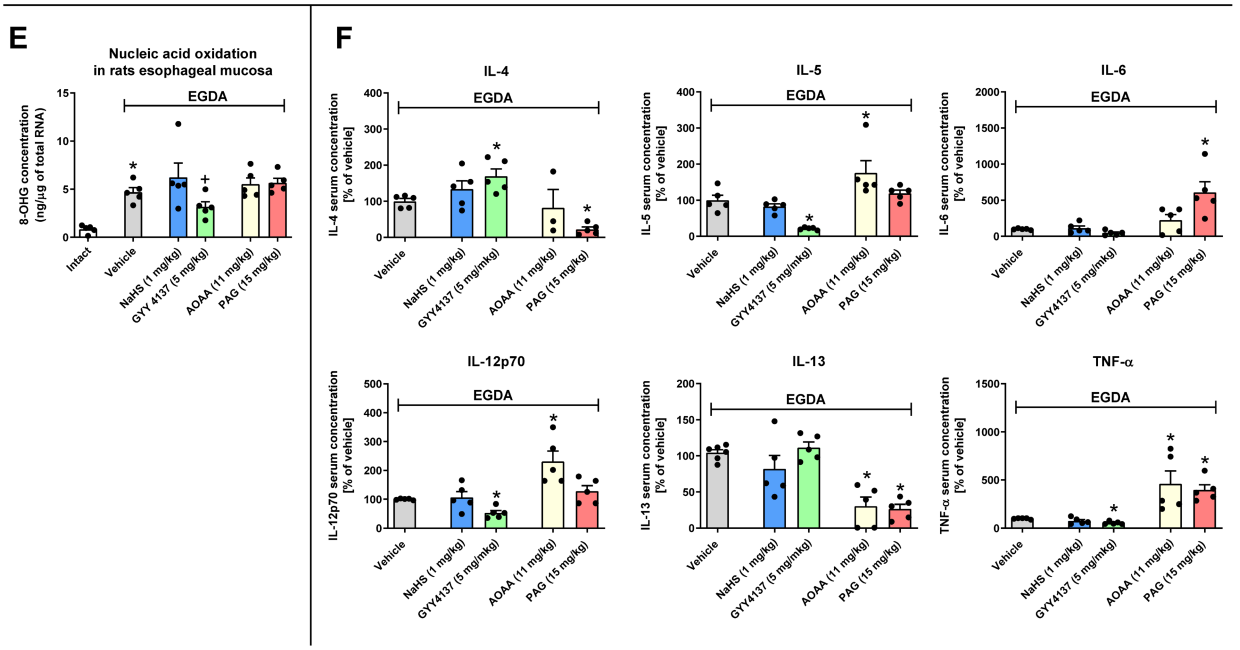

E
Nucleic acid oxidation
in rats esophageal mucosa
8-OHG concentration
(ng/µg of total RNA)
F
IL-4
IL-4 serum concentration
[% of vehicle]
IL-5
IL-5 serum concentration
[% of vehicle]
IL-6
IL-6 serum concentration
[% of vehicle]
IL-12p70
IL-12p70 serum concentration
[% of vehicle]
IL-13
IL-13 serum concentration
[% of vehicle]
TNF-α
TNF-α serum concentration
[% of vehicle]
EGDA
Vehicle
NaHS (1 mg/kg)
GYY4137 (5 mg/kg)
AOAA (11 mg/kg)
PAG (15 mg/kg)

Figure 5.4. Pharmacological modulation of H_2S-bioavailability impacts metaplastic turnovers in esophageal mucosa. (**A**) H_2S-bioavailability in esophageal mucosa of EGDA-rats pretreated i.g. with vehicle (water), NaHS (1 mg/kg), GYY4137 (5 mg/kg), AOAA (11 mg/kg) and PAG (15 mg/kg). Values presented as a mean ± SEM, n=5 samples per group, *p<0.05 vs. Vehicle. (**B**) Macroscopic GERD-induced esophageal damage; (**B1**) Esophageal lesions score of intact and EGDA-rats pretreated i.g. and daily for 70 days with vehicle, NaHS (1 mg/kg), GYY4137 (5 mg/kg), PAG (15 mg/kg) and AOAA (11 mg/kg). Values presented as a median ± IQR, n≥5 samples per group, *p<0.05 vs. Intact, +p<0.05 vs. Vehicle; (**B2**) Representative photographs of esophageal mucosa of each experimental group. Dose-finding data in Figure S5.7. (**C**) Microscopic examination of esophageal epithelium morphology; (**C1**) lesions score of esophageal mucosae of intact rats and those with EGDA pretreated i.g. with vehicle, NaHS (1 mg/kg), GYY4123 (5 mg/kg), PAG (15 mg/kg) and AOAA (11 mg/kg). Values presented as a median ± IQR n≥5 samples per group, *p 0.05 vs. Intact, +p<0.05 vs. Vehicle; (**C2**) representative histological slides of esophageal mucosa. Dose-finding data in Figure S5.7. (**D**) KRT1, KRT4, KRT8 and KRT18 mRNA expression in esophageal mucosa of intact and EGDA-rats pretreated i.g. with vehicle, NaHS (1 mg/kg), GYY4123 (5 mg/kg), PAG (15 mg/kg) or AOAA (11 mg/kg). Values presented as a mean ± SEM, n=5 samples per group, *p < 0.05 vs. Intact, +p<0.05 vs. Vehicle. (**E**) 8-hydroxyguanosine (8-OHG) concentration in esophageal mucosa of intact and EGDA-rats pretreated i.g. with vehicle, NaHS (1 mg/kg), GYY4123 (5 mg/kg), PAG (15 mg/kg) and AOAA (11 mg/kg). Values presented as a mean ± SEM, n=5 samples per group, *p < 0.05 vs. Intact, +p<0.05 vs. Vehicle. (**F**) Multi-target analysis of cytokines panel (IL-4, IL-5, IL-6, IL-12p70, IL-13 and TNF-α) in serum of EGDA-rats pretreated i.g. with vehicle, NaHS (1 mg/kg), GYY4123 (5 mg/kg), AOAA (11 mg/kg) or PAG (15 mg/kg). Values presented as mean ± SEM, n=5 samples, *p<0.05 vs. Vehicle.

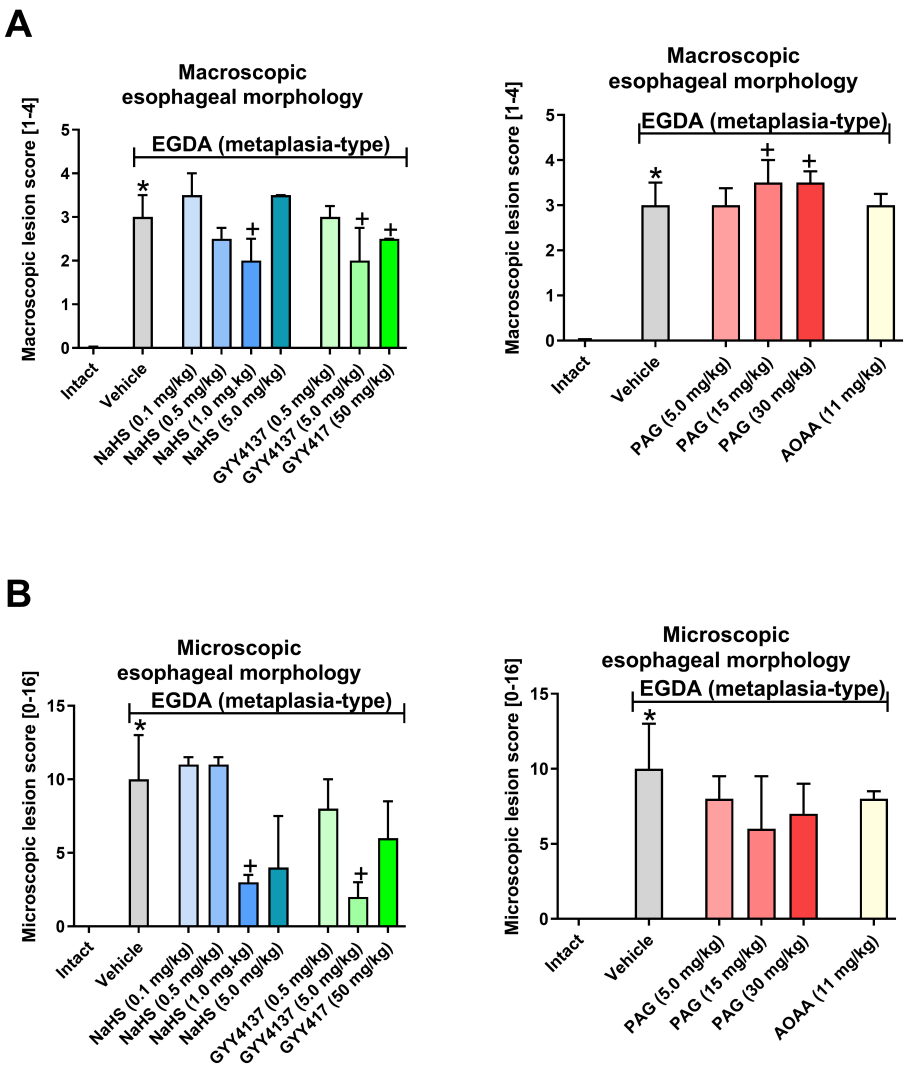


Figure S5.7. Macroscopic GERD-induced esophageal damage. (**A**) Esophageal lesions score of intact, and EGDA-rats pretreated i.g. and daily for 70 days with vehicle, NaHS (0.1–5 mg/kg), GYY4137 (0.5–50 mg/kg), PAG (5–30 mg/kg) and AOAA (11 mg/kg). Values presented as a median ± IQR, n≥5 samples per group, *p<0.05 vs. Intact, +p<0.05 vs. Vehicle. (**B**) Microscopic examination of esophageal epithelium morphology. Lesions score of esophageal mucosae of intact rats and those with EGDA pretreated i.g. with vehicle, NaHS (0.1 – 5 mg/kg), GYY4123 (0.5–50 mg/kg), PAG (5–30 mg/kg) and AOAA (11 mg/kg). Values presented as a median ± IQR n≥5 samples per group, *p 0.05 vs. Intact, $^{+}$p<0.05 vs. Vehicle. *Comment:* NaHS (1 mg/kg) or GYY4137 (5 or 50 mg/kg) decreased the GERD-induced esophageal lesion score on macro- and/or microscopic levels (Figure S5.7A, Figure S5.7B). In contrast, inhibition of CTH by PAG (15 or 30 mg/kg) increased macroscopic lesions score (Figure S5.7A).

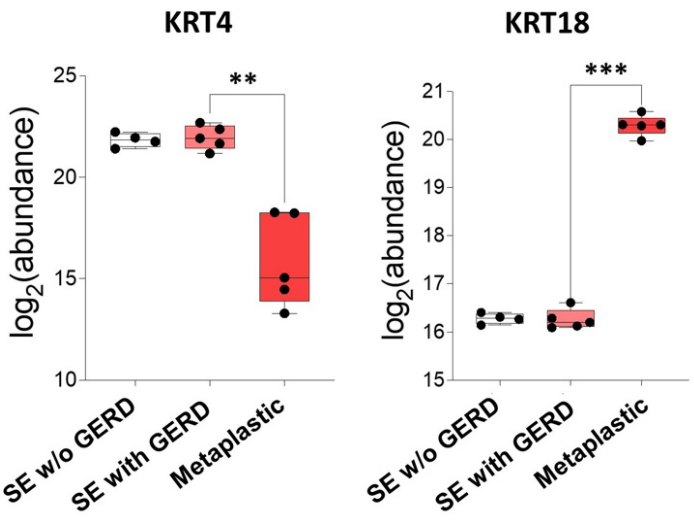


Figure S5.8. **Changes in the abundance of KRT4 and KRT18 proteins** investigated in the squamous epithelium (SE w/o GERD), squamous epithelium exposed to GERD (SE with GERD), and metaplastic segments of human biopsies.

In vitro model of BE.

In parallel, we evaluated the impact of interventionally altered H_2S signaling on BE development in vitro using homogenous human esophageal cell lines. We found that squamous CTH-mutant (K/O) EPC2 with decreased H_2S-levels (Figure 5.2F) are more sensitive to acidified BM (experimental GERD), showing reduced viability compared to wild-type (WT) and CBS-mutant cells (Figure 5.5A). In line with animal and clinical data, these results indicate the predominant role of CTH in the maintenance of H_2S-balance in GERD-exposed esophageal mucosa.

NaHS and GYY4137 restored NES-G2T but not EPC2 or BAR-T viability, that were reduced by acidified BM (Figure 5.5B). These observations for all treatments were dose-sensitive (Figure S5.9) but neither H_2S-donating NaHS and GYY4137 (100 µM each) nor H_2S-enzymes inhibitors (100 µM each) appeared cytotoxic to squamous EPC2, NES-G2T and metaplastic BAR-T w/o experimental GERD (Figure 5.5B). NaHS, GYY4137, AOAA and PAG concentrations were set to 100 µM, also based on PCR experiment where we found that higher doses (500 µM) alone caused significant changes in mRNA expression of selected BE-specific genes in EPC2 cells (Figure S5.10). These results also confirm beneficial bioactivity of H_2S, and that GERD-induced H_2S-depletion is pathogenic for SE cells, initiating metaplastic turnover.

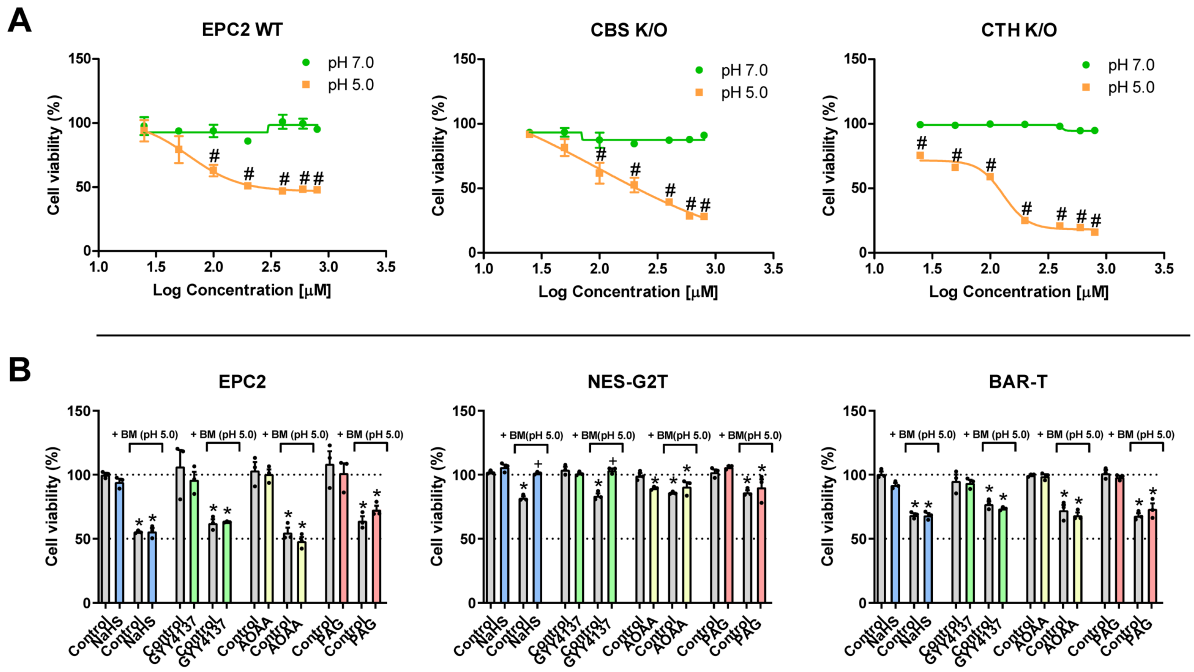
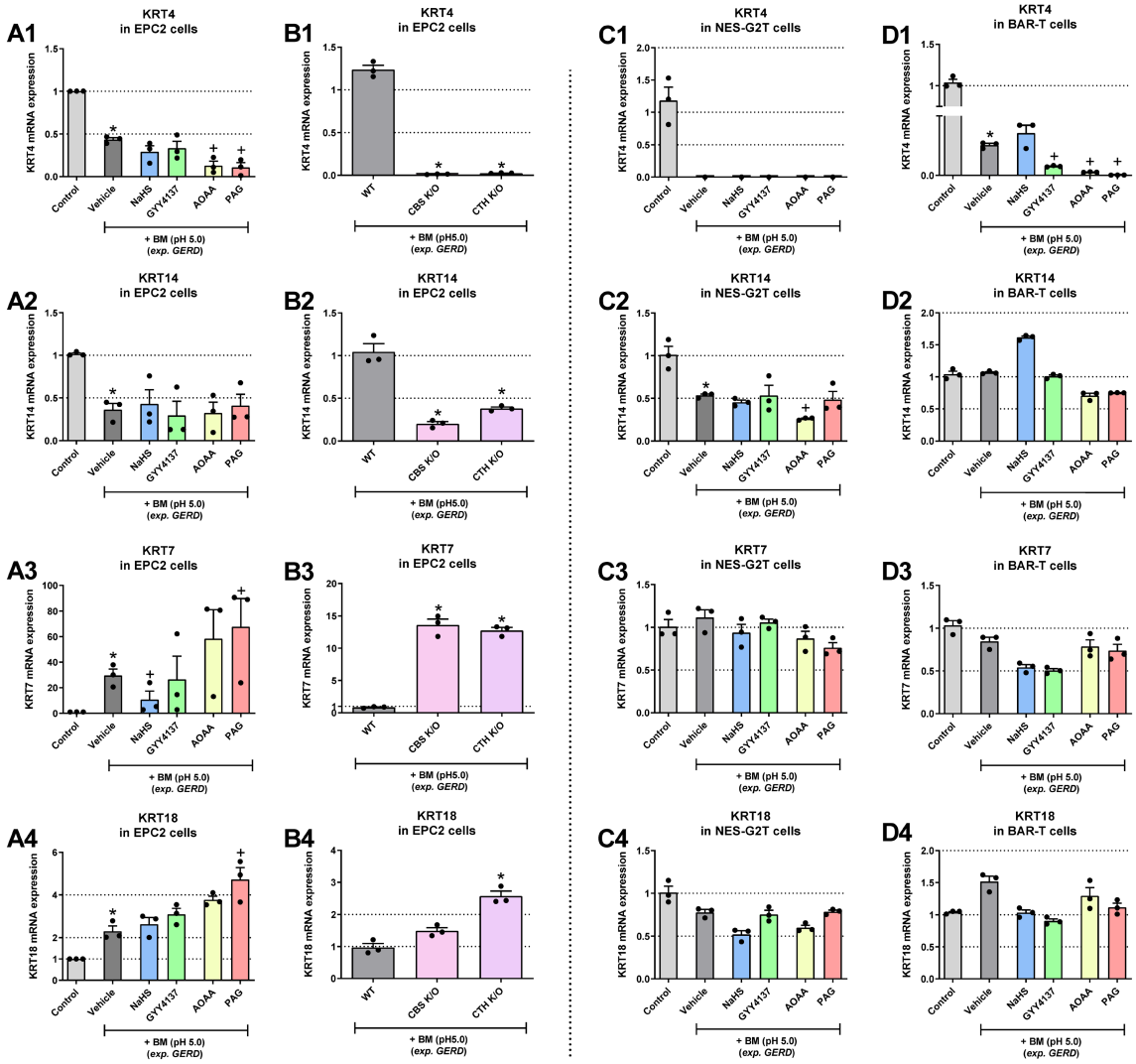


Figure 5.5. Modulation of H_2S bioavailability and the resistance of human esophageal cells to GERD *in vitro*. (**A**) Viability of EPC2 cells +/- CBS or CTH K/O exposed to different bile mixture (BM) concentrations (0-800 μM) applied in regular (pH 7.0) or acidified (pH 5.0) medium. Values presented on log scale as a mean ± SEM, n=3 independent experiments, #p<0.05 vs. 0 μM of BM, pH 5.0. (B) Viability of EPC2, NES-G2T and BAR-T cells exposed or not to acidified BM (100 μM for EPC2, 250 μM for NES-G2T/BAR-T; 30 min) and incubated (24 h) with PAG (**B**), AOAA (C), NaHS (D) and GYY4137 (E) (100 μM each). Values presented as a mean ± SEM, n=3 independent experiments, *p<0.05 vs. Control, +p<0.05 vs. Control + BM. Dose-dependent data in Figure S5.11.

Precisely, following our previously published findings[27] and new clinical data (Figure S5.8), we selected SE-specific (KRT1, KRT4, KRT14, KRT15, KRT24) and two columnar epithelium-specific keratins (KRT7, KRT18). More significant down-regulation of squamous KRT4 after AOAA and PAG treatment and up-regulation of columnar KRT7 and KRT18 after PAG treatment were observed in GERD-exposed EPC2, compared to vehicle (Figure 5.6A). CBS and CTH K/O enhanced metaplasia specific squamous KRT4 and KRT14, and columnar KRT7 mRNA patterns compared to WT cells, all exposed to BM (Figure 5.6B). CTH K/O but not CBS K/O elevated columnar KRT18 expression compared to WT (Figure 5.6B). GYY4137 did not induce any changes, whereas NaHS reversed BM-induced up-regulation of columnar KRT7 vs. vehicle (Figure 5.6A). NES-G2T expressed KRT4 mRNA downregulation after BM. AOAA further decreased squamous KRT14 vs. vehicle (Figure 5.6C). BM-treated BAR-T showed greater down-regulation of squamous KRT4 after AOAA and PAG. BAR-T cells were molecularly more susceptible to acidified BM when incubated with H_2S-inhibitors (Figure 5.6E, Figure S5.11). GYY4137 enhanced BM-induced decrease of KRT4 expression vs. vehicle (Figure 5.6D). Alterations of KRT1, KRT24, KRT15 were also observed (Figure S5.11). All shifts were summarized in Figure 5.6E. Overall, interventional H_2S-depletion enhanced metaplasia-specific molecular pattern in GERD-exposed human squamous and metaplastic cells. These results support our morphological in vivo observations and confirm again that endogenous H_2S maintains physiological balance in esophageal epithelium. H_2S-fall triggers metaplastic-turnover and is BE-specific.



E

	EPC2 + *exp. GERD*	NES-G2T + *exp. GERD*	BAR-T + *exp. GERD*
NaHS (100 µM)	↓KRT7	↔	↔
GYY4137 (100 µM)	↔	↔	↓ KRT4
AOAA (100 µM)	↓KRT4	↓ KRT14	↓ KRT4 ↓ KRT15 ↓ KRT24
PAG (100 µM)	↓ KRT4 ↑ KRT7 ↑ KRT18	↔	↓ KRT4 ↓ KRT15 ↓ KRT24

Figure 5.6. H_2S-dependent molecular response to GERD of squamous and metaplastic human epithelial cells. (**A-B**) SE (KRT4, KRT14) and columnar epithelium-specific (KRT7, KRT18) molecular markers in squamous wild type (WT) EPC2 (A), EPC2+CBS K/O (B), EPC2+CTH K/O (B), NES-G2T (**C**) and metaplastic BAR-T (**D**) cells exposed for 30 min/day to acidified BM for one week. EPC2-WT, NES-G2T and BAR-T cells were additionally cultured with 100 μM of NaHS, GYY4137, AOAA or PAG for one week. Values presented as a mean±SEM, n=3 independent experiments, *p<0.05 vs. Control/WT, +p<0.05 vs. Vehicle. (**E**) The overview of changes in KRTs expression in cells after NaHS, GYY4137, AOAA and PAG administration and exposure to acidified BM treated (exp. GERD); incl. supplementary data in Figure S5.11. ↔ no changes in gene expression, ↑↓ reversion of acidified BM effect, ↑↓ enhancement of acidified BM effect.

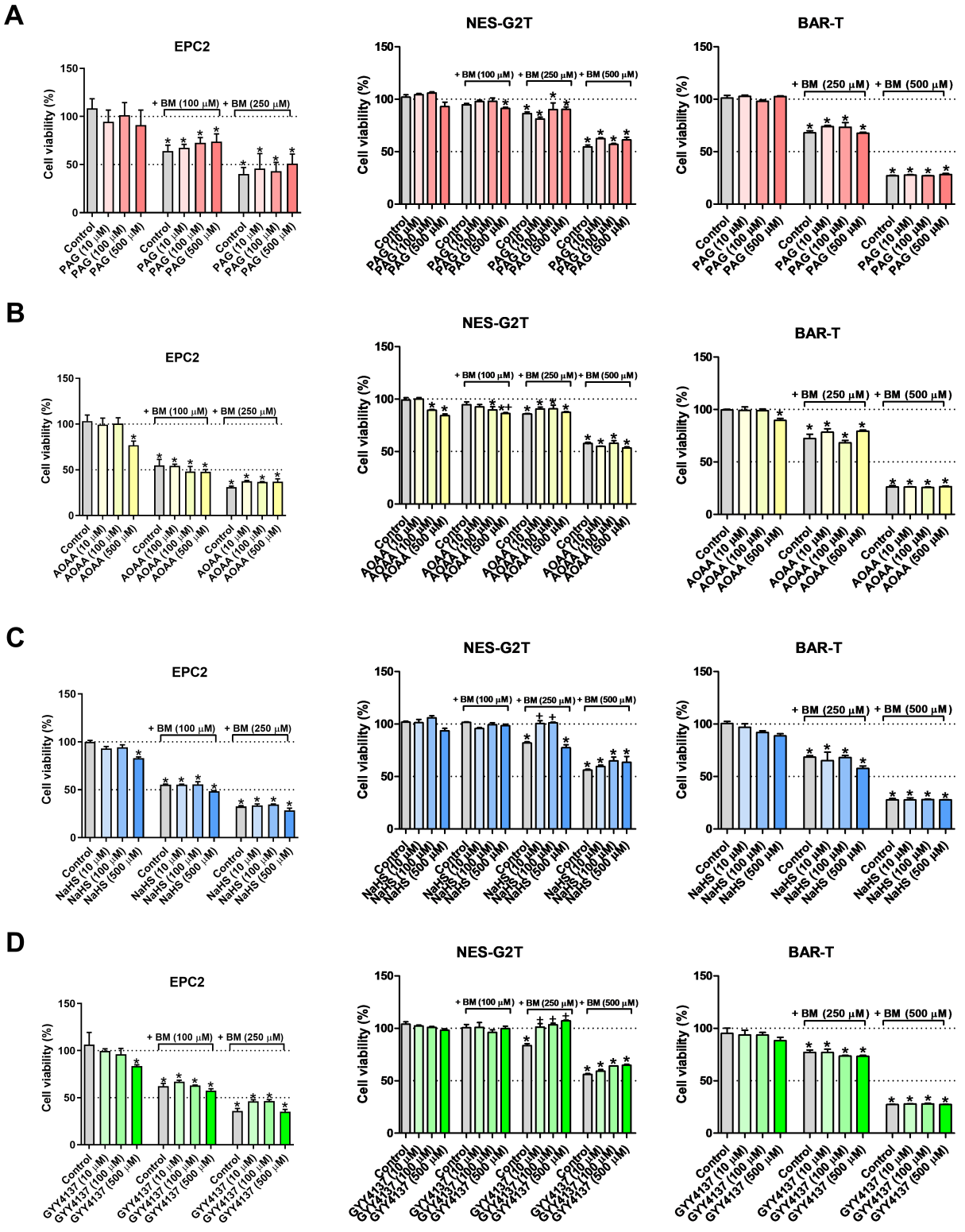

A
EPC2
NES-G2T
BAR-T
Cell viability (%)
+ BM (100 μM)
+ BM (250 μM)
+ BM (500 μM)
Control
PAG (10 μM)
PAG (100 μM)
PAG (500 μM)
B
AOAA (10 μM)
AOAA (100 μM)
AOAA (500 μM)
C
NaHS (10 μM)
NaHS (100 μM)
NaHS (500 μM)
D
GYY4137 (10 μM)
GYY4137 (100 μM)
GYY4137 (500 μM)

Figure S5.9. (**A-D**) Viability of EPC2, NES-G2T and BAR-T cells exposed to acidified BM (0-500 µM; 30 min) and incubated with different concentrations (0-500 µM) of PAG (A), AOAA (B), NaHS (**C**) and GYY4137 (**D**). Values presented as a mean ± SEM, n=3 independent experiments, *p<0.05 vs. Control, +p<0.05 vs. Control + BM

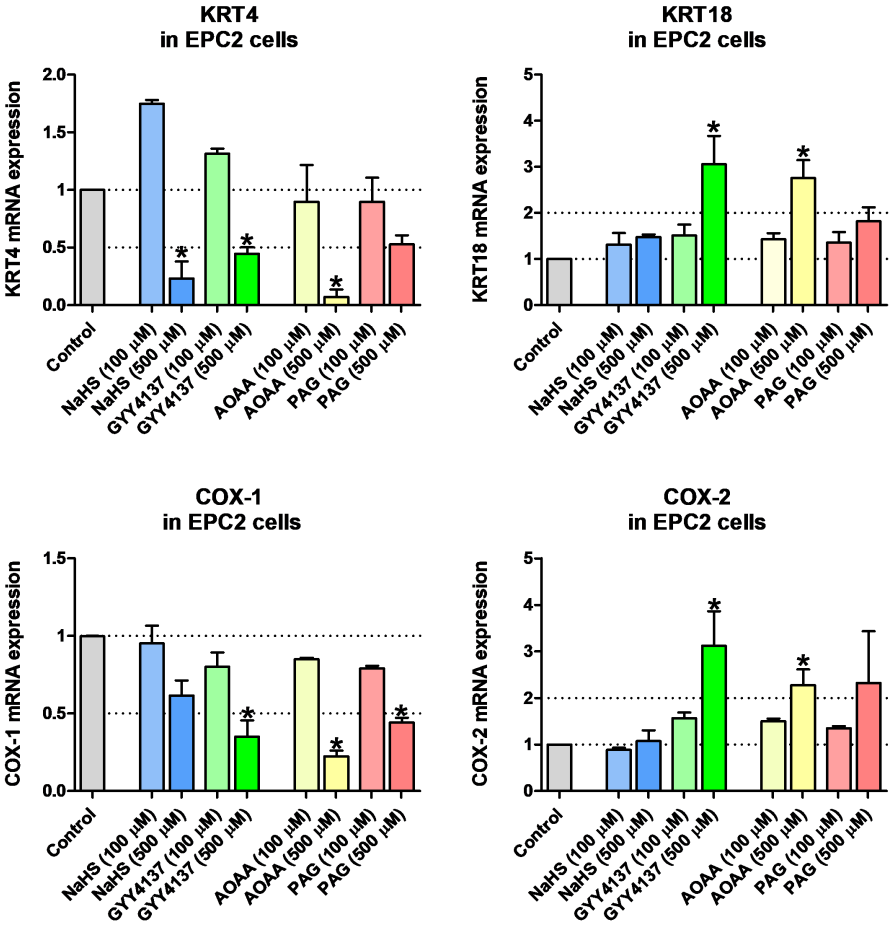


Figure S5.10. Real-time PCR measurement of KRT4, KRT18, COX-1 and COX-2 in EPC2 cells treated 30 min/day with NaHS, GYY4137, AOAA and PAG at 100 µM and 500 µM for one week. Values presented as a mean ± SEM, n=3 independent experiments. *p<0.05 vs. Control.

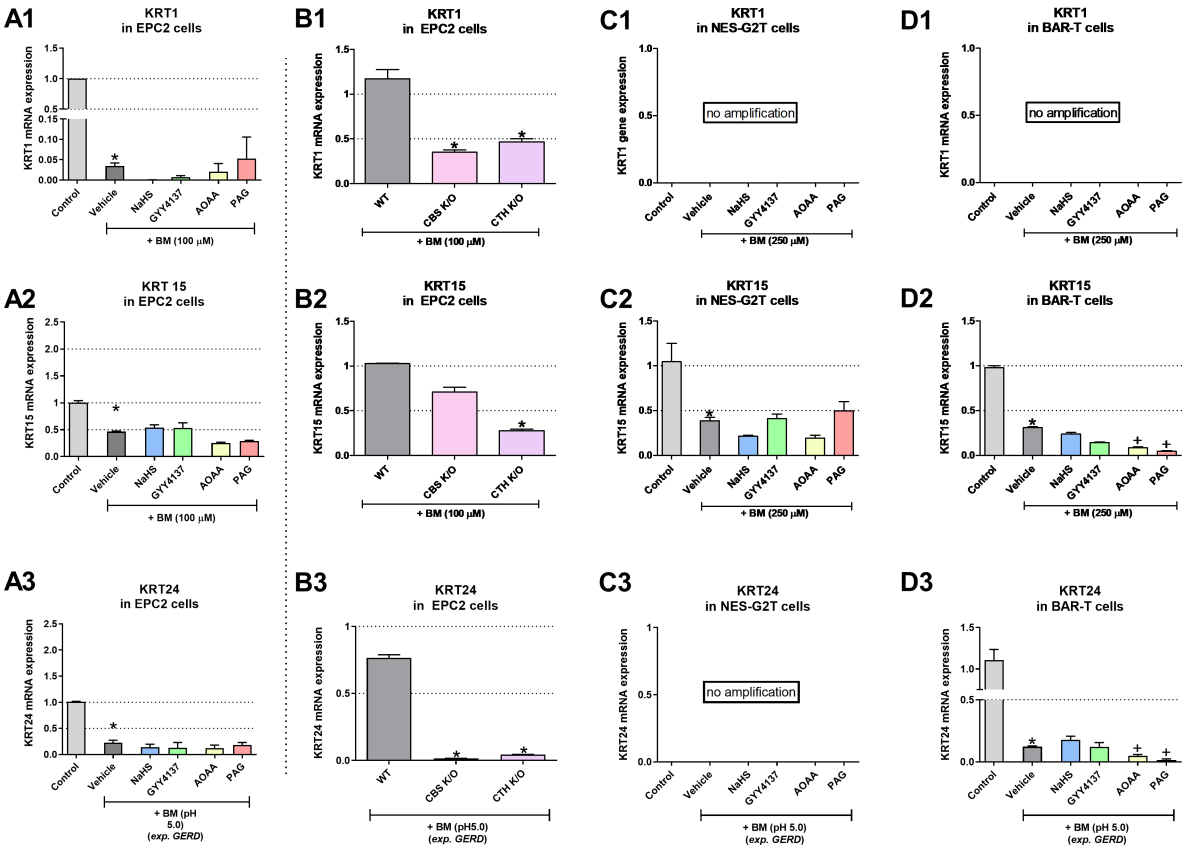


Figure S5.11. Squamous epithelium-specific molecular markers (KRT 1, 15 and 24) in squamous wild type (WT) EPC2 (**A**), EPC2+CBS K/O (**B**), EPC2+CTH K/O (**B**), NES-G2T (**C**) and metaplastic BAR-T (**D**) cells exposed for 30 min/day to acidified BM for one week. EPC2-WT, NES-G2T and BAR-T cells were additionally incubated with 100 μM of NaHS, GYY4137, AOAA or PAG for one week. Values presented as a mean ± SEM, n=3 independent experiments, *p<0.05 vs. Control/WT, +p<0.05 vs. Vehicle.

5.4.4. PSSH-shifts of metaplasia-activating IL-1β, cyclooxygenase (COX)-2/PGE2 and mammalian target of rapamycin (mTOR) pathways. H_2S as a rescue molecule

IL-1β was reported to contribute to BE pathogenesis while gastroprotective PGE2 could enhance the adaptative GERD-resistance of metaplastic tissue[29]. mTOR signaling is crucial for the physiological regeneration of gastric epithelium. Its fall in SE and subsequent rebound accompanies metaplastic turnover in GERD-exposed esophagus[17,30]. These pathways impact each other intracellularly[31]. Thus, based on our clinical data, we considered them as possible targets of H_2S-signaling in esophageal epithelium (Figure 5.7A).

We observed here that interleukin 1 receptor antagonist (IL-1RA) protein (total and persulfidated) is decreased in BE (Figure 5.7A). IL-1RA is a functional antagonist of IL-1β[29]. PGE synthase 2 (PGES2) was decreased in GERD-exposed SE but its total and PSSH protein levels elevated (rebounded) in metaplasia (Figure 5.7A). 15-hydroxyprostaglandin dehydrogenase [NAD(+)] (PGDH), total and PSSH levels increased in BE (Figure 5.7A) but PSSH of PGE2-inactivating prostaglandin reductase 1 (PTGR1) was downregulated (Figure 5.7A). Thus, IL-1β and COX-2/PGE2 pathways emerged here as PSSH/H_2S-sensitive.

Experimentally, GERD up-regulated IL-1β and COX-2, and downregulated COX-1 mRNA expression compared to non-treated EPC2 cells. Indeed, H_2S-donating NaHS or GYY4137 did not alter GERD-effects but CBS-inhibiting AOAA decreased COX-1 and increased COX-2 expression. CTH-inhibiting PAG decreased COX-1 and increased COX-2 and IL-1β mRNA levels, enhancing GERD-effects (Figure 5.7B). Similarly, in EPC2 with CBS or CTH knockouts, COX-2 and IL-1β mRNA were elevated while COX-1

decreased after experimental GERD compared to WT cells (Figure 5.7B). Serum content of IL-1β was elevated in EGDA-rats compared to intact animals (Figure 5.7C). NaHS and GYY4137 decreased while PAG elevated IL-1β. GERD enhanced esophageal IL-1R1 and IL-1R2 but not of IL-1RA mRNA levels in EGDA-rats. NaHS and GYY4137 increased the level of IL-1RA and prevented the EGDA-induced IL-1R1 and IL-1R2 overexpression.

In EGDA-rats, esophageal COX-1 and COX-2 mRNA were decreased and increased, respectively. NaHS or GYY4137 reversed GERD-effects on COXs expression; AOAA also increased COX-1 (Figure 5.7D). Esophageal level of COX-derived PGE2 increased in EGDA-rats compared to physiological mucosa (Figure 5.7E). NaHS and GYY4137 diminished this effect (Figure 5.7E). Similarly, exposure of EPC2 cells to experimental GERD increased PGE2 release that was further elevated by CBS or CTH knockout and PAG, AOAA (Figure 5.7F). Therefore, IL-1β and PGE2 pathways activity was dependent on esophageal H_2S-bioavailability.

Additionally, we clinically confirmed the fall of mTOR protein in GERD-exposed SE that was further elevated (rebounded) in metaplastic segments (Figure 5.7A). Importantly, we also noted the fall in PSSH of mTOR-associated MEAK7 in GERD-exposed SE. Despite its total protein was still downregulated in BE, MEAK7-PSSH was enhanced (rebound) (Figure 5.7A). Total mTOR and MEAK7-PSSH rebound in metaplasia was followed by the functional downstream upregulation of total 40S ribosomal protein S6 (RS6) and PSSH of ribosomal protein S6 kinase alpha-1 (KS6A1) (Figure 5.7A). Experimentally, increased esophageal phosphorylation of mTOR was reported in EGDA-rats and BM-treated EPC2 cells. This effect was reversed by NaHS

and GYY4137 treatment in EPC2 cells and by NaHS in rats (Figure 5.7G,H). Therefore, esophageal activity of mTOR pathway also appeared to be H_2S-sensitive.

Thus, we showed the disease phase-specific, bidirectional PSSH-shifts of the functional antagonist of metaplasia-driving IL-1β (IL1RA) and metaplasia-specific but esophagoprotective PGE2 and mTOR signaling. PSSH-fall indicated functional, pathogenic but transient inactivation of the cytoprotective PGE2 and mTOR in SE. Indeed, PSSH-landscapes of these cytoprotective targets were defensively restored in BE. Of note, under GERD-evoked H_2S-deficiency, PSSH-shifts of other proteins occurred. Nevertheless, selected metaplasia-associated pathways emerged as H_2S-tunable. H_2S-prodrugs enhanced the resistance of SE to GERD, IL-1RA-dependently silenced IL-1β signaling and protected against the dysregulation of PGE2 and mTOR pathways.

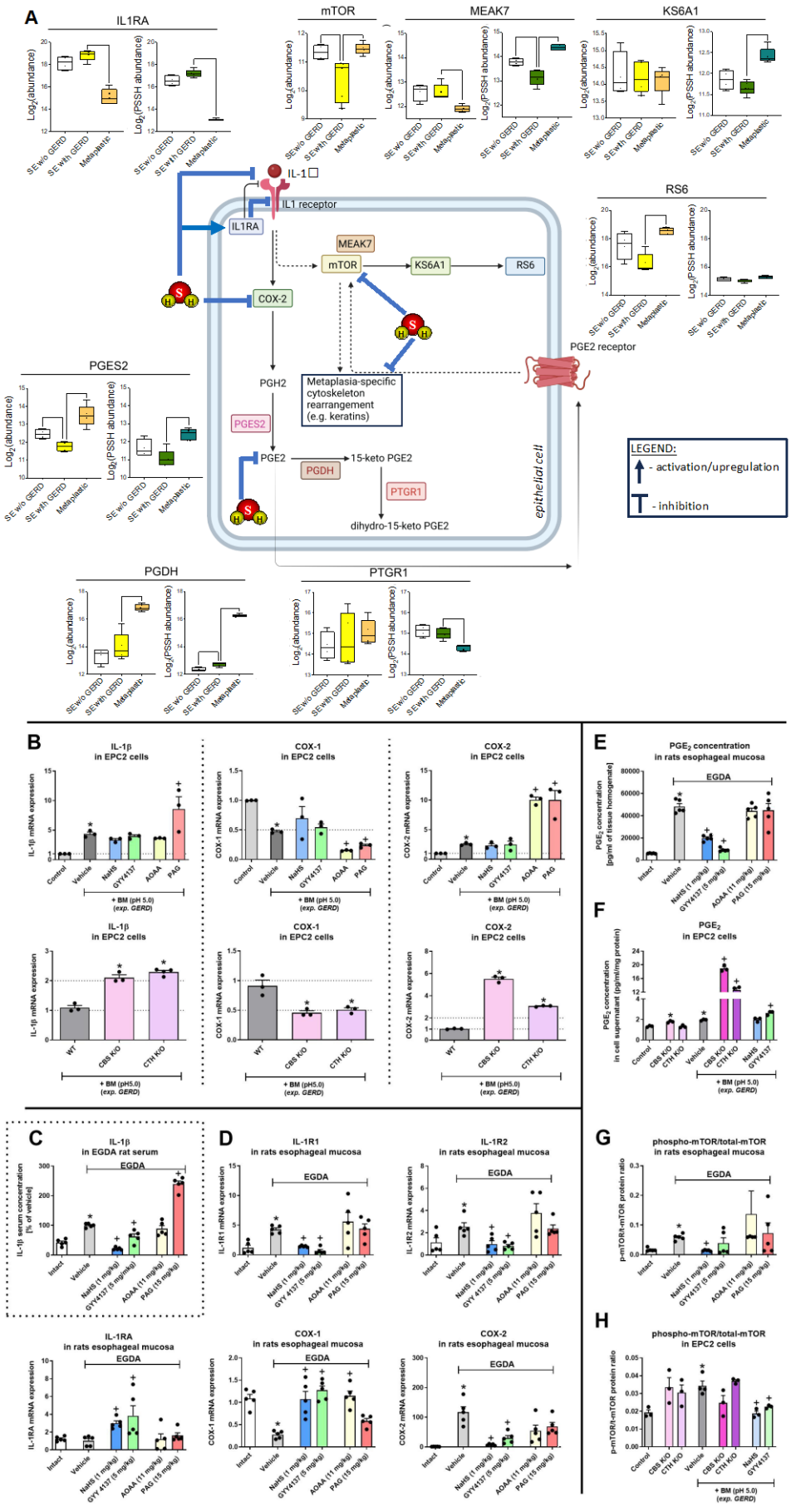

A
IL1RA
mTOR
MEAK7
KS6A1
RS6
PGES2
PGDH
PTGR1
IL-1□
IL1 receptor
IL1RA
MEAK7
mTOR
KS6A1
RS6
COX-2
PGE2 receptor
PGH2
Metaplasia-specific cytoskeleton rearrangement (e.g. keratins)
PGES2
PGE2
PGDH
15-keto PGE2
PTGR1
dihydro-15-keto PGE2
epithelial cell
LEGEND:
- activation/upregulation
- inhibition
SE w/o GERD
SE with GERD
Metaplastic
B
IL-1β in EPC2 cells
COX-1 in EPC2 cells
COX-2 in EPC2 cells
Control
Vehicle
NaHS
GYY4137
AOAA
PAG
+ BM (pH 5.0) (exp. GERD)
WT
CBS KO
CTH KO
+ BM (pH5.0) (exp. GERD)
C
IL-1β in EGDA rat serum
EGDA
IL-1β serum concentration [% of vehicle]
Intact
Vehicle
NaHS (1 mg/kg)
GYY4137 (5 mg/kg)
AOAA (11 mg/kg)
PAG (15 mg/kg)
D
IL-1R1 in rats esophageal mucosa
IL-1R2 in rats esophageal mucosa
IL-1RA in rats esophageal mucosa
COX-1 in rats esophageal mucosa
COX-2 in rats esophageal mucosa
E
PGE2 concentration in rats esophageal mucosa
PGE2 concentration [pg/ml of tissue homogenate]
F
PGE2 in EPC2 cells
PGE2 concentration in cell supernatant [pg/ml/mg protein]
G
phospho-mTOR/total-mTOR in rats esophageal mucosa
p-mTOR/t-mTOR protein ratio
H
phospho-mTOR/total-mTOR in EPC2 cells

Figure 5.7. PSSH-sensitive IL-1β, COX-2/PGE2 and mTOR pathways as mechanistic targets of H_2S-mediated metaplasia inhibition. (**A**) Schematic overview on esophageal IL-1β, PGE2 and mTOR interplay induced by GERD and clinical changes in total and persulfidated (PSSH) proteins for associated targets at subsequent stages of Barrett's metaplasia. (**B**) IL-1β, COX-1/2 mRNA expression in wild type (WT) EPC2 (A), EPC2+CBS K/O (B) or CTH K/O (B) +/- acidified BM (100 µM; 30 min/day) for one week. EPC2 WT were also treated with NaHS, GYY4137, AOAA and PAG (100 µM) for one week. Values are presented as a mean±SEM, n=3 independent experiments, *p<0.05 vs. Control/WT, +p<0.05 vs. Vehicle. (**C**) Il-1β in serum of intact and EGDA-rats treated i.g. with vehicle, NaHS (1 mg/kg), GYY4123 (5 mg/kg), PAG (15 mg/kg) and AOAA (11 mg/kg). Values presented as a mean ± SEM, n = 5 animals, *p < 0.05 vs. Intact, +p<0.05 vs. Vehicle. (**D**) Esophageal IL-1R1, IL-1R2, IL-1RA, COX-1/2 mRNA expression in intact and EGDA-rats treated i.g. with vehicle, NaHS (1 mg/kg), GYY4123 (5 mg/kg), PAG (15 mg/kg) and AOAA (11 mg/kg). Values presented as a mean ± SEM, n=5 animals, *p<0.05 vs. Intact, +p<0.05 vs. Vehicle. (**E**) Esophageal PGE2 concentration in intact and EGDA-rats pretreated i.g. with vehicle, NaHS (1 mg/kg), GYY4123 (5 mg/kg), PAG (15 mg/kg) and AOAA (11 mg/kg). Values presented as a mean ± SEM, n=5 rats/group, *p<0.05 vs. Intact, +p<0.05 vs. Vehicle. (**F**) PGE2 concentration in EPC2 cells +/- CBS or CTH K/O, +/- acidified BM (100 µM; 30 min/day) for one week. Cells were daily co-incubated with NaHS and GYY4137 (100 µM). Values presented as a mean ± SEM, n=3 independent experiments, *p<0.05 vs. Control, +p<0.05 vs. Vehicle. (**G**) mTOR activation (phosphorylation) in esophagus of intact and EGDA-rats pretreated i.g. with vehicle, NaHS (1 mg/kg), GYY4123 (5 mg/kg), PAG (15 mg/kg) and AOAA (11 mg/kg). Values presented as a mean ± SEM, n=5 rats/group, *p<0.05 vs. Intact, +p<0.05 vs. Vehicle. (**H**) mTOR activation in EPC2 cells +/- CBS or CTH K/O, +/- acidified BM (100 µM; 30 min/day) for one week. Cells were daily co-incubated with NaHS and GYY4137 (100 µM). Values presented as a mean ± SEM, n=3 independent experiments, *p<0.05 vs. Control, +p<0.05 vs. Vehicle.

5.5. Discussion

Our data is first to show that equilibrated persulfidomic landscape that relies on H_2S-signaling is physiologically fundamental for esophageal mucosal balance. More importantly, we demonstrated by a recent chemoproteomic method, that under chronic GERD, pathological pathway-specific PSSH-shifts are initiated in physiological SE. We clinically and experimentally showed even more extensive, developmental remodeling of PSSH-pattern, in line with the fall of H_2S/PSSH-bioavailability in endoscopic BE biopsies. Thus, we reinterpreted the current understanding of BE pathogenesis, indicating these events as the new metaplasia-specific phenomena and functional phenotypes detectable even in GERD-exposed SE, controversially, before the onset of metaplasia. Our study uncovers the contribution of altered PSSH-landscape and decreased H_2S-bioavailability in BE etiology.

Reported here, increased proteins of H_2S enzymes (CTH and/or CBS) reflect the compensative epithelial response to the global pathological fall of PSSH and declined H_2S-bioavailability, evidenced in clinical and experimental metaplastic biopsies. *In vitro* model of chronic GERD/BE, utilizing human-derived esophageal cells, in parallel with clinical and *in vivo* data showed GERD-reduced H_2S content, even in the squamous cells, originated from patients with (NES-G2T) or without (EPC2) GERD, but CBS and CTH proteins were unchanged. This discrepancy could result from the cellular heterogenicity of animal and human biopsies, and the infiltration of the immune cells or the shorter duration of GERD *in vitro*, possibly influencing the overexpression of H_2S-enzyme[19]. Nevertheless, metaplastic BAR-T cells had also lower but stable, GERD-resistant H_2S-bioavailability. Interestingly, under additional and chronic interventional

deficiency of endogenous H_2S (genetic or pharmacological), metaplasia-associated morphological and/or molecular changes were accelerated/enhanced in our *in vitro* and *in vivo* models of BE. Thus, we clinically and mechanistically indicate that chronic pathology-driven fall in PSSH-levels and endogenous H_2S-signaling affects physiological balance in esophageal epithelium, initiate pathway-specific PSSH-shifts and developmental, adaptative but pathology-driven molecular rearrangement, leading to BE.

Consequently, we showed that interventionally restored esophageal H_2S by the daily i.g. treatments with various pharmacological H_2S-donors counteracted BE development. We noted that either the direct source of H_2S (NaHS) or slower releasing donor (GYY4137) increased esophageal H_2S-bioavailability and reduced the development of BE-lesions in EGDA rats. Metaplasia-specific mRNA expression pattern for selected keratins and COX-es was either abolished or/and reversed. H_2S-donating GYY4137 diminished mucosal nucleic acids oxidation regardless of long-term GERD. Indeed, oxidative stress and nucleic acids damage can be evoked in esophageal mucosa by bile acids and low pH, triggering BE pathogenesis[18]. Not surprisingly, some molecular metaplasia-associated outcomes were not reversed equally by NaHS and GYY4137, that we consider because of the divergent H_2S-releasing dynamics. We also noted *in vitro* that H_2S-donors enhanced the resistance of human squamous NES-G2T cells to chronic GERD but were molecularly less effective than in rats. These phenomena could be due to the general translational limitations of the *in vitro* models, since we observed here that in rats NaHS and GYY4137 also attenuated, while H_2S-inhibition enhanced GERD/BE-associated systemic inflammation.

Several H_2S-prodrugs, such as H_2S-releasing naproxen-derivative (ATB-346) or mitochondria-targeted H_2S donor (AP39) were recently developed, considered GI-safe and promisingly investigated clinically and experimentally[23,32]. Of note, current clinical pharmacology is based on proton pump inhibitors to target chronic GERD/prevent BE but having debatable effectiveness and clear adverse effects[33]. Initial research attempts were also made in upper GI tract regarding H_2S but were limited to achalasia or acute and transient chemical esophagitis in rats or to basic *in vitro* model[26,34]. However, H_2S-prodrugs and H_2S/PSSH-signaling were never deeply investigated in pathogenesis of esophageal metaplasia. Thus, we are first to evidence that H_2S-therapeutics may be considered as an alternative/additional treatment modality to prevent BE.

Uniquely for GI-research, we implemented here the recent chemoproteomic method that allowed us to clinically evidence the clusters within PSSH (e.g. Table S5.4, clusters 3, 5) and total proteome (e.g. Table S5.2, Cluster 2), suggesting a new potential early biomarker in GERD-exposed SE, preceding BE development. The list includes, but not exclusively, subsequent fall in PSSH of nuclear mitotic apparatus protein 1 (NUMA1)[35] or increase of total and persulfidated NQO1 that are strongly associated with ferroptosis and/or invasiveness of GI cancer[36]. We also defined global but protein-specific PSSH-shifts in metaplastic segments. Our data is the exceptional example of proteomic change in human biopsies representing three clinically subsequent states in esophageal mucosa: SE, SE exposed to GERD and BE. Our persulfidomic approach uncovered >700 new BE-associated pathways that were elusive for routine total proteome evaluation. This includes e.g. the PSSH-fall (w/o total protein change) of DNA replication licensing factor MCM5 in SE of GERD patients. This factor contributes to DNA replication initiation and elongation in eukaryotic cells[37]. In BE biopsies, we showed

e.g. decreased PSSH (w/o total protein change) of translationally controlled tumor protein (TCTP) (w/o total protein change) that regulates apoptosis and mitotic cell cycle[38].

Although total PSSH and H_2S-content declined in BE, PSSH-shifts were bidirectional (up- or downregulation) in protein- and disease state-specific manner. Importantly, functional phenotypes were consistent. This is in line with the persulfides biochemistry since PSSH is the oxidation-sensitive and reversible posttranslational modification. PSSH is protective, regulatory and depends on sulfide signaling[13,14]. Chronic epithelial oxidation and inflammation induced by GERD, could finally exhaust cellular capacity to maintain endogenous H_2S-bioavailability and initiate transpersulfidation. This process is based on the transfer of protein persulfides from one protein to another[13]. Our clinical and experimental data led us to conclude that under H_2S-deficiency persulfidomic landscape of epithelial cells became altered in SE and subsequently led to extensive but (considering pathological microenvironment) the most optimal PSSH-rearrangement and metaplastic-turnover. This allows metaplastic cells of BE to avoid further H_2S-leakage and to adapt esophageal mucosa (at least transiently) to pathological microenvironment.

Interestingly, also previously known, metaplasia-associated pathways revealed their PSSH-shifts. Precisely, PSSH and total proteins for IL1RA/IL-1β, PGE2/COX-2 and mTOR pathways (but not exclusively) were altered in GERD-exposed SE and in BE. Elsewhere, IL-1β induced a stepwise development of BE-lesions in the murine esophagus[20]. COX-2 expression and PGE2 content (catalytic product of COX-1/2[39]) were reported to be enhanced in BE patients[40]. Having observed the clinical fall in PSSH and total IL1RA (endogenous inhibitor of IL-1β[29]) in BE, we demonstrated that restored

H_2S-bioavailability by i.g. treatment of EGDA-rats with H_2S-donors over 10-weeks, upregulated esophageal expression of IL1RA (IL-1β antagonist) and downregulated the release of BE-associated PGE2 and IL-1β. In contrast, pharmacological or genetic inhibition of H_2S-enzymes activated IL-1β and PGE2/COX-2 signaling and promoted BE development.

Souza *et al.* proposed that GERD-exposed squamous esophageal cells undergo paligenosis via reactivation of mTOR. Cells could re-enter the cycle for tissue repair, potentially acquiring regenerative capacity or transdifferentiating into GERD-resistant metaplastic tissue[17]. Metaplastic re-epithelialization of ulcerated esophagus in rat model could be also due to the transcommitment *via* paligenosis of immature regenerative intestinal cells during the wound healing[41,42]. Indeed, our results revealed a GERD-evoked increase in mTOR-phosphorylation of esophageal mucosa of EGDA-rats or in human squamous cells. Also, our clinical analysis indicated a decrease in total mTOR and PSSH of mTOR-associated MEAK7 in GERD-exposed SE; both (and their downstream proteins) further rebounded in metaplasia. Notably, pharmacologically restored H_2S functionally inhibited the activation of mTOR in rats and human cells. Indeed, cysteine reactivity was shown recently to impact proteins phosphorylation[43]. The above-described phenomena led us to conclude that enhanced H_2S levels in SE counteract BE, mechanistically inhibiting metaplasia-specific IL-1β, PGE2 and mTOR cellular interplay (that emerged here to be PSSH-sensitive). These outcomes confirmed our fundamental observation that PSSH-shifts and H_2S-imbalance trigger BE pathogenesis.

Taken together, stable PSSH-landscape and H_2S-bioavailability appeared here not only to significantly regulate physiological balance in esophageal epithelium.

Pathology-driven overload of the anti-oxidative PSSH/H_2S interplay emerged to functionally underlie BE pathogenesis and uncovered the new phenomenon in fundamental and clinical understanding of GI (patho)physiology. Chronic GERD might overload the defensive and anti-oxidative PSSH/H_2S-dependent response of SE, leading to pathway-specific PSSH-shifts and metaplastic turnover. Decline in PSSH and H_2S-levels emerged as metaplasia-specific. Constantly decreased H_2S-bioavailability evokes even greater PSSH-landscape remodeling and cellular rearrangement in BE. These developmental events adaptatively enhance the resistance of metaplastic cells to GERD and prevent further loss of cytoprotective H_2S. Previously discovered molecular regulators of BE pathogenesis showed PSSH-shifts and appeared as H_2S-sensitive. Persulfidomic analysis revealed also new BE-specific pathways that were elusive before. Restoration of esophageal H_2S by i.g. treatment with H_2S-prodrugs inhibits GERD-inducible, metaplasia-driving interplay in SE, including IL-1β, PGE2 and mTOR pathways and prevents BE development. Thus, H_2S-therapeutics could counteract BE development in GERD patients.

5.6. Material and methods

Clinical esophageal biopsies. Three-sets of samples were taken during routine diagnostic/control endoscopies: BE and paired GERD-exposed squamous segments (n=11 patients), as well as squamous segments of patients w/o GERD (n=4). The Barrett's segment was biopsied at least 2 cm above the gastroesophageal junction, recognized endoscopically as typically pink-colored mucosa. Normal squamous epithelium was pinched at least 2 cm proximal of the Barrett's segment. Normal

squamous epithelium of patients without GERD was pinched at least 2 cm proximal of the Z-line. Barrett's metaplasia was confirmed histologically. All patients signed informed consent for the use of their biopsy material and did not have a history of any severe systemic diseases or recently diagnosed malignancies. All patients with BE had proven incompletely differentiated intestinal type of columnar epithelium without dysplasia in the histologic control biopsies with no signs of active or acute inflammation. Clinical protocol was approved by the ethics review committee of Jagiellonian University Medical College (approval no 1072.6120.74.2020, permission date: 01 April 2020).

Evaluation of total persulfidation (PSSH) and persulfidated and total proteome profiles. Pathway-specific qualitative and quantitative persulfidomic PSSH-changes, normalized to total proteome, were evaluated in protein lysates of clinical samples enriched by dimedone-switch method, following the recent protocol by Zivanovic et al.[12]. In similar manner, in-gel analysis of total PSSH was performed.

Persulfidation enrichment for proteomic analysis. Human esophageal biopsies were lysed in HEN (50 mM HEPES, 1 mM EDTA, 0.1 mM neocuproine, 1 % IGEPAL, 2 % SDS, pH 7.4) supplemented with 1 % proteinase inhibitors and 10 mM 4-Chloro-7-nitrobenzofurazan (NBF-Cl). The Qiagen Tissue Lyser II and 5-mm stainless steel beads were used to disrupt the tissues. Persulfidation enrichment was carried out using previously described method[44]. After enrichment, proteins were trypsinized in 50 mM ammonium bicarbonate, 1 mM $CaCl_2$ using 1:20 ratio (Trypsin : protein, w/w). Desalting step was performed on the peptides using Supel™-Select HLB SPE Tube following the manufacturer's recommendations. Samples were dried and then resuspended in 0.1 % trifluoroacetic acid. A quality control step was carried out using an

Dionex UltiMate 3000 (RSLC) system with a PepSwift Monolithic® Trap 200 µm * 5 mm (Thermo Fisher Scientific).

Total proteome analysis. 100 µg of proteins from the persulfidation lysate was taken and precipitated using methanol/chloroform (sample/methanol/Chloroform; 4/4/1) to remove detergent. Proteins pellets were then resuspended with 6 M guanidine hydrochloride in 50 mM ammonium bicarbonate. 50 µg of proteins were trypsinized and peptides were desalted followed by samples quality control as previously described[44].

LC/MS and data analysis. Sample analysis was carried out using an Dionex UltiMate 3000 RSLC Systems (RSLC) system (Thermo Fisher Scientific) connected with an Orbitrap Eclipse™ Tribrid™ Mass Spectrometer via an EASY-spray (Thermo Fisher Scientific). Peptides were separated on Acclaim™ PepMap™ 100 C18 column (Thermo Fisher Scientific) using a 120 min (persulfidation) or 150 min (total proteome) linear gradient from 3 to 35 % B (84 % Acetonitrile, 0.1 % Formic Acid) at a flow rate of 250 nL/min. The timsTOF Pro (Bruker) was used in PASEF mode using Compass Hystar 5.0.36.0. The TIMS setting was as follows: Mass Range 100 to 1700 m/z, 1/K0 Start 1.6 Vs/cm2 End 1.6 Vs/cm2, Ramp time 100 ms, Lock Duty Cycle to 100 %, Capillary Voltage 1500V, Dry Gas 3 l/min, Dry Temp 180°C. PASEF settings: 10 MS/MS scans, charge range 0-5, active exclusion for 0.4 min, Scheduling Target intensity 20000, Intensity threshold 2500, CID collision energy 49 eV.

PEAKS ONLINE software was used for protein identification and quantification. The search parameters were set at 15 ppm for precursor mass tolerance, 0.5 DA for the fragment mass tolerance, specific tryptic digestion and 3 missed cleavages. FDR threshold was set at 1% for PSM and proteins. Proteins with less than 2 unique peptides

were excluded from quantification. For persulfidation analysis, NBF (+163.00961594 Da) on C, K, R, DCP (+168.0786442 Da) on C, N-term acetylation (+42.010565 Da), and methionine oxidation (+15.994915 Da) were added as variable modifications. For total proteome analysis, only DCP was omitted.

Bioinformatic analysis. The total proteome was normalized based on TIC. The persulfidation data set was Normalized using eigenMS on R studio[45]. Both datasets were further tested for significance using Perseus[46]. Statistical analysis of both PSSH and total proteome was carried out using Welch's test, non-paired for the Normal vs Control comparison and paired for the Metaplastic vs Normal comparison. Benjamini-Hochberg p-value correction was used for the persulfidation dataset. The fold Change of significantly changing proteins in the persulfidation dataset were further normalized protein by protein using the fold change calculated in the total proteome data. For persulfidation, the fold change threshold was set at minimum +/- 30 % while the total proteome fold change threshold was set a 100 %. Downstream analyses were performed using the persulfidation data set normalized to the total proteome. Cluster analysis was performed using Fuzzy c-means calculation on R studio[47]. Pathway analysis was performed using DAVID[48] and plotting in Rstudio.

Animal model of GERD: experimental design, data, and samples collection. Animal studies were approved by the Local Animal Care and Use Ethical Committee held by Jagiellonian University Medical College in Cracow and was run in compliance with the European Union regulations, ARRIVE guidelines and with implications for 3Rs principles (approval no 23/2016, permission date: 20 July 2016). Animal studies were performed on male Wistar rats (Rattus norvegicus) in the total number of 80. Rats were

fasted for 24 h before surgery with a free access to drinking water. To induce mixed duodeno-gastroesophageal reflux in male Wistar rats, an anastomosis between the gastroesophageal junction and the duodenum on anterior mesenteric border was created (esophago-gastroduodenal anastomosis, EGDA), as previously described[27]. After the surgical procedure and during the recovery phase, animals were infused subcutaneously (s.c.) with 5-10 mL of isotonic sodium chloride. Rats were fed a standard diet with free access to the drinking water. After the recovery phase, animals were randomized to experimental groups (n=5 each, sufficient to reach the data statistically significant; therefore, additional experiments on larger amount of rats were not required), treated daily for 10 weeks i.g. with: a) water as vehicle, b) sodium hydrosulfide (NaHS, 0.1-5 mg/kg) as spontaneous source of H_2S, c) (4-Methoxyphenyl)-4-morpholinyl-phosphinodithioic acid, sodium salt (GYY4137; 0.5-50 mg/kg) as H_2S donor with slow release rate, d) D,L-propargylglycine (PAG; 5-30 mg/kg) as CTH inhibitor, and e) amino-oxyacetic acid (AOAA; 11 mg/kg) as CBS inhibitor[28,49]. NaHS, PAG and AOAA were purchased from Sigma Aldrich (Saint Louis, MO, USA). GYY4137 was synthesized in-house by Dr. Whiteman lab, as described in. All compounds were dissolved in water.

Macroscopic and microscopic evaluation of esophageal metaplasia; samples collection. After treatments, animals were anesthetized with isoflurane. Esophagus was removed and opened longitudinally. Then rats were sacrificed by intraperitoneal (i.p.) administration of a lethal dose of pentobarbital (Biowet, Pulawy, Poland). Macroscopic examination of the metaplasia-type morphology was done, following previous protocol[27]. Microscopic evaluation of chronic lesions

reflecting/covering the level of metaplasia-type changes was blindly done by a clinical pathomorphologist and scored using the 0-16 points-modification of established scale[27].

The macroscopic degree of the esophageal mucosa injury and disease progression was assessed blindly using following criteria:

0 – physiological normal esophageal mucosa with squamous epithelium, width below 0.5 cm

0.5 – inflammatory lesions without ulcers and without papillomatosis/keratosis reaching up to 1 cm of the esophagus as measured from the anastomosis (upper border)

1 – inflammatory lesions without ulcers and without papillomatosis/keratosis reaching >1 cm up to 2 cm of the esophagus as measured from the anastomosis (upper border)

1.5 – inflammatory lesions without ulcers and without papillomatosis/keratosis reaching >2 cm of the esophagus as measured from the anastomosis (upper border)

2 – inflammatory lesions with macroscopic ulceration and/or papillomatosis/keratosis but without macroscopic transformation into columnar epithelium of the esophageal mucosa surface reaching up to 2 cm of the esophagus as measured from the anastomosis (upper border)

2.5 – inflammatory lesions with macroscopic ulceration and/or papillomatosis/keratosis but without macroscopic transformation into columnar epithelium of the esophageal mucosa surface reaching > 2 cm of the esophagus as measured from the anastomosis (upper border)

3 – macroscopic transformation into columnar epithelium of the esophageal mucosa surface reaching up to 2 cm of the esophagus as measured from the anastomosis (upper border)

3.5 – macroscopic transformation into columnar epithelium of the esophageal mucosa surface reaching > 2 cm of the esophagus as measured from the anastomosis (upper border)

4 – perforation or tumor of the esophageal mucosa

For histology, biopsies containing the esophagus were sectioned and the segments were embedded in paraffin, cut into 4 µm sections using a microtome and stained by hematoxylin/eosin (H&E) for microscopic assessment. Samples were evaluated using a light microscope (AxioVert A1, Carl Zeiss, Oberkochen, Germany). Digital documentation of histological slides was obtained using the ZEN Pro 2.3 software (Carl Zeiss, Oberkochen, Germany).

The microscopic degree of the esophageal mucosa injury was assessed blindly by clinical pathomorphologist using following criteria:

1 – presence of erosions interpreted as superficial mucosal defect located apart from histological border of ulceration area (0 – 1 pt).

2 – percentage (%) of surface covered by ulceration as loss of the full thickness of the epithelium, beyond the basal membrane (0% – 0 pt; 1-29% – 1 pt; 30-59% – 2 pts; 60-100% – 3 pts).

3 – presence of granulation tissue (new connective tissue with new capillaries), regeneration/re-epithelialization and/or goblet metaplasia (0 – 3 pts).

4 – chronic inflammation shown as presence (density) of macrophages, monocytes, and lymphocytes in tissue sections, thickening of squamous epithelium with basal cell layer occupying up to 30% of its height; elongation of connective tissue papillae (0 – 3 pts)

5 – activity of inflammation as presence of neutrophils within inflammatory infiltration (0 – 3 pts).

6 – esophageal wall thickness covered by the inflammatory infiltrate (reached mucous membrane only – 1 pt, extended into muscularis mucosae – 2 pts, extended to submucosa – 3 pts).

Cell culture. The EPC2 cell line transformed with human telomerase reverse transcriptase (hTERT) was a kind gift of K. K. Krishnadath (University of Amsterdam, The Netherlands). EPC2 cell line was cultured in Keratinocyte-SFM medium (Life Technologies/Gibco, Grand Island, NY, USA) supplemented with 50 µg/ml Bovine Pituitary Extract (BPE; Life Technologies/Gibco, Grand Island, NY, USA), 0.2 ng/ml human recombinant Epidermal Growth Factor (EGF; Life Technologies/Gibco, Grand Island, NY, USA), 100 U/ml penicillin and 100 µg/ml streptomycin (Sigma-Aldrich, Saint Louis, MO, USA). The human telomerase-immortalized esophageal squamous cell line established from endoscopic biopsy specimens of normal esophageal squamous mucosa taken from the distal esophagus of GERD patient without Barrett's esophagus (NES-G2T) were developed in Dr. Souza lab. NES-G2T cell line was cultured in 3:1 mixture of Dulbecco's Modified Eagle's Medium (Gibco, Paisley, UK)/Ham's Nutrient Mixture F-12 (Gibco, Grand Island, NY, USA) supplemented with 1% HyClone Cosmic Calf Serum U.S. origin (GE Healthcare Life Sciences, Logan, UT, USA), 400 ng/ml hydrocortisone (Sigma-Aldrich, St Louis, MO, USA), 20 ng/ml of human EGF (Gibco, Life Technologies, Paisley, UK), 5 µg/ml of insulin (Sigma Aldrich St Louis, MO, USA), 0.1 nM cholera toxin (Sigma Aldrich St Louis, MO, USA), 0.02 µM 3,3',5-triiodo-L-thyronine sodium salt (Sigma Aldrich St Louis, MO, USA), 0.18 mM adenine (Sigma-Aldrich St Louis, MO,USA), 5 µg/ml transferrin (Sigma Aldrich St Louis, MO, USA) and 10 U/ml penicillin, 10 µg/ml streptomycin (Sigma-Aldrich, St Louis, MO, USA). The human telomerase-immortalized Barrett’s esophagus cell line (BAR-T) was a kind gift of

Dr. Rhonda Souza (Baylor Scott & White Research Institute, Dallas, TX, USA) and was cultured in Keratinocyte Based Medium 2 (KBM-2) (PromoCell, Heidelberg, Germany) supplemented with 5% Fetal Bovine Serum (Sigma-Aldrich, St Louis, MO, USA), 400 ng/ml hydrocortisone (Sigma-Aldrich, St Louis, MO, USA), 20 ng/ml of human EGF (Gibco, Life Technologies, Paisley, UK), 70 μg/ml of BPE (EMD Millipore Corporation, Billerica, MA, USA), 5 μg/ml of insulin (Sigma Aldrich St Louis, MO, USA), 0.1 nM cholera toxin (Sigma Aldrich St Louis, MO, USA), 20 μg/ml adenine (Sigma-Aldrich St Louis, MO,USA), 5 μg/ml transferrin (Sigma Aldrich St Louis, MO, USA) and 100 U/ml penicillin, 100 μg/ml streptomycin (Sigma-Aldrich, St Louis, MO, USA). All cells' lines were maintained at 37°C and 5% CO2. For subculturing, media were removed, and the cell layer was rinsed with Trypsin-EDTA 0.25% solution.

Cell viability assay. Cell viability was assessed using thiazolyl blue tetrazolium bromide assay (MTT; Sigma-Aldrich, St. Louis, MO, USA). Cells were detached and plated in 96-well plates at a density of 2 x 104 cells/well and placed at 37°C in a 5% CO2 humidified incubator for 24 h. EPC2, NES-G2T and BAR-T cells were exposed to different, cell type-dependent concentrations (0, 100, 250 and 500 μM) of acidified (pH 5.0) bile mixture (BM) for 30 min and subsequently cultured with NaHS, GYY4137, AOAA and PAG at a concentration of 10, 100 or 500 μM for 24 h. EPC2 CBS K/O and EPC2 CTH K/O were exposed to a range (0 – 800 μM) of bile mixture concentrations in acidified (pH 5.0) or regular medium for 30 min. Cells incubated in culture medium alone served as a controls (untreated cells). On the next day, 50 μl of the MTT solution (1 mg/ml stock) was added to each well. The plates were incubated at 37°C in a 5% CO2 humidified incubator for 4 h. The MTT solution was removed and 75 μl of dimethyl sulfoxide (DMSO) were added to each well to dissolve the formazan crystals. The optical

density was measured at 550 nm using a spectrophotometric microplate reader (Tecan Sunrise, Mannedorf, Switzerland). All the data were represented as three independent experiments. The value of untreated cells was taken as 100% of viability.

Generation of the H_2S synthesizing enzymes knock-out (K/O) EPC2 model. EPC2 cells with H_2S-enzymes knockout (K/O) were generated via CRISPR-Cas9 technique[50]. A cystathionine β-synthetase (CBS) and cystathionine γ-lyase (CTH) single guide RNA (sgRNA) targeting exon 3 and exon 1, respectively was cloned into TLCV2 plasmid (Addgene #87360). The sgRNA sequence is listed in Table A. Briefly, following sequence verification, the pTLCV2-CBSsgRNA/pTLCV2-CTHsgRNA was packaged into lentiviral particles by co-transfection into HEK293T cells with pSPAX2 and pMD2.G (Addgene #12260 and #12259, respectively). The supernatant was collected, ultracentrifuged, and used to transduce EPC2 cells. The mixed populations of transduced cells were plated at very low density. Single cell colonies were subsequently isolated and picked from a plate using sterile cloning cylinders 8 mm x 8 mm diameter with silicone grease applied to one end (Sigma-Aldrich, St Louis, MO, USA). Next, DNA was isolated using the commercially available kit with spin columns (Cell Culture DNA Purification Kit, EURx, Gdansk, Poland) and the sequence was verified with primers flanking the sgRNA-site (Table A). Changes in CBS and CTH protein levels in EPC2 CBS K/O and CTH K/O were presented in Figure S3D.

Table A. The list of selected single guide RNA (sgRNA) sequences and primers flanking the sgRNA-site.

No.	Name and symbol	Sequence (5' to 3')	Length (bp)
1	CBS_Guide3sgRNA	For: CACCGAGCATCGGGCCGGATCCACA Rev: AAAC TGTGGATCCGGCCCGATGCTC	-
2	CTH_Guide1sgRNA	For: CACCGTCGCCTGCGTGGCGAAATGT Rev:AAAC ACATTTCGCCACGCAGGCGAC	-
3	CBS_gDNA	For: GTGCAGTTCTTCCTGGGCTT Rev: GAGCCTCATCTACACGGCAT	504
4	CTH_gDNA	For: TGTCAGCCAATAAGGAGCGG Rev: AATGGCAAGCTGGACAAACG	668

Experimental cell-culture models of GERD/BE. EPC2, EPC2-CBS/CTH K/O, NES-G2T and BAR-T cells were exposed daily to bile mixture (BM) for one week. BM consisted of 25% deoxycholic acid, 45% sodium glycocholate hydrate and 30% sodium taurochenodeoxycholate and was prepared in acidified media (pH adjusted to 5.0 with 7.2M HCl) to reflect GERD-induced clinical esophageal microenvironment[27,50]. Daily exposure time (30 min) and final BM concentration was set to 100 μM for EPC2 and EPC2-CBS/CTH K/O and to 250 μM for NES-G2T and BAR-T, based on our optimized protocols[27,51]. Simultaneously, cells were cultured for one week with fresh 100 μM aqueous solution of NaHS, GYY4137, AOAA or PAG (+/- BM).

Assessment of H_2S content in esophageal mucosa by biochemical method. Esophageal H_2S content was measured in homogenized samples using the modified zinc-trapping assay[52,53]. The esophageal biopsies were homogenized in ice-cold 50 mM potassium phosphate buffer with pH 8.0 (12% w/v). Tissue homogenate was placed in the vials containing separate internal tubes with zinc acetate allowing to trap volatile

sulfide. The vials were then flushed with nitrogen gas, capped with an air-tight septum cap, and incubated in a shaking water bath at 37ºC. Subsequently, trichloroacetic acid (50%; 0.5 mL) was injected into the reaction mixture through a septum cap. The mixture remained at 50ºC to allow zinc acetate to trap H_2S. N,N-Dimethyl-p-phenylenediamine sulfate (20 mM; 50µL) in 7.2M HCl and $FeCl_3$ (30 mM; 50µL) in 1.2M HCl were added to the inner tubes. After 20 min, the absorbance at 670 nm was measured by the microplate reader (Tecan Sunrise, Mannedorf, Switzerland). The H_2S concentration was calculated against a calibration curve of known NaHS aqueous solution concentrations.

Determination of H_2S levels (reductant-labile sulfane sulfur (incl. PSSH pool), hydrosulfide anions and undissociated H_2S) in cell homogenates by liquid chromatography tandem mass spectrometry (LC-MS/MS). H_2S level in cell homogenates was determined by liquid chromatography tandem mass spectrometry (LC-MS/MS) using an Agilent Technologies 1200 Series chromatograph coupled with a 6460 Triple Quad Mass Spectrometer (Agilent Technologies, Santa Clara, CA, USA)[54]. The cell pellets were homogenized using ultrasonic homogenizer in ice-cold Tris-HCl buffer solution (100 mM; pH 8.5) at a ratio of 1:4 (*w/v*) followed by centrifugation at 13,000 x g for 10 min. The supernatants (50 µl) were collected, +/- 10 µL of 10 mM dithiothreitol (DTT, Sigma-Aldrich, Saint Louis, MO, USA) was added and then incubated for 15 min at 37 ºC. Next, 10 µL of 1 µg/mL water solution of isotope labelled sodium thiocyanate ($NaS^{13}C^{15}N$; Sigma-Aldrich, Saint Louis, MO, USA) was pipetted as an internal standard (IS) and mixed. Then, 100 µL of a derivatization reagent mixture (20 mM monobromobimane (MBB; Sigma-Aldrich, Saint Louis, MO, USA) in acetonitrile, 2 mg/mL EDTA and 100 mM Tris-HCl (pH 8.5) in proportion 40:10:50, *v:v:v*) was added followed by incubation in a shaker for 60 min at room temperature in the dark. After

incubation, the reaction was stopped by adding 100 µL ice-cold acetonitrile with 10% formic acid (Sigma-Aldrich, Saint Louis, MO, USA). Finally, the samples were centrifuged at 13,000 x g for 10 min and the supernatants were diluted 10 times with distilled water and injected immediately into LC-MS/MS system. Data were collected in multiple reaction monitoring (MRM) mode using the most abundant transitions: m/z 415.2 → m/z 193.1 for the sulfide-dibimane (SDB), monobromobimane-based derivatives of H_2S, and m/z 252.1 → m/z 192.2 for monobromobimane-based derivative of $S^{13}C^{15}N$-anion. The retention times (RT) of SDB and IS with other selected MRM of ions (m/z), collision energies (CE) and fragment or voltages were presented in Table B. The remaining chromatographic and mass spectrometer conditions were presented in Table C. Data acquisition and analysis were performed using Agilent Technologies MassHunter software (version B.04.01). The results were presented as the ratio of signal (peak area) of the SDB to the IS and normalized to protein concentration in cell lysates.

Table B. The retention times (RT) of sulfide-dibimane (SDB) and internal standard (IS) with other selected multiple reaction monitoring (MRM) of ions (m/z), collision energies (CE) and fragment or voltages.

Compound	Precursor ion [m/z]	Product ion [m/z]	Fragmentor voltage [V]	Collision Energy [V]	Retention time [min]
SDB	415.2	223.1 193.1 53.1	170	20 16 72	7.64
IS	252.1	192.2 149.1 52.9	87	12 28 60	7.48

Table C. Chromatographic (LC) and mass spectrometer (MS) conditions

LC Conditions	
Column	Kinetex C18 2.6 µm 100 Å (100 × 4.6 mm) column (Phenomenex, USA)
Mobile phase	A: 0.1% formic acid in water (v/v) B: 0.1% formic acid in acetonitrile (v/v)
Flow rate	0.5 mL/min
Gradient	0.0 min – 5%, 2.0 min – 15%, 6.0 min – 98%, 6.5 min – 98%, 7.0 min – 5%, 14.0 min – 5% (in relation to the content of acetonitrile)
Injection volume	5 µL
MS conditions	
Ionisation mode	+ESI
Capilary voltage	3000 V
Gas (nitrogen) flow rate	11 L/min
Gas temperature	325 °C
Sheath gas flow rate	11 L/min
Sheath gas temperature	325 °C
Nebulizer pressure	40 psi

Analysis of mRNA expression by real-time PCR. Total RNA from cell culture and esophageal mucosa lysates were isolated using commercially available column-based extraction kit (Universal RNA/miRNA Purification Kit, EURx, Gdansk, Poland), according to manufacturer's protocol. RNA concentration was measured using NanoDrop One spectrophotometer (Thermo Fisher Scientific, Waltham, MA, USA).

Reverse transcription of RNA into complementary DNA (cDNA) was performed using the High-Capacity cDNA Reverse Transcription Kit (Applied Biosystems, Foster City, CA, USA). Expression of mRNA was determined using SGqPCR Master Mix (2X) with SYBR-Green (EURx, Gdansk, Poland) or 2XTaqMan Fast Advanced Master Mix (Thermo Fisher Scientific, Vilnius, Lithuania) with 20X TaqMan gene expression assays (Thermo Fisher Scientific, Vilnius, Lithuania). Selected human/rat genes and the corresponding assays or primer sequences for real-time PCR were listed in Tables D-F. PCR amplifications were performed in 96-well plates using the Quant Studio 3 system (Applied Biosystems, Foster City, CA). The relative quantitation of gene expression was performed using the $2^{-\Delta\Delta CT}$ method. $P<0.05$ was interpreted as statistically significant for at least a 2-fold up/down-regulation in relative expression which was considered as biologically relevant.

Table D. The list of selected rat genes and the corresponding PCR primer sequences.

No.	Gene name and symbol	Primer sequence (5' to 3')	NCBI gene reference	Length (bp)
1	Rattus norvegicus prostaglandin-endoperoxide synthase 1, *COX-1*	For: AGGTGTACCCACCTTCCGT Rev: CCAGATCGTGGAGAAGAGCA	NM_017043.4	137
2	Rattus norvegicus prostaglandin-endoperoxide synthase 2, *COX-2*	For: ATCAGAACCGCATTGCCTCT Rev: GCCAGCAATCTGTCTGGTGA	NM_017232.3	179
3	Rattus norvegicus interleukin 1 beta, IL-1β	For: GCTATGGCAACTGTCCCTGA Rev: AGTCAAGGGCTTGGAAGCAA	NM_031512.2	121
4	Rattus norvegicus interleukin 1 receptor antagonist, IL-1RN	For: AAGACCTTCTACCTGAGGAACAACC Rev: GCCCAAGAACACATTCCGAAAGTC	NM_022194.2	117
5	Rattus norvegicus interleukin 1 receptor type 1, IL-1R1	For: GTTTTTGGAACACCCTTCAGCC Rev: ACGAAGCAGATGAACGGATAGC	NM_013123.3	105
6	Rattus norvegicus interleukin 1 receptor type 2, IL-1R2	For: CATTCAGACACCTCCAGCAGTTC Rev: ACCCAGAGCGTATCATCCTTCAC	NM_053953.2	116

Table E. The list of selected human genes (and reference genes) and the corresponding TaqMan assays.

No.	Gene name and symbol	Assay ID	NCBI gene reference
1	β-actin, *ACTB*	Hs99999903_m1	NM_001101.3
2	Keratin 1, *KRT1*	Hs00196158_m1	NM_006121.3
3	Keratin 4, *KRT4*	Hs00361611_m1	NM_002272.3
4	Keratin 7, *KRT7*	Hs00559840_m1	NM_005556.3
5	Keratin 14, *KRT14*	Hs00265033_m1	NM_000526.4
6	Keratin 15, *KRT15*	Hs00267035_m1	NM_002275.3
7	Keratin 18, *KRT18*	Hs02827483_g1	NM_000224.2
8	Keratin 24, *KRT24*	Hs00962561_m1	NM_019016.2
9	Interleukin 1 beta, *IL1β*	Hs01555410_m1	NM_000576.2
10	Prostaglandin-endoperoxide synthase 1, *COX-1*	Hs00924808_m1	NM_000962.3
11	Prostaglandin-endoperoxide synthase 2, *COX-2*	Hs00153133_m1	NM_000963.3
12	Cystathionine-beta-synthase ,CBS	Hs00163925_m1	NM_000071.2
13	Cystathionine gamma-lyase, *CTH*	Hs00542284_m1	NM_001190463
14	Mercaptopyruvate sulfurtransferase, *MPST*	Hs00560401_m1	NM_001013436

Table F. The list of selected rat genes (and reference genes) and the corresponding TaqMan assays.

No.	Gene name and symbol	Assay ID	NCBI gene reference
1	β-actin, ACTB	Rn00667869_m1	NM_031144
2	Glyceraldehyde-3-phosphate dehydrogenase, GAPDH	Rn01462662_g1	NM_017008
3	Keratin 1, *KRT1*	Rn02346048_m1	NM_001008802
4	Keratin 4, *KRT4*	Rn02346072_m1	NM_001008806
5	Keratin 8, *KRT8*	Rn01532759_g1	NM_199370
6	Keratin 18, *KRT18*	Rn01533362_g1	NM_053976
7	Cystathionine-beta-synthase, *CBS*	Rn00560948_m1	NM_012522.2
8	Cystathionine gamma-lyase, *CTH*	Rn07318891_s1	NM_017074.1
9	Mercaptopyruvate sulfurtransferase, *MPST*	Rn00593744_m1	NM_138843.1

Automated capillary immunoblotting. Protein expression analysis was performed by capillary Western blotting using the Jess™ Simple Western system (ProteinSimple, San Jose CA, USA) with a 12–230 kDa separation module (ProteinSimple, SM-W004) according to the manufacturer's protocol. The diluted protein lysates from each sample were combined with a Fluorescent Master Mix in a 4:1 ratio for chemiluminescence and fluorescence detection. Target proteins were detected with the following primary antibodies: β-Actin (1:50 dilution, 8H10D10, Cell Signaling Technology, Danvers, MA, USA); GAPDH (1:50 diluted, 60004-1-Ig, Proteintech Group, Inc, Rosemont, IL, USA), CBS (1:50 dilution, 14787-1-AP, Proteintech Group, Inc, Rosemont, IL, USA); CTH (1:10 dilution, 12217-1-AP, Proteintech Group, Inc, Rosemont, IL, USA); MPST (1:50 dilution, HPA001240, Sigma-Aldrich, Saint Louis, MO, USA). The following secondary anti-rabbit (042-206, ProteinSimple, San Jose, CA, USA) and anti-mouse NIR (043-821, ProteinSimple, San Jose, CA, USA) antibodies were

used. The Compass Simple Western software (version 6.0.0, Protein Simple, San Jose, CA, USA) provided with the JESS instrument was used to process and analyze results. Expression of each target protein was normalized to β-Actin or GAPDH signal.

Target protein detection and quantification in cell and esophageal mucosa lysates using multiplex fluorescent assay. The concentrations of interleukin (IL) 1β, 4, 5, 6, 12p70, 13 and tumor necrosis factor α (TNF-α) were determined in serum samples using MILLIPLEX MAP Kit Rat Cytokine/Chemokine Magnetic Bead Panel (Cat. No. RECYTMAG-65K; EMD Millipore Corporation, Billerica, MA, USA). Results were calculated from standard curves plotted by xPONENT 4.3 software (Luminex Corporation, Austin, TX) using the Median Fluorescent Intensity (MFI) against the concentrations (pg/ml) of indicated analyte. Rat and human total/phosphor mTOR were determined in cell and esophageal mucosa lysates using MILLIPLEX MAP 2-Plex Total/Phospho mTOR - Cell Signaling Multiplex Assay (Cat. No. 48-625MAG; EMD Millipore Corporation, Billerica, MA, USA) and results were expressed as Net Median Fluorescent Intensity (Net MFI).

Determination of 8-hydroxyguanosine (8-OHG) and prostaglandin E2 (PGE2) concentration in esophageal mucosa and cell culture supernatants. Epithelial RNA oxidation expressed by 8-hydroxyguanosine (8-OHG) levels was evaluated by ELISA (589320, Cayman Chemical, Ann Arbor, MI, USA) (25). For the measurement of RNA oxidative damage total RNA was isolated from esophageal biopsies using a commercially available kit with spin columns (GeneMATRIX Universal RNA Purification Kit, EURx, Gdansk, Poland). 8-OHG concentration was expressed as ng of 8-OHG per 1 µg of total RNA.

Prostaglandin E_2 **(**PGE2) concentration in esophageal biopsies or cell supernatants was determined using PGE2-ELISA (ab133021, Abcam, Cambridge, UK/EHPGE2 Thermo Fisher Scientific, Waltham, MA, USA). For the measurement of prostaglandin E2 (PGE2) samples were homogenized and standardized regarding weight and buffer volume. PGE2 concentration was expressed in pg/mL of esophageal tissue homogenate.

Statistical analysis. Analyses were performed using GraphPad Prism 10 (GraphPad Prism Software Inc., San Diego, CA, USA). Results are presented as mean ± standard error of the mean (SEM) or median ± interquartile range (IQR). Student's t-test or Mann–Whitney U test were performed when two experimental groups were compared. For more than two groups, ANOVA with Dunnett's multiple comparison was used. For non-parametric distribution, ANOVA with Dunn's Kruskal-Wallis multiple comparison was used. Statistical significance was set as $p<0.05$.

5.7. References

1. Wallace, J. L. & Wang, R. Hydrogen sulfide-based therapeutics: Exploiting a unique but ubiquitous gasotransmitter. *Nat. Rev. Drug Discov.* **14**, 329–345 (2015).
2. Wallace, J. L., Vong, L., McKnight, W., Dicay, M. & Martin, G. R. Endogenous and Exogenous Hydrogen Sulfide Promotes Resolution of Colitis in Rats. *Gastroenterology* **137**, 569-578.e1 (2009).
3. Sen, N. *et al.* Hydrogen sulfide-linked sulfhydration of NF-κB mediates its antiapoptotic actions. *Mol. Cell* **45**, 13–24 (2012).
4. Flannigan, K. L. *et al.* Impaired hydrogen sulfide synthesis and IL-10 signaling underlie hyperhomocysteinemia-associated exacerbation of colitis. *Proc. Natl. Acad. Sci. U. S. A.* **111**, 13559–13564 (2014).
5. Li, L. *et al.* Anti-inflammatory and gastrointestinal effects of a novel diclofenac derivative. *Free Radic. Biol. Med.* **42**, 706–719 (2007).
6. Fiorucci, S. *et al.* Enhanced activity of a hydrogen sulphide-releasing derivative of mesalamine (ATB-429) in a mouse model of colitis. *Br. J. Pharmacol.* **150**, 996 (2007).
7. Flannigan, K. L., Ferraz, J. G. P., Wang, R. & Wallace, J. L. Enhanced Synthesis and Diminished

Degradation of Hydrogen Sulfide in Experimental Colitis: A Site-Specific, Pro-Resolution Mechanism. *PLoS One* **8**, 71962 (2013).

8. Wallace, J. L. *et al.* Anti-inflammatory and cytoprotective actions of hydrogen sulfide: translation to therapeutics. *Antioxid. Redox Signal.* **22**, 398–410 (2015).
9. Tai, F. W. D. & McAlindon, M. E. Non-steroidal anti-inflammatory drugs and the gastrointestinal tract. *Clin. Med. (Northfield. Il).* **21**, 131–134 (2021).
10. Blackler, R. W. *et al.* Hydrogen sulphide protects against NSAID-enteropathy through modulation of bile and the microbiota. *Br. J. Pharmacol.* **172**, 992–1004 (2015).
11. Wallace, J. L., Caliendo, G., Santagada, V. & Cirino, G. Markedly reduced toxicity of a hydrogen sulphide-releasing derivative of naproxen (ATB-346). *Br. J. Pharmacol.* **159**, 1236 (2010).
12. Zivanovic, J. *et al.* Selective Persulfide Detection Reveals Evolutionarily Conserved Antiaging Effects of S-Sulfhydration. *Cell Metab.* **30**, 1152-1170.e13 (2019).
13. Giovinazzo, D. *et al.* Hydrogen sulfide is neuroprotective in Alzheimer's disease by sulfhydrating GSK3β and inhibiting Tau hyperphosphorylation. *Proc. Natl. Acad. Sci. U. S. A.* **118**, e2017225118 (2021).
14. Vignane, T. & Filipovic, M. R. Emerging chemical biology of protein persulfidation. *Antioxid. Redox Signal.* **39**, 19–39 (2023).
15. Bibli, S. I. *et al.* Mapping the Endothelial Cell S -Sulfhydrome Highlights the Crucial Role of Integrin Sulfhydration in Vascular Function. *Circulation* **143**, 935–948 (2021).
16. Maret-Ouda, J., Markar, S. R. & Lagergren, J. Gastroesophageal Reflux Disease: A Review. *JAMA* **324**, 2536–2547 (2020).
17. Souza, R. F. & Spechler, S. J. Mechanisms and pathophysiology of Barrett oesophagus. *Nat. Rev. Gastroenterol. Hepatol.* **19**, 605–620 (2022).
18. Dvorak, K. *et al.* Bile acids in combination with low pH induce oxidative stress and oxidative DNA damage: relevance to the pathogenesis of Barrett's oesophagus. *Gut* **56**, 763 (2007).
19. Souza, R. F. *et al.* Gastroesophageal Reflux Might Cause Esophagitis Through a Cytokine-Mediated Mechanism Rather Than Caustic Acid Injury. *Gastroenterology* **137**, (2009).
20. Quante, M. *et al.* Bile acid and inflammation activate gastric cardia stem cells in a mouse model of barrett-like metaplasia. *Cancer Cell* **21**, (2012).
21. Shen, F., Zhao, C. S., Shen, M. F., Wang, Z. & Chen, G. The role of hydrogen sulfide in gastric mucosal damage. *Medical Gas Research* vol. 9 88–92 (2019).
22. Fiorucci, S. *et al.* Inhibition of hydrogen sulfide generation contributes to gastric injury caused by anti-inflammatory nonsteroidal drugs. *Gastroenterology* **129**, (2005).
23. Wallace, J. L. *et al.* A proof-of-concept, Phase 2 clinical trial of the gastrointestinal safety of a hydrogen sulfide-releasing anti-inflammatory drug. *Br. J. Pharmacol.* **177**, (2020).
24. Snijder, P. M. M. *et al.* Overexpression of cystathionine γ-Lyase suppresses detrimental effects of spinocerebellar ataxia type 3. *Mol. Med.* **21**, 758–768 (2015).
25. Mishanina, T. V., Libiad, M. & Banerjee, R. Biogenesis of reactive sulfur species for signaling by hydrogen sulfide oxidation pathways. *Nature Chemical Biology* vol. 11 (2015).
26. Rees, J. R., Lao-Sirieix, P., Wong, A. & Fitzgerald, R. C. Treatment for Barrett's oesophagus. *Cochrane Database Syst. Rev.* (2010) doi:10.1002/14651858.cd004060.pub2.
27. Korbut, E. *et al.* Molecular profile of Barrett's esophagus and gastroesophageal reflux disease in the development of translational physiological and pharmacological studies. *Int. J. Mol. Sci.* **21**, (2020).
28. Magierowski, M. *et al.* Exogenous and endogenous hydrogen sulfide protects gastric mucosa against the formation and time-dependent development of ischemia/reperfusion-induced acute

lesions progressing into deeper ulcerations. *Molecules* **22**, (2017).

29. Tambunting, L., Kelleher, D. & Duggan, S. P. The Immune Underpinnings of Barrett's-Associated Adenocarcinogenesis: a Retrial of Nefarious Immunologic Co-Conspirators. *CMGH* vol. 13 (2022).
30. Li, K. *et al.* mTOR signaling regulates gastric epithelial progenitor homeostasis and gastric tumorigenesis via MEK1-ERKs and BMP-Smad1 pathways. *Cell Rep.* **35**, (2021).
31. Kuehn, H. S., Jung, M. Y., Beaven, M. A., Metcalfe, D. D. & Gilfillan, A. M. Prostaglandin E2 activates and utilizes mTORC2 as a central signaling locus for the regulation of mast cell chemotaxis and mediator release. *J. Biol. Chem.* **286**, (2011).
32. Magierowska, K. *et al.* Mitochondria-targeted hydrogen sulfide donors versus acute oxidative gastric mucosal injury. *J. Control. Release* **348**, (2022).
33. Dunbar, K. B., Souza, R. F. & Spechler, S. J. The Effect of Proton Pump Inhibitors on Barrett's Esophagus. *Gastroenterology Clinics of North America* vol. 44 (2015).
34. Stairs, D. B. *et al.* Cdx1 and c-Myc foster the initiation of transdifferentiation of the normal esophageal squamous epithelium toward Barrett's esophagus. *PLoS One* **3**, (2008).
35. Qin, W. Sen *et al.* The short isoform of nuclear mitotic apparatus protein 1 functions as a putative tumor suppressor. *Chin. Med. J. (Engl).* **130**, (2017).
36. Wang, H. *et al.* Emerging mechanisms and targeted therapy of ferroptosis in cancer. *Molecular Therapy* vol. 29 (2021).
37. Rzechorzek, N. J., Hardwick, S. W., Jatikusumo, V. A., Chirgadze, D. Y. & Pellegrini, L. CryoEM structures of human CMG-ATPγS-DNA and CMG-AND-1 complexes. *Nucleic Acids Res.* **48**, (2020).
38. Bommer, U. A. & Telerman, A. Dysregulation of TCTP in Biological Processes and Diseases. *Cells* vol. 9 (2020).
39. Greenhough, A. *et al.* The COX-2/PGE2 pathway: Key roles in the hallmarks of cancer and adaptation to the tumour microenvironment. *Carcinogenesis* vol. 30 (2009).
40. Majka, J. *et al.* Cyclooxygenase-2 (COX-2) is the key event in pathophysiology of barrett's esophagus. lesson from experimental animal model and human subjects. *J. Physiol. Pharmacol.* **61**, (2010).
41. Que, J., Garman, K. S., Souza, R. F. & Spechler, S. J. Pathogenesis and Cells of Origin of Barrett's Esophagus. *Gastroenterology* vol. 157 (2019).
42. Agoston, A. T. *et al.* Columnar-Lined Esophagus Develops via Wound Repair in a Surgical Model of Reflux Esophagitis. *CMGH* **6**, (2018).
43. Kemper, E. K., Zhang, Y., Dix, M. M. & Cravatt, B. F. Global profiling of phosphorylation-dependent changes in cysteine reactivity. *Nat. Methods* **19**, (2022).
44. Vignane, T. *et al.* Protein thiol alterations drive aberrant phase separation in aging. *bioRxiv* 2011–2023 (2023).
45. Karpievitch, Y. V. *et al.* Normalization of peak intensities in bottom-up MS-based proteomics using singular value decomposition. *Bioinformatics* **25**, 2573–2580 (2009).
46. Tyanova, S. *et al.* The Perseus computational platform for comprehensive analysis of (prote)omics data. *Nature Methods* vol. 13 731–740 (2016).
47. RStudio Team. RStudio: Integrated Development Environment for R. (2020).
48. Huang, D. W., Sherman, B. T. & Lempicki, R. A. Systematic and integrative analysis of large gene lists using DAVID bioinformatics resources. *Nat. Protoc.* **4**, 44–57 (2009).
49. Li, L. *et al.* Characterization of a novel, water-soluble hydrogen sulfide-releasing molecule (GYY4137): New insights into the biology of hydrogen sulfide. *Circulation* **117**, (2008).
50. Janmaat, V. T. *et al.* HOXA13 in etiology and oncogenic potential of Barrett's esophagus. *Nat.*

Commun. **12**, (2021).

51. Korbut, E., Krukowska, K. & Magierowski, M. Barrett's Metaplasia Progression towards Esophageal Adenocarcinoma: An Attempt to Select a Panel of Molecular Sensors and to Reflect Clinical Alterations by Experimental Models. *Int. J. Mol. Sci.* **23**, (2022).
52. Yang, G. *et al.* H2S as a physiologic vasorelaxant: Hypertension in mice with deletion of cystathionine γ-lyase. *Science (80-.).* **322**, 587–590 (2008).
53. Paul, B. D. *et al.* Cystathionine γ-lyase deficiency mediates neurodegeneration in Huntington's disease. *Nature* **508**, 96–100 (2014).
54. Pomierny, B. *et al.* The slow-releasing and mitochondria-targeted hydrogen sulfide (H2s) delivery molecule ap39 induces brain tolerance to ischemia. *Int. J. Mol. Sci.* **22**, (2021).

Data availability: Proteomic data is available and stored in the open repository PRIDE (Project accession: **PXD047338**; Project DOI: 10.6019/PXD047338).

Acknowledgments: We would like to thank to Mrs. Anna Chmura (Department of Physiology, Jagiellonian University Medical College in Krakow) for technical preparation of histological slides.

Financial support: This study was sponsored by research grant of M.M., funded by the National Science Centre (Poland): UMO-2016/23/D/NZ4/01913 (Sonata). Supportive financial sources: i) clinical data is a part of the project funded to M.M. by the National Science Centre (Poland): UMO-2019/33/B/NZ4/00616 (Opus), ii) E.K. acknowledges funding from National Science Centre (Poland): 2023/07/X/NZ4/01052 (Miniatura). M.R.F. acknowledges funding from the European Research Council (ERC) under the European Union's Horizon 2020 research and innovation programme (Grant Agreement No. 864921).

Conflict of interest: Authors declare that they have no competing interests.

6. General discussion

Over the last few years, cysteine posttranslational modifications have emerged as an essential part of intra- and extracellular signaling[12,50,93]. Recent proteomic studies suggested that the primate-exclusive cysteines that are more exposed than in other species could be a possible cause of neurodegeneration in primates,[227] underscoring the potential of cysteine PTMs to drive brain damages. However, the attempt to measure these changes remains contradictory. Despite this growing interest, attempts to measure changes in cysteine PTMs remains controversial. While many studies suggest that cysteine residues undergo active remodeling in different pathologies and aging, recent proteomic approaches have found no significant age-related differences in the cysteine redoxome[275].

The significance of chemoselective labeling and enrichment of each cysteine PTM is highlighted by the limitations of approaches using classical thiol-blocking reagents, such as iodoacetamide or N-ethylmaleimide-based probes. These reagents often lack specificity because they label not only PSH and PSSH but also PSOH, resulting in adducts that are cleavable by DTT and TCEP[100]. Consequently, methods designed to detect PSSH[96,276] or "global thiol oxidation" [275] cannot differentiate between PSSH and PSOH[106]. Thus, it is possible to observe "no change" in free thiols while having a significant shift from PSOH to PSSH. Moreover, recent studies have shown that the disulfide adducts formed between commonly used thiol-blocking reagents and PSSH are unstable and can undergo a chemical transformation from disulfide to thioether. This finding casts doubt on the validity of all site-specific PSSH quantifications conducted to date.[105]

To address these issues, we used more specific methods to measure protein sulfenylation[277] and persulfidation[50]. These methods were adapted for proteomic enrichment at the protein level, providing a more reliable label-free quantification of changes in individual proteins. It is worth noting that the approaches used in our study do not quantify the percentage of occurrence of specific cysteine PTMs. Instead, they provide a fold-change comparison to the control sample. This is because it is impossible to use a single method to selectively label all modifications simultaneously, and achieving a fully reduced cysteine proteome is technically infeasible.

Namely, only cysteine PTMs such as PSOH, PSSH, S-nitrosation and disulfides are cleavable with reducing agents such as DTT or TCEP.[92] However, cysteine is a site of plethora of PTMs. For example, sulfinylation and sulfonylation, are irreversible and cannot be reduced back.[91] There are reports of cysteine palmitoylation[278], prenylation,[279] and acetylation,[280] all of which require harsh chemical cleavage with hydroxylamine. Furthermore, cysteines are targets of variety of naturally occurring electrophiles such as HNE,[281] itaconate,[282] fumarate[283], all of which cannot be easily reduced back to thiol.

Further difficulties, often overlooked even in the field of the most studied PTM, i.e. phosphorylation, are that protein levels could change within different conditions and could affect the proteomic data interpretation.

To overcome these challenges, we employed the EigenMS algorithm, adapted from surrogate variable analysis (SVA), to normalize the cysteine PTM datasets[284]. This algorithm identifies complex bias trends due to sample processing or LC-MS measurement[285] and accommodates experimental design or sample groups for normalization. The method preserves the effects of global peptide amount changes

during measurement, making it particularly advantageous for normalizing sulfenylome and persulfidome data (Figure 6.1). However, to avoid overfitting during normalization, it is crucial to randomize and batch-process samples during LC-MS preparations. Using these technical and bioinformatic approaches, we created a comprehensive and reproducible resource dataset of proteins undergoing sulfenylation and persulfidation changes in the aging mouse brain.

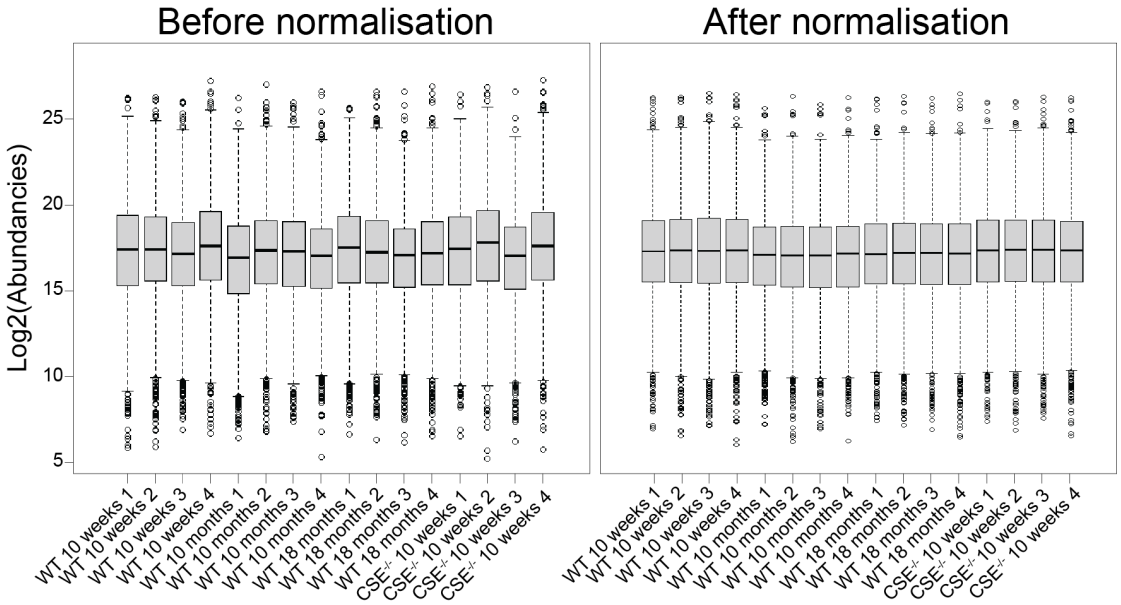


Figure 6.1. Boxplot of the raw and normalized intensities of persulfidome dataset. Persulfidome and sulfenylome dataset were normalized using EigenMS method[284]. This normalization identifies bias trend caused by heavy sample processing. In addition, this normalization takes in account the experimental design preserving global changes inherent to persulfidation and sylfenylation, both occurring through direct chemical reaction.

Furthermore, as additional control, we used double-plotting of our data, where changes of studied cysteine PTM were compared to the changes in total proteome (Extended data Figure 3.2, Extended data Figure 3.4). If changes in proteome would

appear to significantly affect the persulfidome changes, persulfidation/protein level normalization was introduced for each protein (Figure 5.3), in order to fairly present the data.

Applying all these stringent set of criteria for data analysis to the aging brain cysteine PTM analysis, we observed a continuous increase of protein sulfenylation. As a first reaction step for many cysteine modifications, sulfenylation is expected to be transient (Figure 6.2). Almost linear increase in protein sulfenylation observed in aging mouse brain is therefore a strong indicator of increased steady-state levels of ROS (most probably H_2O_2). Contrary to the sulfenylation, we found that protein persulfidation tends to decrease globally with age which we propose contributes to the increase in cysteine overoxidation. This hypothesis was supported by our analysis of the sulfonylome (PSO_3H) in wild-type mice at different ages and in $CSE^{-/-}$ mice.

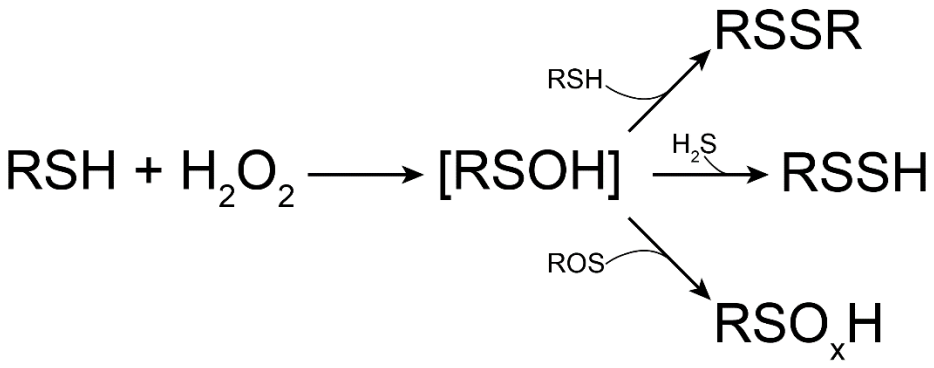


Figure 6.2. Overview of potential fates of sulfenylated cysteines. Sulfenylation of proteins (RSOH) readily react with other thiols, resulting in intra- and inter-molecular disulfide bonds, glutathionylation (RSSR), or persulfidation (RSSH). Additionally, sulfenic acids can further react with reactive oxygen species (ROS), leading to sulfinylation and sulfonylation (RSOxH). Therefore, RSOH is expected to be very transient, given the number of reactions it can undergo.

The absence of CSE-dependent H_2S production resulted in a significant increase in overoxidized peptides in 10-week-old mice when compared to WT. Cysteine sulfonylation is a modification that resembles phosphorylation due to the addition of a bulky, negatively charged group. Many of the cysteines identified in our sulfonylome were located near or within beta-sheet domains, where overoxidation dramatically altered protein structure, increasing beta-sheet content—a hallmark of proteinopathy and aggregation[198,286].

Interestingly, old $CSE^{-/-}$ mice exhibited numerous fibrillary tangles and brain lesions, suggesting that H_2S protection against cysteine over-oxidation of is critical protective mechanism in preventing protein aggregation. $CSE^{-/-}$ mice have already been associated with neurodegeneration such as Alzheimer's and Huntington's disease[39,52]. Our findings confirmed that $CSE^{-/-}$ could be the first mouse model of age-induced neurodegeneration.

6.1. Age-associated imbalance in cysteine PTMs drives aberrant phase separation and aggregation in aging brain

Qualitative analysis of our aging cysteine redoxome data suggested no preference for cellular organelles could be observed. All organelles, as well as cytosol had substantial portion of their cysteine-containing proteins affected by age-induced changes in cysteine redox status. Pathway enrichment analysis also did not provide a clear mechanistic clue as to why neurodegeneration and shorter lifespan are observed in mice lacking CSE.

However, a deeper analysis of our proteomic data revealed that many proteins undergoing a redox switch from persulfidation to sulfenylation and sulfonylation with aging were also associated with liquid-liquid phase separation. Although biomolecular condensates play a central role in diverse cellular processes[231,287–289], aberrant phase separation is closely linked to neurodegenerative diseases[265,268,270]. Notably, we identified two significant components of biomolecular condensates: (i) synapsin 1, responsible for synaptic vesicle cluster formation and regulation of neurotransmitter release[235], and (ii) G3BP2, an essential component of stress granule[247], involved in cellular stress response[244]. Additionally, we identified GAPDH as the first highly structured protein capable of LLPS and transitioning to aggregation, all of which is driven by its cysteine overoxidation (Figure 6.3).

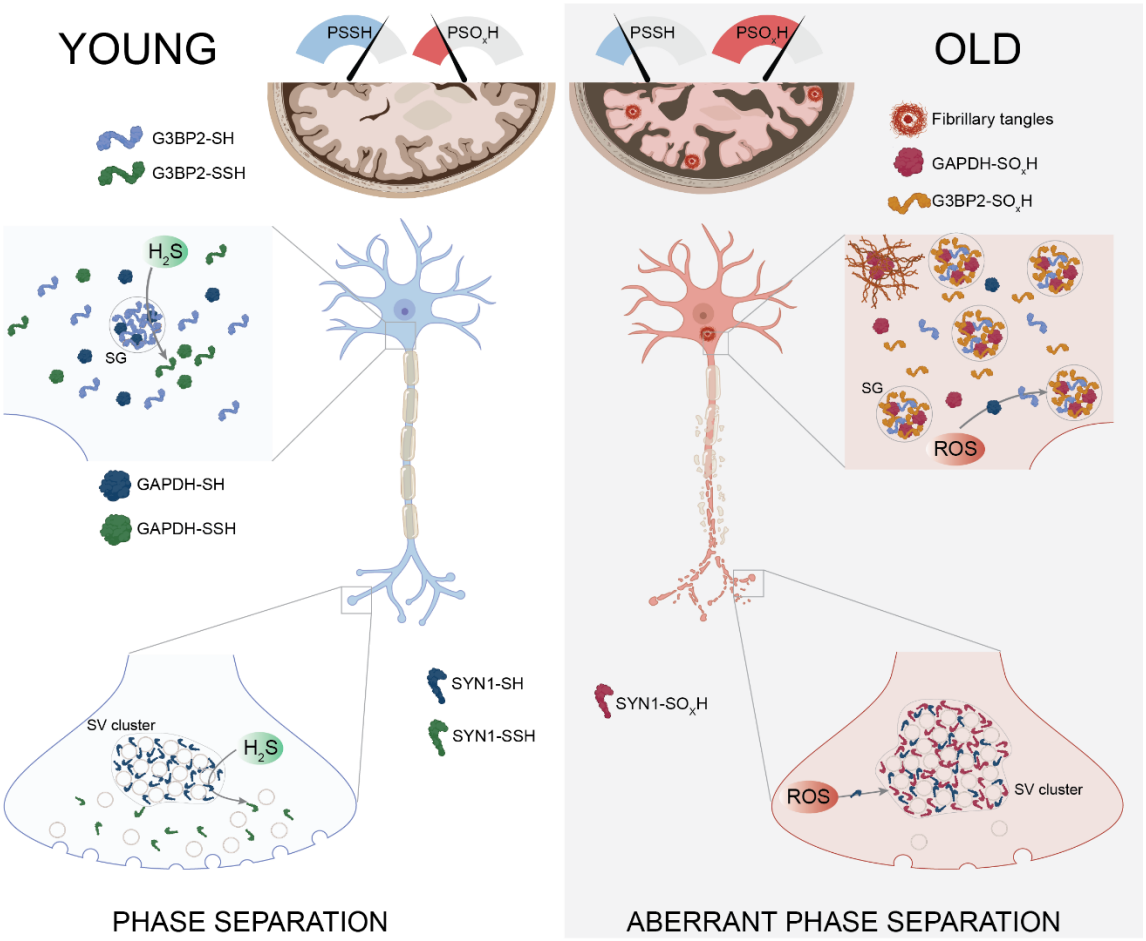


Figure 6.3. Redox switch from PSSH to PSO_xH forces aberrant phase separation predisposing brain to neurodegeneration.

Synapsin 1 is one of the most abundant proteins in the synaptic vesicle[290]. In the presynaptic terminal, it regulates both the axon elongation and the kinetic of synaptic vesicle fusion[291,292]. Synapsin 1's phase separation is crucial for clustering synaptic vesicles that contain neurotransmitters[235]. Upon calcium signaling, Synapsin 1 undergoes phosphorylation, leading to the dissolution of condensates and the release of lipid vesicles and neurotransmitters[235,293]. This phosphorylation appears to be regulated by the palmitoylation of three cysteines: C223, C360, and C370[294]. Accordingly, our proteomic analysis found C360 to be overoxidized in the $CSE^{-/-}$ brain, indicating that this

cysteine is highly reactive. While palmitoylation regulates synapsin 1 phosphorylation[294], we demonstrated that sulfonylation increases synapsin 1's propensity to phase separate. Consequently, when H_2S production is inhibited, susceptibility to ROS-induced overoxidation is increased and synapsin condensates disperse less, resulting in reduced neurotransmitter release. Increasing H_2S levels shortened the timing of neurotransmitter release in response to calcium, without altering its magnitude. Cognitive functions are often linked to neuronal communication, making impaired neurotransmission a key factor in age-related cognitive deficits[295]. Neurodegenerative diseases, often associated with reduced CSE expression[39,52,190,296], are similarly linked to deficits in neuronal transmission. We propose that the age-dependent decline in H_2S production may predispose individuals to impaired neuronal transmission, exacerbating neurodegenerative pathologies. Furthermore, our results suggest that development of H_2S-releasing compounds for prevention and treatment of dementia-associated pathologies might represent a viable drug-development strategy.

While this study focused on the direct effect of cysteine persulfidation and over-oxidation on synapsin 1's condensates, interplay between these modifications, palmitoylation, and phosphorylation of synapsin 1 remains unclear. Additionally, aging is marked by impaired axon regeneration and elongation[297], processes in which synapsin 1 plays a crucial role[37]. However, it remains uncertain whether alterations in synapsin 1's cysteine PTMs contribute to these age-dependent alterations.

6.1.1. G3BP2 redox switch regulates stress granule dynamics

Given that our sulfenylome and sulfonylome data suggest the aging brain is overwhelmed by ROS, it was important to explore the impact of cysteine PTMs imbalances on stress-related phenomena such as stress granules (SGs).

SGs are central to various stress responses, adequately regulating translation[246] and signaling pathways upon stress[298,299]. Comparing our proteomic dataset with proteins found in stress granules revealed a significant overlap (Figure 6.4A). Furthermore, we identified G3BP2, one of the two essential proteins in SG formation[247] and predominantly expressed in the brain[300] (Figure 6.4B).

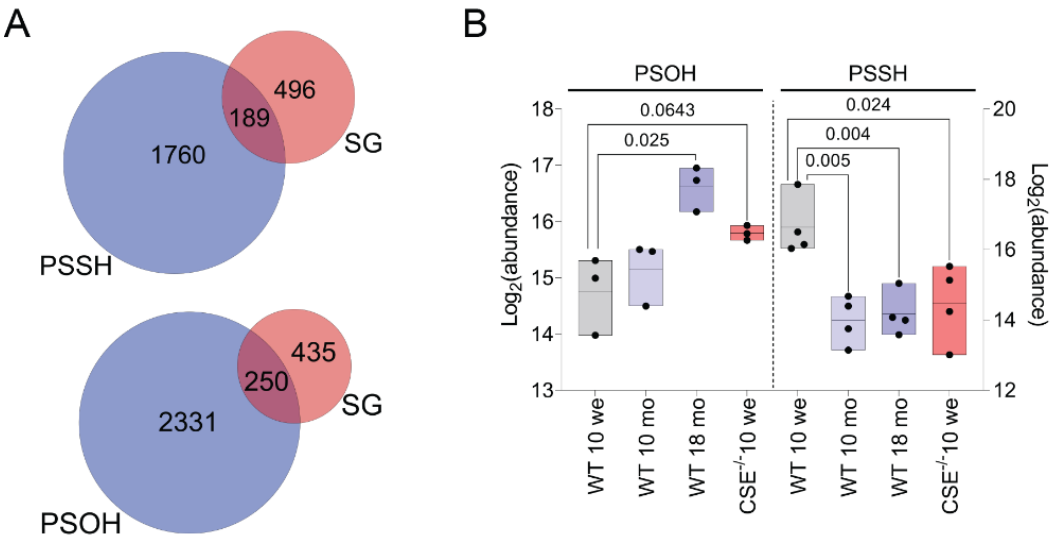


Figure 6.4. Stress granule proteins are both sulfenylated and persulfidated. (**A**) Venn diagram representing the overlap of proteins present in stress granules (SG) and those identified in PSSH and PSOH levels with aging. (**B**) Boxplot of PSOH and PSSH changes of G3BP2. Log2 abundances of G3BP2 PTM in aging WT mice and $CSE^{-/-}$ mice, normalized to total protein levels (n = 4, p-value reported from proteomic analysis; Welch's t-test).

The sulfenylation of C73 on G3BP2 emerged as a critical event that enhanced the protein's propensity to phase separate, leading to the SG assembly under oxidative stress. This finding aligns with previous studies demonstrating that stress granule formation could be initiated upon H_2O_2 treatment[301]. Our results also suggest that the persulfidation of G3BP2 at C73 is crucial for SG disassembly during the recovery phase. Lack of CSE in mouse embryonic fibroblast resulted in impaired recovery and accumulation of stress granules upon recovery, further underscoring the importance of H_2S-controlled protein persulfidation upon stress.

The dysregulation of SG dynamics has been implicated in several neurodegenerative diseases, including amyotrophic lateral sclerosis (ALS)[302,303] and Huntington's disease (HD)[304,305]. As observed in our study, the impaired clearance of SGs in cells lacking adequate persulfidation may contribute to the accumulation of toxic protein aggregates, a hallmark of neurodegeneration[306]. Indeed, STHdh$^{Q111/Q111}$ cells, a model for HD, are known for having lower levels of CSE[50]. Stress granule clearance was also impaired in these cells but could be partially restored using H_2S donors. Therefore, enhancing persulfidation or modulating H_2S levels could be a therapeutic strategy to mitigate the effects of oxidative stress in these diseases.

While we observed a direct effect of cysteine modification on G3BP2 phase separation, we did not address its potential effect on G3BP2 condensates transitioning from liquid to solid state. Additionally, the oxidation and over-oxidation of their cysteine may also affect other stress granule components. Considering that the composition of SGs is time-dependent[245] and stress-specific[244], further studies in WT and CSE$^{-/-}$ cells under oxidative stress are warranted to understand how H_2S deficiency influences the RNA composition of SGs, potentially linking to protein aggregation and

neurodegeneration. However, we did observe that glyceraldehyde-3-phosphate dehydrogenase (GAPDH) enters SG and follows the same trend as G3BP2.

6.1.2. Over-oxidation of GAPDH enhances its phase separation and forces its phase transition to aggregation

GAPDH, a central glycolytic enzyme was, the first protein reported as persulfidated[57] and is known to be a redox-sensitive[307]. The discovery that GAPDH undergoes phase separation upon arsenite treatment was unexpected, given that GAPDH is a highly structured protein, which contradicts the prevailing notion that intrinsically disordered regions drive LLPS[228]. However, we observed GAPDH condensate formation upon both crowding and interaction with RNA, and this LLPS of GAPDH affected its enzymatic activity. Furthermore, in a rather paradigm shifting manner, we also show that once phase separated, cysteine residues of a protein react faster with H_2O_2.

Thus, our study introduces several new concepts:

(i) highly structured protein can undergo liquid-liquid phase separation;

(ii) the protein structure alteration induced by LLPS, regulates enzymatic activity. Although it has been shown that SUMOylation enzymes could be recruited in LLPS and that this increases the SUMOylating rate[308], increased GAPDH activity in LLPS opens a new field of cellular metabolism regulation;

(iii) Reactivity of cysteine residues with ROS can be drastically enhanced by protein conformational changes caused by LLPS.

Previous studies reported GAPDH aggregation in Alzheimer's patients[309,310], a phenomenon that we also observed in CSE$^{-/-}$ brain, supporting the hypothesis that CSE$^{-/-}$ mice could serve as a model for age-induced Alzheimer's disease. However, the mechanism behind GAPDH aggregation was unclear until our study, which highlighted that GAPDH aggregation is driven by its propensity to phase separate.

Overoxidation not only enhances GAPDH's ability to phase separate but also increases its beta-sheet content. These factors together drive the transition from a liquid to a solid phase, leading to protein aggregation. In brain aging, a decrease in persulfidation may result in prolonged GAPDH phase separation, reinforcing over-oxidation and ultimately leading to aggregation. GAPDH may also act as a scaffold, recruiting other proteins into its condensates and further phase transitions from liquid to solid state could bring these clients proteins to aggregate.

While we have addressed the interplay between GAPDH condensates and its activity in vitro, the consequences of its LLPS on cellular metabolism require further exploration. Specifically, the recruitment of other proteins into GAPDH condensates remains an open question. Indeed, as shown for SUMOylation[308], GAPDH condensates could potentially serve as a hub for glycolysis, enhancing the efficiency of the glycolysis pathway by bringing metabolites and enzymes into a thermodynamically favorable environment. Finally, the potential of GAPDH to drive the aggregation of other proteins, particularly in the context of neurodegeneration, needs to be thoroughly investigated to understand its role in disease progression.

Although we discuss the impact of cysteine modifications on three proteins independently from each other, it is important to note that these mechanisms likely occur

simultaneously, collectively predisposing the brain to neurodegeneration (**Figure 6.3**). Further investigations are needed to explore the interplay between these phenomena.

Among some of the unanswered questions are:

(i) What is GAPDH's contribution to unresolved stress granules?

(ii) Does cysteine PTM of G3BP2 alter SG composition, and if so, does it influence the aggregation of other SG specific proteins like TDP-43?

(iii) What are the consequences of unresolved SGs on ROS production and metabolism?

(iv) How do G3BP2 condensates influence synapsin 1 condensate, and vice versa?

6.2. Persulfidation analysis of Barrett's esophagus reveal the essential role of H_2S and persulfidation in the disease

In this thesis we also studied persulfidation changes in Barrett's esophagus (BE) transitioning from BE to esophageal cancer. BE is characterized by the transition from squamous epithelium to metaplastic intestine-like epithelium, often triggered by chronic gastroesophageal reflux (GERD)[311]. These drastic changes are known to be mediated by GERD-induced oxidative stress[311,312]. Aging has been demonstrated to be a strong risk factor for the development of BE[313,314] and for progression to esophageal cancer[315] suggesting that age-induced prolonged exposure to gastric acid eventually leads to further transition from BE to esophageal cancer.

By using samples from human biopsies, we sought to identify both persulfidome and total proteome changes occurring during transitioning from normal epithelium to metaplasia of esophageal cancer and identify potential biomarkers that could help in determining the disease stage and progression.

While oxidative stress role in BE was already addressed[311,312], and few antioxidant dietary therapeutic approaches have been tested[316–318], the role of H_2S and persulfidation in BE has remained unclear. Analyzing human samples, we detected a significant proteome remodeling in the metaplastic tissue (with many proteins showing increased expression) compared to the non-metaplastic tissues subjected to acid reflux from the same patient. These results align with the tissue remodeling that characterize the metaplastic stage of the disease[319].

Interestingly the persulfidome changes largely mirrored the changes in proteins expression. This apparent increase in persulfidation, despite the observed reduction in H_2S levels, led us to adopt a novel normalization approach for persulfidation. Firstly established for phospho-proteomic studies[320], we adapted the method to normalize the persulfidome changes relative to protein expression. This approach allowed us to reinterpret the data, revealing a more profound decrease in protein persulfidation after normalization, consistent with the observed lack of H_2S. However, we also observed an increase in protein persulfidation for a significant number of proteins. One possible explanation for this observation is that the metaplastic remodeling results in an increased expression of proteins containing highly reactive cysteines. In this scenario, even reduced H_2S pool would primarily react with these cysteines, giving an impression of increased persulfidation of those targets. Furthermore, the impact of persulfidation on protein activity needs further investigation. This concept is important, especially if

persulfidation activates protein function, as it could lead to increased activity of specific enzymes.

Finally, our proteomic analysis identified potential biomarkers requiring further validation. Notably, we observed a steady increase of NQO1 expression and persulfidation across disease stages. Interestingly, NQO1 is involved in protection against oxidative stress but has also been implicated in several solid tumor[321]. Furthermore, NOQ1 has been found in brain regions affected by Alzheimer's disease[321,322], and its ability to co-aggregate with β-amyloids was recently demonstrated[323]. However, the effect of persulfidation on NQO1 activity has never been assessed and may present a key factor in aging and age-related diseases.

References

1. Abe, K. & Kimura, H. The possible role of hydrogen sulfide as an endogenous neuromodulator. J. Neurosci. 16, 1066–1071 (1996).
2. Patel, B. H., Percivalle, C., Ritson, D. J., Duffy, C. D. & Sutherland, J. D. Common origins of RNA, protein and lipid precursors in a cyanosulfidic protometabolism. Nat. Chem. 7, 301–307 (2015).
3. Sasselov, D. D., Grotzinger, J. P. & Sutherland, J. D. The origin of life as a planetary phenomenon. Sci. Adv. 6, (2020).
4. Foden, C. S. et al. Prebiotic synthesis of cysteine peptides that catalyze peptide ligation in neutral water. Science (80-.). 370, 865–869 (2020).
5. Filipovic, M. R., Zivanovic, J., Alvarez, B. & Banerjee, R. Chemical Biology of H2S Signaling through Persulfidation. Chem. Rev. 118, 1253–1337 (2018).
6. Giggenbach, W. Optical Spectra of Highly Alkaline Sulfide Solutions and the Second Dissociation Constant of Hydrogen Sulfide. Inorg. Chem. 10, 1333–1338 (1971).
7. Cuevasanta, E., Denicola, A., Alvarez, B. & Möller, M. N. Solubility and permeation of hydrogen sulfide in lipid membranes. PLoS One 7, e34562 (2012).
8. Wang, R. Physiological implications of hydrogen sulfide: A whiff exploration that blossomed. Physiol. Rev. 92, 791–896 (2012).
9. Yamaguchi, Y., Nakamura, T., Kusano, T. & Sano, H. Three Arabidopsis genes encoding proteins with differential activities for cysteine synthase and β-cyanoalanine synthase. Plant Cell Physiol. 41, 465–476 (2000).
10. Álvarez, C., Calo, L., Romero, L. C., García, I. & Gotor, C. An O-Acetylserine(thiol)lyase homolog with l-Cysteine desulfhydrase activity regulates cysteine homeostasis in arabidopsis. Plant Physiol. 152, 656–669 (2010).
11. Aroca, A., Gotor, C. & Romero, L. C. Hydrogen sulfide signaling in plants: emerging roles of protein persulfidation. Frontiers in Plant Science vol. 9 (2018).
12. Filipovic, M. R. & Jovanović, V. M. More than just an intermediate: Hydrogen sulfide signalling in plants. J. Exp. Bot. 68, 4733–4736 (2017).
13. Filipovic, M. R. R., Zivanovic, J., Alvarez, B. & Banerjee, R. Chemical Biology of H2S Signaling through Persulfidation. Chemical Reviews vol. 118 1253–1337 (2018).
14. Kabil, O., Vitvitsky, V., Xie, P. & Banerjee, R. The quantitative significance of the transsulfuration enzymes for H 2S production in murine tissues. Antioxidants Redox Signal. 15, 363–372 (2011).
15. Kabil, O. & Banerjee, R. Enzymology of H2S biogenesis, decay and signaling. Antioxidants and Redox Signaling vol. 20 770–782 (2014).
16. Pol, A. et al. Mutations in SELENBP1, encoding a novel human methanethiol oxidase, cause extraoral halitosis. Nat. Genet. 50, 120–129 (2018).
17. Singh, S., Padovani, D., Leslie, R. A., Chiku, T. & Banerjee, R. Relative contributions of cystathionine β-synthase and γ-cystathionase to H2S biogenesis via alternative trans-sulfuration reactions. J. Biol. Chem. 284, 22457–22466 (2009).
18. Niu, W. N., Yadav, P. K., Adamec, J. & Banerjee, R. S-glutathionylation enhances human cystathionine β-synthase activity under oxidative stress conditions. Antioxidants and Redox Signaling vol. 22 350–361 (2015).
19. Kabil, O., Zhou, Y. & Banerjee, R. Human cystathionine β-synthase is a target for sumoylation. Biochemistry 45, 13528–13536 (2006).
20. Ereno-Orbea, J., Majtan, T., Oyenarte, I., Kraus, J. P. & Martinez-Cruz, L. A. Structural insight into the molecular mechanism of allosteric activation of human cystathionine β-synthase by S-

adenosylmethionine. Proc. Natl. Acad. Sci. U. S. A. 111, E3845–E3852 (2014).

21. Zhu, W., Lin, A. & Banerjee, R. Kinetic properties of polymorphic variants and pathogenic mutants in human cystathionine γ-lyase. Biochemistry 47, 6226–6232 (2008).
22. Chiku, T. et al. H2S biogenesis by human cystathionine γ-lyase leads to the novel sulfur metabolites lanthionine and homolanthionine and is responsive to the grade of hyperhomocysteinemia. J. Biol. Chem. 284, 11601–11612 (2009).
23. Mikami, Y., Shibuya, N., Ogasawara, Y. & Kimura, H. Hydrogen sulfide is produced by cystathionine γ-lyase at the steady-state low intracellular Ca2+ concentrations. Biochem. Biophys. Res. Commun. 431, 131–135 (2013).
24. Yang, G. et al. H2S as a physiologic vasorelaxant: Hypertension in mice with deletion of cystathionine γ-lyase. Science (80-.). 322, 587–590 (2008).
25. Yuan, G. et al. Protein kinase G-regulated production of H2S governs oxygen sensing. Sci. Signal. 8, (2015).
26. Agrawal, N. & Banerjee, R. Human polycomb 2 protein is a SUMO E3 ligase and alleviates substrate-induced inhibition of cystathionine β-synthase sumoylation. PLoS One 3, (2008).
27. Statzer, C. et al. ATF-4 and hydrogen sulfide signalling mediate longevity in response to inhibition of translation or mTORC1. Nat. Commun. 13, 1–15 (2022).
28. Dickhout, J. G. et al. Integrated stress response modulates cellular redox state via induction of cystathionine γ-lyase: Cross-talk between integrated stress response and thiol metabolism. J. Biol. Chem. 287, 7603–7614 (2012).
29. Sun, Q. et al. Structural basis for the inhibition mechanism of human cystathionine γ-lyase, an enzyme responsible for the production of H2S. J. Biol. Chem. 284, 3076–3085 (2009).
30. Nagahara, N., Ito, T., Kitamura, H. & Nishino, T. Tissue and subcellular distribution of mercaptopyruvate sulfurtransferase in the rat: Confocal laser fluorescence and immunoelectron microscopic studies combined with biochemical analysis. Histochem. Cell Biol. 110, 243–250 (1998).
31. Huang, J., Niknahad, H., Khan, S. & O'Brien, P. J. Hepatocyte-catalysed detoxification of cyanide by L- and D-cysteine. Biochem. Pharmacol. 55, 1983–1990 (1998).
32. Yadav, P. K., Yamada, K., Chiku, T., Koutmos, M. & Banerjee, R. Structure and kinetic analysis of H2S production by human mercaptopyruvate sulfurtransferase. J. Biol. Chem. 288, 20002–20013 (2013).
33. Nagahara, N. Regulation of mercaptopyruvate sulfurtransferase activity via intrasubunit and intersubunit redox-sensing switches. Antioxidants and Redox Signaling vol. 19 1792–1802 (2013).
34. Vitvitsky, V., Kabil, O. & Banerjee, R. High turnover rates for hydrogen sulfide allow for rapid regulation of its tissue concentrations. Antioxidants and Redox Signaling vol. 17 22–31 (2012).
35. Watanabe, M. et al. Mice deficient in cystathionine β-synthase: Animal models for mild and severe homocyst(e)inemia. Proc. Natl. Acad. Sci. U. S. A. 92, 1585–1589 (1995).
36. Beyer, K. et al. Cystathionine Beta Synthase as a Risk Factor for Alzheimer Disease. Curr. Alzheimer Res. 1, 127–133 (2005).
37. Ganguly, P. & Alam, S. F. Role of homocysteine in the development of cardiovascular disease. Nutrition Journal vol. 14 (2015).
38. Nakladal, D. et al. Homozygous whole body Cbs knockout in adult mice features minimal pathology during ageing despite severe homocysteinemia. FASEB J. 36, (2022).
39. Paul, B. D. et al. Cystathionine γ-lyase deficiency mediates neurodegeneration in Huntington's disease. Nature 508, 96–100 (2014).
40. Ishii, I. et al. Cystathionine γ-lyase-deficient mice require dietary cysteine to protect against acute lethal myopathy and oxidative injury. J. Biol. Chem. 285, 26358–26368 (2010).

41. Eberhardt, M. et al. H2S and NO cooperatively regulate vascular tone by activating a neuroendocrine HNO-TRPA1-CGRP signalling pathway. Nat. Commun. 5, (2014).

42. Szijártó, I. A. et al. Cystathionine γ-lyase-produced hydrogen sulfide controls endothelial no bioavailability and blood pressure. Hypertension 71, 1210–1217 (2018).

43. Das, A. et al. Impairment of an Endothelial NAD+-H2S Signaling Network Is a Reversible Cause of Vascular Aging. Cell 173, 74-89.e20 (2018).

44. Papapetropoulos, A. et al. Hydrogen sulfide is an endogenous stimulator of angiogenesis. Proc. Natl. Acad. Sci. U. S. A. 106, 21972–21977 (2009).

45. Katsouda, A., Bibli, S. I., Pyriochou, A., Szabo, C. & Papapetropoulos, A. Regulation and role of endogenously produced hydrogen sulfide in angiogenesis. Pharmacological Research vol. 113 175–185 (2016).

46. Peng, Y. J. et al. Hypoxia sensing requires H2S-dependent persulfidation of olfactory receptor 78. Sci. Adv. 9, (2023).

47. Yuan, G. et al. Protein kinase G-regulated production of H2S governs oxygen sensing. Sci. Signal. 8, (2015).

48. Peng, Y. J. et al. Inherent variations in co-h2s-mediated carotid body O 2 sensing mediate hypertension and pulmonary edema. Proc. Natl. Acad. Sci. U. S. A. 111, 1174–1179 (2014).

49. Li, L. et al. Hydrogen sulfide is a novel mediator of lipopolysaccharide-induced inflammation in the mouse. FASEB J. 19, 1196–1198 (2005).

50. Zivanovic, J. et al. Selective Persulfide Detection Reveals Evolutionarily Conserved Antiaging Effects of S-Sulfhydration. Cell Metab. 30, 1152-1170.e13 (2019).

51. Hine, C. et al. Endogenous hydrogen sulfide production is essential for dietary restriction benefits. Cell 160, 132–144 (2015).

52. Giovinazzo, D. et al. Hydrogen sulfide is neuroprotective in Alzheimer's disease by sulfhydrating GSK3β and inhibiting Tau hyperphosphorylation. Proc. Natl. Acad. Sci. U. S. A. 118, e2017225118 (2021).

53. Vandiver, M. S. et al. Sulfhydration mediates neuroprotective actions of parkin. Nat. Commun. 4, (2013).

54. Katsouda, A. et al. MPST sulfurtransferase maintains mitochondrial protein import and cellular bioenergetics to attenuate obesity. J. Exp. Med. 219, (2022).

55. Tiranti, V. et al. Loss of ETHE1, a mitochondrial dioxygenase, causes fatal sulfide toxicity in ethylmalonic encephalopathy. Nat. Med. 15, 200–205 (2009).

56. Módis, K., Coletta, C., Erdélyi, K., Papapetropoulos, A. & Szabo, C. Intramitochondrial hydrogen sulfide production by 3-mercaptopyruvate sulfurtransferase maintains mitochondrial electron flow and supports cellular bioenergetics. FASEB J. 27, 601–611 (2013).

57. Mustafa, A. K. et al. HS signals through protein S-Sulfhydration. Sci. Signal. 2, ra72–ra72 (2009).

58. Paul, B. D. & Snyder, S. H. H2S: A Novel Gasotransmitter that Signals by Sulfhydration. 40, 687–700.

59. Benchoam, D. et al. Acidity and nucleophilic reactivity of glutathione persulfide. J. Biol. Chem. 295, 15466–15481 (2020).

60. Cuevasanta, E. et al. Reaction of hydrogen sulfide with disulfide and Sulfenic acid to form the strongly Nucleophilic Persulfide. J. Biol. Chem. 290, 26866–26880 (2015).

61. Cuevasanta, E. et al. Kinetics of formation and reactivity of the persulfide in the one-cysteine peroxiredoxin from Mycobacterium tuberculosis. J. Biol. Chem. 294, 13593–13605 (2019).

62. Artaud, I. & Galardon, E. A persulfide analogue of the nitrosothiol SNAP: Formation, characterization and reactivity. ChemBioChem 15, 2361–2364 (2014).

63. Ida, T. et al. Reactive cysteine persulfides and S-polythiolation regulate oxidative stress and redox signaling. Proc. Natl. Acad. Sci. U. S. A. 111, 7606–7611 (2014).

64. Abiko, Y. et al. Involvement of Reactive Persulfides in Biological Bismethylmercury Sulfide Formation. Chem. Res. Toxicol. 28, 1301–1306 (2015).

65. Wood, J. L. Sulfane Sulfur. Methods Enzymol. 143, 25–29 (1987).

66. Lang, K. Die Rhodanbildung im Tierkorper [Thiocyanogen in the bodies of animals]. FEBS J 259, 243–256 (1933).

67. Kawamura, S., Nakabayashi, T., Kitao, T. & Tsurugi, J. Aralkyl Hydrodisulfides. VI. The Reaction of Benzhydryl Hydrosulfide with Several Nucleophiles. Journal of Organic Chemistry vol. 31 1985–1987 (1966).

68. Bailey, T. S., Zakharov, L. N. & Pluth, M. D. Understanding hydrogen sulfide storage: Probing conditions for sulfide release from hydrodisulfides. J. Am. Chem. Soc. 136, 10573–10576 (2014).

69. Pan, J. & Carroll, K. S. Persulfide reactivity in the detection of protein S-sulfhydration. ACS Chem. Biol. 8, 1110–1116 (2013).

70. Miljkovic, J. L. et al. Rapid and selective generation of H2S within mitochondria protects against cardiac ischemia-reperfusion injury. Redox Biol. 55, 102429 (2022).

71. Wedmann, R. et al. Improved tag-switch method reveals that thioredoxin acts as depersulfidase and controls the intracellular levels of protein persulfidation. Chem. Sci. 7, 3414–3426 (2016).

72. Yadav, P. K. et al. Biosynthesis and Reactivity of Cysteine Persulfides in Signaling. J. Am. Chem. Soc. 138, 289–299 (2016).

73. Barayeu, U. et al. Hydropersulfides inhibit lipid peroxidation and ferroptosis by scavenging radicals. Nat. Chem. Biol. 19, 28–37 (2023).

74. Brown, E. M. & Bowden, N. B. Stabilities of Three Key Biological Trisulfides with Implications for Their Roles in the Release of Hydrogen Sulfide and Bioaccumulation of Sulfane Sulfur. ACS Omega 7, 11440–11451 (2022).

75. Switzer, C. H., Guttzeit, S., Eykyn, T. R. & Eaton, P. Cysteine trisulfide oxidizes protein thiols and induces electrophilic stress in human cells. Redox Biol. 47, 102155 (2021).

76. Koppenol, W. H. & Bounds, P. L. Signaling by sulfur-containing molecules. Quantitative aspects. Arch. Biochem. Biophys. 617, 3–8 (2017).

77. Everett, S. A. & Wardman, P. Perthiols as Antioxidants: Radical-Scavenging Andprooxidative Mechanisms. Methods in Enzymology vol. 251 (1995).

78. Everett, S. A., Folkes, L. K., Wardman, P. & Asmus, K. D. Free-radical repair by a novel perthiol: Reversible hydrogen transfer and perthiyl radical formation. Free Radic. Res. 20, 387–400 (1994).

79. Chauvin, J. P. R., Griesser, M. & Pratt, D. A. Hydropersulfides: H-Atom Transfer Agents Par Excellence. J. Am. Chem. Soc. 139, 6484–6493 (2017).

80. Jiang, X., Stockwell, B. R. & Conrad, M. Ferroptosis: mechanisms, biology and role in disease. Nature Reviews Molecular Cell Biology vol. 22 266–282 (2021).

81. Wu, Z. et al. Hydropersulfides Inhibit Lipid Peroxidation and Protect Cells from Ferroptosis. J. Am. Chem. Soc. 144, 15825–15837 (2022).

82. Libiad, M., Yadav, P. K., Vitvitsky, V., Martinov, M. & Banerjee, R. Organization of the human mitochondrial hydrogen sulfide oxidation pathway. J. Biol. Chem. 289, 30901–30910 (2014).

83. D'Autréaux, B. & Toledano, M. B. ROS as signalling molecules: Mechanisms that generate specificity in ROS homeostasis. Nature Reviews Molecular Cell Biology vol. 8 813–824 (2007).

84. Ferrer-Sueta, G. et al. Biochemistry of Peroxynitrite and Protein Tyrosine Nitration. Chemical Reviews vol. 118 1338–1408 (2018).

85. Gupta, V. & Carroll, K. S. Sulfenic acid chemistry, detection and cellular lifetime. Biochimica et

Biophysica Acta - General Subjects vol. 1840 847–875 (2014).

86. Paul, B. D. & Snyder, S. H. H 2S signalling through protein sulfhydration and beyond. Nature Reviews Molecular Cell Biology vol. 13 499–507 (2012).

87. Milos. R. Filipovic. Persulfidation (S-sulfhydration) and H2S. in Chemistry, Biochemistry and Pharmacology of Hydrogen Sulfide (eds. Moore, P. K. & Whiteman, M.) vol. 230 29–59 (Springer, Cham).

88. Ono, K. et al. Redox chemistry and chemical biology of H2S, hydropersulfides, and derived species: Implications of their possible biological activity and utility. Free Radical Biology and Medicine vol. 77 82–94 (2014).

89. Xiao, S. et al. A gut microbiota-targeted dietary intervention for amelioration of chronic inflammation underlying metabolic syndrome. FEMS Microbiol. Ecol. 87, 357–367 (2014).

90. Zhang, D. et al. Detection of protein S-sulfhydration by a tag-switch technique. Angew. Chemie - Int. Ed. 53, 575–581 (2014).

91. Akter, S. et al. Chemical proteomics reveals new targets of cysteine sulfinic acid reductase. Nat. Chem. Biol. 14, 995–1004 (2018).

92. Paulsen, C. E. & Carroll, K. S. Cysteine-mediated redox signaling: Chemistry, biology, and tools for discovery. Chemical Reviews vol. 113 4633–4679 (2013).

93. Dóka et al. Control of protein function through oxidation and reduction of persulfidated states. Sci. Adv. 6, (2020).

94. Palde, P. B. & Carroll, K. S. A universal entropy-driven mechanism for thioredoxin-target recognition. Proc. Natl. Acad. Sci. U. S. A. 112, 7960–7965 (2015).

95. Ubuka, T. Assay methods and biological roles of labile sulfur in animal tissues. vol. 781 227–249 (Elsevier, 2002).

96. Gao, X. H. et al. Quantitative H2S-mediated protein sulfhydration reveals metabolic reprogramming during the integrated stress response. Elife 4, (2015).

97. Dóka, É. et al. A novel persulfide detection method reveals protein persulfide- and polysulfide-reducing functions of thioredoxin and glutathione systems. Sci. Adv. 2, (2016).

98. Longen, S. et al. Quantitative Persulfide Site Identification (qPerS-SID) Reveals Protein Targets of H2S Releasing Donors in Mammalian Cells. Sci. Reports 2016 61 6, 1–12 (2016).

99. Fan, K., Chen, Z. & Liu, H. Evidence that the ProPerDP method is inadequate for protein persulfidation detection due to lack of specificity. Sci. Adv. 6, 6477–6491 (2020).

100. Reisz, J. A. et al. Thiol-blocking electrophiles interfere with labeling and detection of protein sulfenic acids. FEBS J. 280, 6150–6161 (2013).

101. Fontaine, S. D., Reid, R., Robinson, L., Ashley, G. W. & Santi, D. V. Long-term stabilization of maleimide-thiol conjugates. Bioconjug. Chem. 26, 145–152 (2015).

102. Bibli, S. I. et al. Mapping the Endothelial Cell S -Sulfhydrome Highlights the Crucial Role of Integrin Sulfhydration in Vascular Function. Circulation 143, 935–948 (2021).

103. Fu, L. et al. Direct Proteomic Mapping of Cysteine Persulfidation. Antioxidants Redox Signal. 33, 1061–1076 (2020).

104. Yang, J. et al. Global, in situ, site-specific analysis of protein S-sulfenylation. Nat. Protoc. 2015 107 10, 1022–1037 (2015).

105. Schilling, D. et al. Commonly Used Alkylating Agents Limit Persulfide Detection by Converting Protein Persulfides into Thioethers. Angew. Chemie 61, 1–13 (2022).

106. Vignane, T. & Filipovic, M. R. Emerging chemical biology of protein persulfidation. Antioxid. Redox Signal. 39, 19–39 (2023).

107. Park, C. M., Macinkovic, I., Filipovic, M. R. & Xian, M. Use of the ‘Tag-Switch’ Method for the

Detection of Protein S-Sulfhydration. in Methods in Enzymology vol. 555 39–56 (Academic Press, 2015).

108. Aroca, A., Benito, J. M., Gotor, C. & Romero, L. C. Persulfidation proteome reveals the regulation of protein function by hydrogen sulfide in diverse biological processes in Arabidopsis. J. Exp. Bot. 68, 4915–4927 (2017).

109. Bernal-Perez, L. F., Prokai, L. & Ryu, Y. Selective N-terminal fluorescent labeling of proteins using 4-chloro-7-nitrobenzofurazan: A method to distinguish protein N-terminal acetylation. Anal. Biochem. 428, 13–15 (2012).

110. Ellis, H. R. & Poole, L. B. Novel application of 7-chloro-4-nitrobenzo-2-oxa-1,3-diazole to identify cysteine sulfenic acid in the AhpC component of alkyl hydroperoxide reductase. Biochemistry 36, 15013–15018 (1997).

111. Klomsiri, C. et al. Use of Dimedone-Based Chemical Probes for Sulfenic Acid Detection: Evaluation of Conditions Affecting Probe Incorporation into Redox-Sensitive Proteins. Methods Enzymol. 473, 77–94 (2010).

112. Garc\'\ia-Calderón, M. et al. Persulfidation protects from oxidative stress under nonphotorespiratory conditions in Arabidopsis. New Phytol. 238, 1431–1445 (2023).

113. Andrews, J. C. THE OPTICAL ACTIVITY OF CYSTEINE. J. Biol. Chem. 69, 209–217 (1926).

114. Vasas, A., Dóka, É., Fábián, I. & Nagy, P. Kinetic and thermodynamic studies on the disulfide-bond reducing potential of hydrogen sulfide. Nitric Oxide - Biol. Chem. 46, 93–101 (2015).

115. Wood, Z. A., Schröder, E., Harris, J. R. & Poole, L. B. Structure, mechanism and regulation of peroxiredoxins. Trends in Biochemical Sciences vol. 28 32–40 (2003).

116. Sueiro-Olivares, M. et al. Fungal and host protein persulfidation are functionally correlated and modulate both virulence and antifungal response. PLoS Biol. 19, e3001247 (2021).

117. Bostelaar, T. et al. Hydrogen Sulfide Oxidation by Myoglobin. J. Am. Chem. Soc. 138, 8476–8488 (2016).

118. Pálinkás, Z. et al. Interactions of hydrogen sulfide with myeloperoxidase. British Journal of Pharmacology vol. 172 1516–1532 (2015).

119. Vitvitsky, V., Yadav, P. K., Kurthen, A. & Banerjee, R. Sulfide oxidation by a noncanonical pathway in red blood cells generates thiosulfate and polysulfides. J. Biol. Chem. 290, 8310–8320 (2015).

120. Ruetz, M. et al. A distal ligand mutes the interaction of hydrogen sulfide with human neuroglobin. J. Biol. Chem. 292, 6512–6528 (2017).

121. Alvarez-Paggi, D. et al. Multifunctional Cytochrome c: Learning New Tricks from an Old Dog. Chem. Rev. 117, 13382–13460 (2017).

122. Vitvitsky, V. et al. Cytochrome c Reduction by H 2 S Potentiates Sulfide Signaling. ACS Chem. Biol. 13, (2018).

123. Wedmann, R. et al. Working with ‘H2S’: Facts and apparent artifacts. Nitric Oxide - Biol. Chem. 41, 85–96 (2014).

124. Lange, M. et al. Direct Zinc Finger Protein Persulfidation by H _{\textrm{2}} S Is Facilitated by Zn ^{\textrm{2+}}. 131, 8081–8085.

125. Yang, J., Gupta, V., Carroll, K. S. S. & Liebler, D. C. C. Site-specific mapping and quantification of protein S-sulphenylation in cells. Nat. Commun. 5, 4776 (2014).

126. Paulsen, C. E. et al. Peroxide-dependent sulfenylation of the EGFR catalytic site enhances kinase activity. Nat. Chem. Biol. 8, 57–64 (2012).

127. Sundaresan, M., Yu, Z.-X., Ferrans, V. J., Irani, K. & Finkel, T. Requirement for Generation of H 2 O 2 for Platelet-Derived Growth Factor Signal Transduction. Science (80-.). 270, 296–299 (1995).

128. Fujii, S., Sawa, T., Motohashi, H. & Akaike, T. Persulfide synthases that are functionally coupled

with translation mediate sulfur respiration in mammalian cells. British Journal of Pharmacology vol. 176 607–615 (2019).

129. Akaike, T. et al. Cysteinyl-tRNA synthetase governs cysteine polysulfidation and mitochondrial bioenergetics. Nat. Commun. 8, 1–15 (2017).

130. Landry, A. P. et al. A Catalytic Trisulfide in Human Sulfide Quinone Oxidoreductase Catalyzes Coenzyme A Persulfide Synthesis and Inhibits Butyrate Oxidation. Cell Chem. Biol. 26, 1515-1525.e4 (2019).

131. Mishanina, T. V., Yadav, P. K., Ballou, D. P. & Banerjee, R. Transient kinetic analysis of hydrogen sulfide oxidation catalyzed by human sulfide quinone oxidoreductase. J. Biol. Chem. 290, 25072–25080 (2015).

132. Goubern, M., Andriamihaja, M., Nübel, T., Blachier, F. & Bouillaud, F. Sulfide, the first inorganic substrate for human cells. FASEB J. 21, 1699–1706 (2007).

133. Kessler, D. Enzymatic activation of sulfur for incorporation into biomolecules in prokaryotes. FEMS Microbiology Reviews vol. 30 825–840 (2006).

134. Lill, R. & Mühlenhoff, U. Iron-sulfur-protein biogenesis in eukaryotes. Trends in Biochemical Sciences vol. 30 133–141 (2005).

135. Mueller, E. G. Trafficking in persulfides: Delivering sulfur in biosynthetic pathways. Nat. Chem. Biol. 2, 185–194 (2006).

136. Zhang, W. et al. IscS functions as a primary sulfur-donating enzyme by interacting specifically with moeb and moad in the biosynthesis of molybdopterin in escherichia coli. J. Biol. Chem. 285, 2302–2308 (2010).

137. Parent, A. et al. Mammalian frataxin directly enhances sulfur transfer of NFS1 persulfide to both ISCU and free thiols. Nat. Commun. 6, 1–12 (2015).

138. Lauhon, C. T. Requirement for IscS in biosynthesis of all thionucleosides in Escherichia coli. J. Bacteriol. 184, 6820–6829 (2002).

139. Libiad, M., Sriraman, A. & Banerjee, R. Polymorphic variants of human rhodanese exhibit differences in thermal stability and sulfur transfer kinetics. J. Biol. Chem. 290, 23579–23588 (2015).

140. Bordo, D. & Bork, P. The rhodanese/Cdc25 phosphatase superfamily. Sequence-structure-function relations. EMBO Reports vol. 3 741–746 (2002).

141. BONOMI, F., PAGANI, S., CERLETTI, P. & CANNELLA, C. Rhodanese-Mediated Sulfur Transfer to Succinate Dehydrogenase. Eur. J. Biochem. 72, 17–24 (1977).

142. Bonomi, F., Pagani, S. & Cerletti, P. Insertion of sulfide into ferredoxins catalyzed by rhodanese. FEBS Lett. 84, 149–152 (1977).

143. Taniguchi, T. & Kimura, T. Role of 3-mercaptopyruvate sulfurtransferase in the formation of the iron-sulfur chromophore of adrenal ferredoxin. BBA - Enzymol. 364, 284–295 (1974).

144. Libiad, M. et al. Thiosulfate sulfurtransferase-like domain-containing 1 protein interacts with thioredoxin. J. Biol. Chem. 293, 2675–2686 (2018).

145. Ploegman, J. H., Drent, G., Kalk, K. H. & Hol, W. G. J. The structure of bovine liver rhodanese. II. The active site in the sulfur-substituted and the sulfur-free enzyme. J. Mol. Biol. 127, 149–162 (1979).

146. Ploegman, J. H., Drent, G., Kalk, K. H. & Hol, W. G. J. Structure of bovine liver rhodanese. I. Structure determination at 2.5 Å resolution and a comparison of the conformation and sequence of its two domains. J. Mol. Biol. 123, 557–594 (1978).

147. Pedre, B. et al. 3-Mercaptopyruvate sulfur transferase is a protein persulfidase. Nat. Chem. Biol. 19, 507–517 (2023).

148. Steudel, R., Drozdova, Y., Miaskiewicz, K., Hertwig, R. H. & Koch, W. How unstable are

thiosulfoxides? An ab initio MO study of various disulfanes RSSR (R = H, Me, Pr, All), their branched isomers R2SS, and the related transition states. J. Am. Chem. Soc. 119, 1990–1996 (1997).

149. Buchanan, B. B., Holmgren, A., Jacquot, J. P. & Scheibe, R. Fifty years in the thioredoxin field and a bountiful harvest. Biochimica et Biophysica Acta - General Subjects vol. 1820 1822–1829 (2012).

150. Lu, J. & Holmgren, A. The thioredoxin superfamily in oxidative protein folding. Antioxidants and Redox Signaling vol. 21 457–470 (2014).

151. Krishnan, N., Fu, C., Pappin, D. J. & Tonks, N. K. Biochemistry: H 2S-induced sulfhydration of the phosphatase PTP1B and its role in the endoplasmic reticulum stress response. Sci. Signal. 4, (2011).

152. Nagy, P. et al. Chemical aspects of hydrogen sulfide measurements in physiological samples. Biochimica et Biophysica Acta - General Subjects vol. 1840 876–891 (2014).

153. Lu, J. & Holmgren, A. The thioredoxin antioxidant system. Free Radical Biology and Medicine vol. 66 75–87 (2014).

154. Hara, M. R. et al. S-nitrosylated GAPDH initiates apoptotic cell death by nuclear translocation following Siah1 binding. Nat. Cell Biol. 7, 665–674 (2005).

155. Jarosz, A. P. et al. Glyceraldehyde 3-phosphate dehydrogenase (GAPDH) is inactivated by S-sulfuration in vitro. doi:10.1016/j.freeradbiomed.2015.09.007.

156. Zhao, K. et al. S-sulfhydration of {MEK}1 leads to {PARP}-1 activation and {DNA} damage repair. embr.201338213 doi:10.1002/embr.201338213.

157. Abdallah, Y. et al. The role of poly(ADP-ribose) polymerase (PARP) in the autonomous proliferative response of endothelial cells to hypoxia. Cardiovasc. Res. 73, 568–574 (2007).

158. Maser, R. S., Monsen, K. J., Nelms, B. E. & Petrini, J. H. J. hMre11 and hRad50 Nuclear Foci Are Induced During the Normal Cellular Response to DNA Double-Strand Breaks †. Mol. Cell. Biol. 17, 6087–6096 (1997).

159. Dove, S. K. et al. Svp1p defines a family of phosphatidylinositol 3,5-bisphosphate effectors. EMBO J. 23, 1922–1933 (2004).

160. Wun, C. L., Quan, Y. & Zhuang, X. Recent Advances in Membrane Shaping for Plant Autophagosome Biogenesis. Front. Plant Sci. 11, 524773 (2020).

161. Aroca, A., Yruela, I., Gotor, C. & Bassham, D. C. Persulfidation of ATG18a regulates autophagy under ER stress in Arabidopsis. Proc. Natl. Acad. Sci. U. S. A. 118, e2023604118 (2021).

162. Ozgur, R., Turkan, I., Uzilday, B. & Sekmen, A. H. Endoplasmic reticulum stress triggers ROS signalling, changes the redox state, and regulates the antioxidant defence of Arabidopsis thaliana. J. Exp. Bot. 65, 1377–1390 (2014).

163. López-Otín, C., Blasco, M. A., Partridge, L., Serrano, M. & Kroemer, G. Hallmarks of aging: An expanding universe. Cell vol. 186 243–278 (2023).

164. López-Otín, C., Blasco, M. A., Partridge, L., Serrano, M. & Kroemer, G. The Hallmarks of Aging. Cell 153, 1194–1217 (2013).

165. Perridon, B., Leuvenink, H., Hillebrands, J.-L., van Goor, H. & Bos, E. The role of hydrogen sulfide in aging and age-related pathologies. 8, 2264–2289.

166. Sun, W. H., Liu, F., Chen, Y. & Zhu, Y. C. Hydrogen sulfide decreases the levels of ROS by inhibiting mitochondrial complex IV and increasing SOD activities in cardiomyocytes under ischemia/reperfusion. Biochem. Biophys. Res. Commun. 421, 164–169 (2012).

167. Elrod, J. W. et al. Hydrogen sulfide attenuates myocardial ischemia-reperfusion injury by preservation of mitochondrial function. Proc. Natl. Acad. Sci. U. S. A. 104, 15560–15565 (2007).

168. Wang, S. S. et al. Hydrogen sulfide promotes autophagy of hepatocellular carcinoma cells through the PI3K/Akt/mTOR signaling pathway. Cell Death Dis. 8, e2688–e2688 (2017).

169. Motta, J. P. et al. Hydrogen sulfide protects from colitis and restores intestinal microbiota biofilm and mucus production. Inflamm. Bowel Dis. 21, 1006–1017 (2015).

170. Motta, J. P. et al. Iron sequestration in microbiota biofilms as a novel strategy for treating inflammatory bowel disease. Inflamm. Bowel Dis. 24, 1493–1502 (2018).

171. Zimmermann, K. K. et al. Hydrogen Sulfide Exerts Anti-oxidative and Anti-inflammatory Effects in Acute Lung Injury. Inflammation 41, 249–259 (2018).

172. Szczesny, B. et al. AP39, a novel mitochondria-targeted hydrogen sulfide donor, stimulates cellular bioenergetics, exerts cytoprotective effects and protects against the loss of mitochondrial DNA integrity in oxidatively stressed endothelial cells in vitro. Nitric Oxide - Biol. Chem. 41, 120–130 (2014).

173. Suo, R. et al. Hydrogen sulfide prevents H2O2-induced senescence in human umbilical vein endothelial cells through SIRT1 activation. Mol. Med. Rep. 7, 1865–1870 (2013).

174. Rios, E. C. S., Szczesny, B., Soriano, F. G., Olah, G. & Szabo, C. Hydrogen sulfide attenuates cytokine production through the modulation of chromatin remodeling. Int. J. Mol. Med. 35, 1741–1746 (2015).

175. Fawcett, E. M., Hoyt, J. M., Johnson, J. K. & Miller, D. L. Hypoxia disrupts proteostasis in Caenorhabditis elegans. Aging Cell 14, 92–101 (2015).

176. Liu, Y. Y., Nagpure, B. V., Wong, P. T. H. & Bian, J. S. Hydrogen sulfide protects SH-SY5Y neuronal cells against d-galactose induced cell injury by suppression of advanced glycation end products formation and oxidative stress. Neurochem. Int. 62, 603–609 (2013).

177. Xue, R. et al. Hydrogen sulfide treatment promotes glucose uptake by increasing insulin receptor sensitivity and ameliorates kidney lesions in type 2 diabetes. Antioxidants Redox Signal. 19, 5–23 (2013).

178. Ohno, K., Okuda, K. & Uehara, T. Endogenous S-sulfhydration of PTEN helps protect against modification by nitric oxide. Biochem. Biophys. Res. Commun. 456, 245–249 (2015).

179. Yang, G. et al. Hydrogen Sulfide Protects Against Cellular Senescence \textit{via} \textit{S} - Sulfhydration of Keap1 and Activation of Nrf2. 18, 1906–1919.

180. Zheng, M. et al. Hydrogen sulfide delays nicotinamide-induced premature senescence via upregulation of SIRT1 in human umbilical vein endothelial cells. Mol. Cell. Biochem. 393, 59–67 (2014).

181. Liu, D. et al. Hydrogen sulfide promotes proliferation and neuronal differentiation of neural stem cells and protects hypoxia-induced decrease in hippocampal neurogenesis. Pharmacol. Biochem. Behav. 116, 55–63 (2014).

182. Liu, Y. et al. Hydrogen sulfide maintains mesenchymal stem cell function and bone homeostasis via regulation of Ca2+ channel sulfhydration. Cell Stem Cell 15, 66–78 (2014).

183. Munaron, L., Avanzato, D., Moccia, F. & Mancardi, D. Hydrogen sulfide as a regulator of calcium channels. Cell Calcium vol. 53 77–84 (2013).

184. Narayan, V. et al. Deep Proteome Analysis Identifies Age-Related Processes in C. elegans. Cell Syst. 3, 144–159 (2016).

185. Walther, D. M. et al. Widespread Proteome Remodeling and Aggregation in Aging C. elegans. Cell 161, 919–932 (2015).

186. Trabzuni, D. et al. Widespread sex differences in gene expression and splicing in the adult human brain. Nat. Commun. 4, (2013).

187. Hernandez, D. G. et al. Integration of GWAS SNPs and tissue specific expression profiling reveal discrete eQTLs for human traits in blood and brain. Neurobiol. Dis. 47, 20–28 (2012).

188. Schaum, N. et al. Single-cell transcriptomics of 20 mouse organs creates a Tabula Muris. Nature 562, 367–372 (2018).

189. Schaum, N. et al. Ageing hallmarks exhibit organ-specific temporal signatures. Nature 583, 596–602 (2020).

190. Petrovic, D., Kouroussis, E., Vignane, T. & Filipovic, M. R. The Role of Protein Persulfidation in Brain Aging and Neurodegeneration. Front. Aging Neurosci. 13, 1–12 (2021).

191. Pan, L. L., Liu, X. H., Gong, Q. H., Yang, H. B. & Zhu, Y. Z. Role of cystathionine γ-Lyase/hydrogen sulfide pathway in cardiovascular disease: A novel therapeutic strategy? Antioxidants and Redox Signaling vol. 17 106–118 (2012).

192. Solberg, O. K., Filkukovà, P., Frich, J. C. & Feragen, K. J. B. Age at Death and Causes of Death in Patients with Huntington Disease in Norway in 1986-2015. J. Huntingtons. Dis. 7, 77–86 (2018).

193. Schlager, G. Longevity in spontaneously hypertensive mice. Exp. Gerontol. 16, 325–330 (1981).

194. Shaposhnikov, M. et al. Overexpression of CBS and CSE genes affects lifespan, stress resistance and locomotor activity in Drosophila melanogaster. Aging (Albany. NY). 10, 3260–3272 (2018).

195. Miller, D. L. & Roth, M. B. Hydrogen sulfide increases thermotolerance and lifespan in Caenorhabditis elegans. Proc. Natl. Acad. Sci. U. S. A. 104, 20618–20622 (2007).

196. Tyshkovskiy, A. et al. Identification and Application of Gene Expression Signatures Associated with Lifespan Extension. Cell Metab. 30, 573-593.e8 (2019).

197. Blackstone, E., Morrison, M. & Roth, M. B. H2S induces a suspended animation-like state in mice. Science (80-.). 308, 518 (2005).

198. Hipp, M. S., Park, S. H. & Hartl, U. U. Proteostasis impairment in protein-misfolding and -aggregation diseases. Trends in Cell Biology vol. 24 506–514 (2014).

199. Filippone, A., Esposito, E., Mannino, D., Lyssenko, N. & Praticò, D. The contribution of altered neuronal autophagy to neurodegeneration. Pharmacology and Therapeutics vol. 238 108178 (2022).

200. Barmaki, H., Nourazarian, A. & Khaki-Khatibi, F. Proteostasis and neurodegeneration: a closer look at autophagy in Alzheimer's disease. Frontiers in Aging Neuroscience vol. 15 1281338 (2023).

201. Lee, J. M., Hammarén, H. M., Savitski, M. M. & Baek, S. H. Control of protein stability by post-translational modifications. Nat. Commun. 14, 1–16 (2023).

202. Schaffert, L. N. & Carter, W. G. Do post-translational modifications influence protein aggregation in neurodegenerative diseases: A systematic review. Brain Sciences vol. 10 232 (2020).

203. Despres, C. et al. Identification of the Tau phosphorylation pattern that drives its aggregation. Proceedings of the National Academy of Sciences of the United States of America vol. 114 9080–9085 (2017).

204. Sadri-Vakili, G. et al. Histones associated with downregulated genes are hypo-acetylated in Huntington's disease models. Hum. Mol. Genet. 16, 1293–1306 (2007).

205. Chung, K. K. K. et al. S-nitrosylation of parkin regulates ubiquitination and compromises parkin's protective function. Science (80-.). 304, 1328–1331 (2004).

206. Rizza, S. et al. S-nitrosylation drives cell senescence and aging in mammals by controlling mitochondrial dynamics and mitophagy. Proc. Natl. Acad. Sci. U. S. A. 115, E3388–E3397 (2018).

207. Bonifati, V. et al. Mutations in the DJ-1 gene associated with autosomal recessive early-onset parkinsonism. Science (80-.). 299, 256–259 (2003).

208. Canet-Avilés, R. M. et al. The Parkinson's disease DJ-1 is neuroprotective due to cysteine-sulfinic acid-driven mitochondrial localization. Proc. Natl. Acad. Sci. U. S. A. 101, 9103–9108 (2004).

209. Kinumi, T., Kimata, J., Taira, T., Ariga, H. & Niki, E. Cysteine-106 of DJ-1 is the most sensitive cysteine residue to hydrogen peroxide-mediated oxidation in vivo in human umbilical vein endothelial cells. Biochem. Biophys. Res. Commun. 317, 722–728 (2004).

210. Oh, S. E. & Mouradian, M. M. Regulation of signal transduction by DJ-1. in Advances in

Experimental Medicine and Biology vol. 1037 97–131 (Springer, Singapore, 2017).

211. Galardon, E. et al. Persulfidation of DJ-1: Mechanism and Consequences. Biomolecules 13, 27 (2023).

212. Akhmadi, A. et al. DJ-1 protects proteins from acylation by catalyzing the hydrolysis of highly reactive cyclic 3-phosphoglyceric anhydride. doi:10.1038/s41467-024-46391-9.

213. Chen, Z. et al. Oxidative stress induced by hydrogen peroxide promotes glycolysis by activating CaMKK/LKB1/AMPK pathway in broiler breast muscle. Poult. Sci. 101, (2022).

214. Eto, K., Asada, T., Arima, K., Makifuchi, T. & Kimura, H. Brain hydrogen sulfide is severely decreased in Alzheimer's disease. Biochem. Biophys. Res. Commun. 293, 1485–1488 (2002).

215. Giuliani, D. et al. Hydrogen sulfide slows down progression of experimental Alzheimer's disease by targeting multiple pathophysiological mechanisms. Neurobiol. Learn. Mem. 104, 82–91 (2013).

216. Xuan, A. et al. Hydrogen sulfide attenuates spatial memory impairment and hippocampal neuroinflammation in beta-amyloid rat model of Alzheimer's disease. J. Neuroinflammation 9, 1–11 (2012).

217. Beurel, E., Grieco, S. F. & Jope, R. S. Glycogen synthase kinase-3 (GSK3): Regulation, actions, and diseases. Pharmacology and Therapeutics vol. 148 114–131 (2015).

218. Sengupta, A. et al. Phosphorylation of tau at both Thr 231 and Ser 262 is required for maximal inhibition of its binding to microtubules. Arch. Biochem. Biophys. 357, 299–309 (1998).

219. Crews, L. & Masliah, E. Molecular mechanisms of neurodegeneration in Alzheimer's disease. Hum. Mol. Genet. 19, R12–R20 (2010).

220. Hooper, C., Killick, R. & Lovestone, S. The GSK3 hypothesis of Alzheimer's disease. Journal of Neurochemistry vol. 104 1433–1439 (2008).

221. Lauretti, E., Dincer, O. & Praticò, D. Glycogen synthase kinase-3 signaling in Alzheimer's disease. Biochimica et Biophysica Acta - Molecular Cell Research vol. 1867 118664 (2020).

222. Zhang, H. et al. Hydrogen sulfide reduces mRNA and protein levels of beta-site amyloid precursor protein cleaving enzyme 1 in PC12 cells. Neurochem. Int. 58, 169–175 (2011).

223. Trottier, Y. et al. Polyglutamine expansion as a pathological epitope in huntington's disease and four dominant cerebellar ataxias. Nature 378, 403–406 (1995).

224. Sbodio, J. I., Snyder, S. H. & Paul, B. D. Transcriptional control of amino acid homeostasis is disrupted in Huntington's disease. Proc. Natl. Acad. Sci. U. S. A. 113, 8843–8848 (2016).

225. Liochev, S. I. Reactive oxygen species and the free radical theory of aging. Free Radical Biology and Medicine vol. 60 1–4 (2013).

226. Lo Conte, M. & Carroll, K. S. The redox biochemistry of protein sulfenylation and sulfinylation. Journal of Biological Chemistry vol. 288 26480–26488 (2013).

227. Venkatachalam, N., Bakavayev, S., Engel, D., Barak, Z. & Engel, S. Primate differential redoxome (PDR) – A paradigm for understanding neurodegenerative diseases. Redox Biol. 36, 101683 (2020).

228. Alberti, S. & Hyman, A. A. Biomolecular condensates at the nexus of cellular stress, protein aggregation disease and ageing. Nature Reviews Molecular Cell Biology vol. 22 196–213 (2021).

229. Banani, S. F., Lee, H. O., Hyman, A. A. & Rosen, M. K. Biomolecular condensates: Organizers of cellular biochemistry. Nature Reviews Molecular Cell Biology vol. 18 285–298 (2017).

230. Hnisz, D., Shrinivas, K., Young, R. A., Chakraborty, A. K. & Sharp, P. A. A Phase Separation Model for Transcriptional Control. Cell vol. 169 13–23 (2017).

231. Demmerle, J., Hao, S. & Cai, D. Transcriptional condensates and phase separation: condensing information across scales and mechanisms. Nucleus vol. 14 (2023).

232. Tang, G. et al. Liquid–liquid phase separation of H3K27me3 reader BP1 regulates transcriptional

repression. Genome Biol. 25, (2024).

233. Cai, D. et al. Phase separation of YAP reorganizes genome topology for long-term YAP target gene expression. Nat. Cell Biol. 21, 1578–1589 (2019).

234. Ivanov, P., Kedersha, N. & Anderson, P. Stress granules and processing bodies in translational control. Cold Spring Harb. Perspect. Biol. 11, (2019).

235. Milovanovic, D., Wu, Y., Bian, X. & De Camilli, P. A liquid phase of synapsin and lipid vesicles. Science (80-.). 361, 604–607 (2018).

236. Hoffmann, C. et al. Synapsin condensation controls synaptic vesicle sequestering and dynamics. Nat. Commun. 14, 6730 (2023).

237. Alberti, S., Gladfelter, A. & Mittag, T. Considerations and Challenges in Studying Liquid-Liquid Phase Separation and Biomolecular Condensates. Cell vol. 176 419–434 (2019).

238. Wang, B. et al. Liquid–liquid phase separation in human health and diseases. Signal Transduction and Targeted Therapy vol. 6 (2021).

239. Zaslavsky, B. Y., Ferreira, L. A. & Uversky, V. N. Driving forces of liquid-liquid phase separation in biological systems. Biomolecules vol. 9 (2019).

240. Nott, T. J. et al. Phase Transition of a Disordered Nuage Protein Generates Environmentally Responsive Membraneless Organelles. Mol. Cell 57, 936–947 (2015).

241. Molliex, A. et al. Phase Separation by Low Complexity Domains Promotes Stress Granule Assembly and Drives Pathological Fibrillization. Cell 163, 123–133 (2015).

242. Li, P. et al. High-throughput and proteome-wide discovery of endogenous biomolecular condensates. Nat. Chem. 16, 1101–1112 (2024).

243. Yang, P. et al. G3BP1 Is a Tunable Switch that Triggers Phase Separation to Assemble Stress Granules. Cell 181, 325-345.e28 (2020).

244. Aulas, A. et al. Stress-specific differences in assembly and composition of stress granules and related foci. J. Cell Sci. 130, 927–937 (2017).

245. Hu, S. et al. Time-resolved proteomic profiling reveals compositional and functional transitions across the stress granule life cycle. Nat. Commun. 14, 1–17 (2023).

246. Anderson, P. & Kedersha, N. Visibly stressed: The role of eIF2, TIA-1, and stress granules in protein translation. Cell Stress and Chaperones vol. 7 213–221 (Elsevier, 2002).

247. Matsuki, H. et al. Both G3BP1 and G3BP2 contribute to stress granule formation. Genes to Cells 18, 135–146 (2013).

248. Banani, S. F. et al. Compositional Control of Phase-Separated Cellular Bodies. Cell 166, 651–663 (2016).

249. Sanchez-Burgos, I., Espinosa, J. R., Joseph, J. A. & Collepardo-Guevara, R. Valency and binding affinity variations can regulate the multilayered organization of protein condensates with many components. Biomolecules 11, 1–19 (2021).

250. Alberti, S. & Hyman, A. A. Are aberrant phase transitions a driver of cellular aging? BioEssays 38, 959–968 (2016).

251. Harmon, T. S., Holehouse, A. S., Rosen, M. K. & Pappu, R. V. Intrinsically disordered linkers determine the interplay between phase separation and gelation in multivalent proteins. Elife 6, (2017).

252. Franzmann, T. M. et al. Phase separation of a yeast prion protein promotes cellular fitness. Science (80-.). 359, (2018).

253. Choi, J. M., Holehouse, A. S. & Pappu, R. V. Physical Principles Underlying the Complex Biology of Intracellular Phase Transitions. Annual Review of Biophysics vol. 49 107–133 (2020).

254. Garaizar, A., Espinosa, J. R., Joseph, J. A. & Collepardo-Guevara, R. Kinetic interplay between

droplet maturation and coalescence modulates shape of aged protein condensates. Sci. Rep. 12, 1–13 (2022).

255. Jawerth, L. et al. Protein condensates as aging Maxwell fluids. Science (80-.). 370, 1317–1323 (2020).

256. Li, J. et al. Post-translational modifications in liquid-liquid phase separation: a comprehensive review. Mol. Biomed. 2022 31 3, 1–17 (2022).

257. Luo, Y. Y., Wu, J. J. & Li, Y. M. Regulation of liquid-liquid phase separation with focus on post-translational modifications. Chem. Commun. 57, 13275–13287 (2021).

258. Tourrière, H. et al. The RasGAP-associated endoribonuclease G3BP mediates stress granule assembly. in Journal of Cell Biology vol. 222 (2023).

259. Gwon, Y. et al. Ubiquitination of G3BP1 mediates stress granule disassembly in a context-specific manner. Science (80-.). 372, eabf6548 (2021).

260. Markmiller, S. et al. Active Protein Neddylation or Ubiquitylation Is Dispensable for Stress Granule Dynamics. Cell Rep. 27, 1356-1363.e3 (2019).

261. Liang, P., Zhang, J. & Wang, B. Emerging Roles of Ubiquitination in Biomolecular Condensates. Cells vol. 12 2329 (2023).

262. Yasuda, S. et al. Stress- and ubiquitylation-dependent phase separation of the proteasome. Nature 578, 296–300 (2020).

263. Dao, T. P. et al. Ubiquitin Modulates Liquid-Liquid Phase Separation of UBQLN2 via Disruption of Multivalent Interactions. Mol. Cell 69, 965-978.e6 (2018).

264. Kato, M. et al. Redox State Controls Phase Separation of the Yeast Ataxin-2 Protein via Reversible Oxidation of Its Methionine-Rich Low-Complexity Domain. Cell 177, 711-721.e8 (2019).

265. Zbinden, A., Pérez-Berlanga, M., De Rossi, P. & Polymenidou, M. Phase Separation and Neurodegenerative Diseases: A Disturbance in the Force. Developmental Cell vol. 55 45–68 (2020).

266. Klaips, C. L., Jayaraj, G. G. & Hartl, F. U. Pathways of cellular proteostasis in aging and disease. Journal of Cell Biology vol. 217 51–63 (2018).

267. Mackenzie, I. R. et al. TIA1 Mutations in Amyotrophic Lateral Sclerosis and Frontotemporal Dementia Promote Phase Separation and Alter Stress Granule Dynamics. Neuron 95, 808-816.e9 (2017).

268. Wegmann, S. et al. Tau protein liquid–liquid phase separation can initiate tau aggregation. EMBO J. 37, 1–21 (2018).

269. Qamar, S. et al. FUS Phase Separation Is Modulated by a Molecular Chaperone and Methylation of Arginine Cation-π Interactions. Cell 173, 720-734.e15 (2018).

270. Wang, A. et al. A single N-terminal phosphomimic disrupts TDP-43 polymerization, phase separation, and RNA splicing. EMBO J. 37, (2018).

271. Dormann, D. et al. Arginine methylation next to the PY-NLS modulates Transportin binding and nuclear import of FUS. EMBO J. 31, 4258–4275 (2012).

272. Monahan, Z. et al. Phosphorylation of the FUS low-complexity domain disrupts phase separation, aggregation, and toxicity. EMBO J. 36, 2951–2967 (2017).

273. Go, Y. M., Chandler, J. D. & Jones, D. P. The cysteine proteome. Free Radical Biology and Medicine vol. 84 227–245 (2015).

274. Sies, H. Hydrogen peroxide as a central redox signaling molecule in physiological oxidative stress: Oxidative eustress. Redox Biology vol. 11 613–619 (2017).

275. Xiao, H. et al. A Quantitative Tissue-Specific Landscape of Protein Redox Regulation during Aging. Cell 180, 968-983.e24 (2020).

276. Bithi, N. et al. Dietary restriction transforms the mammalian protein persulfidome in a tissue-specific and cystathionine γ-lyase-dependent manner. Nat. Commun. 12, (2021).

277. Fu, L., Liu, K., Ferreira, R. B., Carroll, K. S. & Yang, J. Proteome-Wide Analysis of Cysteine S-Sulfenylation Using a Benzothiazine-Based Probe. Curr. Protoc. Protein Sci. 95, e76 (2019).

278. Martin, B. R., Wang, C., Adibekian, A., Tully, S. E. & Cravatt, B. F. Global profiling of dynamic protein palmitoylation. Nat. Methods 9, 84–89 (2012).

279. Storck, E. M. et al. Dual chemical probes enable quantitative system-wide analysis of protein prenylation and prenylation dynamics. Nat. Chem. 11, 552–561 (2019).

280. James, A. M., Smith, A. C., Smith, C. L., Robinson, A. J. & Murphy, M. P. Proximal Cysteines that Enhance Lysine N-Acetylation of Cytosolic Proteins in Mice Are Less Conserved in Longer-Living Species. Cell Rep. 24, 1445–1455 (2018).

281. Parvez, S., Long, M. J. C., Poganik, J. R. & Aye, Y. Redox signaling by reactive electrophiles and oxidants. Chemical Reviews vol. 118 8798–8888 (2018).

282. Qin, W. et al. S-glycosylation-based cysteine profiling reveals regulation of glycolysis by itaconate. Nat. Chem. Biol. 15, 983–991 (2019).

283. Blewett, M. M. et al. Chemical proteomic map of dimethyl fumarate-sensitive cysteines in primary human T cells. Sci. Signal. 9, (2016).

284. Karpievitch, Y. V. et al. Normalization of peak intensities in bottom-up MS-based proteomics using singular value decomposition. Bioinformatics 25, 2573–2580 (2009).

285. Karpievitch, Y. V., Dabney, A. R. & Smith, R. D. Normalization and missing value imputation for label-free LC-MS analysis. BMC Bioinformatics 13 Suppl 1, 1–9 (2012).

286. Fink, A. L. Protein aggregation: Folding aggregates, inclusion bodies and amyloid. Fold. Des. 3, R9–R23 (1998).

287. Strom, A. R. et al. Phase separation drives heterochromatin domain formation. Nature 547, 241–245 (2017).

288. Zeng, M. et al. Phase Transition in Postsynaptic Densities Underlies Formation of Synaptic Complexes and Synaptic Plasticity. Cell 166, 1163-1175.e12 (2016).

289. Sabari, B. R. et al. Coactivator condensation at super-enhancers links phase separation and gene control. Science (80-.). 361, (2018).

290. Song, S. H. & Augustine, G. J. Synapsin isoforms and synaptic vesicle trafficking. Molecules and Cells vol. 38 936–940 (2015).

291. Hendricks, B. K. & Shi, R. Mechanisms of neuronal membrane sealing following mechanical trauma. Neuroscience Bulletin vol. 30 627–644 (2014).

292. Coleman, W. L. & Bykhovskaia, M. Synapsin I accelerates the kinetics of neurotransmitter release in mouse motor terminals. Synapse 63, 531–533 (2009).

293. Bonanomi, D. et al. Phosphorylation of synapsin I by cAMP-dependent protein kinase controls synaptic vesicle dynamics in developing neurons. J. Neurosci. 25, 7299–7308 (2005).

294. Yan, P. et al. Crosstalk of Synapsin1 palmitoylation and phosphorylation controls the dynamicity of synaptic vesicles in neurons. Cell Death Dis. 13, 1–15 (2022).

295. Vanguilder, H. D., Yan, H., Farley, J. A., Sonntag, W. E. & Freeman, W. M. Aging alters the expression of neurotransmission-regulating proteins in the hippocampal synaptoproteome. J. Neurochem. 113, 1577–1588 (2010).

296. Snijder, P. M. M. et al. Overexpression of cystathionine γ-Lyase suppresses detrimental effects of spinocerebellar ataxia type 3. Mol. Med. 21, 758–768 (2015).

297. van Erp, S. et al. Age-related loss of axonal regeneration is reflected by the level of local translation. Exp. Neurol. 339, (2021).

298. Takahara, T. & Maeda, T. Transient Sequestration of TORC1 into Stress Granules during Heat Stress. Mol. Cell 47, 242–252 (2012).

299. Thedieck, K. et al. XInhibition of mTORC1 by astrin and stress granules prevents apoptosis in cancer cells. Cell 154, 859–874 (2013).

300. Kennedy, D. et al. Characterization of G3BPs: Tissue specific expression, chromosomal localisation and rasGAP120 binding studies. J. Cell. Biochem. 84, 173–187 (2002).

301. Emara, M. M. et al. Hydrogen peroxide induces stress granule formation independent of eIF2α phosphorylation. Biochem. Biophys. Res. Commun. 423, 763–769 (2012).

302. Li, Y. R., King, O. D., Shorter, J. & Gitler, A. D. Stress granules as crucibles of ALS pathogenesis. Journal of Cell Biology vol. 201 361–372 (2013).

303. Streit, L. et al. Stress induced TDP-43 mobility loss independent of stress granules. Nat. Commun. 13, 1–18 (2022).

304. Gutierrez-Garcia, R. et al. G3BP1-dependent mechanism suppressing protein aggregation in Huntington's models and its demise upon stress granule assembly. Hum. Mol. Genet. 32, 1607–1621 (2023).

305. Marcelo, A., Koppenol, R., de Almeida, L. P., Matos, C. A. & Nóbrega, C. Stress granules, RNA-binding proteins and polyglutamine diseases: too much aggregation? Cell Death and Disease vol. 12 1–17 (2021).

306. Ross, C. A. & Poirier, M. A. Protein aggregation and neurodegenerative disease. Nat. Med. 10, S10 (2004).

307. Talwar, D. et al. The GAPDH redox switch safeguards reductive capacity and enables survival of stressed tumour cells. Nat. Metab. 2023 54 5, 660–676 (2023).

308. Peeples, W. & Rosen, M. K. Mechanistic dissection of increased enzymatic rate in a phase-separated compartment. Nat. Chem. Biol. 17, 693–702 (2021).

309. Wang, Q. et al. Proteomic analysis of neurofibrillary tangles in Alzheimer disease identifies GAPDH as a detergent-insoluble paired helical filament tau binding protein. FASEB J. 19, 1–12 (2005).

310. Lazarev, V. F. et al. Extracellular gapdh promotes alzheimer disease progression by enhancing amyloid-β aggregation and cytotoxicity. Aging Dis. 12, 1223–1237 (2021).

311. Lee, J. S. et al. Involvement of oxidative stress in experimentally induced reflux esophagitis and Barrett's esophagus: Clue for the chemoprevention of esophageal carcinoma by antioxidants. Mutat. Res. - Fundam. Mol. Mech. Mutagen. 480–481, 189–200 (2001).

312. Wetscher, G. J. et al. Reflux esophagitis in humans is mediated by oxygen-derived free radicals. Am. J. Surg. 170, 552–557 (1995).

313. Den Hoed, C. M., Van Blankenstein, M., Dees, J. & Kuipers, E. J. The minimal incubation period from the onset of Barrett's oesophagus to symptomatic adenocarcinoma. Br. J. Cancer 105, 200–205 (2011).

314. Van Blankenstein, M., Looman, C. W. N., Johnston, B. J. & Caygill, C. P. J. Age and sex distribution of the prevalence of Barrett's esophagus found in a primary referral endoscopy center. Am. J. Gastroenterol. 100, 568–576 (2005).

315. Kambhampati, S., Tieu, A. H., Luber, B., Wang, H. & Meltzer, S. J. Risk Factors for Progression of Barrett's Esophagus to High Grade Dysplasia and Esophageal Adenocarcinoma. Sci. Reports 2020 101 10, 1–10 (2020).

316. Kubo, A. et al. Dietary antioxidants, fruits, and vegetables and the risk of barrett's esophagus. Am. J. Gastroenterol. 103, 1614–1623 (2008).

317. Kang, J. H. E., Luben, R., Alexandre, L. & Hart, A. R. Dietary antioxidant intake and the risk of developing Barrett's oesophagus and oesophageal adenocarcinoma. Br. J. Cancer 118, 1658–1661 (2018).

318. Peng, D., Zaika, A., Que, J. & El-Rifai, W. The antioxidant response in Barrett's tumorigenesis: A double-edged sword. Redox Biology vol. 41 101894 (2021).

319. Spechler, S. J. & Goyal, R. K. Barrett's Esophagus. N. Engl. J. Med. 315, 362–371 (1986).

320. Wu, R. et al. Correct interpretation of comprehensive phosphorylation dynamics requires normalization by protein expression changes. Mol. Cell. Proteomics 10, (2011).

321. Ross, D. & Siegel, D. The diverse functionality of NQO1 and its roles in redox control. Redox Biology vol. 41 101950 (2021).

322. SantaCruz, K. S., Yazlovitskaya, E., Collins, J., Johnson, J. & DeCarli, C. Regional NAD(P)H:quinone oxidoreductase activity in Alzheimer's disease. Neurobiol. Aging 25, 63–69 (2004).

323. Martínez-Limón, A. et al. Recognition of enzymes lacking bound cofactor by Protein quality control. Proc. Natl. Acad. Sci. U. S. A. 113, 12156–12161 (2016).